UNIVERSITY OF SOUTHERN QUEENSLAND

Monitoring Damage in Advanced Composite Structures Using Embedded Fibre Optic Sensors

by

Gayan Chanaka Kahandawa

A dissertation submitted for the award of
DOCTOR OF PHILOSOPHY

Supervised by

Dr Jayantha Ananda Epaarachchi

Associate Professor Hao Wang

Faculty of Engineering and Surveying
University of Southern Queensland
Toowoomba, QLD, 4350, Australia

October, 2012

Gayan Kahandawa

Abstract

Fibre Bragg Grating (FBG) sensors are extremely sensitive to changes of strain, and are therefore an extremely useful candidate for Structural Health Monitoring (SHM) systems of composite structures. Sensitivity of FBGs to strain gradients originating from damage was observed as an indicator of initiation and propagation of damage in composite structures. To date there have been numerous research works done on distorted FBG spectra due to damage accumulation under controlled environments. Unfortunately, a number of related unresolved problems remain in FBG-based SHM systems development, making the present SHM systems unsuitable for real life applications. The work presented in this thesis highlights the application difficulties in using FBG for the SHM of advanced composite structures. The breakthrough technologies presented in this thesis resolve those major problems.

As a solution to cope with complicated FBG responses, a novel signal processing approach was introduced using Artificial Neural Networks (ANN). To accommodate complete FBG spectral data into an ANN, a novel FBG data decoding system was developed. The Fixed FBG Filter Decoding System (FFFDS), along with an ANN was found to be an excellent tool for addressing real-time data input to in-situ FBG-based SHM systems. Several experimental studies have been used to investigate the decoding system and performance of the ANN for damage detection in composite structures. The proposed system has identified a delamination within 0.01% error levels.

Even though previous work has used the distortion of FBG spectra to detect damage in composite structures, to date there is no clear definition for distortion of the FBG spectra. This is a major shortcoming in FBG-based SHM system development. This thesis presents two novel concepts, “Distortion” and “Distortion Index”. These have been used to define distortion of FBG spectra, and have been successfully used for damage identification and quantification in composite structures.

A case study was also conducted to develop optimum the FBG sensor network for efficient damage detection in a composite structure. A detailed procedure was proposed for the optimization of FBG networks. The proposed optimization procedure extensively used finite element analysis (FEA), thereby eliminating expensive and time consuming prototype component testing for optimized sensor locations.

Finally, developed decoding systems and the optimization methodology have been verified successfully using a representative sample. It was concluded that the breakthrough technologies developed under this thesis will exclude the major remaining problems associated with the development of SHM systems for advanced composite structures. Further, a few logical improvements were recommended for the development of next generation SHM systems.

Certification of Dissertation

I certify that the ideas, experimental work, results, analysis and conclusions reported in this dissertation are entirely my own effort, except where otherwise acknowledged. I also certify that the work is original and has not been previously submitted for any award, except where otherwise acknowledged.

……………………………………………….. / /
Signature of Candidate
Endorsed:

……………………………………………….. / /

Signature of Supervisor/s

……………………………………………….. / /
Signature of Supervisor/s

Acknowledgement

I would like to extend my deepest gratitude to my supervisor Dr Jayantha Epaarachchi for giving me the opportunity to undertake a PhD at the University of Southern Queensland (USQ). I am greatly indebted to him for his continuing confidence in me as well as for giving me constant support throughout these years. I am also thankful to my associate supervisor, Assoc. Prof Hao Wang. Discussions with him helped me better understand the overall research environment. His valuable suggestions were essential to improving the quality of this research.

I would like to thank The Boeing Company, for the financial and technical assistance given to this project. The support of Mr Peter Birt and Mr David Followell is gratefully acknowledged.

I greatly appreciate the academic, financial and technical support of the Faculty of Engineering and Surveying and the Centre of Excellence in Engineered Fibre Composites (CEEFC), which made this research possible. I would like to acknowledge the USQ postgraduate scholarships awarded to me to pursue my PhD study. I especially thank Prof Alan Lau, Director of CEEFC, for his continuous support that facilitated my work throughout. I am very thankful for the technical and administrative support from Wayne Crowell and Martin Geach and to all the staff and postgraduate students at CEEFC for the suggestions, support and friendship.

I would also like to thank Prof John Canning and the staff of the interdisciplinary Photonics Lab, (iPL) University of Sydney, for their technical and materials support.

The most important “*thank you*” goes to my dear wife, Poorni. Thank you for your love, for your endless patience, for comforting and encouraging me during the challenging periods. Without your support I would not have been able to complete this undertaking. I also want to thank my family, Mother and Father, who have

always believed in my capabilities. Thanks also to my son, Haridu and daughter, Hesara for sacrificing their play time and allowing me to work overtime.

To those whom I failed to mention but have played a great part of this endeavour, thank you very much.

Associated Publications

US Patent Application

Gayan Chanaka Kahandawa Appuhamillage, Jayantha Epaarachchi, Hao Wang (2012). SIGNAL MONITORING SYSTEM AND METHODS OF OPERATING SAME

Journal

Kahandawa, G., Epaarachchi, J., Wang, H., & Lau, K.T. (2012). Use of FBG sensors for SHM in aerospace structures. *Photonic Sensors, 2*(3), 203-214. doi: 10.1007/s13320-012-0065-4

Kahandawa, G., Epaarachchi, J., Wang, H., Followell, D. & Birt, P (2012) Use of fixed wavelength Fibre-Bragg Grating (FBG) filters to capture time domain data from the distorted spectrum of an embedded FBG sensor to estimate strain with an Artificial Neural Networks. *Sensors and Actuators A: Physical* (*Accepted*)

Kahandawa, G., Epaarachchi, J., Canning, J., & Lau, K.T. (2013). Novel approach for Optimisation of fibre Bragg grating sensor network for efficient damage detection in composite structures. *Journal of Multifunctional Composites* (*Accepted*)

Kahandawa, G., Epaarachchi, J., Wang, H., & Lau, K.T. (2012). Concept of Distortion Index for assessment of damage accumulation in a composite structures using spectral distortion of embedded FBG sensors. *Structural Health Monitoring* (*under review*)

Kahandawa, G., Epaarachchi, J., Wang, H., Canning, J., & Lau, K.T. (2012). Extraction and processing of real time strain of embedded FBG sensors using a fixed filter FBG circuit and an artificial neural network. *Measurment (under review)*

Refereed Conference Proceedings

Kahandawa, G. C., Epaarachchi, J. A., & Wang, H. (2011). Identification of distrotions to FBG spectrum using FBG fixed filters. Paper presented at the ICCM18, Jeju Island, Korea.

Kahandawa, G. C., Epaarachchi, J. A., Wang, H., & Canning, J. (2010). Effects of the self distortions of embedded FBG sensors on spectral response due to torsional and combined loads. Paper presented at the APWSHM3, Tokyo, Japan.

Kahandawa, G. C., Epaarachchi, J. A., Wang, H., Followell, D., Birt, P., Canning, J., & Stevenson, M. (2010). An investigation of spectral response of embedded Fibre Bragg Grating (FBG) sensors in a hollow composite cylindrical beam under pure torsion and combined loading. Paper presented at the ACAM 6, Perth, Australia.

Kahandawa, G.C., Epaarachchi, J.A., Wang, H, & Aravinthan, T (2010). The developments of structural health/integrity monitoring systems using FBG sensors at CEEFC of USQ. Paper presented at Southern Region Engineering Conference (SREC 2010), Toowoomba, Australia.

Kahandawa, G., Epaarachchi, J., & Wang, H. (2012). Use of FBG sensors in SHM of aerospace structures. Paper presented at the Third Asai Pacific Optical Sensors Conference (APOS 2012), Sydney, Australia.

Kahandawa, G.C., Hafizi, Z.M., Epaarachchi, J.A., & Lau, K.T. (2012) Detecting delamination in a composite structure using an Embedded FBG – AE hybrid System. Paper presented at the ACAM 7, Adilade, Australia.

Kahandawa, G.C., Epaarachchi, J.A, Wang, H., & Lau, K.T., (2012). Prediction of obsolete FBG sensor using ANN for efficient and robust operation of SHM systems. Paper presented at the APWSHM 2012, Melbourne, Australia.

Kahandawa, G.C., Epaarachchi, J.A., Wang, H., & Lau, K.T. (2012). Use of network of FBG sensors for efficient detection of delamination in FRP structures. Paper presented at the ACCM8, KualaLumpur, Malaysia.

Kahandawa, G.C., Epaarachchi, J.A., Lau, K.T., & Canning, J. (2013). Estimation of strain of distorted FBG sensor spectra using a fixed FBGfilter circuit and an artificial neural network. Paper accepted at the IEEE ISSNIP 2013, Melbourne, Australia.

Table of Contents

Table of Figures

List of Tables

CHAPTER 1
Introduction

1.1 Background and Significance

Fibre reinforced polymer (FRP) composites have been used as an engineering material for more than six decades. The main attraction of the FRP is its superior strength-to-weight ratio. Aircraft and defence industries have been spending billions of dollars on investment in these composites to produce lightweight subsonic and supersonic aircrafts. Other desirable properties, such as the ease of fabrication of complex shapes and the ability to tailor desirable properties to suit different engineering applications, are enviable for an advanced material. Since research and development in the aircraft industry and space exploration agencies have been focused on FRP for many years, most of the advanced fibre composites available today, have one way or another, their origins in these fields.

The weight-save or positive weight spiral in the aircraft industry is directly translated to the enhancement of the load carrying capacity of civil aircraft, while for the fighters, it will be translated to the performance enhancement (mainly on the fuel carrying capacity versus the flying speed). As composites are partially made from polymer-based materials, they possess very good damping and fatigue resistance properties as compared with traditional metallic materials.

The commercial aircraft industry is gradually replacing metallic parts with FRP composites as much as possible. Hence, the FRP composites are frequently applied to primary load-bearing structures in the newly developed aircraft such as Boeing 787 and Airbus 380. However, the main disadvantages of using FRP composites in the aircraft industry are their difficulty for repair, anisotropic behaviour, high initial setup cost, and most importantly the complex failure criteria. Because of these undesirable properties, the FRP composite structures in the aircraft need to be closely monitored to prevent unexpected failure.

FRP composite structures can include stress-concentrated regions such as pin-loaded holes and other cut-outs. These stress concentrations easily induce damage that includes concurrent splitting, transverse cracking, and delamination (F. Chang & Chang, 1987; Kamiya & Sekine, 1996; Kortscho & Beaumont, 1990). Unlike metals, the failure modes of composites are very difficult to predict. Therefore, there are no established standards for composite materials. For this reason, it is essential to monitor advance composites regularly. In view of the aforementioned issues, a structural health monitoring (SHM) technique has recently been developed for these composite structures (F. K. Chang, 2003; Zhou & Sim, 2002).

Monitoring of composites began with damage detection technologies such as vibration and damping methods (Adams, Cawley, Pye, & Stone, 1978). Then sophisticated offline non-destructive test (NDT) methods were developed for the safe operation of composite structures. However, with the increasing complexity of structures, offline NDT was insufficient and developments of online SHM systems became vital.

The process of implementing the damage detection and characterization strategy for engineering structures is referred to as SHM. Here, the indicator for damage is defined as changes to the material properties or changes to the structural response of the structure. The SHM process involves the observation of a system over time using periodically sampled dynamic response measurements from an array of sensors.

To address complex failure modes of FRP composites, a SHM system must be efficient, robust and accurate. Due to recent developments in the aerospace industry, utilization of FRP composites for primary aircraft structures, such as wing leading-edge surfaces and fuselage sections, has increased. This has led to a rapid growth in the field of SHM. Impact, vibration, and loading can cause damage, such as delamination and matrix cracking, to the FRP composite structures. Moreover, the internal material damage can be undetectable using conventional techniques, making inspection of the structures for damage and clear insight into the structural integrity difficult using currently available evaluation methods.

The SHM system developed to monitor aircraft and space structures must be capable of identifying multiple failure criteria of FRP composites (Reveley, Kurtoglu, Leone, Briggs, & Withrow, 2010). Since the behaviour of composites is anisotropic, multiple numbers of sensors must be in service to monitor these structures under multi-directional complex loading conditions. The layered structure of the composites makes it difficult to predict the structural behaviour only by using surface sensors. To address this issue, embedded sensors must be used, and the sensors used must possess sufficient durability as it is not possible to replace embedded sensors after fabrication of the parts.

The Fibre Bragg Grating (FBG) sensor is one of the most suitable sensors for the SHM of aircraft structures. The diminutive FBG sensors can be embedded in FRP composites during the manufacturing of the composite part with no adverse effect on the strength of the part. This sensor has a narrowband response with a wide operating range, hence can be highly multiplexed. This nonconductive sensor can operate in electromagnetically noisy environments without any interference. The FBG sensor is made up of glass possessing a long life time comparable to that of FRP composites. Because of its low transmission loss, the sensor signal can be monitored from longer distances making it suitable for remote sensing (K. O. Hill & Meltz, 1997; Kersey et al., 1997).

The FBG sensor's capability of detecting strain gradients along its length can be used to identify the strain variations at a critical part in the FRP composites structure through an optical phenomena called chirp, in the reflected spectra of the FBG sensor (P. C. Hill & Eggleton, 1994; Kersey et al., 1997). This phenomenon has been used for decades of research to detect damage in the composite structures (Okabe, Yashiro, Kosaka, & Takeda, 2000; Takeda, Okabe, & Takeda, 2002). But there are numerous cases reported where the chirp or the distortion of the FBG spectrum was not limited to stress concentrations (Y. Wang et al., 2008). There are other causes of chirp, and it is necessary to eliminate such effects to identify damage accurately.

As such, there are many remaining unresolved problems and engineering challenges in FBG-based SHM systems. An extraction of important data from FBG spectra is a significant problem, which remains unsolved after many decades of research work. It is clear that the multiple causes lead to distortion to the FBG response spectra. Most of the effects cannot be eliminated in advanced aerospace applications. In order to identify damage from the distortions to the FBG response spectra, the individual contribution from each effect needs to be identified and eliminated. To unambiguously identify the effects from the damage, extensive computational power is required for post-processing of the spectral data. Figure 1-1 shows FBG response spectra from an FBG embedded near a damaged location with the part under the complex multi-directional loading.

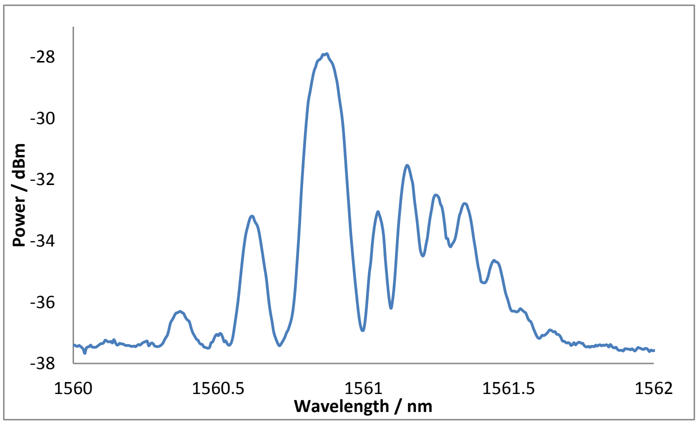

Figure 1-1: Distorted FBG spectra due to multiple effects

With the complex layout of composite structures, it is difficult to embed two sensors identically in two similar structures. The sensitivity of FBG is nano-meter range and small shift of location makes the two environments different to two sensors. As a result, it is difficult to compare fine spectral data of two spectra from two FBG sensors. Consequently, it is impossible to have universal decision making algorithms to work with FBG sensors. This complication is a major unsolved problem in the FBG-based SHM. Scarcity of adaptive decision making systems needs to be addressed.

The manufacturing of advanced composite component with embedded sensors is another significant engineering challenge associated with FBG-based SHM systems. The number of sensor must be optimized, and there should be backup systems in place for any redundant sensors after manufacture. Further, the embedded FBG network must be robust enough for compensating situations such as redundant sensors during operations. These unresolved critical problems have caused barriers to the development of SHM systems.

As a consequence, in a controlled/special laboratory environment, it is possible to discuss and interrelate the FBG spectra with the damage by creating an artificial damage and observing spectrum of an FBG which is embedded closer to the damage location. But in the general application if such spectrum is observed, it is not possible to interpret the spectrum in order to identify the damage. In general application, identification of relevant features from the spectra is essential for damage detection.

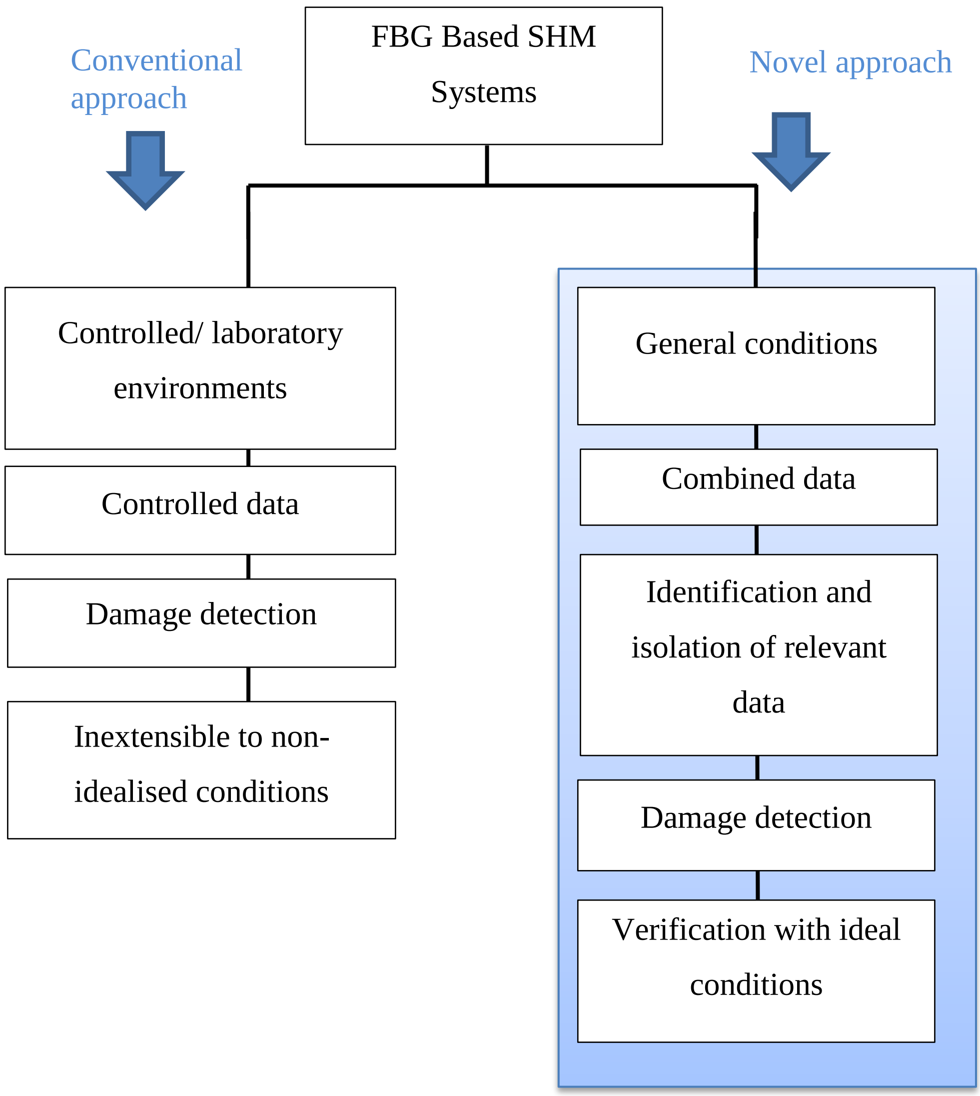

Figure 1-2: Novel approach to FBG-based SHM systems

Most of the research work on FBG-based SHM systems are on controlled environments. But the inherent properties (non-unique/non-repeatable) of FBG sensors make the systems inextensible for general applications. This prevents the reductionist method of isolating and studying effects individually, which is needed to work with FBG sensors in general conditions and to study the system as a whole, thus making SHM systems valid for real applications. Therefore the research work in this thesis addresses the fundamental unresolved problems in application of FBG-based SHM systems for real structures. As such, the research work planned here is a breakthrough for FBG-based SHM systems.

1.2 Objectives

The aim of this study is to investigate the unresolved problems associated with applications of FBG-based SHM systems. The main objectives of the study are the following:

- Identification of a/the general damage matrix which can be monitored using FBG-based SHM system
- Identification of spectral distortion of an FBG sensor in the real world environment in the vicinity of the damage
- Identification of limitations of FBGs in detection of damage
- Development of a method to quantify spectral distortion with respect to the quality of damage
- Optimisation of the FBG network
- Development of a damage detection matrix and decision making algorithms and development of FBG-based SHM systems.

1.3 Innovation and expected outcomes

The main objective of this research is to develop a FBG-based SHM system that can cope with general FRP applications, rather than for a particular idealised condition.

To achieve the set objectives, this study will follow a bottom up concept. First, the complex damage mechanism of the composite will be identified with the critical cause of damage. Subsequently, the damage will be quantified and monitoring indicators will be established. Building upon this foundation, the project will carefully devise mechanisms and algorithms to:

- Extract useful data related to damage identification from distorted FBG spectra
- Analyse extracted FBG spectral data to identify strain field at the FBG location
- Optimisation of the FBG sensor network
- Identify and quantify the damage
- Issue a warning to a monitoring system

Therefore, research work planned in this thesis was carefully selected to address most of the unsolved problems in the application of FBG-based SHM systems. As a consequence the experience gained from this research will be the first information of its kind. The following expected outcomes are innovative technologies in the FBG-based SHM field:

- Decoding system for FBG spectra
- An ANN based decision making algorithm
- FBG sensor network optimising procedures
- FBG-based SHM system for general/real application

The developed system is "Patent" pending. The industry partner, The Boeing Company, USA, organised the patent application with the US Patent office (Appendix A).

1.4 Outline of the thesis

This thesis is divided into 6 chapters which describe the different investigations conducted in this study:

- The first chapter outlines the background, research gap, significance and objectives of this study. Further it details the outline of this thesis
- Chapter 2 gives an overview of the composites used in the aerospace industry. The advantages of the use of composites in aerospace applications and the drawbacks are also discussed. Furthermore, the complex failure criteria of the composite materials and the requirement of reliable SHM systems for safe operation of FRP structures will be discussed
- Chapter 3 outlines the use of embedded FBG sensors for SHM of composite structures. The desirable properties of FBG sensors for damage detection in FRP structures are investigated. Then, the unresolved problems associated with the real application of FBG sensors will be discussed

- Chapter 4 introduces the use of ANN, for post-processing of FBG spectral data. A novel decoding system will be introduced to decode complex response spectra of an FBG. Finally, the procedures will be discussed and the integration of the decoding system and ANN for damage detection will be demonstrated experimentally

- Chapter 5 will demonstrate procedures for optimising a FBG sensor network for efficient damage detection in a composite structure using the system introduced in Chapter 4.

- The main body of the thesis ends with Chapter 6 which presents the main conclusions of the research and the recommendations for future work.

CHAPTER 2

Damage in composite structures

2.1 Introduction

Composite material is a combination of two or more chemically different materials with a distinct interface between them. The constituent materials retain their original properties and the composite materials provide combined properties which are different from the constituents. There is neither chemical reaction between constituents, nor change to the chemical structure of the constituents. One of the constituents makes a continuous phase which is called the matrix. The others act as reinforcement (Mallick, 1997).

The matrix material of a composite can be polymer, metal or ceramic, hence composite materials are classified as polymer matrix composites (PMC), metal matrix composite (MMC) and ceramic matrix composites (CMC). Figure 2-1 illustrates the evaluation of composite materials.

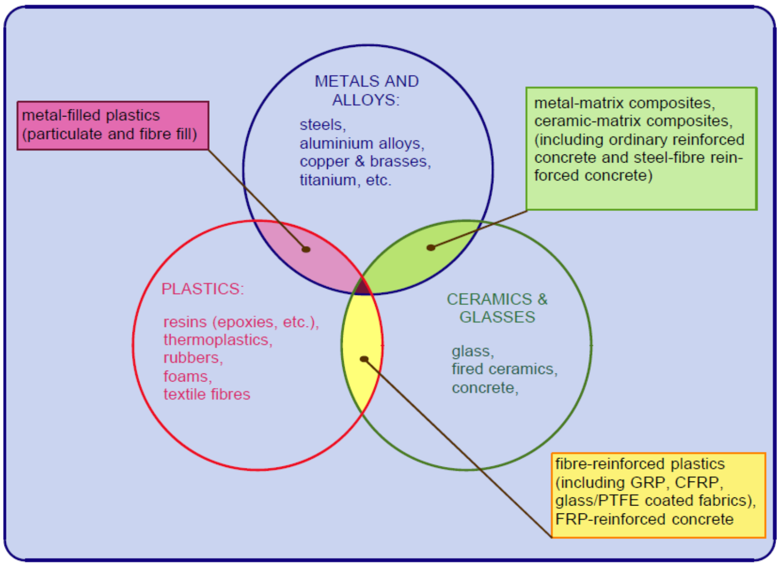

Figure 2-1: Composite materials

The majority of the composites, Glass Fibre Reinforced Polymer (GFRP) and Carbon Fibre Reinforced Polymer (CFRP), are based on a polymer matrix. The development of PMCs for structures started in 1950s, and they are by far the most common fibre reinforced composite material in use today. The matrix is a key factor determining the characteristics of a composite material. In the applications of glass fibre reinforced plastics the resin used comes with two parts, the resin and the hardener. The resin/hardener ratio also effects the mechanical properties of a composite (d'Almeida & Monteiro, 1998).

Fibres are the principle load carrying component in fibre reinforced composites. The effectiveness of fibres in composite materials depends on the size, type, volume fraction and orientation of fibres in the matrix. A large variety of fibre types are available for engineering fibre reinforced composite materials. The most common fibre types are glass fibre and carbon fibre.

Glass fibre composites are popular for applications such as boats, body parts of vehicles, small aircrafts, durable goods and consumer goods applications because of their low cost. The comparative strength with carbon fibre is less but the cost and simple manufacturing technology makes glass fibre popular in low-end applications.

Carbon fibre provides tensile modules of 188.9 GPa, which is closer to ferrous materials and, most importantly, the strength to weight ratio is superior. For this reason, carbon fibre composites have replaced the metallic parts used in most aircraft and military applications.

2.1.1 Glass fibres

Glass fibres are manufactured by drawing molten glass into very fine threads and then immediately protecting them from contact with the atmosphere or with hard surfaces in order to preserve the defect free structure that is created by the drawing process. Synthetic fibres are as strong as any of the newer natural fibres but they lack rigidity on account of their molecular structure. The properties of glasses can be modified to a limited extent by changing the chemical composition of the glass, but the only glass used to any great extent in composite materials is ordinary borosilicate glass, known as E-glass. The largest volume usage of composite materials involves E-glass as the reinforcement. S-glass has somewhat better properties than E-glass, including higher thermal stability, but its higher cost has limited the extent of its use. The stiffness of experimental calcium aluminate glass fibres can be as high as 180GPa.

2.1.2 Carbon fibres

By oxidising and pyrolysing a highly drawn textile fibre, such as poly acrylonitrile (PAN), to prevent it from shrinking in the early stages of the degradation process, and subsequently hot-stretching it, it is possible to convert the fibre to a carbon filament with an elastic modulus that approaches the value that would predict from a consideration of the crystal structure of graphite. However, the final strength is usually well below the theoretical strength of the carbon-carbon chain (Watt, 1970). The influence of strength limiting defects is considerable, and clean-room methods of production can result in substantial increases in the tensile strength of commercial materials. Prior to sale, fibres are usually surface-treated by chemical or electrolytic oxidation methods to improve the quality of adhesion between the fibre and the matrix in a composite. Depending on processing conditions, a wide range of mechanical properties (controlled by structural variation) can be obtained, and fibres can, therefore, be chosen from this range so as to give the desired composite properties. Recent developments in this field have led to the use of pitch as a precursor in place of textile fibres, and these newer materials have extremely high stiffness, compared to PAN based fibres, but rather lower strengths (Fitzer & Heine, 1988).

2.1.3 The matrix of composites

The matrix binds the fibres together, holding them aligned in the important stressed directions. Loads applied to the composite are then transferred into the fibres, the principal load-bearing component, through the matrix, enabling the composite to withstand compression, flexural and shear forces, as well as tensile loads. The ability of composites reinforced with short fibres to support loads of any kind, is dependent on the presence of the matrix as the load-transfer medium, and the efficiency of this load transfer is directly related to the quality of the fibre/matrix bond.

The matrix must also isolate the fibres from each other so that they can act as separate entities. Many reinforcing fibres are brittle solids with highly variable strengths. When such materials are used in the form of fine fibres, not only are the fibres stronger than the monolithic form of the same solid, but there is the additional benefit that the fibre aggregate does not fail catastrophically. Moreover, the fibre bundle strength is less variable than that of a monolithic rod of equivalent load-bearing ability. But these advantages of the fibre aggregate can only be realized if the matrix separates the fibres from each other so that cracks are unable to pass unimpeded through sequences of fibres in contact (which would result in completely brittle composites).

The matrix should protect the reinforcing filaments from mechanical damage (eg. abrasion) and from environmental attack. Since many of the resins which are used as matrices for glass fibres prevent diffusion of water, this function is often not fulfilled in many GFRP materials and the environmental damage that results is aggravated by stress. In cement, the alkaline nature of the matrix itself is damaging to ordinary glass fibres and alkali-resistant glasses containing zirconium have been developed (Proctor & Yale, 1980) in an effort to counter this effect. For composites like MMCs or CMCs operating at elevated temperature, the matrix would need to protect the fibres from oxidative attack.

A ductile matrix will provide a means of slowing down or stopping cracks that might have originated at broken fibres. Conversely, a brittle matrix may depend upon the fibres to act as matrix crack stoppers.

Through the quality of its ‘grip’ on the fibres (the interfacial bond strength), the matrix can also be an important means of increasing the toughness of the composite. By comparison with the common reinforcing filaments, most matrix materials are weak and flexible, and their strengths and moduli are often neglected in calculating composite properties. But metals are structural materials in their own right and in MMCs their inherent shear stiffness and compressional rigidity are important in determining the behaviour of the composite in shear and compression. The potential for reinforcing any given material will depend to some extent on its ability to carry out some or all of these matrix functions.

2.2 Applications of Composites

Composite materials have been used a wide range of applications such as aerospace, automobile, bio-engineering, structural engineering, marine engineering, sports.

In the aerospace industry, a wide range of load-bearing and non-load-bearing components are already in use in both fixed-wing and rotary wing aircraft. Many military and civil aircraft now contain substantial quantities of lightweight, high-strength carbon-, Kevlar- and glass-fibre composites, as laminated panels, mouldings, and sandwich composite structures with metallic or resin-impregnated paper honeycomb core materials. They are used in air frames, wing spars, spoilers, tail-plane structures, fuel tanks, drop tanks, bulkheads, flooring, helicopter rotor blades, propellers, and structural components, pressured gas containers, radomes, nose and landing gear doors, fairings, engine nacelles (particularly where containment capability is required for jet engines), air distribution ducts, seat components, access panels, and so forth.

Many modern light aircraft are being increasingly designed to contain as much lightweight composite material as possible. For elevated-temperature applications carbon-fibre-reinforced composite is in use. Concord's disk brakes used this material, rocket nozzles and re-entry shields have been fashioned from it, and there are other possibilities for its use as static components in jet engines. Rocket motor casings and rocket launchers are also frequently made of reinforced plastics. A particularly interesting (and important) application of composites is in its development in Australia as a means of repairing battle damage (patching) in metal aircraft structures.

Space applications offer many opportunities for employing light-weight, high-rigidity structures for structural purposes. Many of the requirements are the same as those for aeronautical structures, since there is a need to have low weight and high stiffness in order to minimize loads and avoid the occurrence of buckling frequencies. Dimensional stability is at a premium, for stable antennae and optical platforms, for example, and materials need to be transparent to radio-frequency waves and stable towards both UV radiation and moisture.

2.3 Failure modes of Composites

Damage in the FRP structures can be defined as the changes to material properties and/or changes to the structural response of the structure. Damage can be in both matrix and/or fibre.

Many reinforced plastics consist of brittle fibres, such as glass or carbon, in a weak, brittle polymer matrix, such as epoxy or polyester resin. An important characteristic of these composites, however, is that they are surprisingly tough, largely as a result of their heterogeneous nature and construction. During deformation, micro-structural damage is widespread throughout the composite, but much damage can be sustained before the load-bearing ability is impaired. Beyond some critical level of damage, failure may occur by the propagation of a crack which usually has a much more complex nature than cracks in homogeneous materials. Crack growth is inhibited by the presence of interfaces, both at the microstructural level between fibres and matrix, and at the macroscopic level as planes of weakness between separate laminae in a multi-ply laminate. The fracturing of a composite therefore involves not only the breaking of the load-bearing fibres and the weak matrix, but a complex combination of crack deviations along these weak interfaces.

Composite materials can be analysed in different levels as shown in the Figure 2-2. The analysis of damage in composite structures starts from micromechanics to macro-mechanics. The failure of composites begins with micro-cracks in the matrix. The micro-cracks increase in number under increasing deformation. Due to a mismatch in the elastic module between the neighbouring layers, there exists an onset of delamination. As the critical value of the strain energy release rate is reached, the delaminations start growing rapidly. As a result, under the condition that the matrix crack density is very high and that the angle plies can no longer take tensile load, the entire tensile load is transferred through the 0^o fibres. With further tensile loading, the 0^o fibres break. This is the final stage of failure. Under compressive load also, the laminates start buckling at the delaminated zone and may fail instantaneously.

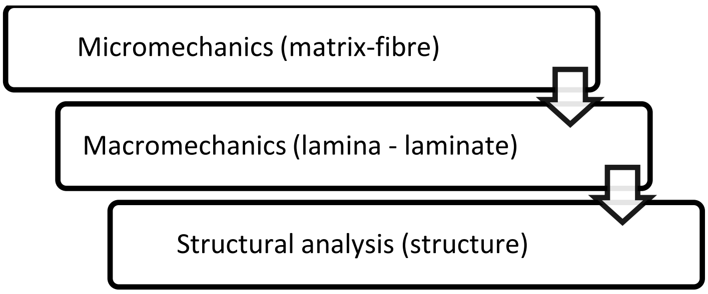

Figure 2-2: Levels of analysis for damage in composites

The evolution of a matrix crack as the initial stage of damage, followed by delamination, is also true for composites subjected to impact load (Marshall, Cox, & Evans, 1985). In most of the damage models reported in literature are transverse matrix cracks, splitting, delamination etc. and a combination of those are considered. The degradation of effective elastic module of damaged laminates used as the damage parameters. Once estimated through on-line health monitoring, such parameters can further be correlated to damage states.

Numerous failure theories have been proposed and are available to the composite structural designer (Daniel & Ishai, 2005). The failure theories have been classified into three groups, limit or non-interactive theories (maximum stress, maximum strain); interactive theories (Tsai-Hill, Tsai-Wu); and partially interactive or failure mode-based theories (Hashin-Rotem, Puck). The validity and applicability of a given theory depend on the convenience of application and agreement with experimental results.

Sun (2000) reviewed six failure theories and showed comparisons of theoretical predictions with experimental results for six different composite material systems under various loading conditions . He included uniaxial (normal and shear) loading, off-axis loading and biaxial (normal and shear) loading later. It was found, as observed previously, that most theories differed little from each other in the first quadrant (tension-tension). The biggest differences among theories occurred under combined transverse compression and shear. In this case, predictions of the Tsai-Wu interactive theory were in better agreement with experimental results than other theories.

Hinton (2004) experimentally evaluated the predictive capabilities of current failure theories (Hinton, Soden, & Kaddour, 2004). One observation of this exercise was that, even for the unidirectional lamina, predictions of the various theories differed by up to 200-300% from each other. The difficulty in evaluating failure theories is much greater in the case of a multidirectional laminate. Since the failure modes greatly depends on material properties and type of loading, different failure theories work well with different applications.

With the difficulty of evaluation of failure, SHM plays a major role in composite structures.

2.3.1 Delamination

Delamination, which is the failure of the interface between two plies, is known as the silent killer of the composite structures. It is caused by normal and shear tractions acting on the interface, which may be attributed to transverse loading, free edge effect, ply-drop-off, or local load introduction. Delamination can significantly reduce the structural stiffness and the load carrying capacity and, therefore, is considered as one of the critical failure modes in laminated composites.

A laminate is constructed from groups of individual unidirectional plies which are laid at various angles, depending upon design requirements, or from layers of woven cloth laid at various angles to the main stress axes. The tension/shear coupling effects cause shear stresses to be developed in the plane of the laminate, especially near free edges, when the material is stressed. As inter-laminar planes in non-woven composites are always planes of weakness, the inter-laminar shear stresses may easily become large enough to disrupt or delaminate a composite well before its overall tensile strength is reached. A crack travelling through a given ply may therefore find it energetically favourable to deviate along an inter-laminar plane. Under such circumstances, considerations of fibre debonding and pull-out are of little significance.

For prediction of onset of interface damage, numerical methods have been developed based on the interface strength. A general, strength based First Ply Failure (FPF) criterion suitable for the assessment of interface damage has been proposed by Puck and Scharmann (1998). For the prediction of formation of an initial delamination in an intact interface a strength/energy approach is proposed (Wimmer, Schuecker, & Pettermann, 2009) which combines strength criteria with fracture mechanics. For the simulation of delamination growth fracture mechanics are frequently used. It is widely accepted that conventional fibre reinforced epoxy resins show brittle fracture behaviour. Consequently, local material non-linearity in the vicinity of the delamination front are neglected and Linear Elastic Fracture Mechanics (LEFM) can be used. Several techniques based on LEFM have been developed and are utilized successfully within the framework of the Finite Element Method (FEM) for the simulation of delamination growth, such as crack tip elements (Jha & Charalambides, 1998), the Virtual Crack Extension Technique, and the Virtual Crack Closure Technique (VCCT) (Liu et al.). Wimmer and Pettermann (2008) suggested a numerically efficient semi-analytical approach for the prediction of delamination growth and its stability was also proposed. An alternative method that takes into account the non-linear interface behaviour at the delamination front introduces a cohesive zone (Barenblatt, H.L. Dryden, & Howarth, 1962). Based on this idea, Cohesive Zone Elements (CZE) have been developed within the FEM (Alfano & Crisfield, 2001) for the simulation of delamination.

Among the failure modes of composite structures, delamination is the most dangerous failure. In real applications, it is difficult to predict the behaviour of delaminations. The hidden nature of the growth of delamination can result in sudden failure of composite structures. Consequently, for safer operation of composite structures, it is vital to have SHM systems on board to identify delaminations both qualitatively and quantitatively.

2.4 Modelling of multilayer composite structures

Fibre-reinforced composites are modern construction materials from which products used in many areas are made. These materials are characterised by very good mechanical properties. They are ideal for structural applications where high strength and stiffness are required. The mechanical properties of the composite are not only defined by the properties of reinforcing fibres and their percentage participation in this material; the full advantages of such materials are obtained when the fibres are optimally distributed and oriented in each layer, with respect to the assumed objective behavioural measure in the optimisation process under the structure's actual loading conditions.

In the process of modelling composite structures, two major approaches, Equivalent Single Layer (ESL) and Layer Wise (LW) models are used.

2.4.1.1 Equivalent Single Layer (ESL) modelling

The ESL description represents the composite stack as a single layer, whose stiffness properties are "equivalent" to the multilayered structure. This approach permits the exploitation of established models developed for homogeneous structures, such as Bernoulli and Timoshenko beams, and Kirchhoff and Reissner-Mindlin plates. In an ESL model, the number of DOF is independent from the number of layers constituting the laminate (Reddy, 1993). From the FEM modelling point-of-view, the ESL description is thus easily embedded into standard element formulations by simply declaring a composite cross-section. If the layer wise variation of parameters is required, layer wise modelling should be used.

2.4.1.2 Layer Wise (LW) modelling

In a Layer-Wise description, each separate layer of the laminate is explicitly represented with its own degree of freedom (DOF). Since this description introduces a number of DOF that depends on the number of layers constituting the laminate, the LW approach can rapidly become very complicated. FEM modelling of an LW approach relies classically on the use of solid brick elements that are stacked on each other to form the whole laminate (Barbero & Reddy, 1991). ABAQUS also permits staking of continuum-based (solid) shells in order to reduce the conditioning problems related to the very different element edge lengths (the laminate thickness generally being much smaller than the in-plane dimensions).

The LW modelling method consumes higher modelling time and calculations time of the computer. It is clear that a simplified method as the ESL requires less design time and less computing time. Instead, the LW may require a discrete design and calculation time that could become significant with the use of many finite elements over the composite cross-section.

For the research work in this thesis, it is essential to have LW modelling. The embedded FBG sensors report the strain between layers and hence, FEA data should be available layer wise for comparison reasons. In the ABAQUS modelling environment for composites, two different element types (the conventional shell and continuum shell) have been commonly used.

The conventional shell is the planar 2D representation of a solid element, even if deformable in the 3D space. A thickness is given to the planar element by assigning a section. In this case it is a composite one. However, since the geometry is defined in the two-dimensional space, it is not possible to assign an element to each layer of the composite. This would always lead to an ESL model.

For LW modelling, solid elements should be used. The promising solid element used in composite modelling is the continuum shell element. Continuum shell elements are three-dimensional stress/displacement elements for use in modelling structures that are generally slender, with a shell-like response but continuum element topology.

2.4.2 Modelling composite structures using FEA

Due to the anisotropic nature of composites, the material properties are commonly different in the three principal directions. The reinforcement of a composite is typically assigned the 1-direction, whereas the 2 and 3-directions are known as the transverse directions. Unlike 2-D conventional shell elements, the orientation of material properties must be explicitly assigned when using 3-D continuum elements.

Figure 2-3 shows a composite plate that has been built with continuum shell elements. The global coordinate system is used to define the material orientation. The global system does not rotate with the curvatures of the model, thus incorrectly defining material properties for any portion of this curved plate not lying in the x-y plane. Discrete or local coordinate systems can be used for which a normal and reference direction can be assigned depending on the reinforcement and transverse directions of the material. It is very important to have the material orientation right for the accurate modelling of composite structures. Throughout the modelling used in this study, the material properties used are, E1=34.412 GPa, E2=6.531 GPa, E3=6.531 GPa, ν12=0.217, ν13=0.217, ν23=0.336, G12=2.433 GPa, G13=2.433

GPa, and G23=1.698 GPa. Direction 1 is the direction of angle x axis, while directions 2 and 3 are y and z respectively.

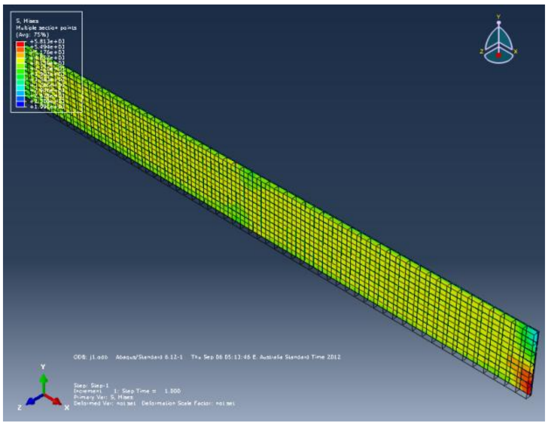

Figure 2-3: Composite plate modelled in ABAQUS

2.4.2.1 Continuum shell elements

Composite layups are normally structures with significantly smaller thicknesses compared to other dimensions. Shell elements are used to model such structures. Normally conventional shell elements can be used to model structures in which the thickness is significantly smaller than the other dimensions. It is possible to define the thickness in the property module while creating the section. In contrast, in assigning continuum shell elements to solid parts, ABAQUS determines the thickness from the geometry of the part. From a modelling point-of-view continuum shell elements look like three-dimensional continuum solids, but their kinematic and constitutive behaviour is similar to conventional shell elements. For example, conventional shell elements have displacement and rotational degrees of freedom, while continuum solid elements and continuum shell elements have only displacement degrees of freedom (Figure 2-4).

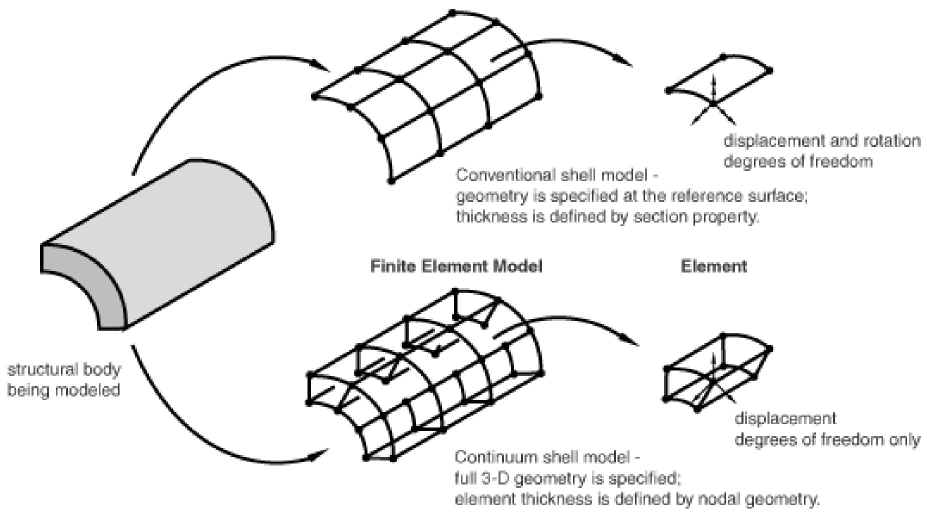

Figure 2-4: Conventional shell elements and continuum shell elements in ABAQUS (ABAQUS Analysis User manual)

Throughout the study, continuum shell elements (SC8R) have been used they provide both top surface and bottom surface strains. SC8R stands for continuum stress/displacement shell with 8 nodes and reduced integration (Figure 2-5). It is desirable to have strain variations at exact locations when it comes to comparison of strain readings obtained from embedded sensors (as discussed in Chapters 3 and 4).

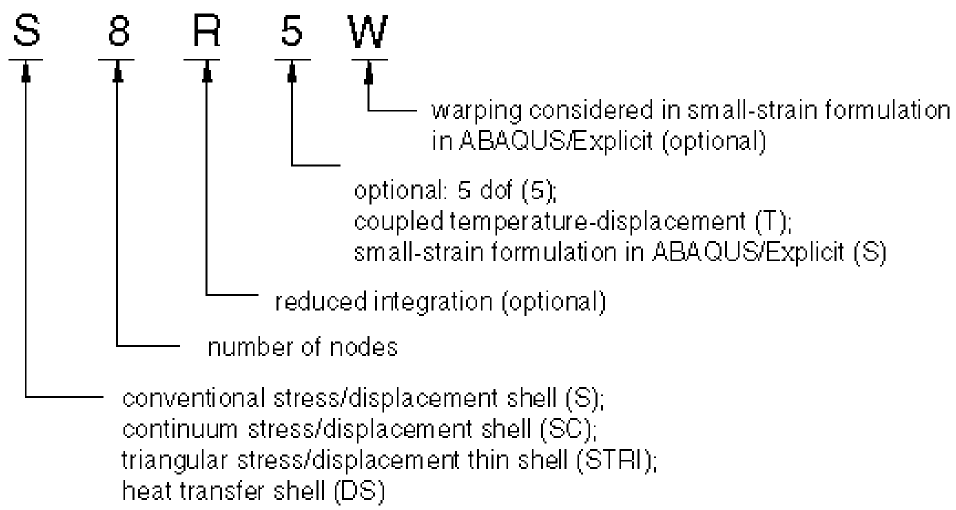

Figure 2-5: SC8R elements in ABAQUS (ABAQUS Analysis User manual)

2.4.3 Modelling plated structures

Plated structures are widely used in many engineering constructions ranging from aircraft to ships, and from off-shore structures to bridges and buildings. Given their diverse use in severe loading environments, it is vital that their behaviour is analysed and understood. When it comes to FRP composite plated structures, the layer wise behaviour needs to be analysed to model the complete structure. To model the deformation of laminated plates, approaches based on the classical laminate beam or plate theory have been developed (Crawley & Lazarus, 1989). These approaches should be restricted to thin plate applications since the linear strain distribution through the thickness and zero transverse shear stress is assumed. However, the transverse shear stresses are usually important in composite laminates. As a result, it is necessary to use shear deformation theory to address moderately thick and thick laminate constructions. The first-order shear deformation theory has been used for modelling the laminates using FEA. Furthermore, the Layer Wise theory and Three-dimensional (3D) coupled-analysis model have also been used.

In the damage detection of FRP composite structures, damage can be initiated from the inside of the structure as a crack or delamination. That is the key advantage of using embedded FBG sensors for damage detection in FRP composite structures. An FEA with LW modelling is essential for comparison and verification of experimental results.

Following case study was carried out to verify the FEA modelling with experimental results for a composite laminate with embedded FBG sensors. Principle of FBG is given in Chapter 3.

2.4.3.1 Sample Fabrication and experimentation

A FBG sensor with a cantered wavelength about 1550 nm was fabricated on 9um core and 125um clad diameter telecommunication grade glass fibre. The grating length was 10mm. To ensure maximum bonding between the FBG sensor and the matrix of resin in the GFRP material, the acrylate layer of the fibre was removed. An extra protective layer of rubber was applied to the fibre to enhance the sensor robustness.

The sample was fabricated with 10 layers of E-Glass fibre in the orientation 0/90/±45/90/0/0/90/±45/90/0. Kenetix R246TX epoxy resin was used as the matrix material. The FBG sensor was embedded between non-parallel layers, 3 and 4, as shown in Figure 2-6.

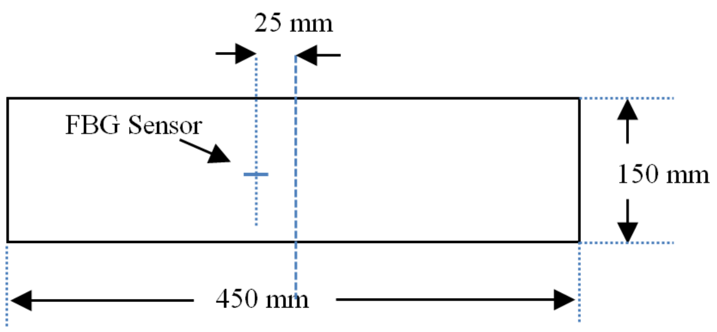

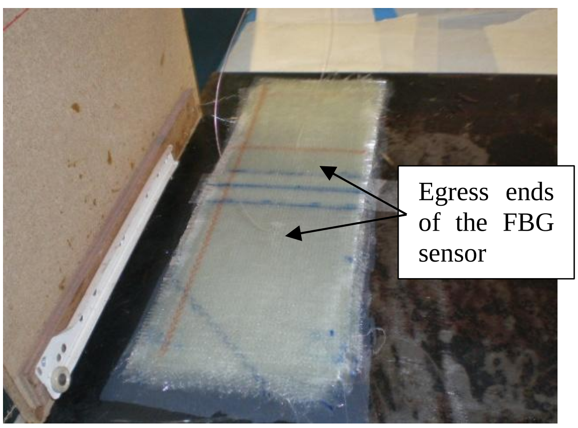

Figure 2-6: Location of the FBG sensor in the specimen between layers 3 and 4

The specimen was loaded on a four points bending test rig in steps of 25N up to 1000N maximum load using an MTS (universal Material Testing System) as shown in Figure 2-7. The specimen was simply supported with a support span of 400 mm and loaded with loading span of 150 mm as shown in the Figure 2-7(a). The response spectrum of the FBG sensor was recorded at each loading step using the setup shown in the Figure 2-7(b). Micron Optics 3.1 sm125 optical spectrum analyser was used to recode FBG spectrum and the response spectrum of the FBG sensor for no load condition and 1000N flexural load is given in the Figure 2-8. The applied load shifted the peak location of the sensor which is used to calculate stain.

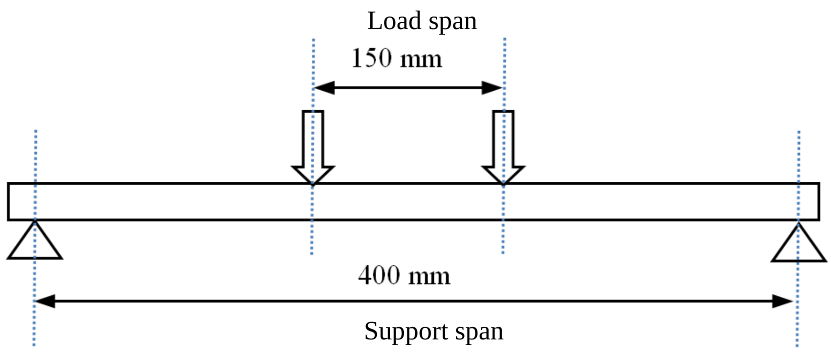

(a)

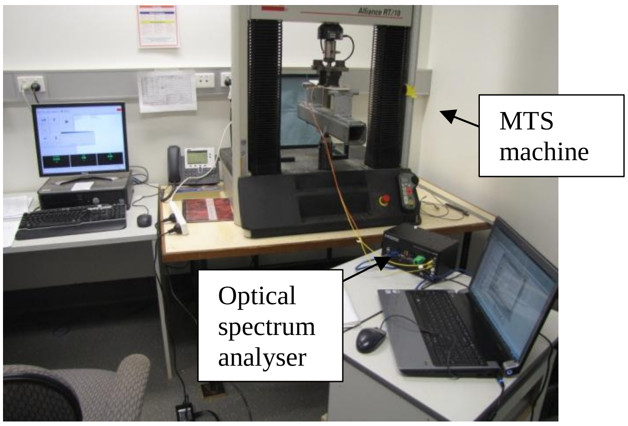

(b)

Figure 2-7: Experimental setup

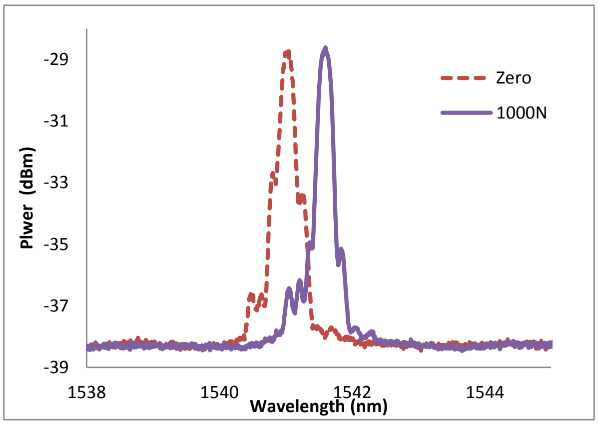

Figure 2-8: Response spectrum of the FBG sensor

2.4.3.2 FEA model of the plate

A detailed finite element model (FEM) was developed for the specimen using commercial software, ABAQUS using continuum shell elements which is SC8R: An 8-node quadrilateral in-plane general-purpose shell element, reduced integration with hourglass control, finite membrane strains.

Figure 2-9 shows the ply stack plot of the composite layup. The plies are starting from the bottom and ply 10 is the top most one. The element size was selected as 10 mm for the FEA mesh. As FBG sensors provide the average strain along the gauge length, which is 10mm in this case. The FEA mesh in 10mm is also needed for comparison.

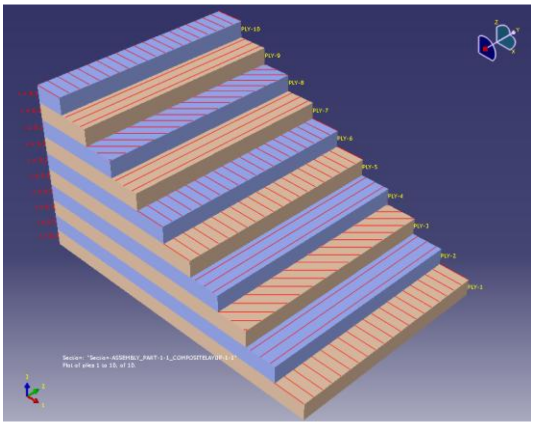

Figure 2-9: ply stack plot of the composite layup

The model was loaded similar to the four point bending experiment up to 1000N load. This FEA data was generated for strain at each layer for each loading step. Figure 2-10 gives the stress variation (S11) in the plate, in x direction, which is under 1000N bending load. At the same loading, the deflection of the plate is given in the Figure 2-11.

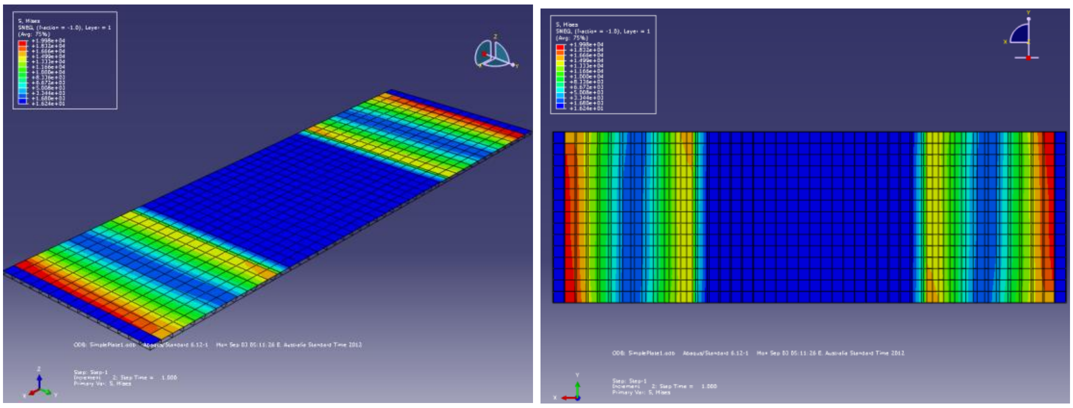

Figure 2-10: Stress variation in the model in 1000N load

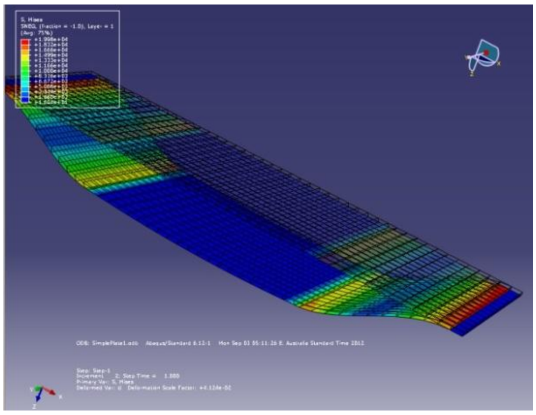

Figure 2-11: Deflection of the specimen at 1000N load

The main purpose of FEA modelling in this study is to obtain layer by layer strain variation with the loading. The FBG sensors are embedded in between layers, and hence will be measuring the strains at the location of embedment. For the SHM of composite structures, simple surface measurements and interpolation will not be sufficient. The anisotropic properties and different orientations of the reinforcement fibre layers make the monitoring insufficient only from the surface. Figure 2-12 gives the strain variation in different plys, while the structure is under 1000N flexural load.

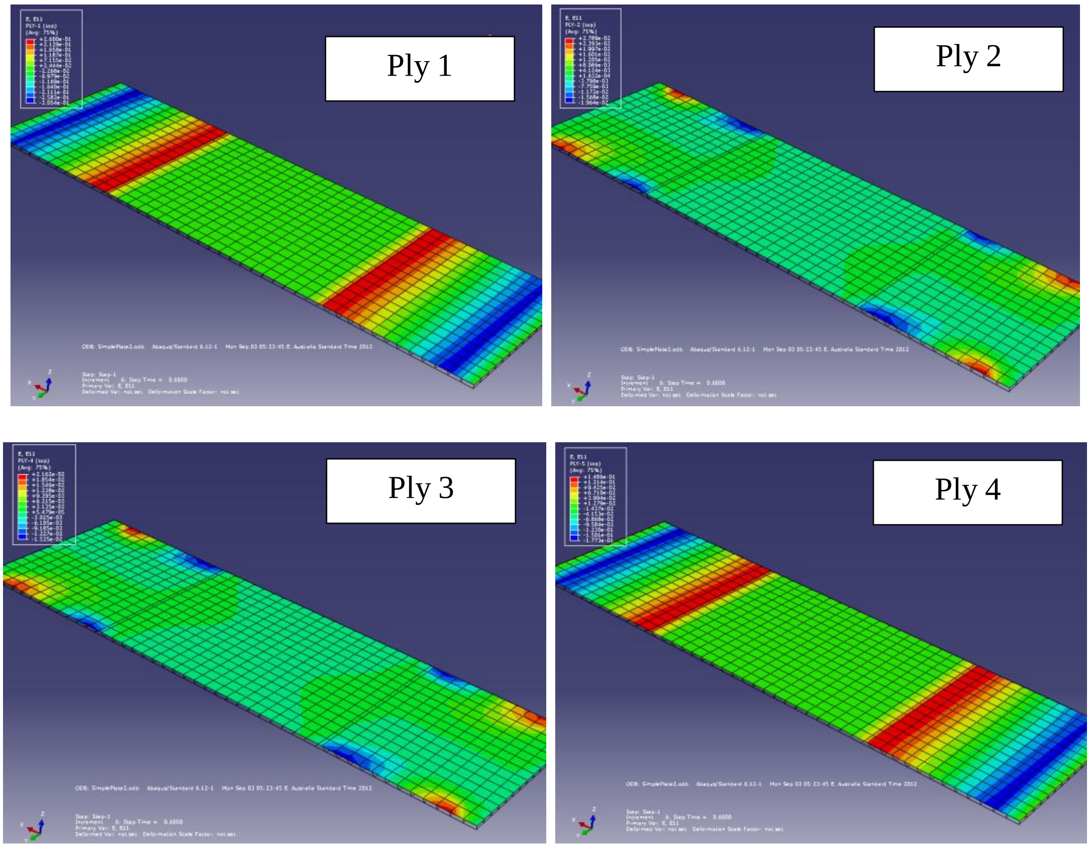

Figure 2-12: Strain variation in different layers of the specimen

The location of the embedded FBG sensor is between layers 3 and 4, and the centre of the FBG is 25 mm shifted from the centre of the specimen as given in the Figure 2-6. Similarly, an element (element 293) at the same location as the model was selected to extract strain for comparison with the experimental results as shown in the Figure 2-13.

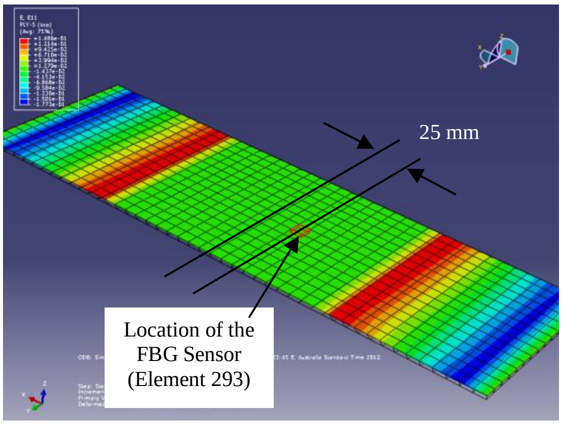

Figure 2-13: The element corresponding to the location of the FBG sensor

2.4.3.1 Results and validation of the FEA model

The strain values of each loading step for each ply were recorded for the element 293. The strain variation of the each ply (ply 1 to 10) is given in Figure 2-14. As illustrated in the Figure 2-14, the ply 1 is under tension while the ply 10 is under compression as a result of bending loading and loading direction.

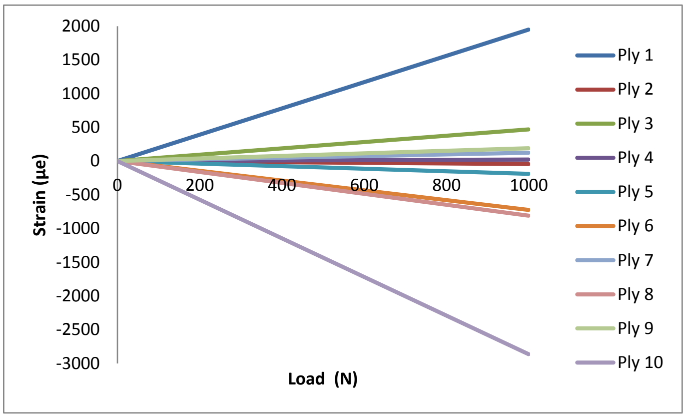

Figure 2-14: Strain variation with bending loading (ply by ply)

As the FBG sensor was embedded between ply 3 and 4, for comparison purposes, the top surface strain from ply 3 is used. Figure 2-15 shows the variation of FBG readings and the top surface strain for the element 293 for ply 3.

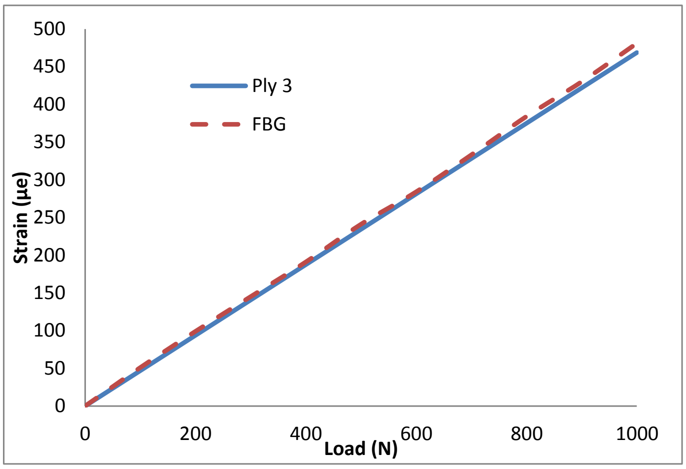

Figure 2-15: comparison of FBG reading with strain extracted from Element 293, ply 3

The strain calculated using the peak shift of the FBG sensor and the strain extracted from the FEA model from the same location is with similar agreement as shown in the Figure 2-15. The negligible mismatch towards the higher loading is due to the experimental conditions (effects) which embedded FBG sensor would undergo during operation. FBG sensor interrogation, strain calculations using FBG sensors and various other effects on FBG sensor readings are thoroughly discussed in the Chapter 3.

2.4.4 Modelling tabular structures

Tubes and pipes made of composite glass fibre/epoxy resin are widely used in engineering structures such as aircraft, construction, chemical, civil infrastructures and defence industries. Depending on the structural composite, components will undergo both static and dynamic loading during their operational lifetime. A good example is a helicopter or wind turbine blade in dynamic applications which undergo millions of cycles of severe multi-axial loadings during their operational lifetime (Figure 2-16) (Epaarachchi & Clegg, 2006). The major drawback for designers of Fibre Reinforced Polymer (FRP) materials is the complexity of the failure modes.

The failure modes in anisotropic composite materials are more complex than the isotropic materials under the multi-axial complex loading which tubes will experience during the operation. (Eric, 1995; Lee, Hwang, Park, & Han, 1999)

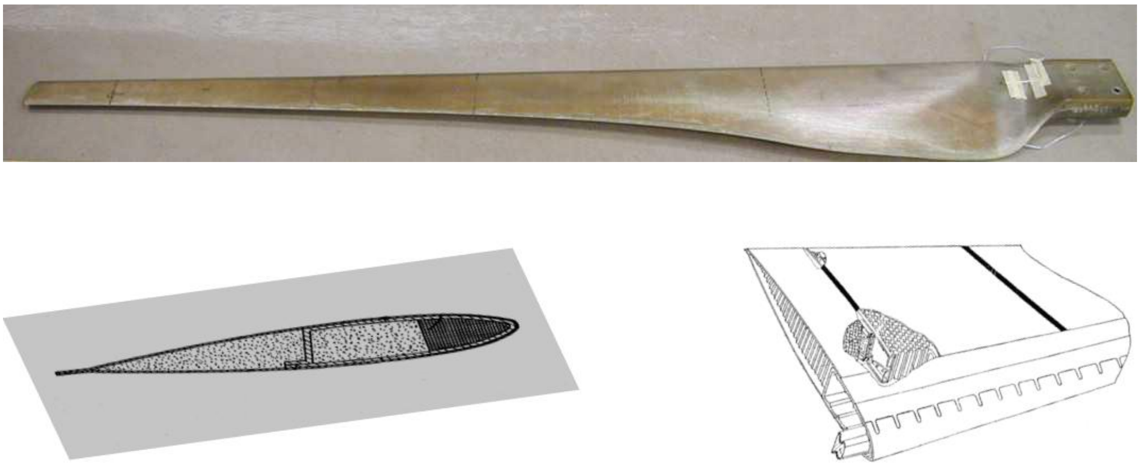

Figure 2-16: Wind turbine blade

2.4.4.1 Fabrication of the specimens

FBG sensors which operate in the range of a 1550nm centre wavelength were fabricated on 5μm core and 125μm clad diameter telecommunication grade glass fibre. The grating length is 10mm. To ensure maximum bonding between the FBG sensor and matrix of resin in the GFRP material, the acrylate layer at the grating region of the fibre was removed. Extra protective layer of rubber was applied to the fibre to maximise the handling of samples without damage to the sensors.

The specimen was fabricated with six layers of biaxial glass fibre with $90^{o}\backslash45^{o}\backslash45^{o}\backslash45^{o}\backslash45^{o}\backslash90^{o}$. Kenetix R246TX resin is used as the matrix. The inner diameter of the tube is $\varnothing = 50$mm and the thickness, $\Delta\varnothing$, is in the range of $\Delta\varnothing = 3$mm (Figure 2-17). The dimensions were selected according to the recommended geometry by Hodgkinson (2000) for torsion shear testing of thin-walled tubes to ensure the shear stress is uniformly distributed around the circumference and along the axis of the tube. The wall thickness is made small compared to the mean radius so that the through-thickness shear gradient is negligible. The ends of the specimens are over layered with additional layers and tapered to promote failure with in gauge length. The tab thickness is 10mm.

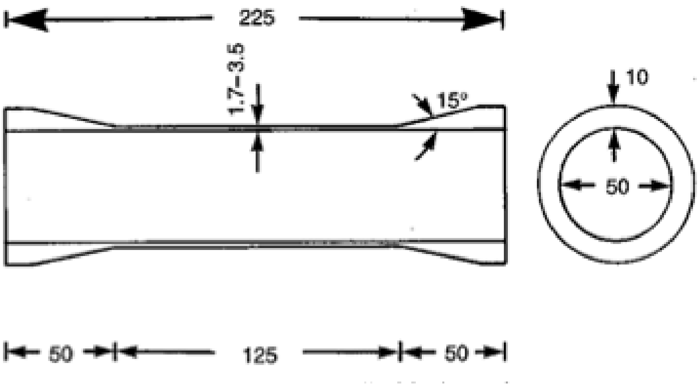

Figure 2-17: Thin-walled cylindrical specimen.

The specimen was fabricated with a rosette attached to the outer surface of the tube at the centre of the tube and with an FBG sensor located between layers 5 and 6, at an angle of 45° to the axis of the tube (Figure 2-18). The rosette was attached above the FBG sensor (Figure 2-19).

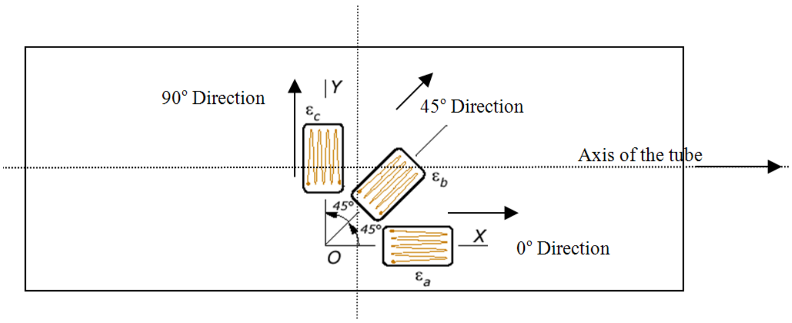

Figure 2-18: Rosette attached to the specimens.

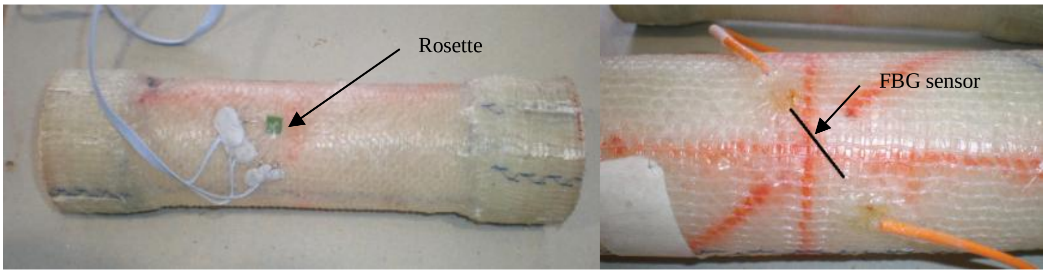

Figure 2-19: Specimen with rosette strain gauges and embedded FBG sensor.

2.4.4.2 Experimentation and results

The torsional testing equipment and the test configuration are shown in Figure 2-20. The torsional testing equipment was designed and manufactured at the Centre of Excellence in Engineering Fibre Composites (CEEFC), University of Southern Queensland (USQ) by the author (Appendix B). The specimens were mounted on the torsion test machine with one end fixed. The other end of the specimen was supported with roller supports to avoid bending of the samples. Torque was applied by loading the arm attached at the roller support side by means of a screw jack. Applied torque is measured using an S type load-cell with 0-2kN range.

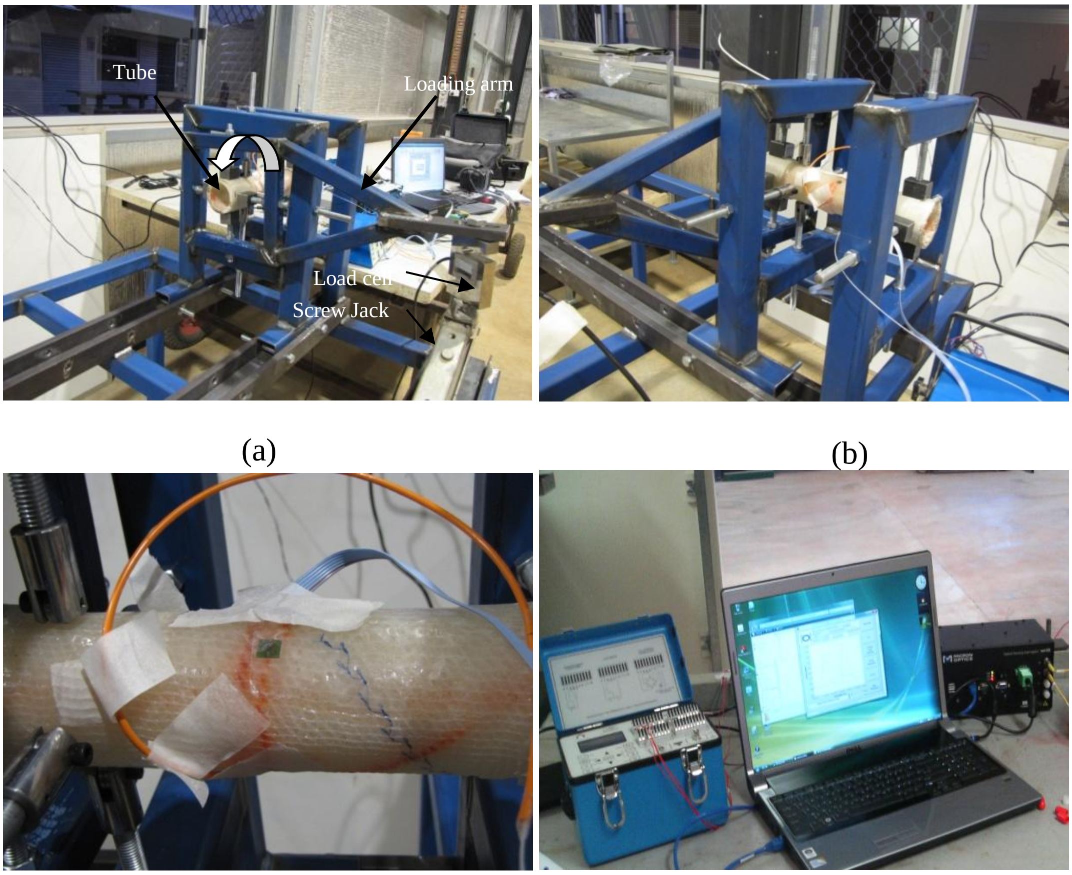

(a) (b)

(c) (d)

Figure 2-20: Torsional test setup.

The specimen was torsional loaded in 50 Nm increments as shown in Figure 2-20, and the strain gauge readings and FBG spectra were recorded. A Vishay Micro-Measurements P3 strain indicator was used to measure the strain from rosette and Micron Optics 3.1 sm125 optical spectrum analyser was used to measure the FBG spectrum Figure 2-20(d). The specimen was loaded three times to ensure reliability of the readings. The data were stored for post processing.

The reading from the legs 0^{o} and the 90^{o} of the rosette (Figure 2-18) were used to verify the loading condition. Low reading of the 90^{o} leg is evidence for a minimal bending moment on the tube since the 90^{o} leg lies parallel to the axis of the tube. The strain value of the FBG sensor was calculated using peak shift. Since apodisation was present, averaging of the FBG spectrum was not accurate. A peak detection algorithm was used to capture the peak of the spectrum. Experimental results observed from the FBG sensors were compared with the strain values from rosette as shown in Figure 2-21.

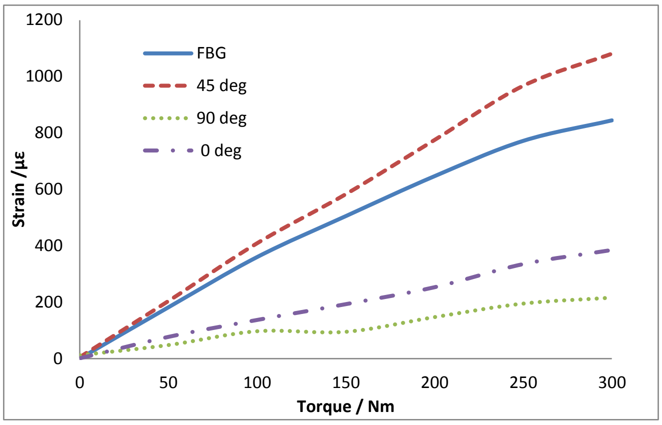

Figure 2-21: Variation of FBG and rosette readings

A FEA model of the specimen is given in Figure 2-22. Figure 2-23 shows the principal strain, shear strain, FBG and FEA results for specimen. Finite element results show good agreement with the experimental results. The FBG sensor reading and FEA results of layer 5, where the FBG sensors are embedded, indicated an excellent agreement.

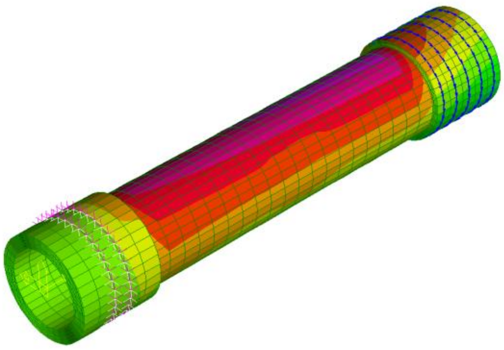

Figure 2-22: FEM of the specimen

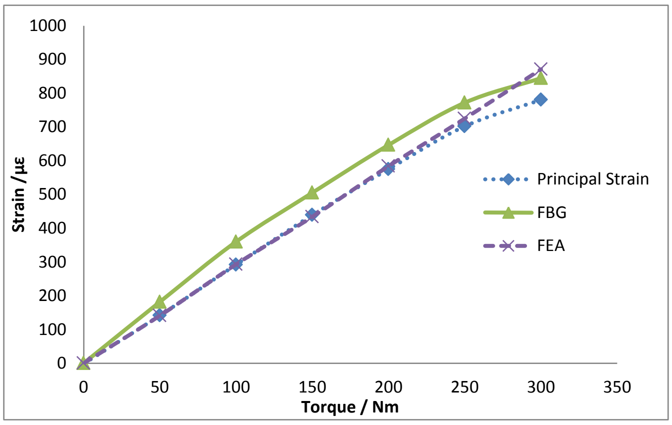

Figure 2-23: Variation of strain with the applied torque for the specimen

2.4.5 Modelling of a complex structure: helicopter blade shank fitting

When it comes to modelling of aerospace structures, it is rare to have simple structures such as plates and tubes. The complex structural elements used in aerospace applications need to be monitored with SHM systems as complexity increases the damage initiation risk. In the design stage of composite structures, and also for development of SHM systems for monitoring structures, it is essential to have reliable FEA modelling techniques. The following study details the modelling of a blade shank fitting which connects a blade of a helicopter to hub. With the modelling results, the representative sample has been fabricated and tested for verification. Figure 2-24 illustrates a drawing of a helicopter rotor blade shank fitting.

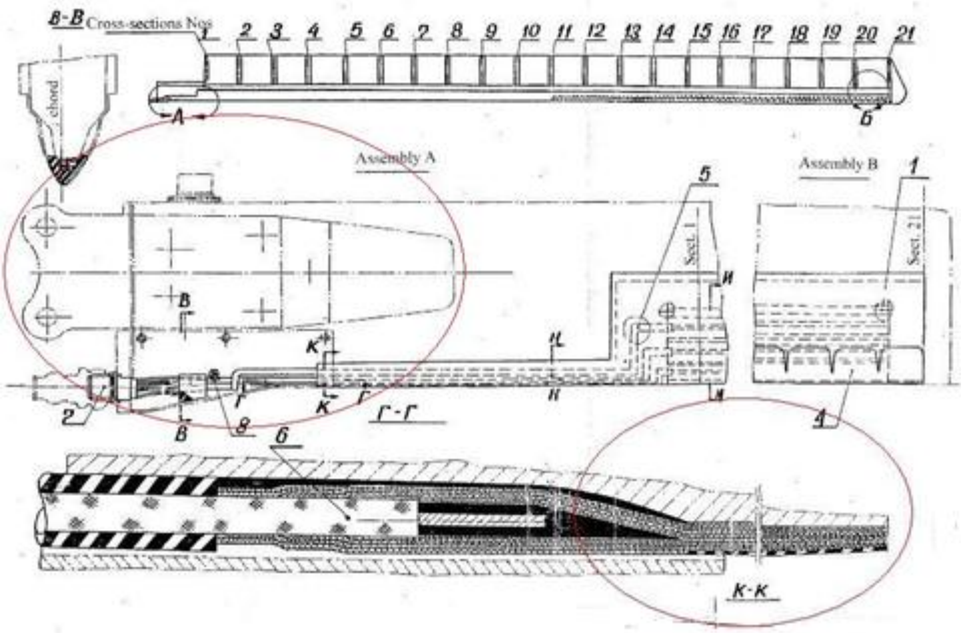

Figure 2-24: Helicopter rotor blade shank fitting (Bell helicopter, structural repair manual-BHT-MED-SRM-1)

The geometric parameters of the component are given in the Figure 2-25. The component, modelled in commercial FEA package ABAQUS, is shown in Figure 2-26. The holes available in the blade shank fitting were used to connect the helicopter blade and the hub using bolts. Consequently, in the FEA model, the boundary conditions were selected to be compatible with real applications.

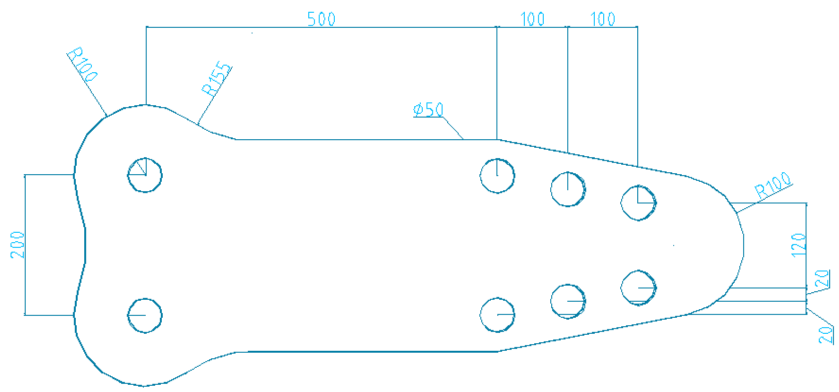

Figure 2-25: Dimensions of the component in millimetres (mm)

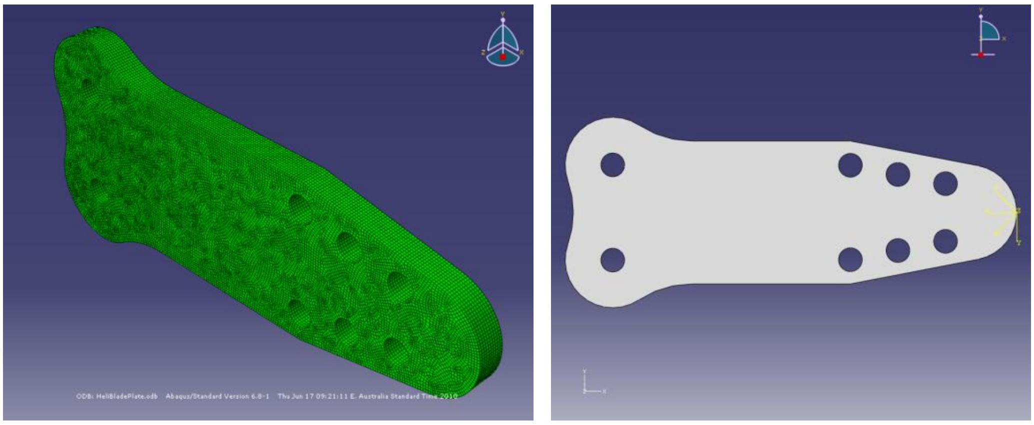

Figure 2-26: FEA model of the connector

The model was loaded in tension bending and torsional combined loading as illustrated in Figure 2-27. In real application, the connector is subjected to similar load cases as the helicopter blade is applying axial load due to centrifugal action, bending load due to gravitation load and torsional load due to pitching of the blade.

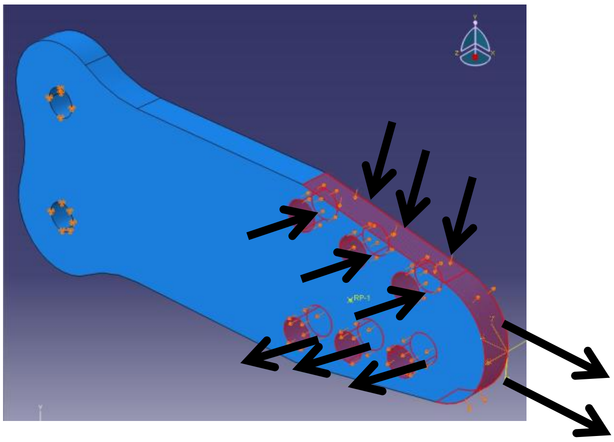

Figure 2-27: Combined loading used in the model

Figure 2-28 shows the stress variation of the component under combined loading.

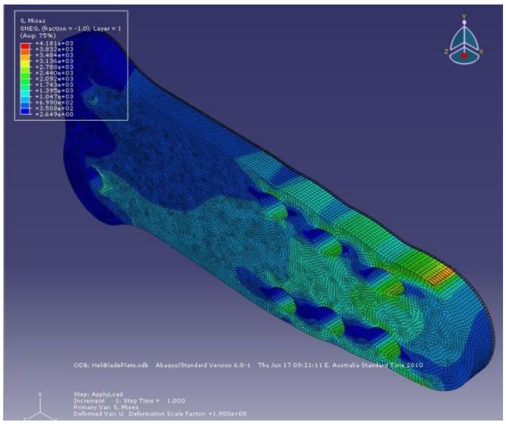

Figure 2-28: Stress variation of the model under combined loading

2.4.5.1 Fabrication of the specimen

The blade shank fitting was fabricated with ten layers. The layup orientation was [0/90/45/-45/0]s. Kenetix R246TX resin was used as the matrix. Wet bagging was used for the fabrication of the sample. In the wet bagging process the initial layup procedure is similar to the hand layup, but after completing the part, a vacuum was applied to the sample as shown in the Figure 2-30(a). The vacuum removes the air trapped in the specimen and presses the layup evenly providing better properties and surface finish (Figure 2-30(b)). The cured plate was shaped to the geometry of the connector and the connecting holes were created using drilling as shown in the Figure 2-30(c). Finally, two strain gauges were attached to the specimen closer to the drill holes as shown in the Figure 2-30(d). The locations of the sensors are given in the Figure 2-29. Sensor 1 was attached in parallel to x direction and sensor 2 was placed 45^{o} to the x direction.

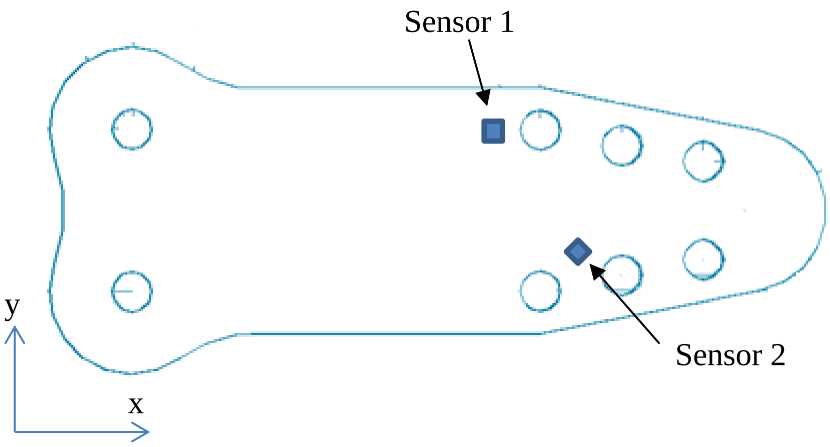

Figure 2-29: Locations of the two strain gauges

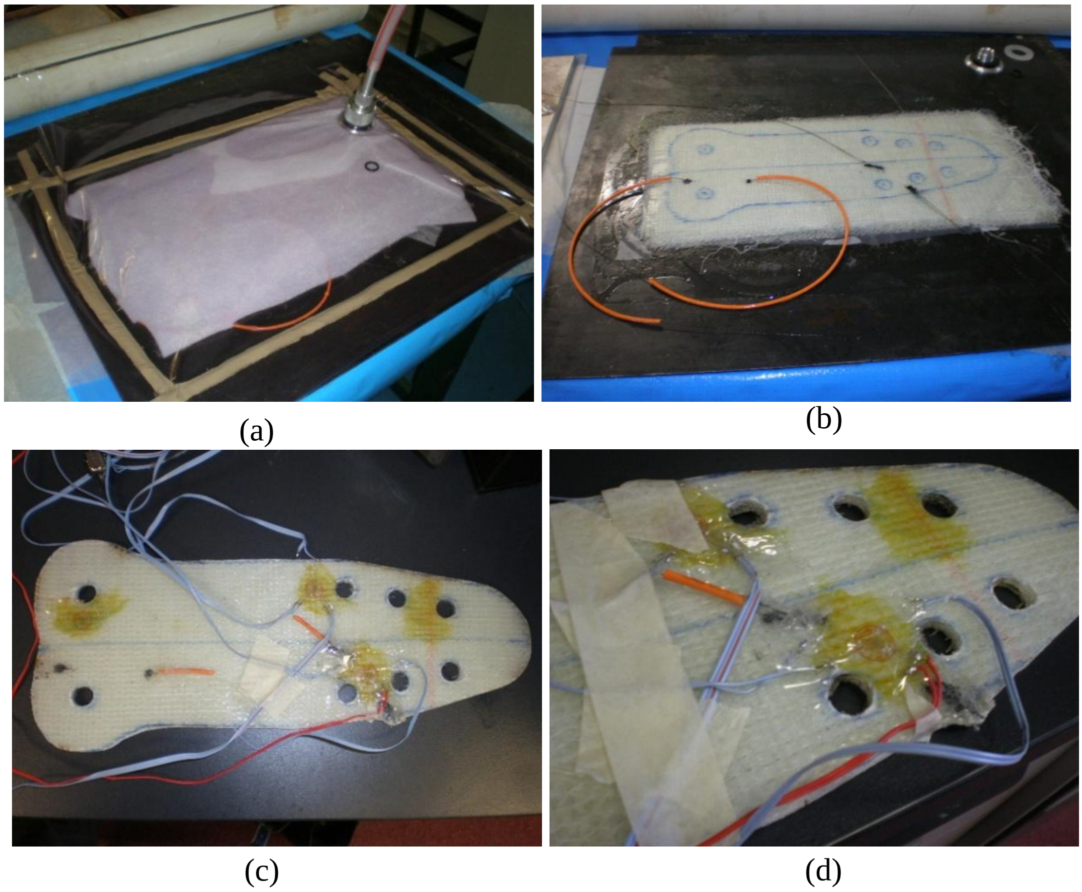

Figure 2-30: Fabrication of the sample

2.4.5.2 Experimentation

For the loading of the specimen, two fasteners were fabricated (Figure 2-31). The fasteners were designed to load the specimen using a MTS machine.

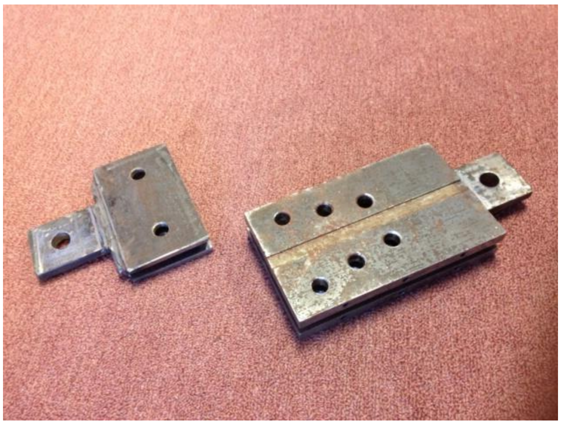

Figure 2-31: Fasteners used to load the specimen

The specimen was loaded in tension as shown in the Figure 2-32. The sample was loaded for a maximum load of 2000N in 100N steps and the strain from the strain gauges was recorded.

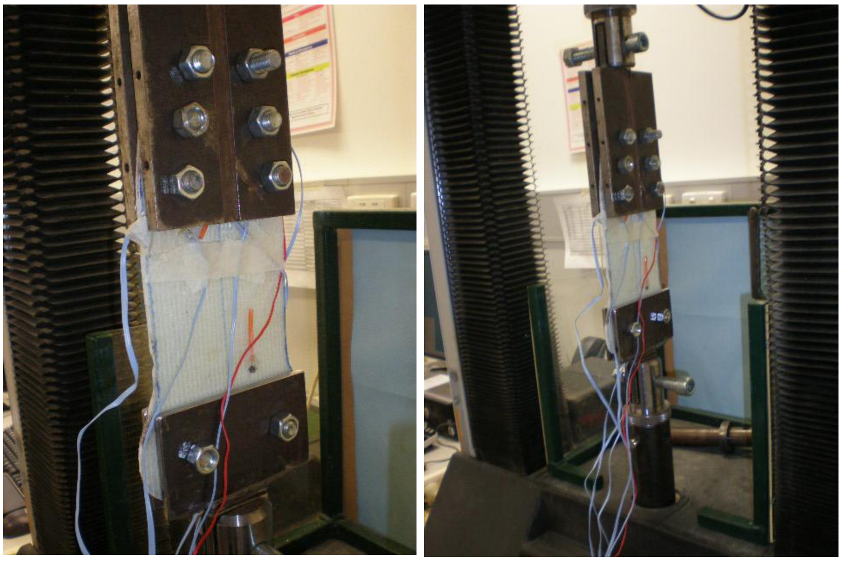

Figure 2-32: Tensile testing of the specimen

2.4.5.3 Results and verification of the FEA model

The strain readings obtained from the strain gauges is used to compare the FEA model. For the strain gauge locations, the surface strain in location of the sensor 1, x direction strain (E11) was used, and for the sensor 2, 45^{o} direction strain (E12) was used. Locations of the elements corresponding to sensor 1 and sensor 2, are shown in the Figure 2-33.

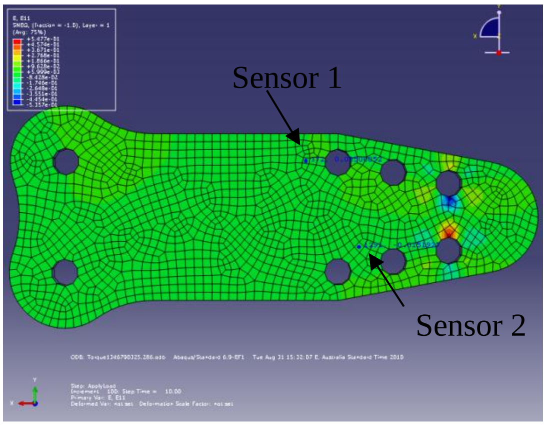

Figure 2-33: Extraction of strain readings from the model

Figure 2-34 shows the comparison of strain readings obtained from sensor 1 with the FEA results. The comparison of sensor 2 with the FEA results is given in Figure 2-35.

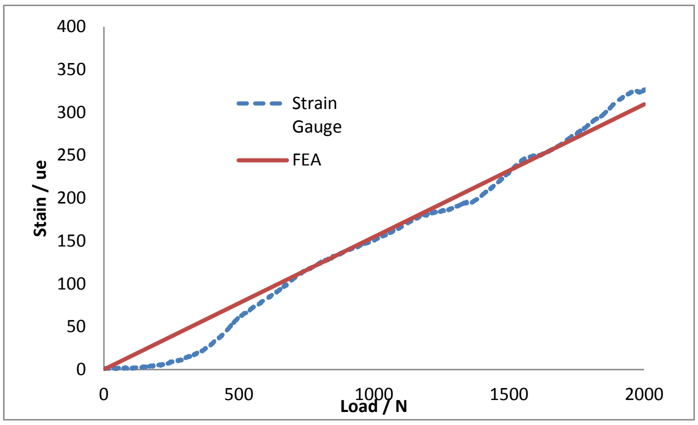

Figure 2-34: Comparison of sensor 1 with FEA

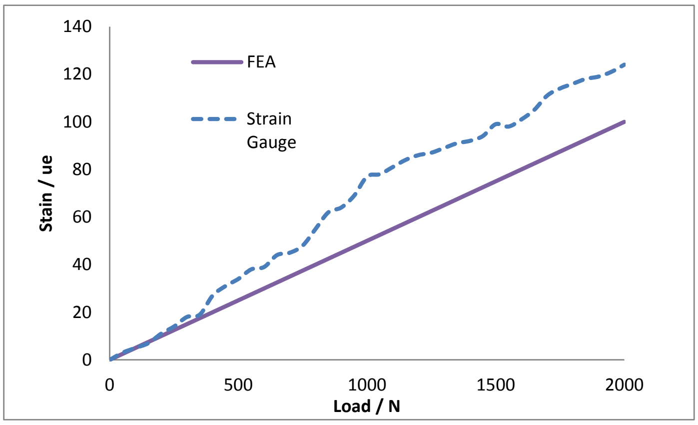

Figure 2-35: Comparison of sensor 2 with FEA

From the results, it can be seen that using FEA for complicated composite structures can be questionable. Even though the FEA model estimates the strain closely in some cases, complicated geometries might affect the predictability. Local stress concentrations may affect the strain gauge readings. A detailed investigation on those effects will be given in Chapter 3.

2.5 Modelling damage in composite structures: Delamination

Delamination damage is one of the most common structural damage types in laminated composites, and can result from impact, overload, or fatigue crack growth from defects along or near the adhesion layer. Delamination leads to a reduction in stiffness and strength of the composite structure and potentially to catastrophic failure. Early detection of delamination damage is therefore vital for high risk and high value assets such as aircraft and civil infrastructure. An important aspect of any damage detection technique, especially displacement and strain based approaches, is an understanding of the mechanical behaviour of a delaminated composite component under a wide range of load and geometry conditions. This knowledge is achieved through theoretical modelling such as by simplified beam or plate models as seen in Wildy et al. (Wildy, Cazzolato, & Kotousov, 2010) or extensive finite element analysis (FEA) (Waldron et al., 2002). Theoretical modelling can also provide ‘ideal’ comparisons for undamaged and damaged components, and can be used to evaluate the success and range of applicability of new damage detection methods. Simple beam or plate models are particularly good for this as they allow for a wide variation of input parameters without the computational and time constraints of FEA methods.

In the scope of this research work FEA is used for several aspects. One of the key aspects is to identify the stress concentrations in composite structures, to detect delamination initiation locations. Furthermore, the stress concentrations have been used to locate the embedded sensors for damage monitoring. For this process, it is extremely important to determine the stress field around initiated damage while the structure is under operational loading, in the modelling environment. If the sensors were located outside the stress field, those sensors will not be able to detect damage in ordinary strain-based methods.

Consequently, it is extremely important to model delamination using FEA accurately in order to place sensors effectively in the process of designing efficient SHM systems. The following examples of FEA models were developed to model composite components with delamination. First in a simple beam structure, and then, in a complicated structure.

2.5.1 Modelling of plate with a delamination

A GFRP composite plate with twenty ply was used as the model. The composite layup of [90/0/90/-45/45/-45/45/90/0/90]s was used. The geometric parameters of the plate are given in Figure 2-36.

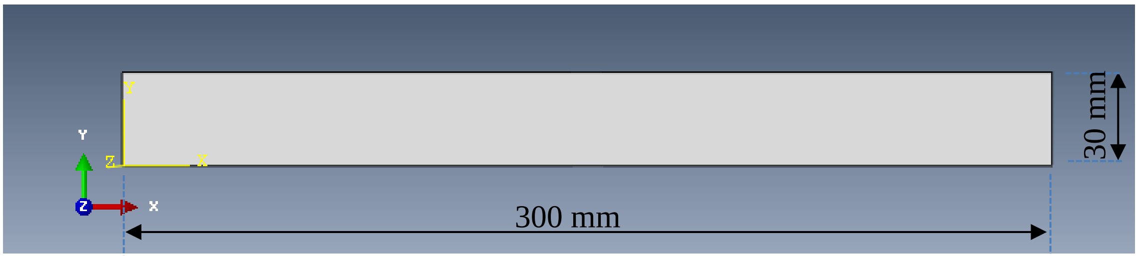

Figure 2-36: Geometric parameters of the plate

The plate was modelled in two parts as shown in Figure 2-37. Part 1 consisted of three (3) ply in orientation [90/0/90] and part two consisted the remaining ply [/-45/45/-45/45/90/0/90/90/0/90/0/-45/45/-45//90/0/90/0/90]. For the model, continuum shell elements have been used.

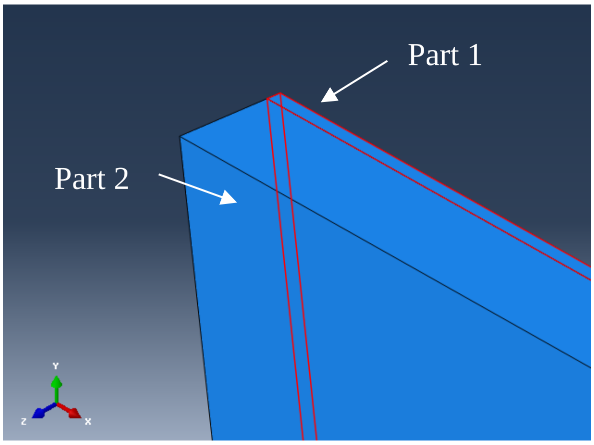

Figure 2-37: Two parts of the model

In the part 1, 10mm partition was created as shown in the Figure 2-38 which acted as the delamination of the model.

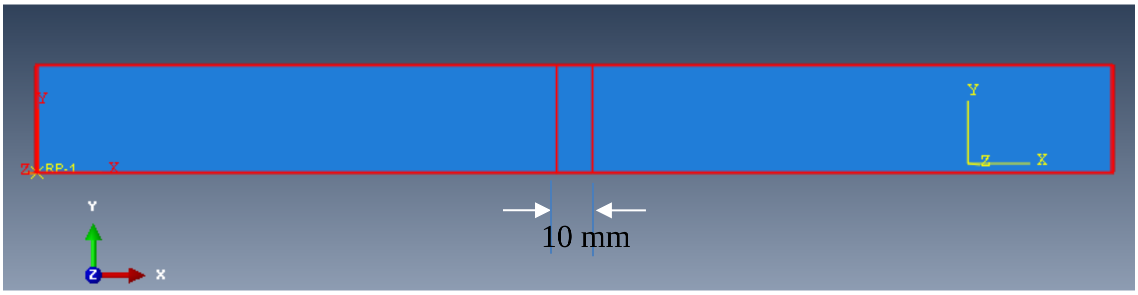

Figure 2-38: Partition of the part 1

The two parts were placed together, part 2 on top of part 1. The two parts were tied only on the two contact surfaces as shown in the Figure 2-39. The partitioned areas were not connected to each other.

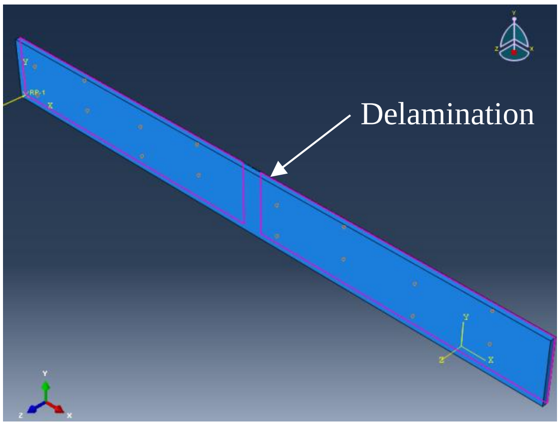

Figure 2-39: Contact surfaces of the two parts

By not connecting the partitioned area of part 1 to part 2, between ply 3 and ply 4 there was no connections in that particular area. Hence, this partitioned area acted as an ideal delamination. The surface interaction in the partitioned area was set to frictionless.

An axial load of 100N and bending load of 50 N was applied one end of the plate while the other end was rigidly fixed (Figure 2-40).

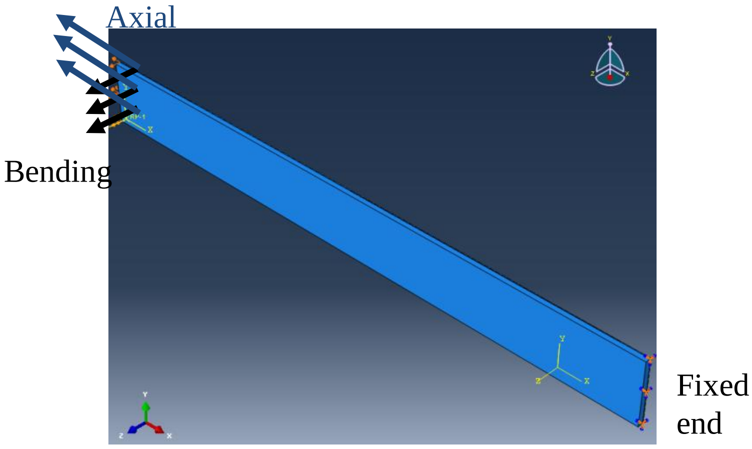

Figure 2-40: Load applied to the plate

2.5.1.1 FEA Results

The stress variation of the plate is given in Figure 2-41. The stress variation from the simulated delamination was identified from the stress field. Furthermore ply by ply strain variation was also possible to obtain. Figure 2-42 shows the strain variation in ply 3 and ply 4.

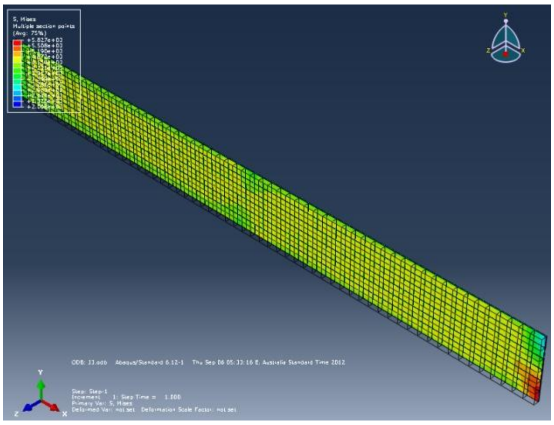

Figure 2-41: Stress variation of the plate

The strain variation in ply 3 and ply 4 were not similar, as ply 3 consisted of 90^o fibre and in ply 4 it was -45^o fibres. The capability of obtaining ply by ply strain distribution was used to obtain FEA data to compare with embedded sensor readings.

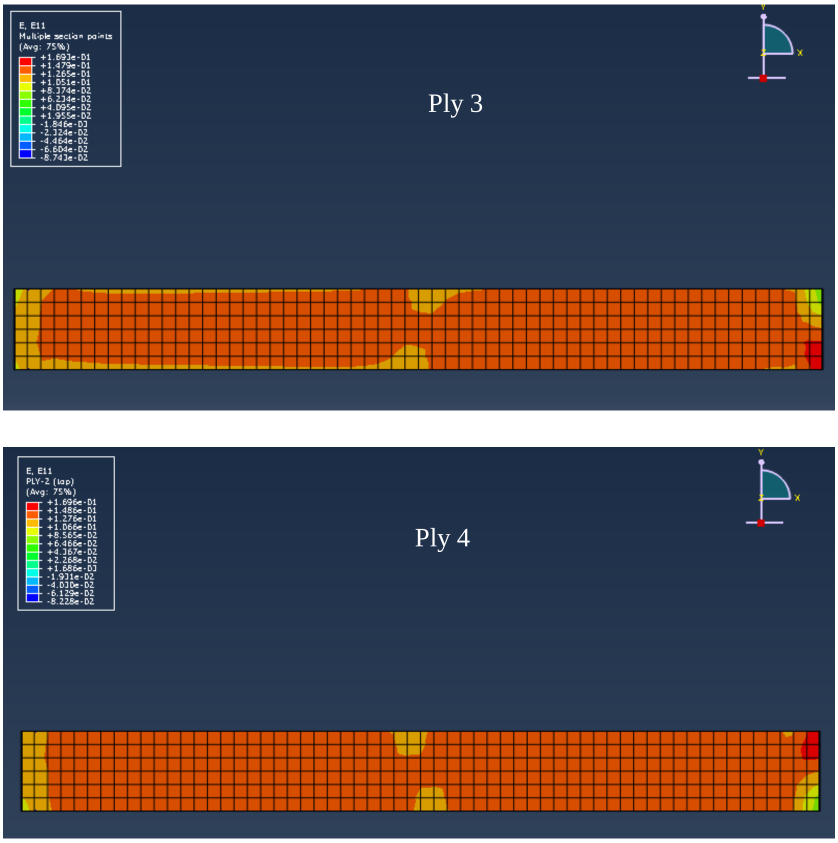

Figure 2-42: Strain variation in ply 3 and 4

The effect of the delamination can be visualising even from the surface strain readings. Figure 2-43 shows the stress variation obtained at the surface of the plate.

Figure 2-43: Strain variation of the ply 20, surface of the plate

Throughout the study, the aforementioned method was used for the modelling of delaminations. In the Chapter 3, the use of fibre optic sensors for the monitoring of damage (SHM) will be discussed. Delamination is used as the simulated defect for most of the study. Modelling and experimental study was simultaneously carried out by comparing results from each method, modelling and experiments. The ply by ply strain data was used to compare with embedded FBG sensor readings. In the experimental study, embedded FBG sensors were used to monitor strain in order to monitor damages. The capability of obtaining ply by ply strain values provides strain readings at exact FBG embedded location for accurate verifications.

CHAPTER 3
Structural health monitoring using FBG sensors

3.1 Introduction

The process of implementing a damage detection and characterization strategy for engineering structures is referred to as structural health monitoring (SHM). The SHM process involves the observation of a system over time using periodically sampled structural response measurements from an array of sensors. Most of offline non-destructive test (NDT) methods do not fall into SHM.

With the complex failure modes of FRP composites, (as discussed in Chapter 2) the need for SHM of composite structures becomes critical. With the recent developments in the aerospace industry, utilization of FRP composites for primary aircraft structures, such as wing leading-edge surfaces and fuselage sections, has increased. This is one of the major reasons for the rapid growth in the research fields related to SHM. Impact from flying objects, excessive vibration, and loading can cause damage such as delamination and matrix cracking to the FRP composite structures. Moreover, the internal material damage in the FRP composite structures can be invisible to the human eyes. In some cases, delaminations and cracks remain closed while the structure is under no loaded condition. As a consequence, inspection for damage and clear insight into the structural integrity become difficult using currently available evaluation methods.

The SHM system developed to monitor aircraft and space structures must be capable of identifying the multiple failure criteria of FRP composites (Reveley et al., 2010).

Since the behaviour of most composites is anisotropic, multiple numbers of sensors must be in service to monitor these structures under multi-directional complex loading conditions. The layered structure of the composites makes it difficult to predict the structural behaviour by using surface mounted sensors only. To address this issue embedded sensors need to be used, and these sensors must be robust enough to service the structure's lifetime. It is impossible to replace embedded sensors after fabrication of the parts.

The Fibre Bragg Grating (FBG) sensor is one of the most suitable sensors for the SHM of aircraft FRP structures. The FBG sensors can be embedded into FRP composites during the manufacture of the composite part with no adverse effect on the strength of the part as the sensor is diminutive in size. Furthermore, this sensor is suitable for networking as it has a narrowband response with wide wavelength operating range, hence can be highly multiplexed. As it is a nonconductive sensor it can also operate in electromagnetically noisy environments without any interference. The FBG sensor is made up of glass which is environmentally more stable and with a long lifetime similar to that of FRP composites. Because of its low transmission loss, the sensor signal can be monitored from longer distances making it suitable for remote sensing (K. O. Hill & Meltz, 1997; Kersey et al., 1997).

The FBGs' capability of detecting stress gradients along its grating length can be used to identify the stress variations in the FRP composites by means of chirp in the reflected spectra of the FBG sensor (P. C. Hill & Eggleton, 1994); (Le Blanc, Huang, Ohn, & Measures, 1994). This phenomenon can be used to detect damage in the composite structures (Okabe et al., 2000) (Takeda et al., 2002). But, it has been reported that the chirp of the FBG spectrum is not only due to stress concentrations caused by damage accumulation in the composite structure (Y. Wang et al., 2008). There are other reasons for chirping of spectra other than existence of damage and eliminating such effects during the processing of spectra is necessary to identify damage accurately. Section 3.4 will discuss the other effects that cause distortions to the FBG spectra.

The most recent development in the fibre optic sensor field is the pulse-pre-pump Brillouin optical time domain analysis (PPP-BOTDA)(Che-Hsien, Nishiguti, & Miyatake, 2008). The PPP-BOTDA is capable of achieving a 2cm spatial resolution for strain measurements. The PPP-BOTDA based system has been successfully used in various industrial applications, however, PPP-BOTDA is so far only able to measure the static or quasi-static strain.

3.2 Fibre Bragg Grating (FBG) sensors

Fibre Bragg Gratings (FBGs) are formed by constructing periodic changes in the index of refraction in the core of a single mode optical fibre. This periodic change in index of refraction is typically created by exposing the fibre core to an intense interference pattern of UV radiation. The formation of permanent grating structures in optical fibre was first demonstrated by Hill and Meltz in 1978 at the Canadian Communications Research Centre (CRC) in Ottawa, Ontario. In ground breaking work, they launched high intensity Argon-ion laser radiation into germanium doped fibre and observed an increase in reflected light intensity. After exposing the fibre for a period of time it was found that the reflected light had a particular frequency. After the exposure, spectral measurements were taken, and these measurements confirmed that a permanent narrowband Bragg Grating filter had been created in the area of exposure. This was the beginning of a revolution in communications and sensor technology using FBG devices.

The Bragg Grating is named for William Lawrence Bragg who formulated the conditions for X-ray diffraction (Bragg's Law). These concepts, which won him the Nobel Prize in 1915, related energy spectra to reflection spacing. In the case of Fibre Bragg Gratings, the Bragg condition is satisfied by the abovementioned area of the modulated index of refraction in two possible ways based on the Grating's structure. The first is the Bragg Reflection Grating, which is used as a narrow optical filter or reflector. The second is the Bragg Diffraction Grating which is used in wavelength division multiplexing and de-multiplexing of communication signals.

The gratings first written at CRC, initially referred to as "Hill gratings", were actually a result of research on the nonlinear properties of germanium-doped silica fibre. It established, at the time, a previously unknown photosensitivity of germanium-doped optical fibre, which led to further studies resulting in the formation of gratings, Bragg reflection, and an understanding of its dependence on the wavelength of the light used to form the gratings. Studies of the day suggested a two-photon process, with the grating strength increasing as a square of the light intensity (Lam & Garside, 1981). At this early stage, gratings were not written from the "side" (external to the fibre) as commonly practiced now, but were written by creating a standing wave of radiation (visible) interference within the fibre core introduced from the fibre's end.

After their appearance in late 1970s, the FBG sensors had been using for SHM of composite materials efficiently for more than two decades. Recent advances in FBG sensor technologies have provided great opportunities to develop more sophisticated *in situ* SHM systems. There have been a large number of research effort on the health monitoring of composite structures using FBG sensors. The ability to embed them inside FRP material between different layers provides a closer look at defects. The attractive properties such as small size, immunity to electromagnetic fields, and multiplexing ability are some of the advantages of FBG sensors. The lifetime of an FBG sensor is well above the lifetime of the FRP structures and also it provides the measuring of multiple parameters such as load/strain, vibration and temperature (Kashyap, 1999).

3.2.1 Evolution of FBG sensors

The Hill´s gratings were made in the fibre core by a standing wave of 488nm argon laser light (K. O. Hill, Fujii, Johnson, & Kawasaki, 1978). The grating exposure in this case was shown to be a two-photon process. Hill et al., (1978) found a 4% back reflection due to variation in refractive index. The field did not progress until Meltz et al, of United Technologies proposed that fibre gratings could be formed by exposure through the cladding glass of two interfering beams of coherent UV light, thus exciting the 240 nm band directly by one photon absorption (Meltz, Morey, & Glenn, 1989).

Reliable fabrication of Bragg gratings depends on a detailed knowledge of the underlying mechanisms of photo-induced index changes. The basis of all proposed mechanisms is the ionization of GeO_2 deficiency centres that exhibit an absorption band centred at 240 nm. Hand and Russell (1990) suggested that the photo-induced index changes in optical fibres originate from the bleaching of the 240 nm band and the creation of two bands at 281 and 213 (Hand & Russell, 1990). Their work explained a photo-induced index change of almost 10% at visible wavelengths. However, experimental measurements show much larger index changes.

To explain the observed large index changes, Sceats et al. (1993) proposed thermo-elastic stress relaxation of the glass network caused by the formation of regions of low density around broken Ge-Si bonds (stress relief model) (Sceats, Atkins, & Poole, 1993). Alternatively, Bernardin and Lawandy suggested in 1990, that UV irradiation may induce rearrangement of the molecular structure, leading to a compaction of the glass matrix; referred to as the compaction model (Bernardin & Lawandy, 1990). The fabrication of FBG sensors has been developed to commercial level and main techniques used are Split Beam Interferometer, Phase Mask Technique and Point-by-Point Method.

3.2.2 Fabrication of FBG sensors

In 1989, Meltz et.al showed that it was possible to write gratings from outside the fibre (Meltz et al., 1989). This proved to be a significant achievement as it made possible future low cost manufacturing methods of Bragg Gratings and enabled continuous writing or “writing-on-the-fly”. With this method of writing gratings, it was discovered that a grating made to reflect any wavelength of light could be created by illuminating the fibre through the side of the cladding with two beams of coherent UV light. By using this method (holography) the interference pattern (and, therefore, the wavelength of reflected light from the grating) could be controlled by the angle between the two beams, something not possible with the internal writing method, as seen in Figure 3-1. The figure shows two methods of manufacturing a side-written grating. Figure 3-1(b) shows the light beam incident to the fibre with a phase mask. In Figure 3-1(a), the two coherent beams of light form an interference pattern which creates a standing wave with variable intensity of light. The variable radiation intensity occurs within the fibre core. This variation in radiation intensity creates a modulated index of refraction profile within the fibre core. In Figure 3-1(b) the modulation is created by using a single light beam and a phase mask. In areas where the mask allows light transmission, the index of refraction is changed within the core, creating the grating. This technique is particularly useful to write gratings quickly. Both of these methods allowed for “tuning” of the grating to whatever wavelength was desired. This, in itself was an important development, as it allowed gratings to be easily written at various wavelengths to follow the communications industry’s changing source wavelengths. In addition, it was found at the time that this method was far more efficient.

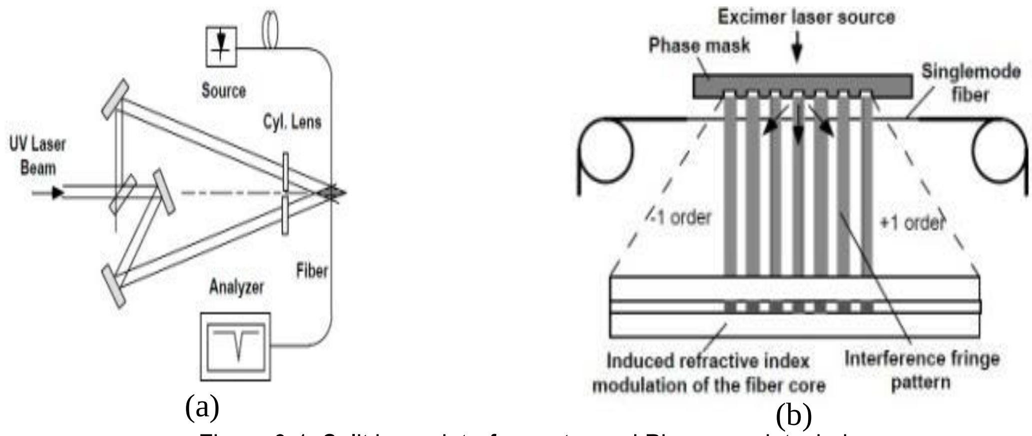

Figure 3-1: Split beam interferometer and Phase mask technique

As described earlier, the first method of fabricating gratings was internal writing through standing waves of radiation and the second method was the holographic side writing of gratings. Today, both of these methods have been surpassed by the use of the phase mask (Anderson, Mizrahi, Erdogan, & White, 1993; K.O. Hill, Malo, Bilodeau, Johnson, & Albert, 1993). The phase mask is a planar slide of silica glass or similar structure which is transparent to UV light. A periodic structure with the appropriate periodicity is etched onto the glass slide to approximate a square wave using photolithography (as viewed from the side) As shown in Figure 3-2: Use of phase mask for fabrication of grating, the optical fibre is placed very close to the phase mask while the grating is written. UV light is introduced to the fibre and is diffracted by the periodic structure of the phase mask, creating the grating structure described above. The periodic structure created in the fibre is half that of the spacing of the periodic structure in the phase mask. In this manufacturing technique, the periodicity of the FBG is independent of the wavelength of the UV light source. The wavelength of the UV light source is selected based on the absorbance spectra of the doped optical fibre core, thereby maximizing the source’s efficiency in writing gratings. Use of phase masks reduce costs, and made greater precision Bragg gratings possible by simplifying the manufacturing process. In addition, the phase mask technique made it possible to automate grating writing, and to write multiple gratings on a fibre simultaneously. The phase mask procedure allowed for the efficient writing of other types of gratings such as chirped gratings which have non-constant periodicities for a wider spectral response.

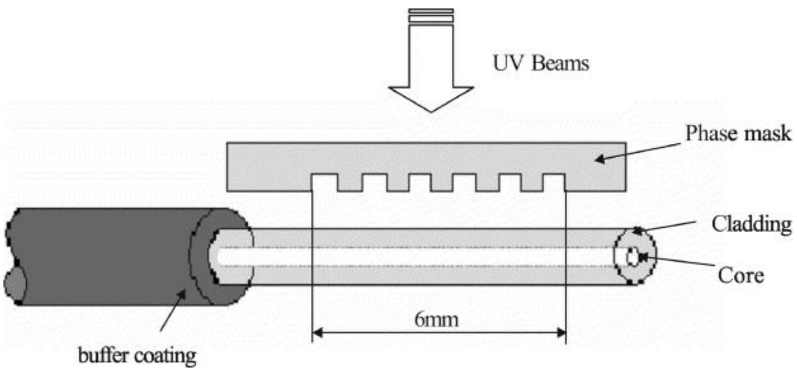

Figure 3-2: Use of phase mask for fabrication of grating

The process of writing a grating using the phase mask method is illustrated in the Figure 3-3. The FBG sensors used in this work was fabricated at interdisciplinary Photonics Lab (iPL) at the University of Sydney. After completing training on fabrication of FBG sensors, the author fabricated the sensors for the complete research work presented in this thesis.

The Figure 3-3(a, b) shows the setup for the grating writing process with the phase mask and mirror arrangements to direct the laser to the phase mask and the phase mask mounted just above the fibre respectively. Figure 3-3(c) shows the writing in progress and the Figure 3-3(d) shows the corresponding response from the created grating.

The reference spectrum shown in the Figure 3-3(d) was used to maintain the consistent reflection power of the sensors. When the reflected spectrum from the grating reached the reference spectrum power, the writing process was terminated. Excessive exposure of the fibre to the laser will broaden the reflection spectra as shown in the Figure 3-4, which makes it hard to track the peak of the spectrum.

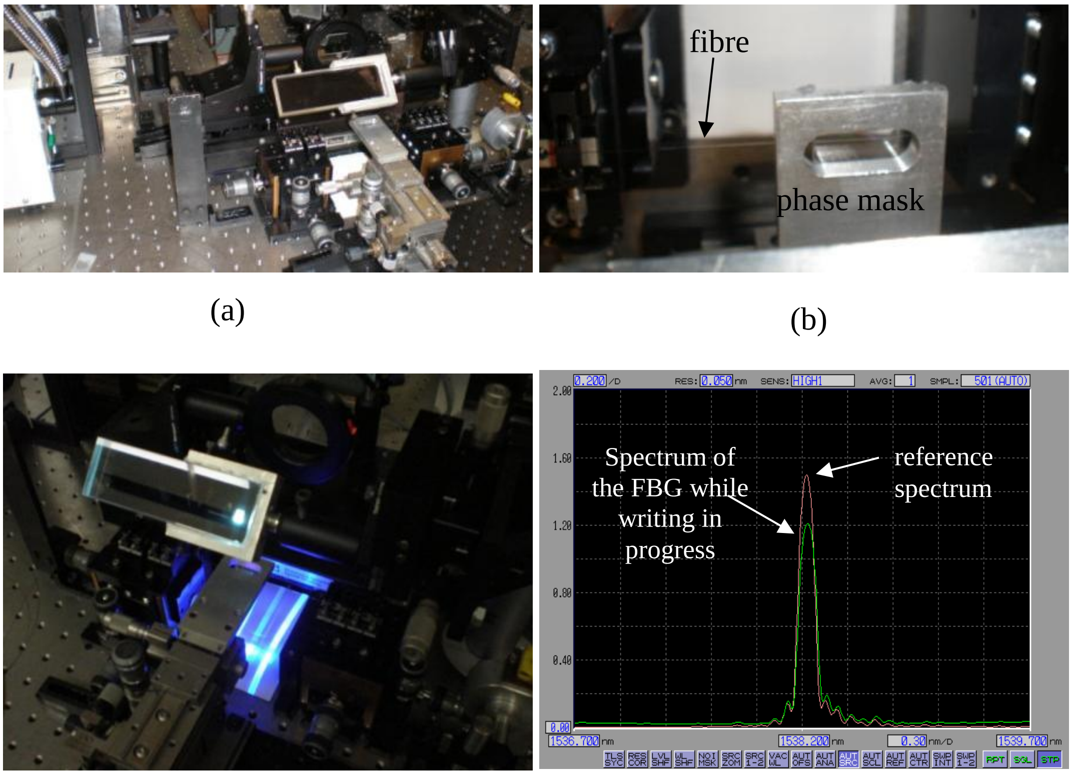

(a) (b)

(c) (d)

Figure 3-3: Fabrication of FBG sensor using phase mask method (a) setup for the writing, (b) phase mask, (c) writing in progress, and (d) response of the grating

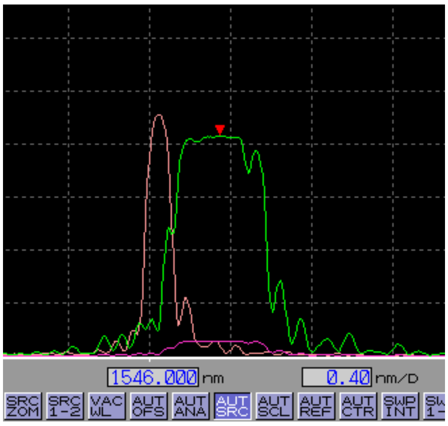

Figure 3-4: Broadening of the reflection spectra due to over exposure to laser light

The side lobes are one of the major drawbacks of using phase mask technique for FBG fabrication. As shown in the Figure 3-5: Side-lobes of an FBG sensor response spectrum, side-lobes of an FBG sensor response spectrum, are inherent to a particular phase mask and will be written to all FBG sensors fabricated using that phase mask. Apodisation technique can be used to get rid of those side lobes, but it will extinguish the uniformity of the grating length (λ) which drops the sensitivity of the sensor for SHM purposes.

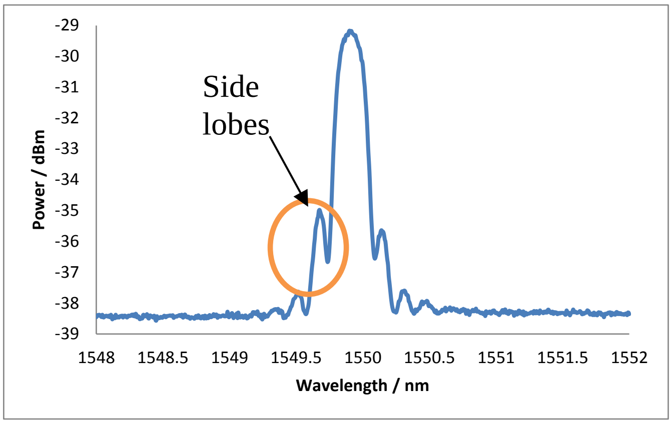

Figure 3-5: Side-lobes of an FBG sensor response spectrum

3.2.2.1 Apodisation of FBG sensors

The side-lobes of the response spectra of an FBG sensor is not always desirable for some applications (Rego, Romero, Frazao, Marques, & Salgado, 2002). The cause of the side-lobes is the abruption of the grating at the beginning and exit of the sensor. The rectangular function of the grating yields to a *sinc* function, with its associated side-lobes structure apparent in the reflection spectrum.

The suppression of the side-lobes by gradually increasing the coupling coefficient at the beginning of the grating and gradually decreasing at the exit form, is called apodisation of the reflection spectrum of an FBG sensor.

However, simply changing the refractive index modulation amplitude change local Bragg wavelength and this is not desirable for FBG sensors used in damage detection. The variable Bragg wavelength makes the tracking difficult for strain gradients along the length of the FBG sensor. This is significant as is used to detect the damage which causes the strain gradient.

Thought out the work presented in this thesis, all the sensors used were not subjected to apodisation.

3.2.3 Principle of Bragg Grating

As described previously, FBG sensors are fabricated in the core region of specially fabricated single mode low-loss germanium doped silicate optical fibres. The grating is the laser-inscribed region which has a periodically varying refractive index. This region reflects only a narrow band of light corresponding to the Bragg wavelength λ_B, which is related to the grating period Λ_o

$$\lambda_B = \frac{2n_o \Lambda_o}{k} \tag{3-1}$$

Where k is the order of the grating and n_o is the initial refractive index of the core material prior to any applied strain.

Due to the applied strain, ε, there is a change in the wavelength, $\Delta\lambda_B$, for the isothermal condition,

$$\frac{\Delta\lambda_B}{\lambda_B} = \varepsilon\, P_e \tag{3-2}$$

where P_e is the strain optic coefficient and is calculated as 0.793.

The Bragg wavelength is also changing with the reflective index. Any physical change in the fibre profile will cause variation of the reflective index. The variation of the Bragg wave length λ_B,as a function of change in the refractive index $\Delta\delta n$, and the grating period $\delta\Lambda_o$, is given below.

$$\delta\lambda_{Bragg} = 2\Lambda_o \eta \Delta\delta n + 2n_{eff}\delta\Lambda_o \tag{3-3}$$

where η is the core overlap factor of about 0.9 times the shift of the Bragg wavelength, n_{eff} is the mean refractive index change, and Λ_o is the grating period.

For the Gaussian fit, the sensor reflectivity can be expressed as

$$s(\lambda, \lambda_s) = y_0 + S_0 \exp[-\alpha_s(\lambda - \lambda_s)^2] \tag{3-4}$$

where y_0 is the added offset to represent the dark noise, α_s is a parameter related to the full width at the half maximum (FWHM), λ is the wavelength, λ_s is the central wavelength, and S_0 is the initial reflectivity of the fibre.

3.3 Embedded FBG sensors

In the layered FRP composite structure, it is difficult to use surface or external sensors to monitor inside damage effectively. The ability to embed FBG sensors inside FRP sandwich panels between different layers provides a closer look at defects such as delaminations and cracks. The FBG sensor is sensitive to stress gradients along the gauge length of the sensor and displays them as chirp (or distortion) from its response spectra.

Embedding FBG sensors in structures introduces loads and strain in all directions to the FBG sensor, not just in the axial direction as the structure undergoes loading. This concept is further complicated by issues of embedment into FRP composites, where FBG fibre size and alignment are important issues. In addition, the introduction of embedded fibre sensors can cause residual stresses and concentrated stresses in the FRP composite that need to be eliminated or accounted for when analysing the structure as a whole. Those effects influencing the FBG sensor are discussed in Section 3-4,

3.3.1 Embedding process

A major advantage of using FRP composites is the possibility of deciding on the number of layers and layup orientation based on the required structural behaviour. In a FRP composite aerospace structure there are a number of layers with multiple orientations. The layers are placed one on top of the other and hence it is possible to embed FBG sensors in any layer during the manufacturing of the structure.

The process of embedding FBG sensors in FRP composites is quite complicated. The level of difficulty is largely dependent on the geometry of the part, lay-up configuration and embedding location of the sensors in the part. In general, FBG sensors will be placed closer to critical sections of the structure where high stress concentrations are predicted. However, in reality locating FBG sensors in predicted locations are not always possible. On the other hand, reliance on a single sensor is not recommended as it is not possible to replace failed embedded sensors after manufacturing. As a result, many FBG sensors need to be embedded in the surrounding area closer to the critical locations of the structure in order to capture strain levels reliably.

As such, multiplexed FBG sensors play a critical role in the SHM of aerospace structures. Normally in FRP, the damage starts from stress concentrations. In the process of implementing SHM systems, identification of the locations that have potential for damage is essential. Finite Element Analysis (FEA) techniques are being widely used to identify stress concentrations and, hence, to locate FBG sensors. It is less likely that FBG sensors are placed in simple planer structures in real applications, apart from where the requirement is mere strain rather than the damage detection.

Figure 3-6 shows the FEA analysis on a base of a helicopter blade using commercial FEA software, ABAQUS. From the FEA results the stress concentrated points have been identified and the ply with the maximum stress was selected to embed the FBG sensor. This process is discussed in detail in the Chapter 5. To monitor the stress concentration in Figure 3-6, FBG sensors were placed as shown in the Figure 3-7(a). Figure 3-7(b) shows the completed part with embedded FBG sensors.

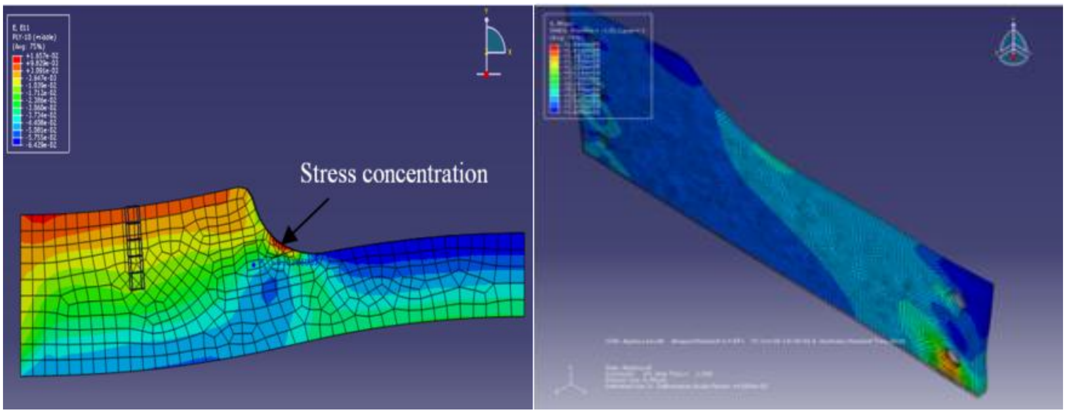

Figure 3-6 FEA analysis of helicopter blade base

Manufacturing difficulty is the main problem with placing FBG sensors in a complicated location. The aerospace industry's advanced manufacturing technologies, (such as pre-preg and autoclave process) creates a hazardous environment for brittle sensor. Every precaution needs to be taken to not apply loads on the sensor in the non-cured resin matrix during the manufacturing process. With applied pressures as high as 700kPa, even the egress ends of the sensors need to be supported to avoid breakage. It is essential to develop methods to protect FBG sensors during the FRP composite manufacturing processes. Since there is no way of replacing damaged FBG sensors after manufacturing of the component, a strict set of procedures must be developed to follow during manufacture.

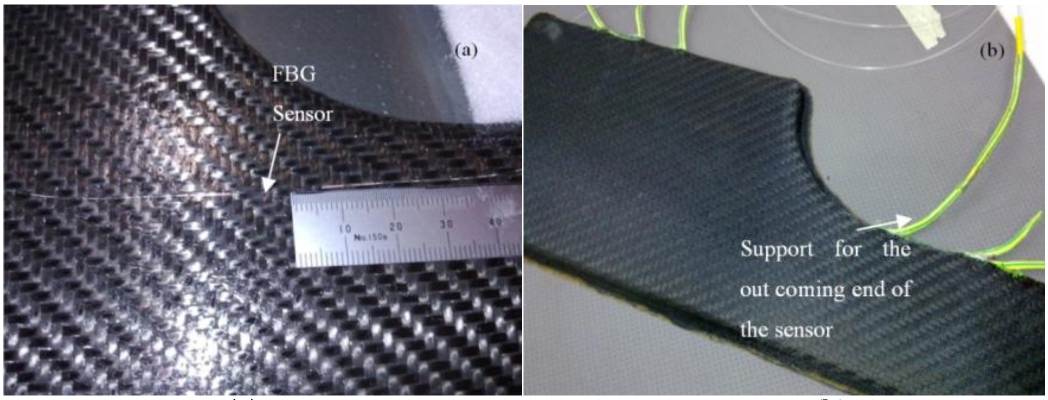

(a) (b)

Figure 3-7: (a) Embedding FBG sensors and the support for the out coming end before sending to the autoclave (b) Cured sample from the autoclave

Figure 3-7(b) shows a support given to the egress end of the sensor. Sometimes it is helpful to have an extra protective layer of rubber applied to the fibre to maximize the handling of samples without damage to the sensors.

Figure 3-8 shows the use of a hand layup process to fabricate a FRP panel with embedded FBG sensors. Since the FBG sensors are brittle, it is necessary to be particularly careful during the process. Silicon rubber was applied to the egress end of the sensors to provide extra protection. Careful attention when rolling near FBG sensors is essential, as shown in Figure 3-8(d).

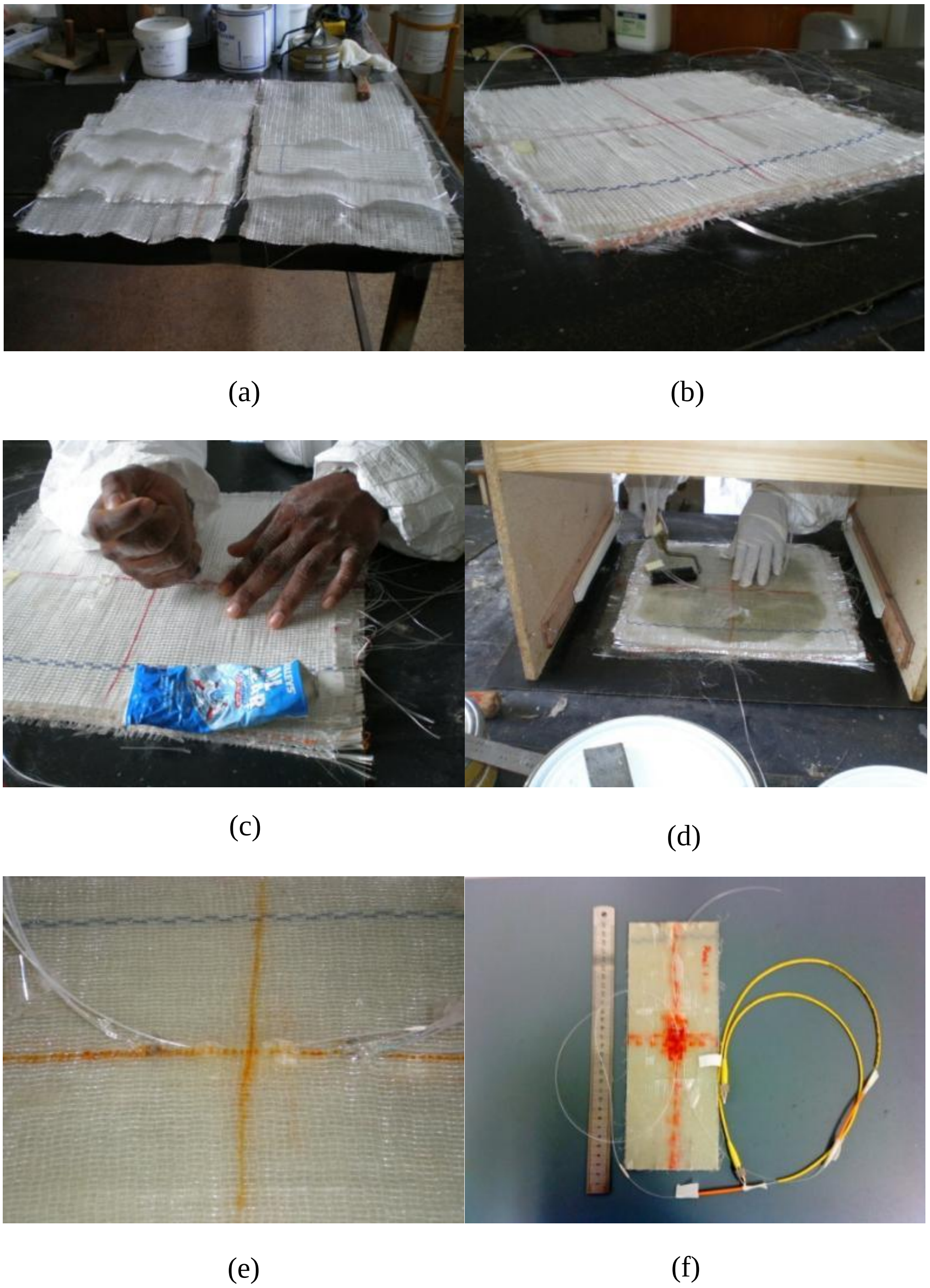

Figure 3-8: Hand layup process to fabricate FRP panel (a) Glass fibre fabric with different fibre orientations (b) Placement of FBG sensors (c) Application of protective silicon to egress ends of the sensor (d) Rolling (e) FBG sensor ends coming out of the panel (f) Cured panel with embedded FBG sensors

As a precaution to avoid premature failure of FBG sensors during the fabrication, protective tubing was used (as shown in Figure 3-8(f)). Only the part of sensor imbedded in the panel was kept outside the tube. The sensor part outside the panel was supported from the top with a wooden frame to avoid contact with the wet top surface of the panel, as shown in Figure 3-8(d). For the egress ends of the sensor, silicon was applied to provide flexibility while protecting the ends (Figure 3-8(d)).

FRP composite production methods are currently expensive and do not always produce composites with predictable traits. The autoclave process is extremely costly in terms of capital, skilled labour and time. Quality control is very difficult with the hand layup method. A cheaper alternative is the vacuum bag and oven process, which requires fewer and cheaper materials, and produces composites with similar traits. The vacuum used has a maximum pressure of 80kPa, which can still produce quality laminates. However, most of the aerospace grade composites use autoclave curing to obtain the required quality.

3.4 Effects on embedded FBG sensors

Though the embedded FBG sensor is used to monitor strain in order to detect damage, there are several effects that interfere with the response spectra of the sensor. During the curing of resin, the shrinkage affects the sensor and leaves it permanently compressed. On the other hand, loading on the composite is affecting the sensor by leading to transverse loads applied to the sensor.

3.4.1 Curing effect on FBG sensors

During the curing process the FRP composite is subject to shrinkage. The amount of shrinkage depends on the resin and the fibre fraction. The shrinkage applies a compressive loading on an FBG sensor and, as shown in the Figure 3-9, the peak of the FBG sensor moves to a new centre location after curing. It was found that pre-tensioning of the sensor is a possible solution to avoid there shrinkage effects. Pre-tensioning can be used to locate the peak in a desirable position as well. There is no significant longitudinal shrinkage of the sensor if the sensor is embedded between unidirectional parallel fibres and is parallel to the fibres. However, restricting to this orientation is difficult in real applications.

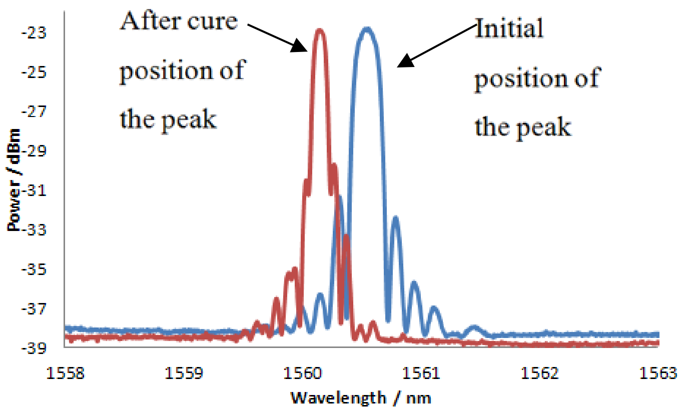

Figure 3-9: Movement of the peak during curing due to shrinkage of thin FRP plate

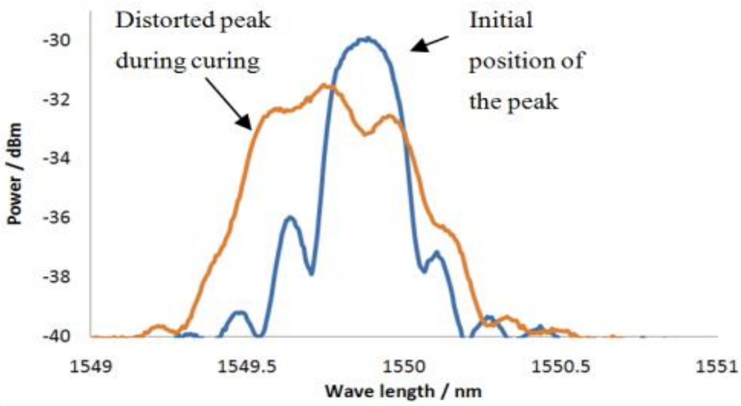

Figure 3-10: Distortion of the peak during curing, due to shrinkage of thick (8 mm) FRP plate

The lateral shrinkage can be neglected for the thin FRP plates. However, in considerably thicker structures, lateral shrinkage is considerable and will distort the response spectra of the sensor (Figure 3-10), especially when the FBG sensor is embedded between non-parallel fibres. The sensor becomes distorted due to uneven transverse loads applied by adjacent fibres as discussed in Section 3.5. To minimise the distortion to the FBG sensor caused by shrinkage during the curing, pre-tensioning of the sensor can be used.

Figure 3-11 shows the setup used to pretension the FBG sensor during the fabrication of an FRP panel. Pre-tensioning allows the sensor to be aligned with the fibres of the FRP panel if embedded between parallel fibres. Also, if adequate pre-tension is applied, during the shrinkage of the resign used for the FRP panel, the fibre remains straight (Figure 3-12). Further, there is no significant distortion to the FBG spectrum and peak relocation is also minimal.

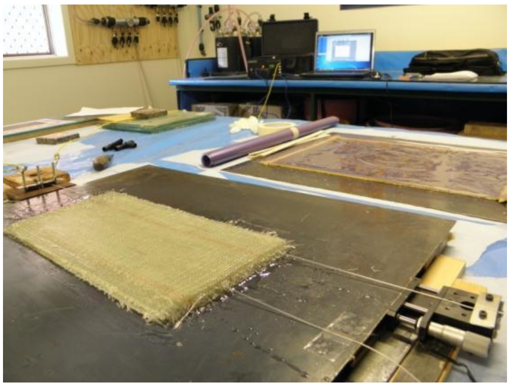

Figure 3-11: Pre-tensioning of FBG sensor during fabrication of an FRP panel

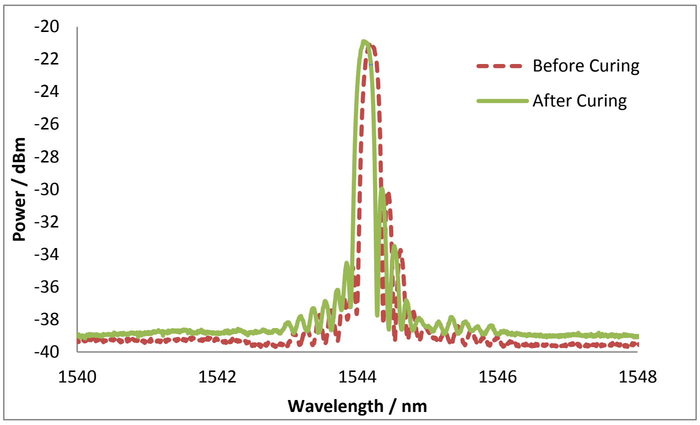

Figure 3-12: Pre-tensioned FBG before and after the curing process

3.4.2 Loading effect of FBG sensor

FBG sensors are very good in strain measurements and the linear unidirectional sensitivity in the axial direction of the sensor is desirable for accurate and reliable strain readings. In such applications, the FBG sensor undergoes pure elongation or contraction and hence, the cross-section always remains in a circular shape. In multidirectional loading cases, an FBG sensor may be subjected to torsional deformations other than linear elongation or contraction. For example, when a torque is applied to a composite sample which has an embedded FBG sensor, it undergoes a twist which may cause changes to its cross-section.

Another possibility of changed cross-section of FBG sensors under torsional loading is due to micro-bending of the grating. The embedded sensor is not always laid on the matrix and there is a possibility of laying an FBG between reinforced fibre mats. In that situation, when the structure is subjected to lateral pressure, the fibre sitting on the FBG sensor will press the FBG sensor against the fibres, causing the sensor to experience micro-bends. These changes of the cross-section of the FBG lead to changes in the refractive index of the core material of the sensor. Since the changes are not uniform along the grating length, the refractive index of the sensor unevenly varies along the grating length of the sensor causing distortion in the FBG spectra.

It is obvious that the distortion of FBG sensors depends on the type of loading. The effect of the twist and micro-bending of FBG sensors under multi-axial loading has been identified as the causes for this discrepancy. The change of section geometry of the FBG sensor due to micro-bending and twisting, leads to a variation of the refractive index of the FBG core material which causes distortion of the FBG response spectra. Figure 3-13 illustrates a distorted FBG sensor response due to tension and torsion combined loading on the FRP panel which the FBG is embedded.

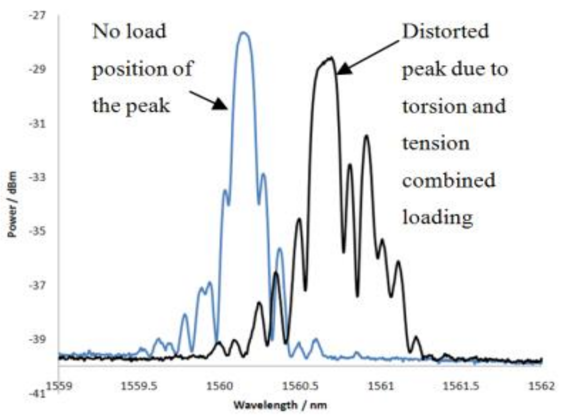

Figure 3-13: Distortion of the peak due to applied torsion and tension combined loading

3.4.2.1 Effect of transverse loading on refractive index of FBG sensor

The effect of transverse loading on the refractive index of glass fibre core material has been investigated by many researchers (S. A. Mastro, 2005). The simplest case to begin the analysis of the FBG is a diametrically loaded cross-section of an optical fibre with no coating or jacket and is been comprised only with silica. The load case can be defined by the Hertz solutions for stress states in disks and spheres under diametrical compression under point loading (Procopio, Zavaiangos, & Cunnigham, 2003). The Hertz approximation assumes very small strains and shape change, point loading, and frictionless contact. These assumptions are appropriate for a high Young's modulus material like silica optical fibre (E=69 GPa). Hertz's approximations were first formulated for brittle high modulus materials. Plane strain is also assumed. Equations 3-5 and 3-6, give the stress in x and y directions while the fibre is under point load, P (Figure 3-14).

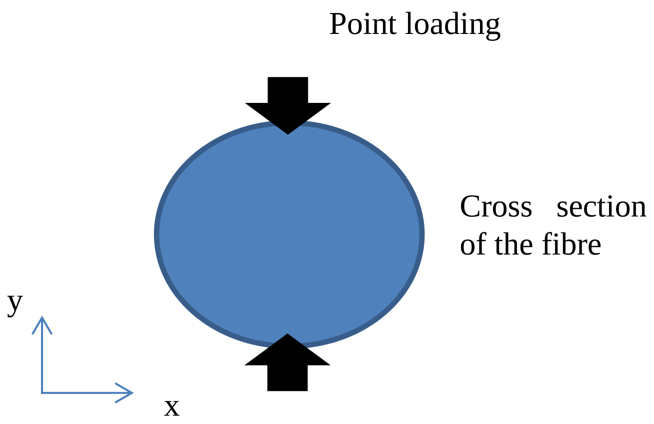

Figure 3-14: Transvers loading on cross-section of the fibre

Hertz formulated the normal stresses within the disk to be:

$$\sigma_x = \frac{-2P}{\pi t}\left\{\frac{x^2(R-y)}{\beta_1^4} + \frac{x^2(R+y)}{\beta_2^4} - \frac{1}{2R}\right\} \quad (3\text{-}5)$$

$$\sigma_y = \frac{-2P}{\pi t}\left\{\frac{(R-y)^3}{\beta_1^4} + \frac{(R+y)^3}{\beta_2^4} - \frac{1}{2R}\right\} \quad (3\text{-}6)$$

where P is the load (diametric point load per unit thickness), R is the radius, t is the thickness, and $\beta_1^2 = (R-y)^2 + x^2$, $\beta_2^2 = (R+y)^2 + x^2$. The Hertz solution predicts that maximum stresses will occur in the centre of the disk, and that stress is tensile along the x axis. The solution of these equations give the normal stresses in the x and y direction for any location (x,y) within the optical fibre cross section.

Using the stress at these locations, a map of stress for both σ_x and σ_y can be created for the fibre core. If these values are combined with a relation for photoelasticity, which directly relates the state of stress to the change in index of refraction, then a map of the index of refraction can be created for the optical fibre core. Photoelasticity relates the change in the index of refraction to the stresses in the fibre by:

$$\left(\Delta n_{eff}\right)_x(x,y,z) = -\frac{\left(\Delta n_{eff,0}\right)^3}{2E}\begin{Bmatrix} (p_{11}-2\upsilon p_{12})\sigma_x(x,y,z) + \\ [(1-\upsilon)p_{12}-\upsilon p_{11}]\left[\sigma_y(x,y,z)\right] + [\sigma_z(x,y,z)] \end{Bmatrix} \quad (3\text{-}7)$$

$$\left(\Delta n_{eff}\right)_y(x,y,z) = -\frac{\left(\Delta n_{eff,0}\right)^3}{2E}\begin{Bmatrix} (p_{11}-2\upsilon p_{12})\sigma_y(x,y,z) \\ +[(1-\upsilon)p_{12}-\upsilon p_{11}][\sigma_x(x,y,z)] + [\sigma_z(x,y,z)] \end{Bmatrix} \quad (3\text{-}8)$$

where n_{eff} is the effective index of refraction, E is the Young's modulus, ν is the Poisson's ratio, *p* is the photo elastic constant, and $\sigma_{x,y,z}$ are normal stresses. The above analysis was completed for the simplest case, a cylindrical uncoated silica fibre with a circular cross section (Figure 3-15).

Equations 3.7 and 3.8 gives the variation of the effective index of refraction with the stress in x and y directions of the fibre.

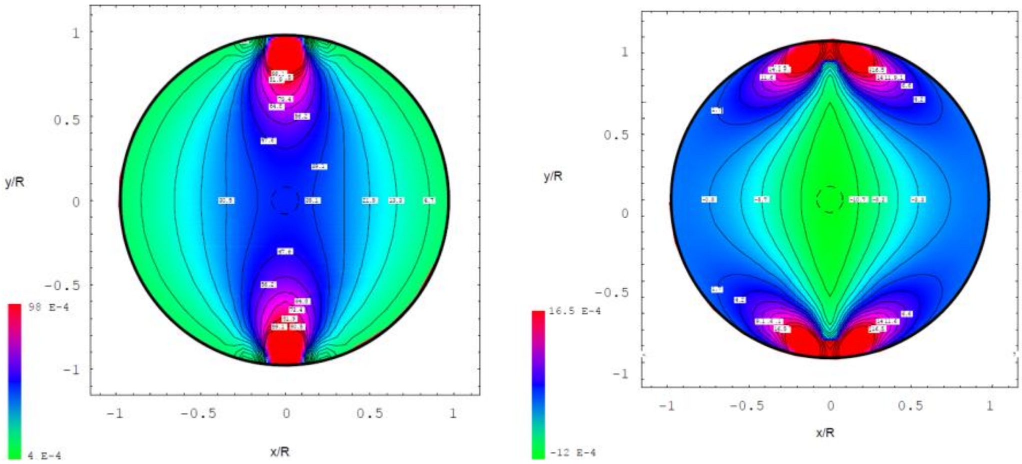

Figure 3-15: Index of reflection change under transverse loading (a) x direction, (b) y direction (S. Mastro, 2005)

The uneven loading on the fibre makes an uneven distribution of the index of reflection along the length of the FBG sensor making the reflection spectra distorted. Experimental verification of the transverse loading effect on the FBG sensor spectrum distortion is given in Section 3.5.

3.5 Self-distortion of the FBG sensor

Although the linear unidirectional sensitivity is excellent, this sensitivity creates difficulties for accurate and reliable strain readings in the multidirectional loading conditions created in real fibre composite applications. If the FBG sensor undergoes pure tension or compression, the cross-section always remains in a circular shape. In multidirectional loading cases, FBG sensors are subject to torsional deformations and bending in addition to tension or compression. When a torsional load is applied to a composite sample which has an embedded FBG sensor within it, the embedded FBG sensor undergoes a twist which will cause changes to its cross-section. Another possibility of changed cross-section of FBG sensors under torsional loading is due to micro-bending of the grating (Martelli, Canning, Gibson, & Huntington, 2007). The embedded sensor is not always lying on the matrix and there is a possibility of lying an FBG between reinforced fibre mats. The fibres near the FBG sensor will press the FBG sensor against the fibres when the structure is subjected to lateral pressure, causing the sensor to experience micro bends (Y. Wang et al., 2008). The changes of the cross-section of FBG sensor changes the refractive index of the core material of the sensor as discussed in Section 3.4.2.1. Since the changes are not uniform along the grating length, the refractive index varies unevenly along the grating length of the sensor causing distortions in the FBG spectra.

The following section details a pilot studies which was undertaken to investigate the several effects on self-distortion of FBG spectra.

3.5.1 Torsional loading of FBG sensor: Experimental verification

3.5.1.1 Fabrication of the specimens

Two tabular-specimens were fabricated (Specimen 1 and Specimen 2) with 6 layers of biaxial glass fibre fabric in the orientation of $[90^{o}\backslash 45^{o}\backslash 45^{o}]_{s}$. Kenetix R246TX epoxy resin was used as the matrix material. The inner diameter of the tube was $\varnothing$ = 50mm and the thickness, $\Delta\varnothing$, is $\Delta\varnothing$ = 3mm. The dimensions were selected according to the recommended geometry by Hodgkinson (2000) for torsion shear testing of thin-walled tubes to ensure that the shear stress is uniformly distributed around the circumference and along the axis of the tube. The wall thickness is made small compared to the mean radius so that the through-thickness shear gradient is negligible. The ends of the specimens are over-layered with additional layers and tapered to promote failure within the gauge length. The tab thickness was 10mm (Figure 3-16) .

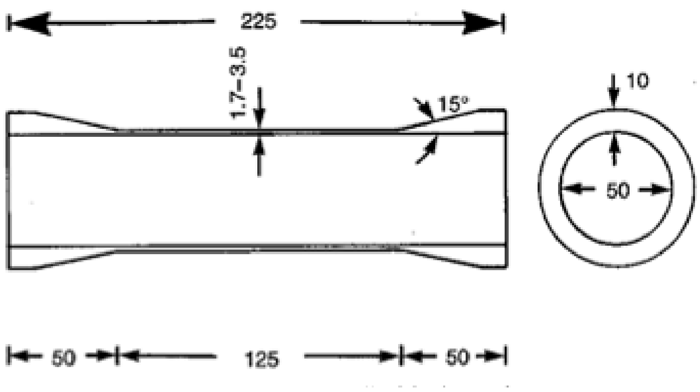

Figure 3-16: Configuration of thin-walled cylindrical specimen

FBG sensors which operate in the range of 1550nm centre wavelength were fabricated on 9µm core and 125µm clad diameter telecommunication grade glass fibre (SMF28). The grating length was 10mm. To ensure maximum bonding between the FBG sensor and matrix of resin in the GFRP material, the acrylate layer at the grating region of the fibre was removed. An extra protective layer of rubber was applied to the ends of the fibre which were located outside the sample to improve the flexibility of handling of samples without damaging the sensors. Specimen 1 was fabricated with an FBG sensor located in between layers 5-6, at an angle of 45^{o} to the axis of the tube (Figure 3-17(a)).

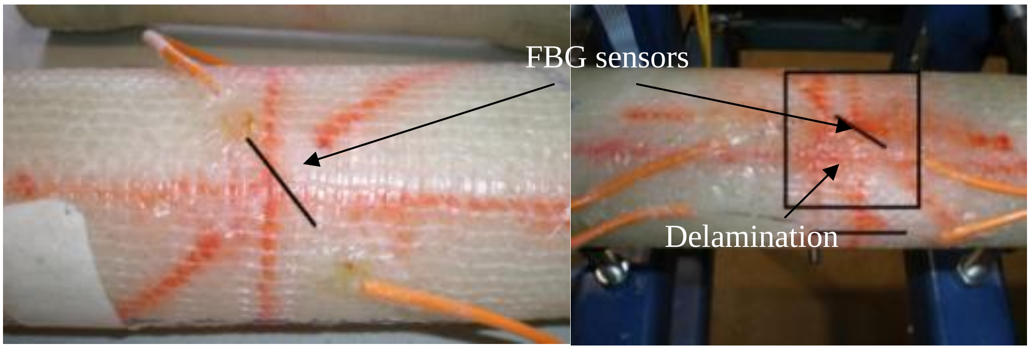

(a) Specimen 1

(b) Specimen 2

Figure 3-17: Specimen 1 and 2 with embedded FBG sensors

Specimen 2 was fabricated with an embedded delamination between the layers 4-5 at the centre of the tube (Figure 3-17(b)). Two FBG sensors were placed in the sides of the delamination between the 4th and the 6th layers. One FBG sensor was attached parallel to the axis of the tube and the other FBG was placed directly above the delamination at a 45^{o} angle to the axis of the tube between layers 5-6.

Figure 3-18 shows the configuration of the embedded delamination between the layers 4-5 in the centre of the tube.

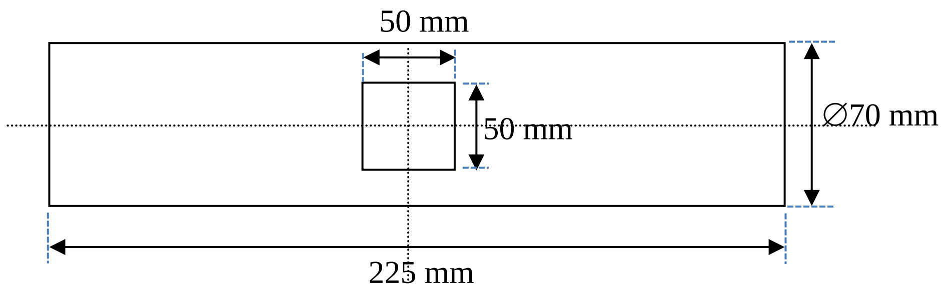

Figure 3-18: Configuration of the Delamination in the Specimen 2

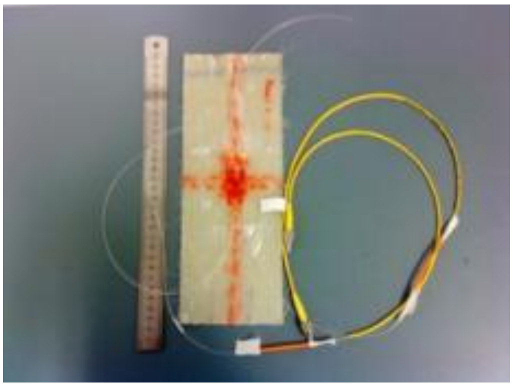

Figure 3-19: A view of a plate specimen (Specimen 3 and 4) with an embedded FBG sensor

In addition to cylindrical samples, two plates were fabricated (Specimen 3 and Specimen 4) as shown in Figure 3-19. The lay-up configuration was [0/0/90]s for Specimen 3 and for Specimen 4 was [0/+45/-45]s. In both panels the FBG sensor was placed in-between the outer layers. In Specimen 3, between 0/0 layers and in

Specimen 4, between 0/+45 layers. In panel 3, the FBG sensor was placed between parallel fibre layers and in Specimen 4, between non-parallel fibre layers.

3.5.1.2 Experimentation

The torsional testing equipment and the test configuration is shown in Figure 3-20. The torsional testing equipment was designed by the author and manufactured at the Centre of Excellence in Engineering Fibre Composites (CEEFC), University of Southern Queensland (USQ). Manufacturing drawings and specifications are given in Appendix B. Specimens were mounted on the torsion at test equipment with one end fixed. The other end of the specimen was supported with roller supports to avoid bending of the samples. Torque was applied by loading the arm attached at the roller support side by means of a screw jack. Applied torque was measured using an S type 0-2 kN range load-cell as shown in Figure 3-20(b). When applying a bending load, the roller support could be removed.

The specimen was loaded in 50 Nm increments, and FBG spectra were recorded. A Micron Optics sm125, optical spectrum analyser was used to measure FBG spectra. Each specimen was loaded three times to maintain the consistency of the readings. The data was recorded and stored for post processing.

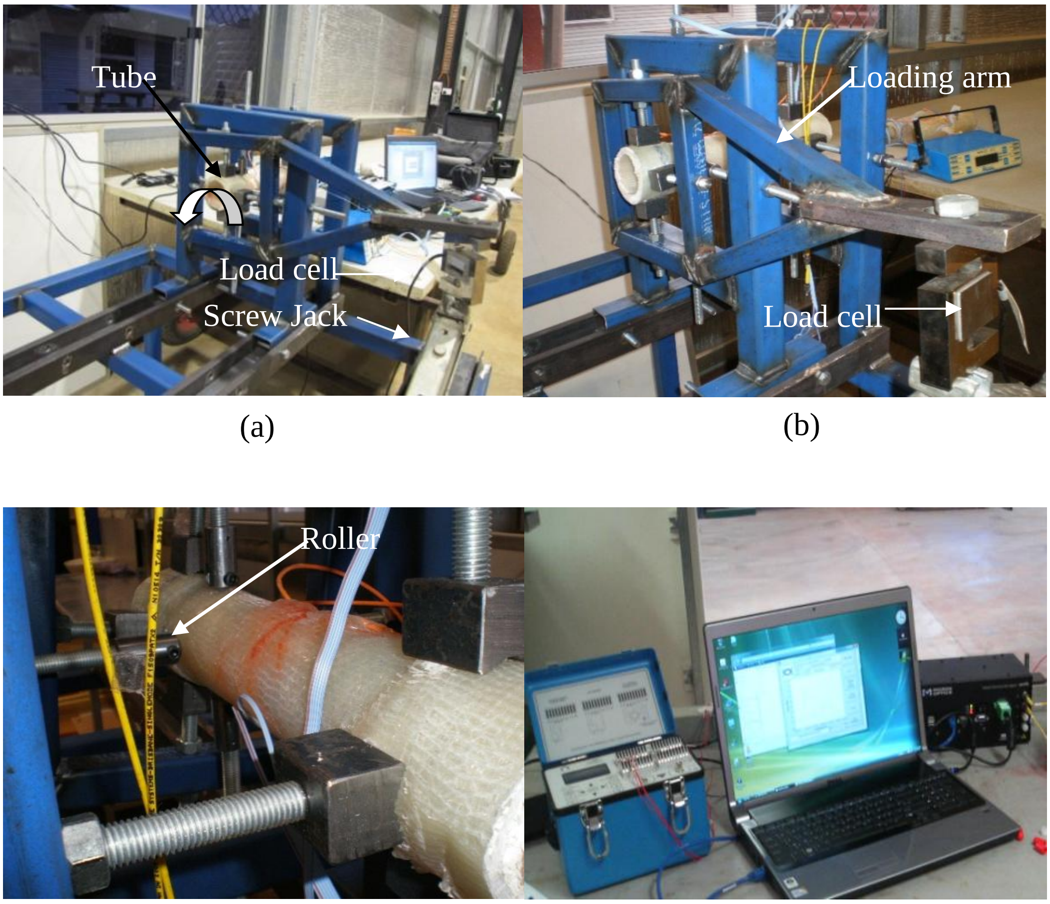

(a) (b)

(c) (d)

Figure 3-20: Torsional test setup

A lateral pressure of 6MPa was applied to the embedded FBG sensors in Specimens 3 and 4 by means of a load of 2250 N on an area of 25 X 15 mm^2 (as shown in Figure 3-21) and the spectra were recorded.

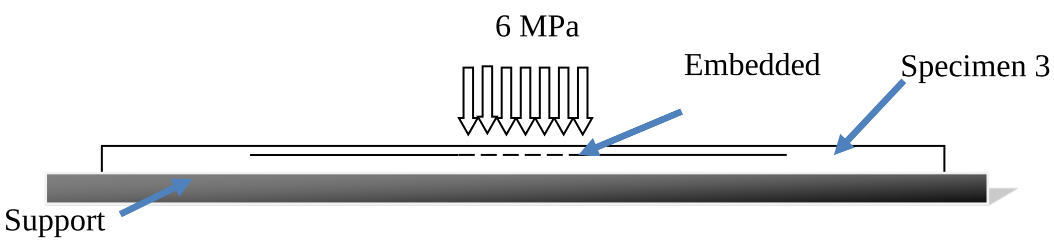

Figure 3-21: Lateral loading of FBG sensor in Specimens 3 and 4

Subsequently, Specimens 3 and 4 were loaded on a mechanically operated testing machine as shown in Figure 3-23. The panels were subjected to a torque and axial load independently, and subsequent combined axial and torsional loads (Figure 3-23). The machine was used to apply axial tension to the specimen by moving top and bottom supports. The torque was applied on the other hinge by means of a handle fixed to one support while the other support was fixed. The rotating handle is shown in Figure 3-23(b).

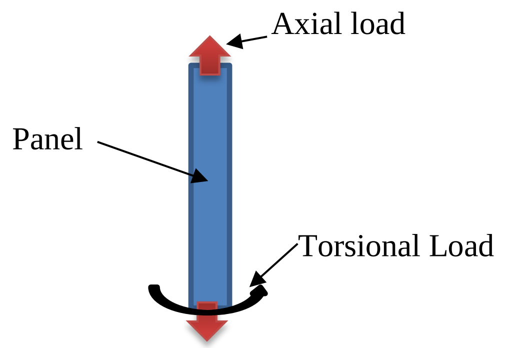

Figure 3-22: Axial and torsion combined loading on the panel

Initially, Specimen 3 was subjected to a 10 Nm torque without any axial load. Then the specimen was loaded with axial loads of 420 N and 730 N and finally, combined axial and torsional loading was applied. The FBG spectrum was recorded for three load cases, namely pure axial, pure torsion and combined loading.

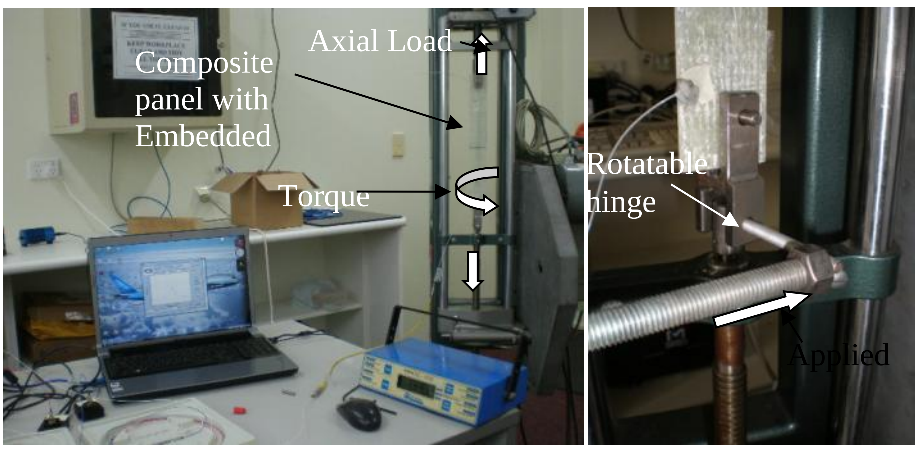

(a) (b)

Figure 3-23: Axial and torsional loading on FBG

3.5.1.3 Results and discussion

Spectrum of sensors embedded in Specimen 1 and 2: The reflected spectrum of the sensor embedded in Specimen 1 was distorted with applied torque as shown in Figure 3-24. Figure 3-24(a) shows the response spectra of the FBG while the tube is under 300 Nm torsional load and Figure 3-24(b) shows the response spectra under 425 Nm torsional loads. Since there is no significant defect at the vicinity of the embedded FBG sensor of Specimen 1, the main peak of the spectrum can be clearly distinguished from the other peaks. With the incremental increase in torque, the main peak moves rightward while the distortion of the spectra also varied significantly.

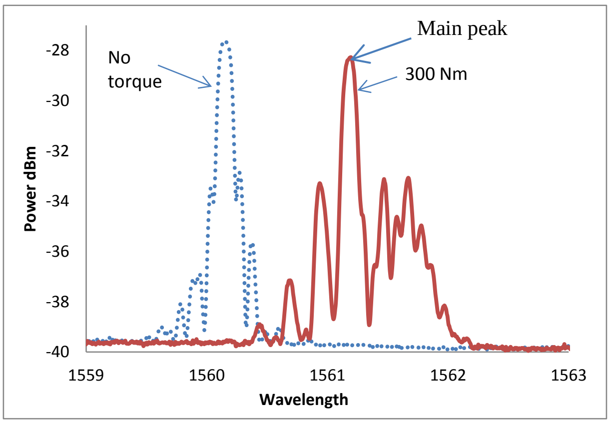

(a)

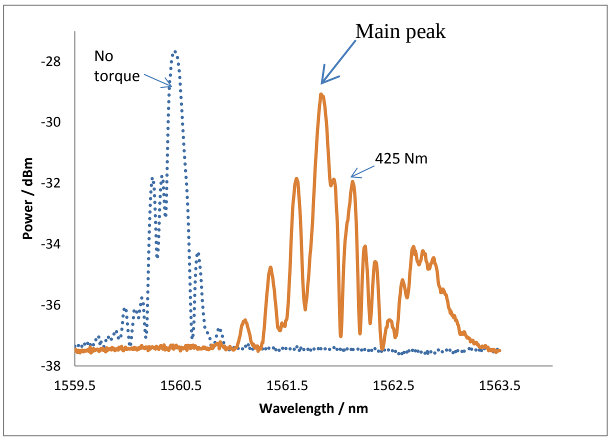

(b)

Figure 3-24: Reflected spectrum of the FBG sensor embedded in Specimen 1 under torsional loading.

Figure 3-25 shows the reflected spectrum of the FBG sensor embedded in Specimen 2, parallel to the axis of the tube. The specimen is under torsional loading of 300 Nm as shown in Figure 3-26. As the bending of the beam is minimal, the original peak must be intact. However, the presence of the delamination in the same layer and possible micro-bending due to torsional loading has distorted the spectrum with the increased toque. In this case the track of the main peak was lost.

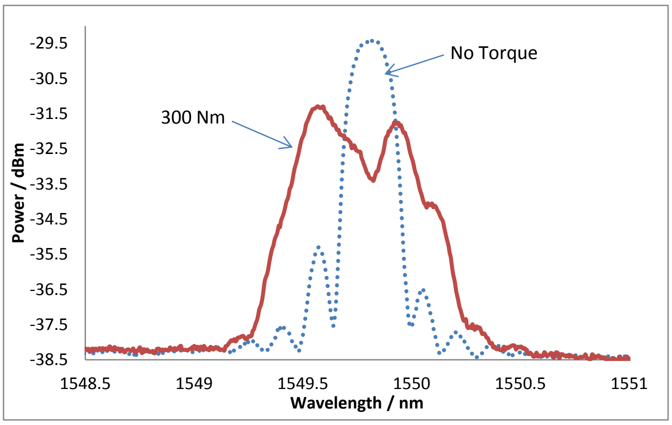

Figure 3-25: Reflected spectrums of the FBG sensor which is parallel to the axis of Specimen 2

Figure 3-26 shows the reflected spectrum of the FBG sensor embedded in Specimen 2 at an angle of 45^{o} to the long axis and above the delamination. The 45^{o} sensor was positioned between layers 5 and 6 and in the centre of the long axis as in Specimen 1. The peak movement of the sensor was minimal compared to Specimen 1. The two peaks observed in 300 Nm loading (Figure 3-26(a)) were further widened (Figure 3-26(b)) with increased loading due to the stress concentration and the distortion of the sensor's cross-sectional geometry. The other important observation here is the disappearance of sharp peaks (Figure 3-26) which may be a combined effect of the delamination and the section geometry distortion.

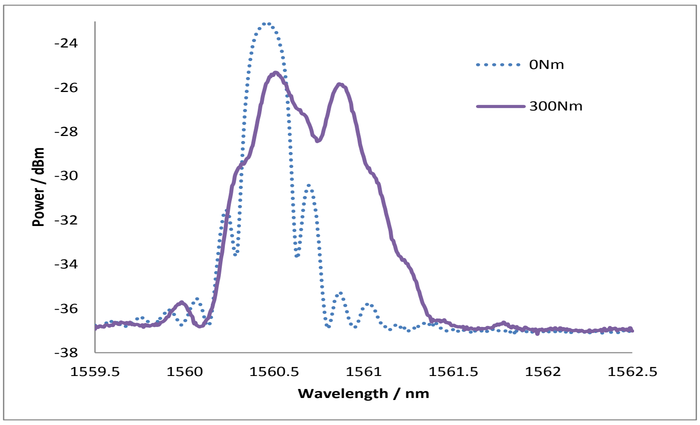

(a)

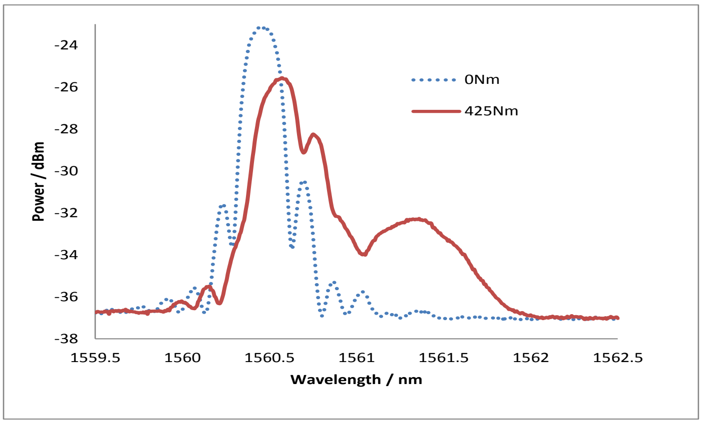

(b)

Figure 3-26: Reflected spectra of the FBG sensors in the 45^{o} direction embedded in the Specimen 3

Figure 3-27 provides a simple explanation to this discrepancy. As shown in Figure 3-27(a), the pressure load applied on FBG sensor by the outer glass fibre layers, can distort the cross section of FBG to an oval shape. Since the FBG sensor is placed in-between non-parallel fibre layers, micro bending of the sensor is also possible. The top 90^{o} layer fibres undergo tension due to the torsional loading on the tube. Due to the large diameter of the FBG sensor, compared to the diameter of glass fibres, there are additional transverse forces on the FBG sensors which lead to micro-bending as shown in Figure 3-27(b).

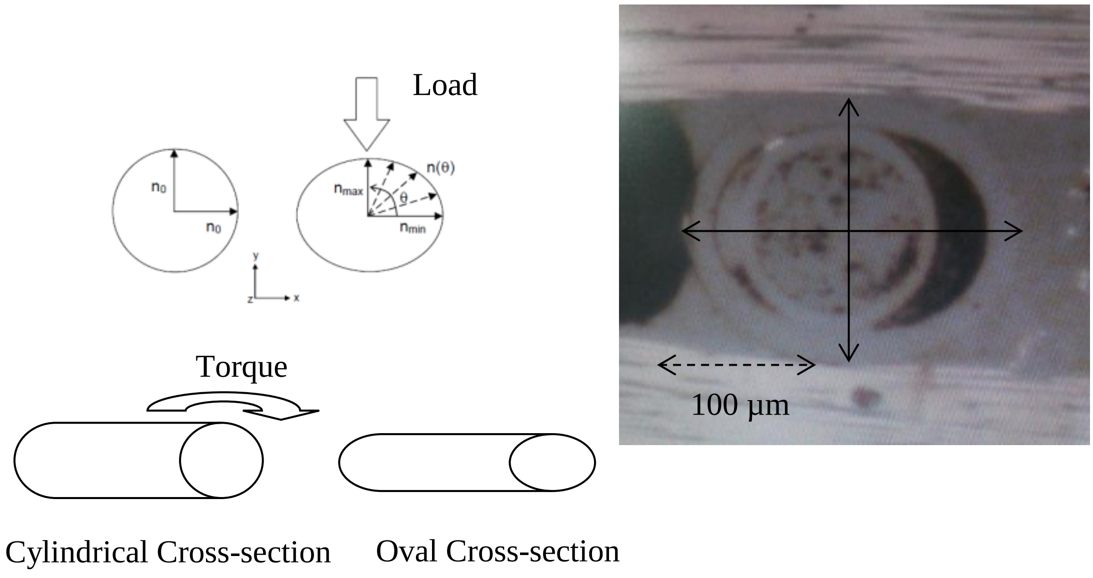

(a) Deformation of the cross-section of the sensor due to torsional loading

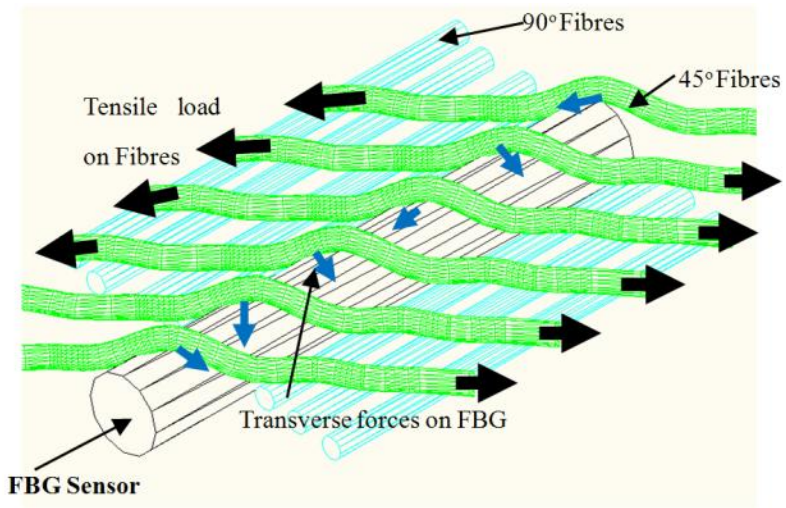

(b) Micro-bending of the sensor

Figure 3-27: Transverse loading on FBG sensor

Both these effects will lead to a variation of the refractive index of the core material, causing the chirped spectrum as shown in the Equation 3.3.

This explanation also supports the observations reported by Wang et al (2007) and Yiping et al (2005). (H. Wang, Ogin, Thorne, Reed, & Ussorio, 2007; Yiping et al., 2008). Theoretical explanation for this discrepancy was provided by Mestro, (2005) as discussed in Section 3.4.2.1.

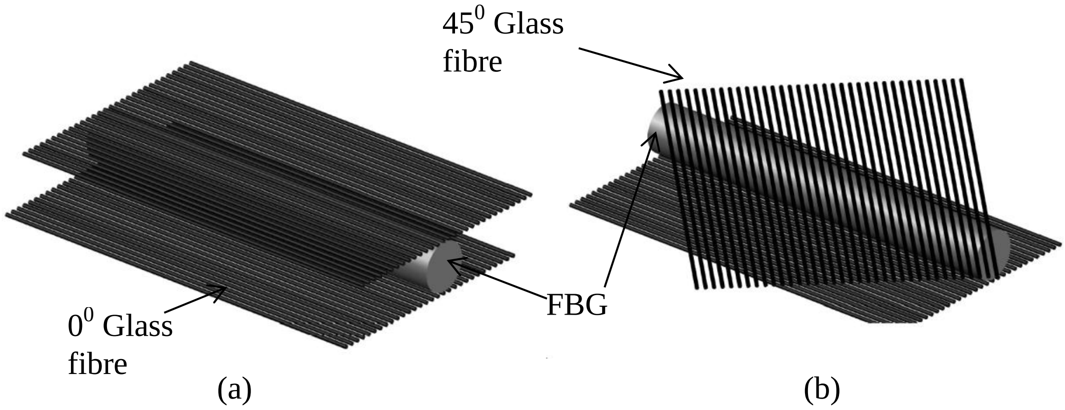

Figure 3-28: Embedment of FBG sensor between glass fibre

Spectra of embedded FBGs inside Specimens 3 and 4: Specimen 3 with an FBG between layers 1 and 2, both with 0^o fibre direction, (Figure 3-28(a)) did not show any significant distortion to the spectrum under lateral pressure loading, as shown in Figure 3-29(a). There is no or negligible possibility of micro-bending happening in the FBG sensor since the glass fibres and FBG are parallel to each other. The spectrum of FBG in Specimen 4 between layers 1 and 2, which are in 45^o angle to each other (Figure 3-28 (b)), was distorted as shown in Figure 3-29(b), under lateral pressure loading. The overlapping glass fibres applying individual small transverse forces on the FBG, as explained in the above section, could possibly be the cause of this behaviour.

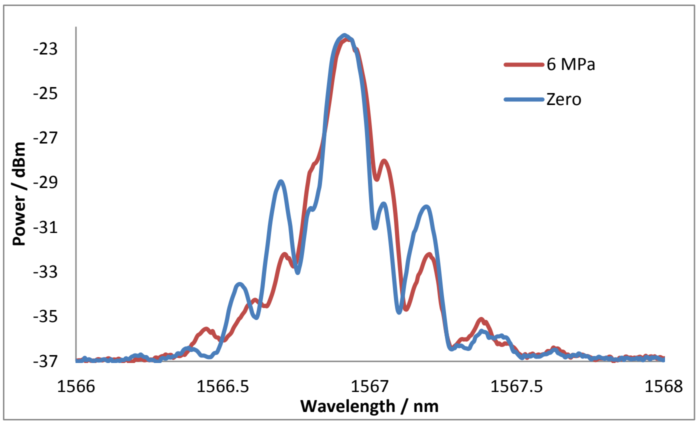

(a) Specimen 3

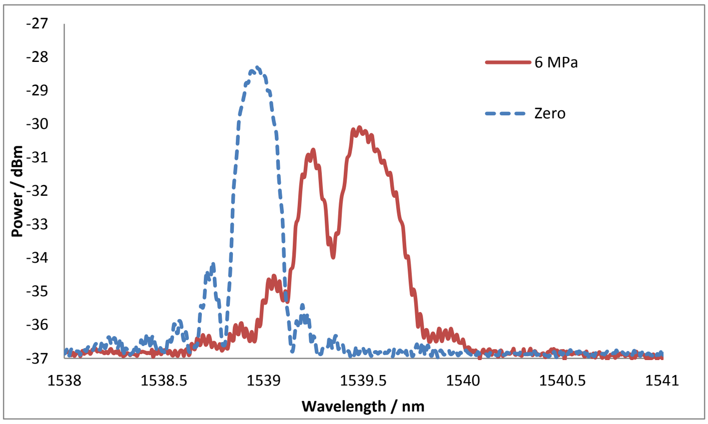

(a) Specimen 4

Figure 3-29: Chirp in the FBG sensors due to lateral loading

Figure 3-30 shows the distortion of the spectrum of the FBG sensor embedded in Specimen 3 due to applied torque of 10 Nm only. Figure 3-31(a) and (b) show the chirp of FBG spectrum with 420N and 730N axial load combined with the 10 Nm torque.

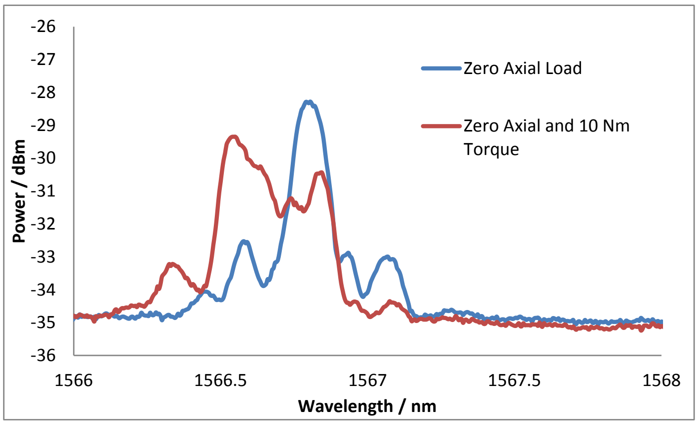

Figure 3-30: Spectra of embedded FBG in Specimen 3 under an applied torque

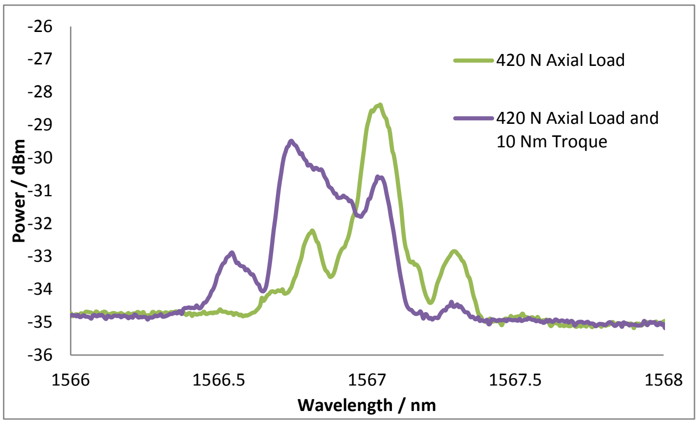

(a)

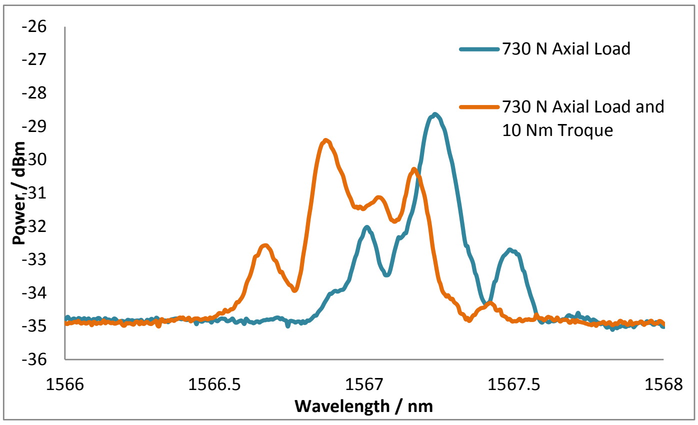

(b)

Figure 3-31: Spectra of embedded FBG in Specimen 3 under pure axial and combined torque and axial load

With the applied axial load, the peak of the spectrum moved smoothly rightwards. While the axial load was fixed at 420 N, a torque of 10 Nm was applied to the specimen. The spectrum chirped as shown in the Figure 3-31(a). The peak of the spectrum moved leftward, while axial load remained at 420 N. The process was repeated with a higher axial load, 730 N and the results demonstrated similar travel, as shown in Figure 3-31(b). Specimen 3 had an embedded FBG sensor between parallel glass fibre layers. By twisting the panel, the FBG also twisted, but the possibility of micro-bending was minimal. Hence, the results obtained in Figure 3-30 and Figure 3-31, representing the twisting effect on the FBG. Therefore, the use of FBG sensors to measure axial strain in a twisted sample did not produce accurate results.

The FBG sensors which were embedded in torsionally loaded composite samples have shown substantial distortion in reflected spectra without any significant damage at the vicinity of the grating. On the other hand, it has been observed that the effects of stress concentrations due to a delamination have also caused distortion of the spectra of the FBG sensor as expected. As such, it can be concluded that the distortion of FBG sensors is dependant on the type of loading. The effect of the twist and micro-bending of FBG sensors under multi-axial loading is the cause of this discrepancy. The change of section geometry of the FBG sensor leads to variation of refractive index of the FBG core material along the length which causes distortions to the FBG response spectrum. The effect of twist and micro-bending was independently identified by separately subjecting an FBG sensor to twist and micro-bending. It has been observed that twisting causes chirp with smooth peaks (Figure 3-29(a) on FBG spectra whereas micro-bending causes small sharp peaks (Figure 3-29(b). Since the effect of the loading on the FBG sensors is significant, these effects must be accounted for in the post-processing of the spectra for damage identification in an advanced SHM system.

3.6 Distortion of the embedded FBG sensor spectra

The majority of research work on FBG sensors in SHM of composite structures has focused on investigation of the spectra of FBG sensor embedded in the vicinity of damage. Observations of the distorted sensor spectra due to stress concentrations caused by delaminations and cracks have been used to estimate the damage conditions. Many researchers have investigated purposely damaged axially loaded specimens, and the changes of FBG spectra were attributed to the damage and successfully identified the damage (Takeda, Okabe, & Takeda, 2008). In real life situations, the applied loads are not limited to uni-axial loads and hence the performance of FBGs in multi-axial loading situation needs to be investigated for a complete understanding of damage status. The FBG spectral response is significantly complicated under multi-axial loading conditions (G. Kahandawa, Epaarachchi, Wang, & Lau; Sorensen, Botsis, Gmur, & Cugnoni, 2007). The distortion of FBG spectra is not only due to the accumulated damage, but also the loading types. In the previous section, it was shown that embedding FBGs between non-parallel fibre layers and the application of torque caused substantial distortions to the FBG spectra.

Even through the distortion of the response spectra of an FBG sensor has been widely used in SHM applications to detect structural integrity, unfortunately there is still no definite method available to quantify the distortion. This has been a significant drawback in the development of SHM systems using embedded FBG sensors for decades. Quantification of distortion of the FBG sensor will allow referencing and comparison to monitor for the progressive damage status of a structure. An explicit method to quantify distortion to the sensor including self-distortion needs to be developed.

The next section will introduce a novel method, the "Distortion Index" to quantify distortion in the FBG spectrum. The Distortion Index is calculated related to the original spectrum before the presence of any damage.

3.6.1 Concept of Distortion Index

The Distortion Index (DI) is introduced to create a correlation between the damage and the distortion of the response spectra of a FBG sensor. This index provides the ability to generalise the distortion of FBG spectra for a particular structure. The index can be used to quantify the damage in the structure relative to its original condition, which can be the condition of structure during a regulated time, (i.e. a month of uninterrupted operation or the first hours in operation).

In the early stages of operation of a structure, to a standardised load case, the DI can be calculated and recorded. For comparison reasons, it is possible to define a particular load case for a structure. The defied load case should be repeatable. After several years of operation, the structure can be subjected to that same (defined) load case, and the DI can be recalculated. If the structural integrity is intact, the DI should be equal to the previous value.

Even through the distortion of the FBG sensor has been used for several decades to investigate damage in composite structures, there is no clear definition for quantifying distortion of FBG spectra. The suggested method first defines distortion of the FBG spectrum in order to introduce the Distortion Index.

3.6.1.1 Distortion (Ds)

Distortion (Ds) is defined using the Full-Width Half-Maximum (FWHM) value of FBG spectra and the maximum power of the FBG response spectrum. FWHM is an expression of the extent of a function given by the difference between the two extreme values of the independent variable at which the dependent variable is equal to half of its maximum power (Figure 3-32).

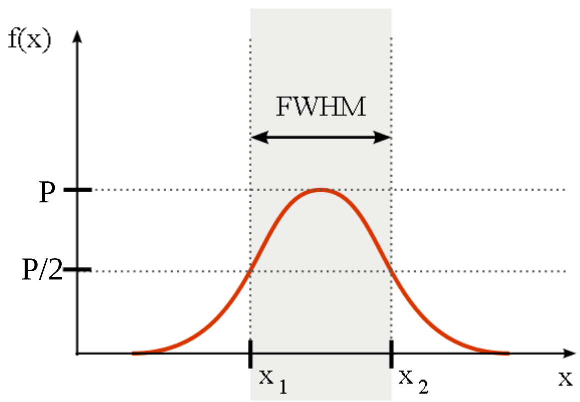

Figure 3-32: Full width at half maximum

Generally for a FBG response spectrum, the FWHM value increases with the distortion while the peak value decreases. $FWHM = (x_2 - x_1)$.

For the comparison, the distortion Ds and the distortion index DI, need to be calculated for the same load case. Distortion of the peak at a particular load case, D_s, can be expressed as:

$$\mathrm{D_s} = \frac{\mathrm{FWHM}}{\mathrm{P}} \tag{3-9}$$

where, P is the peak strength of the FBG sensor reflection spectra in dB as shown in the Figure 3-33.

3.6.1.2 Distortion Index, DI

With the calculated Distortion value, the Distortion Index, (DI) can be calculated.

Distortion Index, DI at the same load case:

$$\mathrm{DI} = \frac{\mathrm{D_{si}}}{\mathrm{D_{s0}}} \tag{3-10}$$

where $\mathrm{D_{si}}$ is the current distortion and $\mathrm{D_{s0}}$ is the distortion at the original condition (no damage).

If there is no damage present in the structure, D_{si} is equal to D_{s0} for the same load case. In that case the Distortion Index (DI) is equal to unity. With the presence of damage, the response spectrum of an FBG sensor broadens (FWHM increases), while the peak power of the spectrum decreases. As a result D_{si} increases making the Distortion Index, DI value above unity. This phenomenon can be used to identify the presence of damage in a structure.

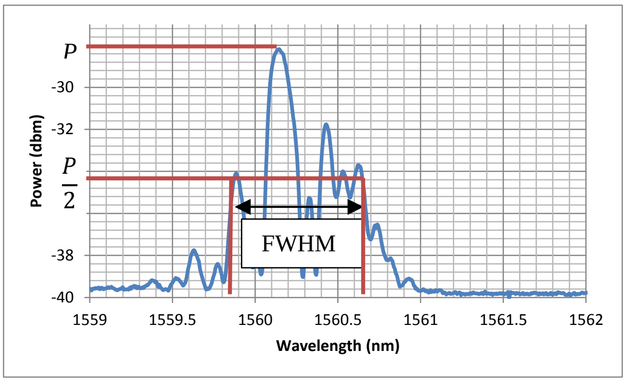

Figure 3-33: Peak value and the FWHM of FBG response spectra

To verify the Distortion Index, it is better to use several load cases to calculate distortion and corresponding Distortion Indices. At the initial stage, the structure can be subjected to several known load cases, and corresponding distortion, D_{s0} can be recorded. In future operations, those load cases can be used to calculate the Distortion Index in order to identify damage. In the following experiment, the Distortion Index has been calculated to investigate the relationship of DI to a growing defect.

3.6.2 Experimental Investigation of the Distortion Index

An experimental study was conducted to investigate the Distortion Index and its suitability for referencing to damage growth. Two test specimens were fabricated using a glass/epoxy composite. On one specimen a cut was placed along the transverse direction through the laminate, and on the other specimen, a hole was drilled through the thickness to simulate damage. FBG sensors were embedded in the vicinity of the damage. To ensure maximum bonding between the FBG sensor and the matrix of resin in the GFRP material, the acrylate layer of the fibre was removed. An extra protective layer of rubber was applied to the fibre to enhance sensor robustness.

3.6.2.1 Fabrication of specimens

Specimen 1:

In a glass/epoxy composite sample with stack sequence of $[0/0/90/90/-45/45/90/0]_S$. a rectangular slot was created during the fabrication of the specimen as shown in the Figure 3-34. The slot was used as the controllable defect for the experiment. The initial width of the cut was 10 mm which is considered as no damage or damage size 0 mm (Figure 3-34(b).

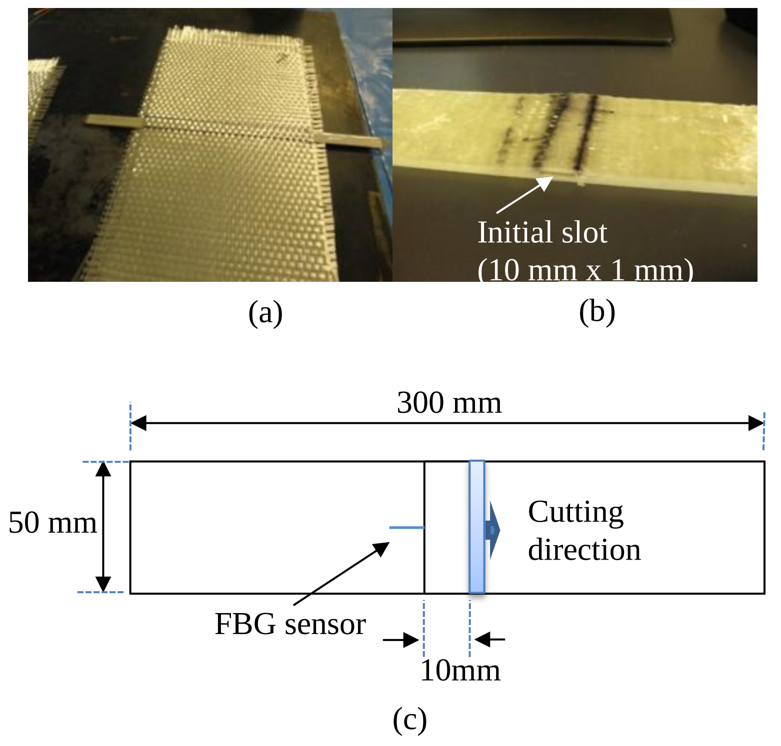

Figure 3-34: Fabrication of the specimen with damage

A FBG sensor with centre wavelengths at 1539 nm was embedded above the cut on the top layer, as shown in the Figure 3-34(c). The cut was used as a controllable defect, as the size of the cut was increased using a thin hacksaw, as shown in the Figure 3-35.

Figure 3-35: Increasing the damage size by cutting

For comparison, the FBG response for 100N load in each damage size, 0mm to 10mm, (which is cut size from 10 mm to 20 mm) was used. Distortion and the Distortion Index for each damage size were calculated.

Specimen 2:

The sample was fabricated with 10 layers of E-Glass fibre in the orientation $[0/90/\pm45/90/0]_S$. Kenetix R246TX epoxy resin was used as the matrix material. The FBG sensor at the centre wave length 1560 nm was embedded between non-parallel layers, 3 and 4, 15 mm away from the centre of the hole, as shown in Figure 3-36.

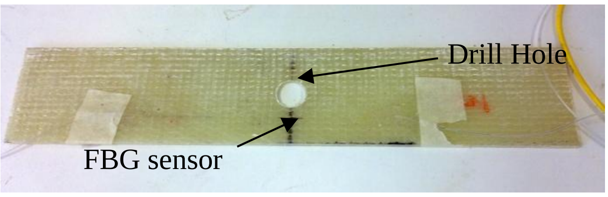

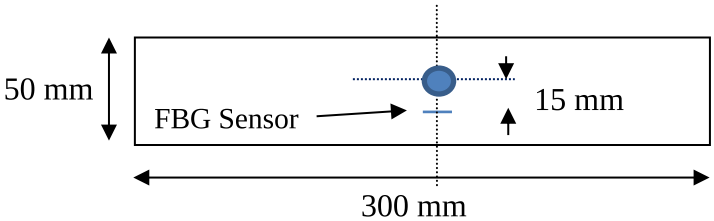

Figure 3-36: Location of the FBG sensor in the specimen between layers 3 and 4

The drill hole was used as a controllable defect, as the size of the hole was increased using a drill, as shown in the Figure 3-36.

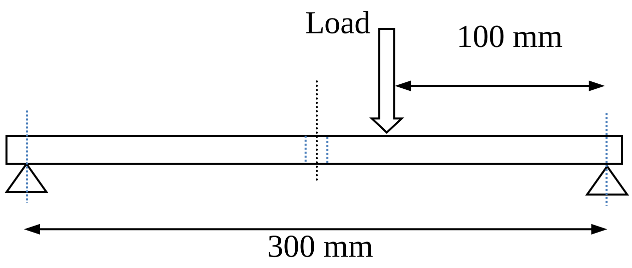

Figure 3-37: Experimental setup

The loading setup for the specimens is given in Figure 3-37. To avoid loading directly above the defect and the FBG sensor, the load was applied 25mm from the centre of the specimen as shown in the Figure 3-37.

Specimen 2 was loaded in 10N steps up to 100N for each damage size (hole diameter 5mm, 8mm, 10mm, 12mm and 16 mm) and the spectral response was recorded.

3.6.2.2 Results and Discussion

Specimen 1:

Figure 3-38 shows the spectral response of the embedded FBG sensor in Specimen 1 under the same loading value, 100N with different damage sizes. Figure 3-38(a) shows the initial spectrum which is considered to be the non-damaged condition. Figure 3-38(b) to Figure 3-38(f) show the distorted spectrum with damage sizes 3,5,7,9 and 10 mm.

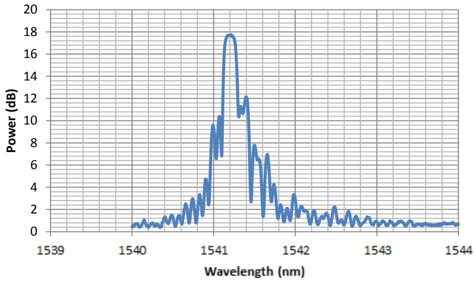

(a) No damage

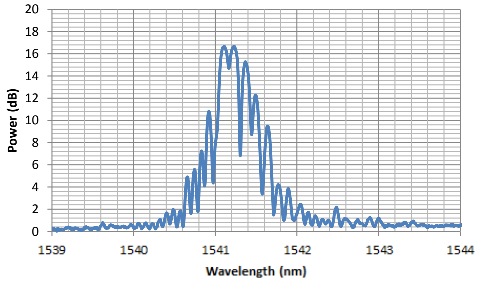

(b) 13mm

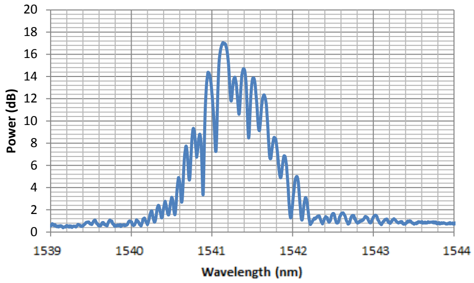

(c) 15mm

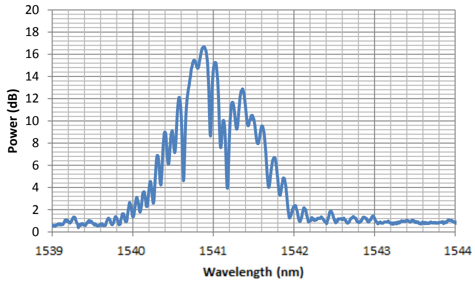

(d) 17mm

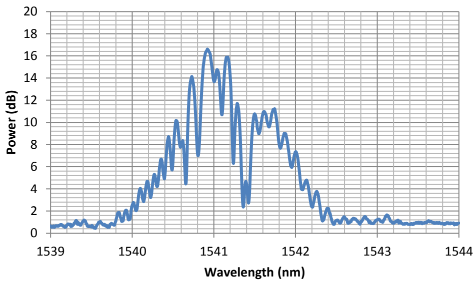

(e) 19mm

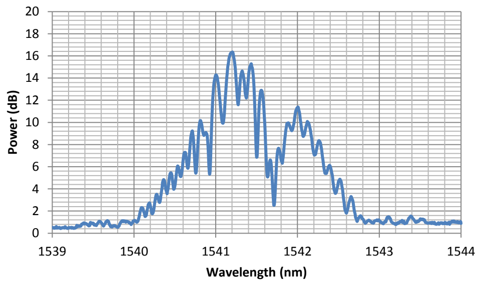

(f) 20mm

Figure 3-38: Spectral response of the FBG sensor at 100N loading for different damage sizes

The original cut (10 mm) was created during the fabrication of the specimen. The FBG sensor was embedded with the presence of the cut. As such, the distortion is minimal due to the original size of the cut 10 mm as shown in the Figure 3-38(a). Therefore, it was assumed that the distortion due to 10 mm cut is negligible compared to the subsequent extended cuts, and hence the spectra at the 10mm cut was taken as the original no damage condition. Even with presence of distortion, a spectrum can be used as no damage status, knowing the cause of distortion is not damage. Figure 3-39 illustrates the cut size and the damage size conceded in this study.

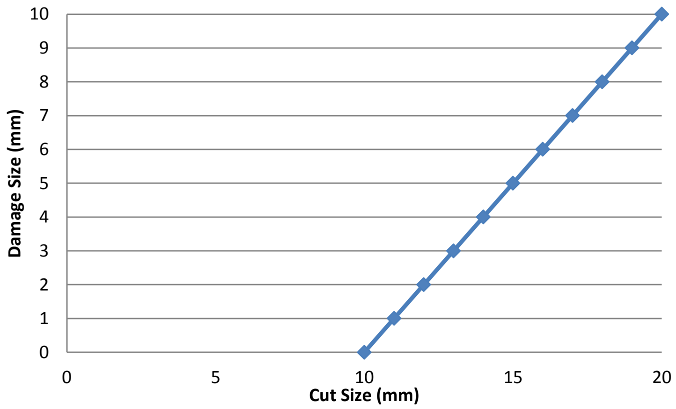

Figure 3-39 : Relationship of damage size to the cut size

The results show a significant distortion to the FBG response spectra with the damage growth. Distortion of the spectrum and the Distortion Index for each damage size were calculated using the Equations 1 and 2. Figure 3-40 shows the Distortion Index values respectively for the damage sizes 0 to 10.

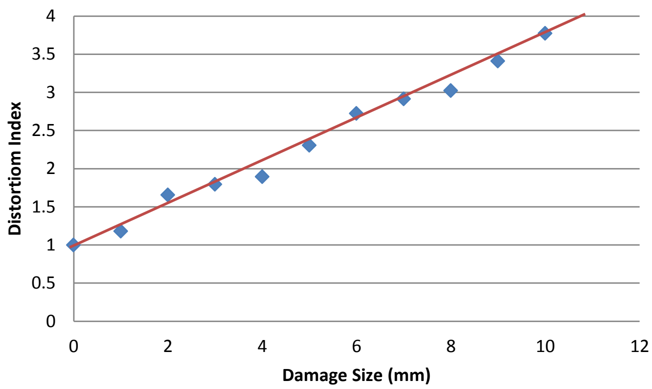

Figure 3-40: Variation of Distortion Index with the damage size

Specimen 2:

Figure 3-41shows the spectral response of the embedded FBG sensor in Specimen 2 under the same loading value 100N, with different damage sizes. Figure 3-41(a) shows the initial spectrum which is the non-damaged condition. Figure 3-41(b) to

Figure 3-41(f) shows the distorted spectrum with damage sizes (hole diameters) 5, 8, 10, 12 and 16 mm.

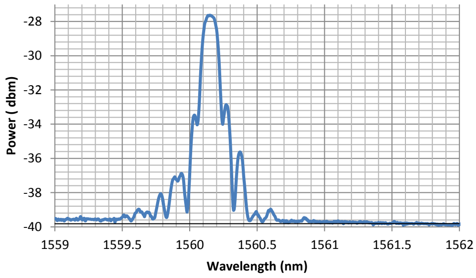

No damage

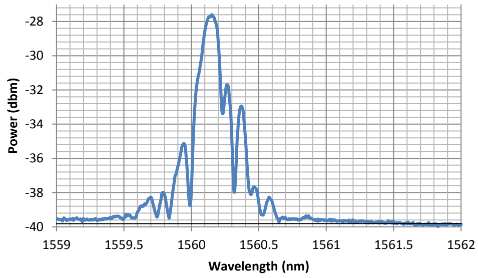

(b) 5mm diameter

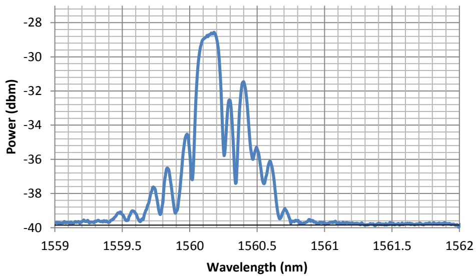

(c) 8mm diameter

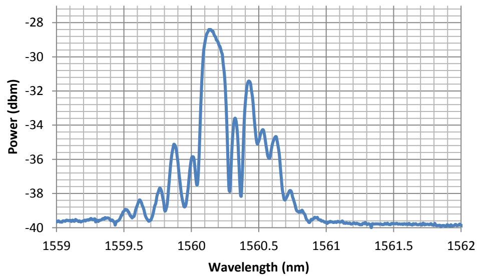

(d) 10mm diameter

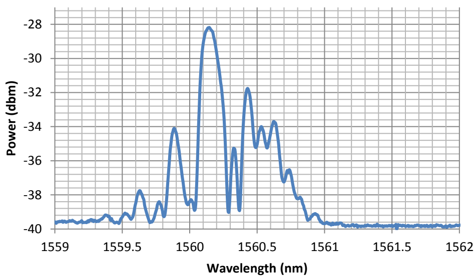

(e) 12mm diameter

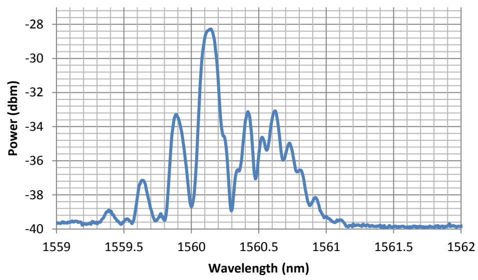

(f) 16mm diameter

Figure 3-41: Spectral response of the FBG sensor at 100N loading for different damage size (hole diameter)

The results show a significant distortion to the FBG response spectra with damage growth. Distortion of the spectrum and the Distortion Index for each damage size were calculated using the Equations 1 and 2. Figure 3-42 gives the Distortion Index values respectively for the damage sizes 0 to 16 mm.

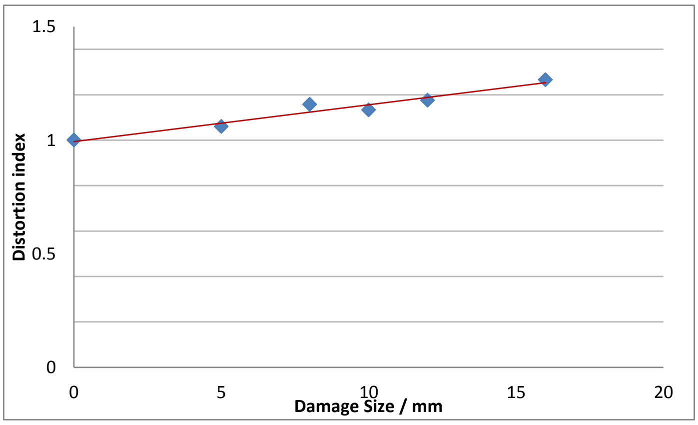

Figure 3-42: Variation of Distortion Index with the damage size (hole diameter)

Figure 3-40 and Figure 3-42, shows the variation of the Distortion Index with the damage growth. It has been observed that, with the growth of the damage, the Distortion Index increases. Due to increased damage size, the FBG response spectrum is broadened. The peak strength of the spectra is decreased as the reflection energy from the FBG sensor, i.e. total area under the curve, is a constant. As a result, the distortion value of the sensor rises with the damage size growth.

3.6.2.3 Conclusion

The distortion of FBG spectra has been quantified as D_s. A Distortion Index (DI) was defined to reflect the increased size of the damage. It has been seen that the Distortion Index can be used to quantify damage in composite structures. In this study the damage size was increased linearly and the corresponding increase of DI has shown a linear trend. However, the linear trend may not be true as distortion of FBG spectra is dependent on the damage type and propagation, loading type and fibre orientation. It can be concluded that the Distortion index (DI) can be devised to rank damage condition in a particular composite component or a structure.

3.7 Damage detection in composite structures using FBG sensors

From the observations discussed earlier in this chapter, it is clear that multiple causes lead to the distortion to the FBG response spectra. Most of the effects such as the embedment of FBG sensor only between parallel fibre laminates, parallel to the fibre orientation, and multidirectional loading on FBG sensor, cannot be eliminated in advanced aerospace applications. In order to identify damage from the distortions to the FBG response spectra, the individual effect from each effect needs to be identified and eliminated. To identify the pure effects from the damage, distinguished from the other effects, extensive computational power is required for post-processing of the spectral data. Figure 3-43 shows FBG response spectra from an FBG embedded near a damaged location with the part under the complex multi-directional loading.

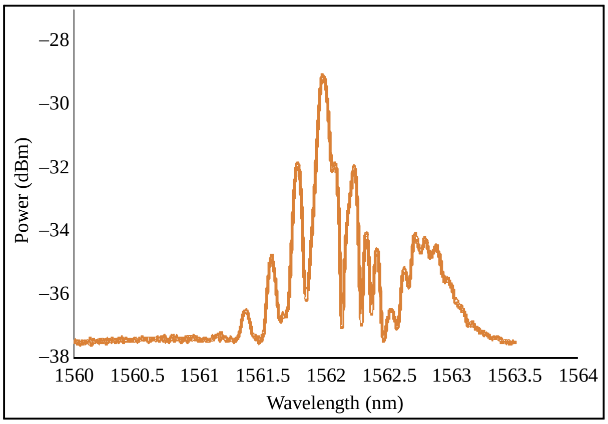

Figure 3-43: Distorted FBG spectra due to multiple effects

As a consequence, in the laboratory environment, it is possible to discuss and interrelate the FBG response spectra with the damage by creating an artificial damage and observing spectrum of an FBG which is embedded closer to the damage location. But in real applications, if such a spectrum is observed, it is very difficult to interpret the spectrum in order to identify the damage. The one directional accuracy, which is if there is a known damage in the structure, response spectra (distortion) of embedded FBG can be explained, but if distorted response spectrum is observed, it is not possible to identify it as a presence of damage. This incongruity made some of the SHM researchers disappointed and discouraged. There was a huge demand for an out of the box approach to overcome this discrepancy.

The system discussed in the Chapter 4 is a novel approach to overcome the complications above mentioned. The approach is to develop a system to adapt to the initial conditions of the structure and to identify new conditions by comparing them with the initial condition. The response of the FBG during the undamaged states of the structure is recorded, and this recorded data is used as a “reference”. Therefore, the isolation of possible “reference” data from a distorted spectrum of any embedded FBG sensor will definitely provide the subsequent distortions to the spectra caused by accumulated damage.

The main difficulty for this approach is to develop a system to reference the FBG response spectra. Historically, statistical methods such as artificial neural networks (ANN) have been used to analyse such complicated data associated with a large number of random variables. The main advantage is the ability to train an ANN with undamaged data, and subsequently, the trained ANN can be used to distinguish any new spectral variation. In order to input spectral data to the ANN, decoding system needs to be developed. To address the above issues, the “fixed FBG filter decoding system” was developed to capture the distortion to the FBG sensor response spectra.

CHAPTER 4

Decoding FBG sensor response spectra using fixed wavelength FBG filters and use of Artificial Neural Networks for damage detection

4.1 Introduction

The SHM systems use in damage detection in FRP composites must be capable of identifying the complex failure modes of composite materials. The damage accumulation in each layer of a composite laminate is primarily dependent on the properties of the particular layer (McCartney, 1998, 2002) and the loads which are imposed onto the layer. As such, the layered structure of the composite laminates makes it difficult to predict the structural behaviour using only surface attached sensors. Over the past few years, this issue has been critically investigated by many researchers using embedded FBG sensors (Eric, 1995; Lee et al., 1999; Takeda et al., 2002; Takeda, Okabe, & Takeda, 2003; Takeda et al., 2008).

Observations of the distorted FBG spectrums produced by these sensors have been used to estimate the damage in composites. The majority of the research works were focused on the investigation of the spectra of FBG sensors embedded in the vicinity of damage loaded with unidirectional loading. However, in real life situations, the applied loads are not limited to uni-axial loads and hence the performance of FBGs in multi-axial loading situation needs to be investigated for comprehensive damage characterization.

The FBG spectral response is significantly complicated by multi-axial loading conditions (Sorensen et al., 2007), fibre orientation, and the type of damage present in the structure (G. C. Kahandawa, Epaarachchi, Wang, & Canning, 2010; G. C. Kahandawa, Epaarachchi, Wang, Followell, et al., 2010). It has been shown that FBG's embedded between non-parallel fibre layers and subjected to torque create significant distortions in the spectra (Figure 4-1).

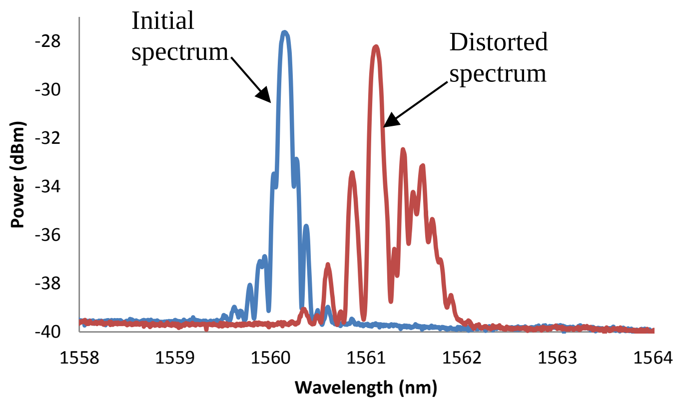

Figure 4-1: A typical distortion of FBG spectra

It is clear that the cause of the distortion of FBG spectra depends, not only on the consequences of accumulated damage, but also on loading types and the fibre orientation. Embedding FBGs in between non-parallel fibre layers and the application of torsional loading to the component have caused substantial distortions to FBG spectra. In order to identify damage using the response of the FBG sensor, the other effects imbedded in the response needs to be identified and eliminated. The introducing referencing technique for the FBG spectrum using fixed wavelength FBG filters, provides the capability of identifying the variations to the FBG spectrum and distinguish the other effects causing distortions. Consequently, elimination of distortions caused by other effects will permit identification of distortions of FBG spectra caused by the damage. The proposed system is used to capture the distortions of reflected spectra of an embedded FBG sensor inside a composite laminate, thus enabling a quantitative estimate of the damage size in the vicinity of the sensor.

The aforementioned effects on the FBG spectrum along with the accumulation of damage make the response of the FBG highly non-linear. The nonlinearity of the response varies from structure to structure hence the estimation of transfer functions is extremely difficult. In this scenario, statistical methods provide promising results for data processing. Among the methods available, the ANN has provided proven results for non-linear systems with high accuracy. Application of ANNs is an efficient method for modelling non-linear characteristics of physical parameters and creates a system which is sensitive to wide range of noise.

The decoding of spectral data to feed in to ANN was addressed using a fixed filter FBG decoding system. The main objectives in this work are to decode the spectral data to determine the average strain at the embedded location. Furthermore, identification of damage also will be discussed. This method eliminates lengthy post-processing of data, and bulky equipment for data acquisition (as shown in Figure 4-2).

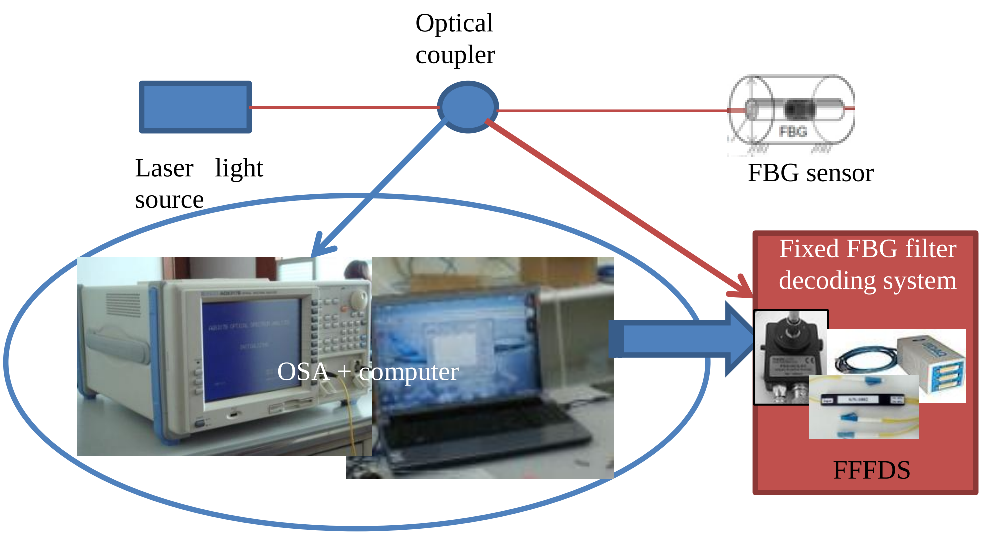

Figure 4-2: Replacement of OSA with Fixed filter decoding system (FFFDS)

Hereafter, the Fixed FBG Filter Decoding System is referred to FFFDS.

4.2 ANN based damage detection

With the complex damage modes of composite materials and complex spectral responses of FBG sensors under complex operational loading, the damage detection in composite materials using FBG sensors becomes extremely difficult. Incorporation of multiple sensor readings is also a challenging task. Further, extraction of important date and the elimination of valueless data imbedded in the response spectra of an FBG, is a challenging task. Even through it is possible to avoid these complications in the laboratory environment, in real applications these are not avoidable. To overcome these difficulties the introduced novel fixed FBG filter decoding system (FFFDS) with an artificial neural network (ANN) is being used.

The FFFDS uses the desirable characteristics of ANN to work and train with complications, to identify the real working environment. As a result of considering the working environment as the base (reference), the system's sensitivity to changes such as damage, was remarkably improved. The following section introduces the field of Artificial Neural Networks and the characteristics.

4.2.1 Introduction to Neural Networks

Artificial Neural Networks (ANN) are commonly referred as “Neural Networks” (Haykin, 1998). This concept emerged while scientists were looking for a solution to replicate human brain. In some cases like identification and prediction, the human brain tracks the problem more efficiently than other controllers. That is because the human brain computes in an entirely different way from the conventional digital computer.

The human brain is a highly complex, non-linear and parallel computer (information processing system) (Kartalopoulos, 1995). It has the capacity to organize its structure constituents, known as neurons, so as to perform certain computation many times faster than the fastest digital computer available today.

For an example, in human vision, the human routinely accomplishes perceptual recognition tasks such as recognizing a familiar face embedded in an familiar scene in approximately 100-200ms, whereas tasks of much lesser complexity may take hours on a conventional computer (Freeman & Skapura, 2007). Hence, we can say that the brain processes information super-quickly and super-accurately. It can also be trained to recognize patterns and to identify incomplete patterns. Moreover, the trained network works efficiently even if certain neurons (inputs) failed. The attraction of ANN, as an information processing system is due to the desirable characteristics presented in the next section.

4.2.1.1 Characteristics of ANN

From the mathematical perspective, the neural network is a dynamic system that can be modelled as a set of coupled differential equations (Kartalopoulos, 1995). The neural networks are characterized by:

1. Collective and synergistic computation:
   - Program is executed collectively and synergistically
   - Operations are decentralized
2. Robustness:
   - Operation is insensitive to scattered failures
   - Operation is insensitive to partial inputs or inaccurate inputs
3. Learning:
   - Network makes associations automatically
   - Program is created by the network during learning
   - Network adapts with or without a teacher
4. Asynchronous operation

All aforementioned characteristics are common to the human brain as ANN is an engineered human brain.

4.2.1.2 Engineering of Brains

Discovering how the human brain works has taken an ongoing effort that began more than 2000 years ago with Aristotle and Heraclitus, and has continued with the work of Ramony Cajal, Colgi Hebb, and others (Kartalopoulos, 1995). The Better we understand the brain, the better we can replicate it.

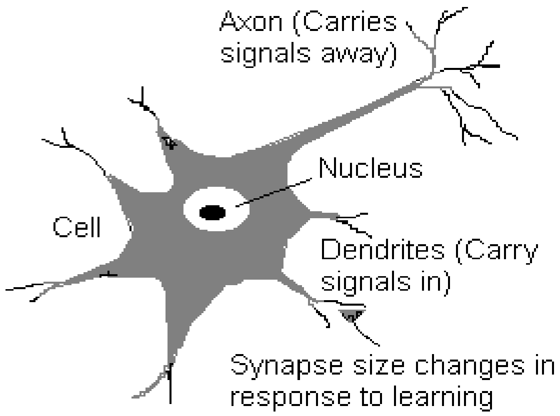

Figure 4-3: The biological neuron (Kartalopoulos, 1995)

4.2.1.3 Neuron Physiology

The neuron is the fundamental unit of and the nervous system (Figure 4-3), particularly the brain (Eccles, 1977; Nicholls, Martin, & Wallance, 1992). It works as an amazingly complex biochemical and electric signal processing unit.

The word neuron came from Greek and means the nerve cell. The neuron is the fundamental unit of nervous system. Considering its microscopic size, it is an amazing processor. Neurons receive and combine signals from many other neurons through filamentary input paths called dendrites (Figure 4-4).

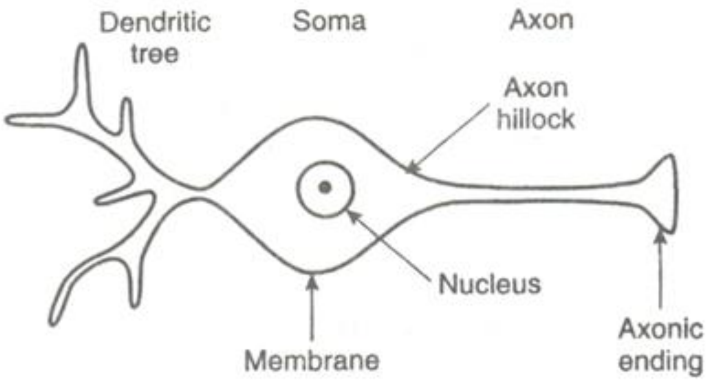

Figure 4-4: Parts of the neuron (Kartalopoulos, 1995)

Dendrites are bunched into highly complex “dendritic trees”. Dendritic trees are connected with the main body of the nerve cell, the soma. The soma has a pyramidal or cylindrical shape. The outer body of the cell is the membrane. The interior of the cell is filled with intercellular fluid and the outside of the cell is filled with extracellular fluid. The membrane and substances inside and outside the neuron play an important role in its operation. When excited above a certain level, the threshold, neuron fire. It transmits an electrical signal, action potential, along a signal path called an axon. The axon meets the soma at the axon hillock and it ends in a tree of filamentary paths called the axonic endings that are connected with dendrites of other neurons.

The connection, or junction, between a neuron’s axon and another neuron’s dendrite is called a synapse. In Greek, synapse means the contact. A synapse consists of the presynaptic terminal, the cleft or the synaptic junction, and the postsynaptic terminal (as shown in Figure 4-5).

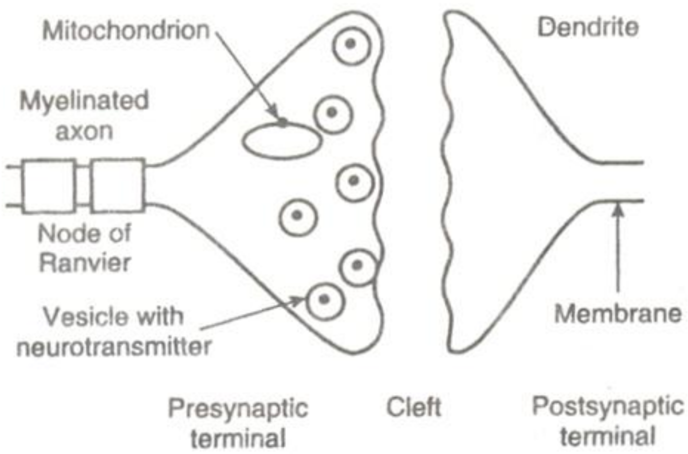

Figure 4-5: The synapse (Kartalopoulos, 1995)

A single neuron may have 1000 to 10000 synapses and may be connected with some 1000 neurons (Kartalopoulos, 1995). Not all the synapses are excited at the same time and according to the received sensory pattern via the synapses probably excites a relatively small percentage of sites, and an almost endless number of patters can be presented without saturating the neuron's capacity (D.L.Alkon & Rasmussen, 1988).

When the action potential reaches the axon ending, chemical massage known as neurotransmitter is released. The neurotransmitters are stored in tiny spherical structures called vesicles. Neurotransmitters are responsible for effective communication between neurons. The neurotransmitter drifts across the synaptic junction and initiates the depolarization of postsynaptic membrane and, thus, voltage moves across the membrane of the receiving neuron causing postsynaptic potential changes. Depending on the type of neurotransmitter, the postsynaptic potential is excitatory (more positive) or inhibitory (more negative).

Decoding at the synapse is accomplished by temporal summation and spatial summation (D.L.Alkon & Rasmussen, 1988). The total potential charge from temporal summation and spatial summation is encoded as a nerve impulse transmitted to another cell. All integrated signals are combined at the soma and, if the amplitude of the combined signal reaches the threshold of the neuron, it produces an output signal.

4.2.2 Artificial Neural Networks (ANN)

Artificial neural networks emanate from the biological principle described above, and mathematics have attempted to accurately describe the biological behaviour of neurons and their network. The neural networks consist of two sections, architecture and neurodynamics. Architecture defines the network structure, which is the number of neurons in the network and neuron interconnectivity. The neurodynamics of neural networks defines their properties, which are how the neural network learns, recalls, associates, and continuously compares new information with existing knowledge, and how it classifies new information, and how it develops new classifications as necessary.

The information processing of a neural network are not with a sequential algorithm as in most of the information processors. The information processing of neural networks is based on parallel decomposition of complex information into basic elements (Kartalopoulos, 1995).

4.2.2.1 Basic Model of a Neuron

The problem now is how to model this neural network artificially. Over the last 100 years, serious attempts to create a neuron model have made remarkable progress (Akers, 1989). The artificial neuron is the fundamental unit (or the building block) of the artificial neural network, and the model is shown in Figure 4-6. Even through the term artificial neuron is used, it does not even closely describe the biological neuron.

The model artificial neuron has a set of n inputs x_j, where the subscript j takes value from 1 to n. Each input x_j is weighted before reaching the main body of the processing element by the weight factor w_j. In addition, it has bios term w_0, a threshold value Ө that has to be reached or exceeded for neuron to produce a signal, a linearity factor F that acts on the produced signal R, and an output O after the nonlinear function. O constitute input signal to other neurons.

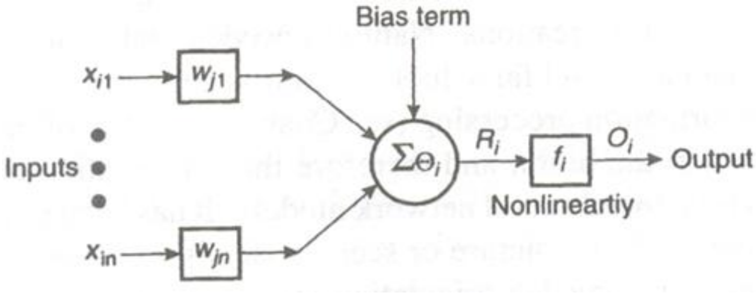

Figure 4-6: Basic Neuron Model (Kartalopoulos, 1995)

When a neuron is part of a network, an additional subscript, i, is needed to distinguish the neuron. Hence input, weight, activation signals, output, threshold and nonlinear function are written as x_{ij}, w_{ij}, R_i, O_i, F_i respectively.

The transfer function of the basic neuron model is described below

$$O_i = F_i\left(\sum_{j=1}^{n} w_{ij} x_{ij}\right) \quad \text{4-1}$$

The neurons firing condition is

$$\sum_{j=1}^{n} w_{ij} x_{ij} \geq \Theta_i \quad \text{4-2}$$

The purpose of non-linearity function is to ensure that the neuron's response is bounded. That is, the actual response of neuron is conditioned, as a result of small or large activating stimuli that is controllable. Commonly used nonlinearities are the hard limiter, sigmoid and ramp function.

4.2.2.2 Learning in ANN

Learning is the process by which the neural network adapts itself to a stimulus. After making the proper parameter adjustments, it produces the desired response. Learning is a continuous process, and if stimulus appears at the network, the network either recognizes it or it develops a new classification. In the learning process, the network adjusts its parameters. The synaptic weights, in response to an input stimulus, so that its actual output response converges to desired output response. When the output response is the same as the desired response, the network has completed the learning process.

For different structures of neural networks, the learning process is not the same. Just as different learning methodologies suit different peoples different learning techniques suit different artificial neural networks. Some of the common learning techniques are supervised learning, unsupervised learning, reinforced learning and competitive learning.

4.2.2.3 Neural Network Topologies

As an artificial neural network consists of many neurons, the interconnectivity between neurons casts them in to different topologies. Some of the most popular topologies are shown in Figure 4-7. Normally a network contains an input layer, output layer and one or more hidden layers between the input and output layers. Hidden layers are so named because their outputs are not directly observable.

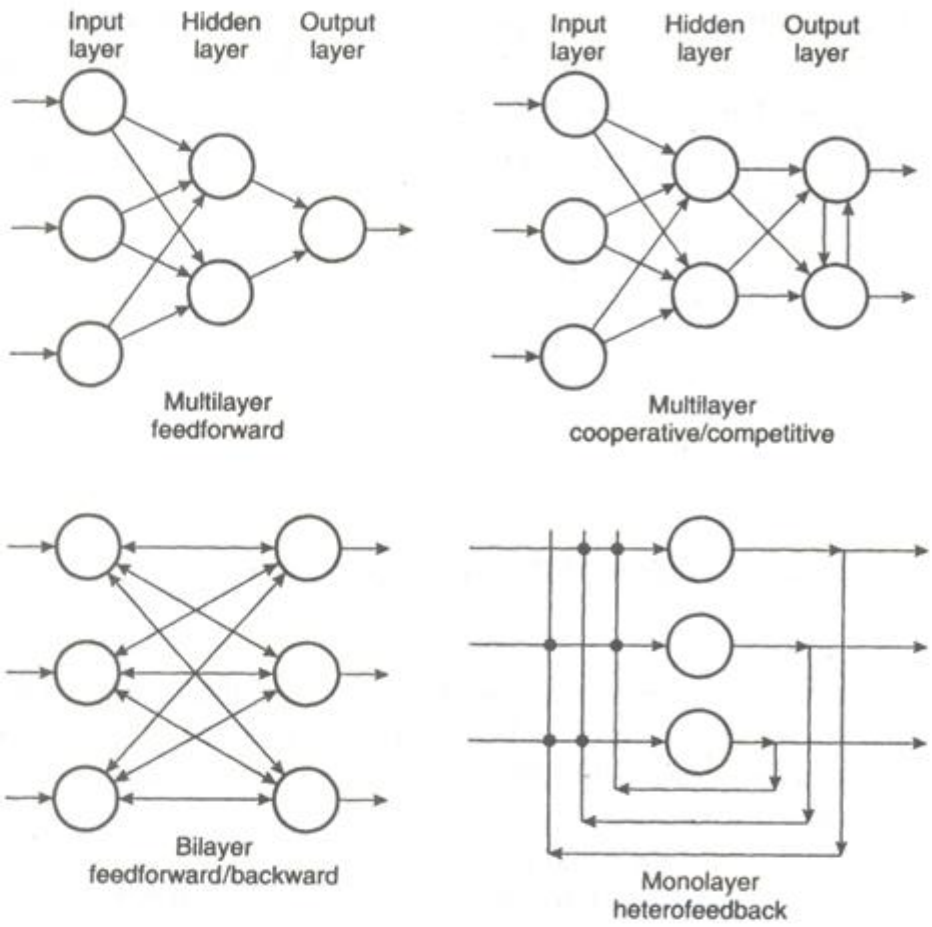

Figure 4-7: Common neural network topologies

4.2.2.4 Multilayer ANN

The fundamental model of an artificial neural network is a network with one layer of neurons (output layer only, without hidden layers) (Bishop, 1995). The simplest network consists of just one neuron with the function g chosen to be the identity function, $g(v) = v$ for all v.

Multilayer neural networks are undoubtedly the most popular networks used in advance applications. While it is possible to consider many activation functions, in practice it has been found that the logistic (also called the sigmoid) function $g(v) = ev /(1+ev)$ as the activation function (or minor variants such as the tanh function) works best. In fact the revival of interest in neural networks has been sparked by successes in training neural networks using this function in place of the historically (biologically inspired) step function, the “perceptron”.

Using a linear function does not achieve anything (in a multilayer network) that is beyond what can be done with single layer networks with linear activation functions. The practical value of the logistic function arises from the fact that it is almost linear in the range where g is between 0.1 and 0.9 but has a squashing effect on very small or very large values of *v*.

In theory, it is sufficient to consider networks with two layers of neurons, one hidden and one output layer. This is, certainly the case for most applications. There are, however, a number of situations where three and sometimes four and five layers have been more effective. For prediction the output node is often given a linear activation function to provide forecasts that are not limited to the zero to one range. An alternative is to scale the output to the linear part (0.1 to 0.9) of the logistic function.

Unfortunately there is no clear theory to guide us in choosing the number of nodes in each hidden layer or indeed the number of layers. The common practice is to use trial and error, though there are schemes for combining optimization methods such as genetic algorithms with network training for these parameters. Since trial and error is a necessary part of neural net applications, it is important to have an understanding of the standard method used to train a multilayered network: back propagation.

It is no exaggeration to say that the speed of the back propagation algorithm made neural networks a practical tool in the manner that the simplex method made linear optimization a practical tool. The revival of strong interest in neural networks in the mid 80's was, in large measure, due to the efficiency of the back propagation algorithm.

4.2.2.5 The Backward Propagation Algorithm

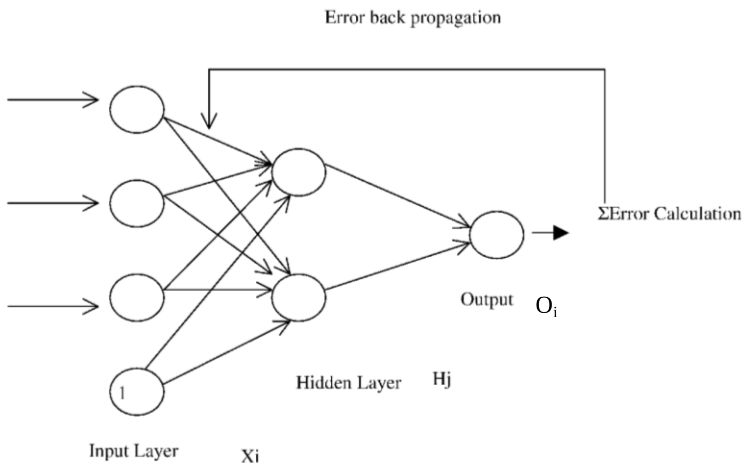

Figure 4-8: Back propagation algorithm

There is a minor adjustment for prediction problems where predicting continuous numerical value is attempted. In that situation, the activation function changes for output layer neurons, for the identification of function that has *output value=input value*. An alternative is to rescale the logistic function to permit the outputs to be approximately linear in the range of dependent variable values. The back propagation (BP) algorithm cycles through two distinct passes, a forward pass followed by a backward pass through the layers of the network. The algorithm alternates between these passes several times as it scans the training data. Typically, the training data has to be scanned several times before the networks "learns" to make good classifications.

> *Thought out the work presented in this thesis, all the Artificial Neural Networks use back propagation as the learning algorithm.*

A theoretical explanation of the BP used in this study is given below. Consider a multi-layer perceptron (MLP) with N_i inputs and N_o outputs. Given an input vector x $\in R^{NI}$ and an output vector y $\in R^{No}$, the output of a given neuron $k(y_k^p)$ with N input connections when a pattern p is presented to the network is given as a function of its activation (a_k^p) given by equation

$$y_k^p \quad = F_k(a_k^p) = F_k\left(\sum_{j=1}^{N} w_{jk} y_j^p + \theta_k\right) \qquad 4\text{-}3$$

Where F_k is the activation function of the neuron k, w_{jk} represents the weight associated with the connection between neuron j and neuron k, y_j^p is the output of neuron j and θ_k is the bias. Note, that in the case of the input layer, y_j^p is equal to x_j^p. The gradient descent rule (BP) minimizes the quadratic error function, given in equation 4.4

$$E^p \quad = \frac{1}{2}\sum_{o=1}^{No}\left(d_o^p - y_o^p\right)^2 \qquad 4\text{-}4$$

where d_o^p is the desired output when the pattern p is presented to the network and y_o^p is the neuron output. Following the minimization process, the network weights are adjusted by

$$\Delta_p w_{jk} = \gamma \delta_k^p y_j^p + \alpha \Delta_q w_{jk} \qquad 4\text{-}5$$

where γ is the learning rate, δ_k^p the local gradient of neuron k, $\Delta_q w_{jk}$ is the change made to the weight w_{jk} when the last pattern q was presented to the network and α is the momentum term.

4.3 Use of ANN in SHM of composite structures

ANN based systems have been used in different SHM stages by several researches, as illustrated graphically in Figure 4-9. Hosni et al. (Hosni Elhewy, Mesbahi, & Pu, 2006) used ANN for the reliability analysis of structures. They used an ANN (1 hidden layer and 10 PEs) to predict the structural response of a structure to random variables. Mechanical properties of the material, thickness of the plates, angle of orientation and in-plane loads were used as the inputs to the network. 120 data sets were used to train the network. Then the output of the ANN was used to estimate the reliability using first order and second momentum (FORM), or the Monte Carlo simulation method (MCS). They used an ANN to replace a FEA and save computational time, and to estimate limit state function for the structure.

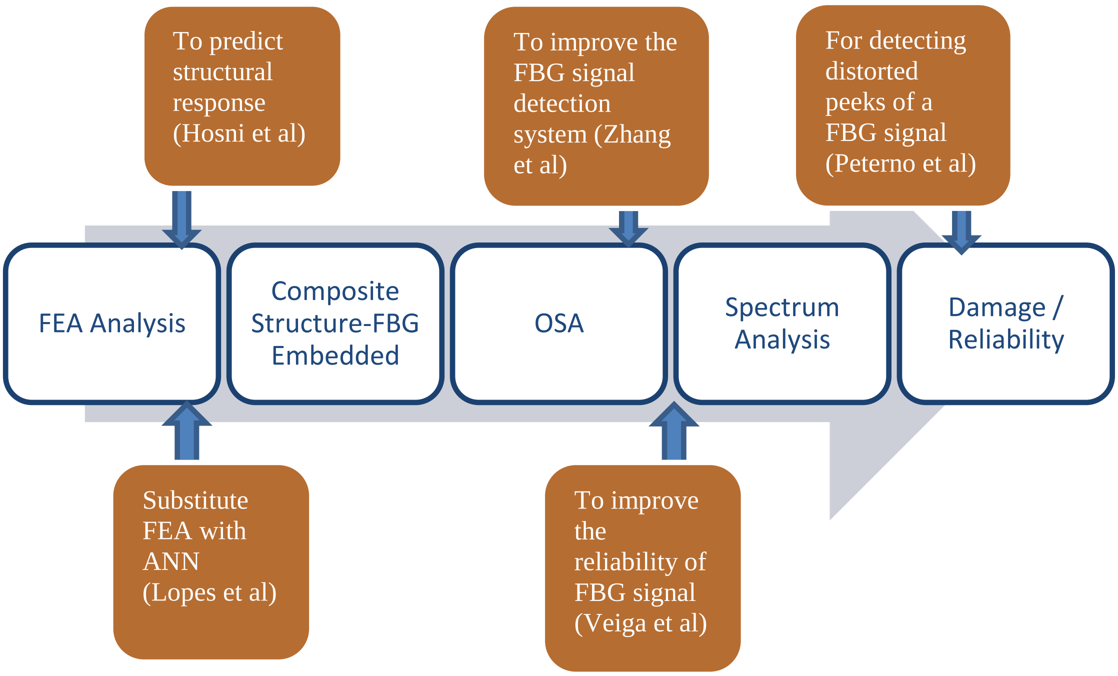

Figure 4-9: Use of ANN in SHM applications

Lopes et al. in 2010 used the ANN to save computer processing time on reliability analysis of laminate composite structures (P. A. M. Lopes, Gomes, & Awruch, 2010). The research work targeted the optimisation of structural performance and substituted the FEA with two types of ANN models (MPL and RBN), and used Monte Carlo simulation, FORM and FORM with multiple check points to compare the solution. It was reported that the ANN is saving a considerable amount of processing time.

Garg et al. used a spectral finite element (SFEA) and neural network to estimate the damage model parameters of a composite structure (Garg, Roy Mahapatra, Suresh, Gopalakrishnan, & Omkar, 2004). They used acoustic wave excitation (AE) signals and an ANN for spectral signal processing of the AE signals. Fourier spectral data was the input to the ANN and, for training, SFEM data was used. Output was the span-wise location of the damage, length of the damage zone and stiffness degradation factor. The results reported were up to a good standard for both damage location and size.

Lewis et al. in 2007 tried an ANN to interpret a complex optical spectrum and time resolved signals from optical fibre sensors (not FBG). A three layer feed forward network with one hidden layer was used.

ANN is famous for the classification of spectral data. Zhang et al., used an ANN to improve the FBG signal detection system (Zhang, Zhao, & Rong, 2008). They used an ANN to eliminate errors in the conversion of optical signal to electrical signal. Veiga et al. used an ANN to improve the reliability of the FBG signal under power variations of light source (Veiga, Encinas, & Zimmermann, 2008).

Paterno et al. used ANN for FBG peak detection (Paterno, Silva, Milczewski, Arruda, & Kalinowski, 2006). They used Gaussian, Polynomial or Lorentzian fit to avoid ambiguity in the detection of the peak. This fitting is further improved using a green function and input to the ANN using radial basis function. The improved accuracy was reported.

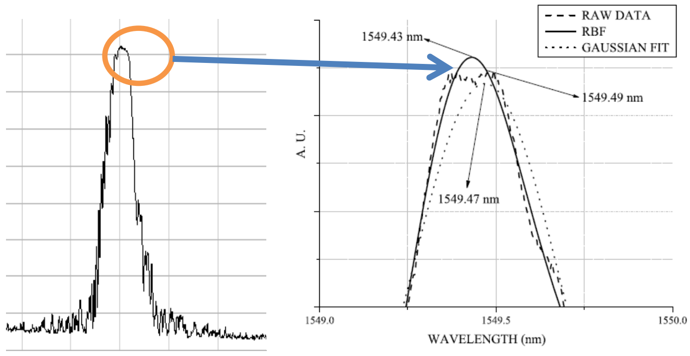

Figure 4-10: Peak detection of distorted response of an FBG using ANN (Paterno et al., 2006)

The versatility of ANN for the processing of non-linear parameters was proven by researchers all over the world and in many fields. The ANN holds a strong reputation for human brain type identification and prediction. In this case, when it comes to identification of damage in composite structures, and prediction of strain using highly distorted FBG response spectra, the use of an ANN is highly advantageous.

The main difficulty of using an ANN for processing of FBG spectral data is the difficulty of decoding data to feed into the ANN. During the decoding, the vital data imbedded in the spectrum must be preserved. The FBG spectrum carries the information about the strain gradient of its physical embedded location, and this vital data must be fed into the ANN. The damage initiation in the composite changes the strain gradient and hence is considered to be important information for damage detection. For the aforementioned task, FFFDS has been introduced. The decoding system consists of a tuneable laser, fixed FBG filters, optical couplers and photo detectors. This system eliminates the use of sophisticated and expensive equipment such as optical spectrum analysers and data acquisition systems.

4.4 Novel method to decode FBG spectral data as ANN input: Fixed filter FBG decoding system (FFFDS)

During the past decade, many systems for decoding FBG spectra using fixed FBG filters have been developed (Lewis et al., 2007; P. A. M. Lopes, Gomes, & Awruch; Luiz C. S. Nunes, Olivieri, Kato, Valente, & Braga, 2007; Veiga et al., 2008; Zimmermann, Veiga, & Encinas, 2008). Figure 4-11 illustrates a general arrangement of a fixed FBG filter system. The system consists of a tuneable laser (TLS), fixed FBG filter, optical couplers (CP) and photo detector (PD). A high frequency data acquisition system (DAQ) has been used to acquire the PD voltage values.

Figure 4-11 illustrates the simplest form of this system, using only one (1) FBG filter, which is the building block of the complete decoding system. Tuneable laser light, A, is transmitted to the FBG sensor and the reflected light, B, of the FBG sensor is fed to the FBG filter through an optical coupler. The intersection of the wavelengths reflected from the sensor and the wavelengths' reflected light, C, by the filter (λ_I), or conversely, the wavelengths which are not transmitted through the filter, are reflected to the photo-detector. L_1 and L_2 are the light transmitted through the FBG sensor and filter respectively.

While the sensor receives the total wavelength range from the tuneable laser source, the filter only receives the wavelengths reflected by the sensor. Hence, the filter can only reflect light (to the photo-detector) if the wavelength from the sensor is within the filter's grating range (λ_I). The reflected light of the filter is captured using the photo-detector, converted to a voltage, and recorded in the DAQ system. A system can be implemented with multiple FBG filters with λ_n wavelengths as required for a specific application.

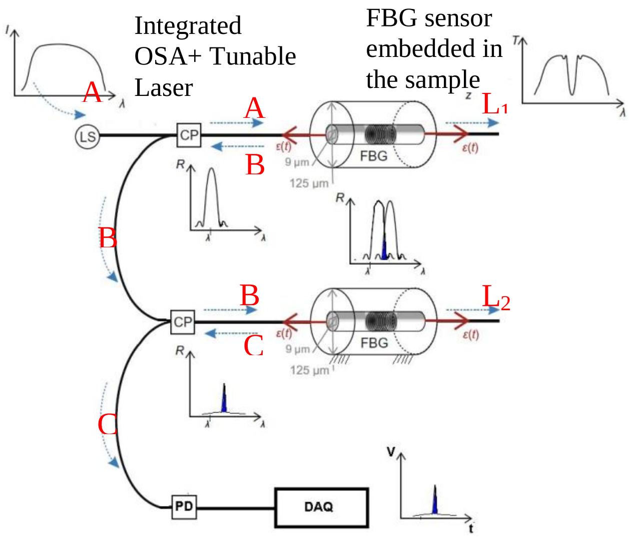

Figure 4-11: FBG spectrum decoding system

Figure 4-12 shows the reflected spectra of the FBG sensor and the filter. The filter can only reflect light if the received wavelength from the sensor reflection is within the filter's grating range. Thus, the filter reflects the intersection as shown in Figure 4-12.

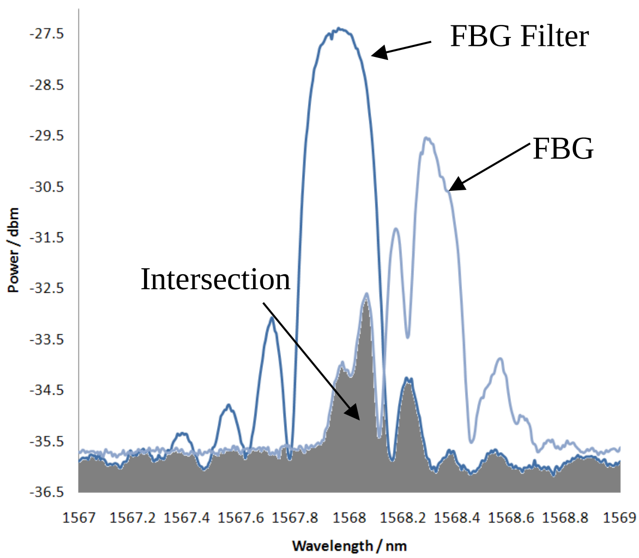

Figure 4-12: Intersection of the FBG spectra

The reflected light of the FBG filter was captured using the PD and the voltage was recorded using the DAQ. Figure 4-13 shows the PD voltage in the time domain corresponding to the intersection of the spectra shown in Figure 4-12. Tuneable laser sweeping frequency allows transformation of voltage reading to time domain. Since the filter spectrum is fixed, the intersection of the two spectra only depends on the sensor spectrum position. Variation of the intersection can be used to identify the location of the peak, the strain at sensor, and the damage status of the structure. Any distortion to the spectrum is visible from the PD voltage-time plot (Figure 4-13). By matching the tuneable laser swept frequency with the DAQ sampling frequency, it is possible to transform voltages to respective wavelength values accurately. More filter readings will increase the accuracy, the operating range and robustness of the system.

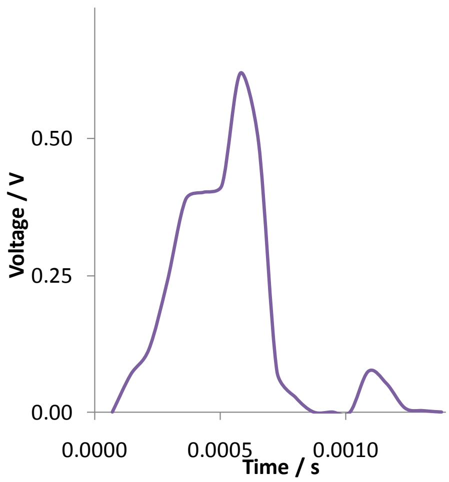

Figure 4-13: PD reading due to the intersection of the FBG spectra

There were several attempts to fit the FBG spectra using mathematical functions such as the commonly used Gaussian curve fit (L. C. S. Nunes, Valente, & Braga, 2004). Sensor reflectivity can be expressed as

$$S(\lambda, \lambda_s) = y_o + S_o \exp[-\alpha_s(\lambda - \lambda_s)^2] \qquad \text{4-6}$$

Where y_o is the added offset to represent the dark noise, as α is a parameter related to full width at half maximum (FWHM) and λ is the wave length. Unfortunately Gaussian fit always gives an error for a distorted spectrum as shown in Figure 4-14(a). Realistically, a distorted spectrum must be considered as a piece wise continuous function, f_{pc} in order to capture the distortion (Figure 4-12). Consequently, optical power, P, of the distorted signal can be obtained using the following integral.

$$P = \beta \int_{t_a}^{t_b} f_{pc} \, dt \qquad 4\text{-}7$$

where β is a constant dependent on the power of the source, and, t_a and t_b are the integral limits in the time domain Figure 4-14(b)). The power integral at each point can be used to estimate the strain in the sensor by using an ANN. The sensitivity of the integrated data depends on the integral limits - larger integration limits reduce the sensitivity and very small limits cause data to scatter. Both cases make the algorithms inefficient. Optimum limit values have to be set to achieve better results.

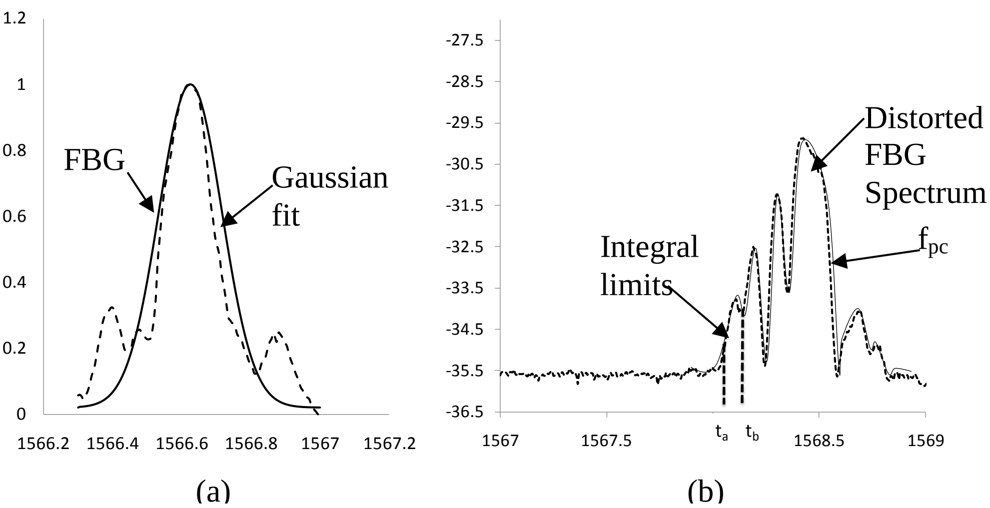

Figure 4-14: Gaussian fit and the piecewise continuous function

4.5 Application of Fixed wavelength filters and ANN for FBG data processing and damage identification

The fixed wavelength filters and data capturing system is used to decode spectral data from an FBG sensor to a form which can be fed into an ANN in order to estimate strain and/or damage in a composite structure.

Figure 4-16 illustrates a data flow diagram of the structural strain and damage assessment process. First, reflected spectral data from the FBG sensor mounted on the structure is entered into an FBG filter. The reflected spectral data from the FBG filter (representing the spectral intersection of the reflected FBG sensor data and the inherent filter characteristics) is entered into a photo-detector. The voltage time domain output of the photo detector is entered into a data acquisition unit. The data is then processed and entered into a neural network. Finally, the neural network output is the state of strain and/or damage (Figure 4-15).

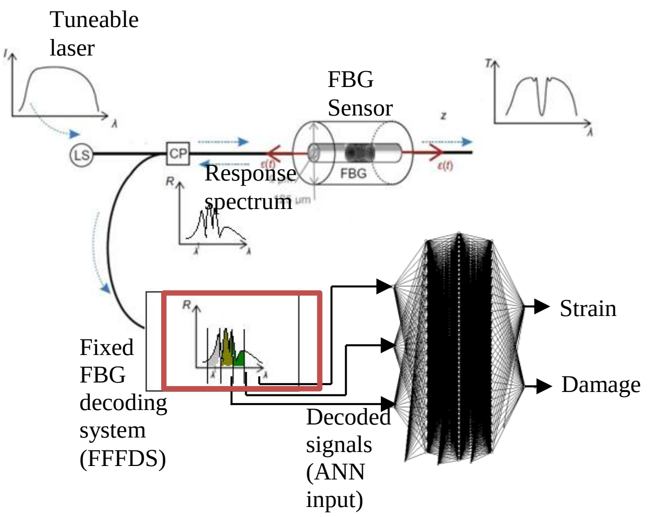

Figure 4-15: Decoding FBG spectrum using Fixed FBG's and use of ANN

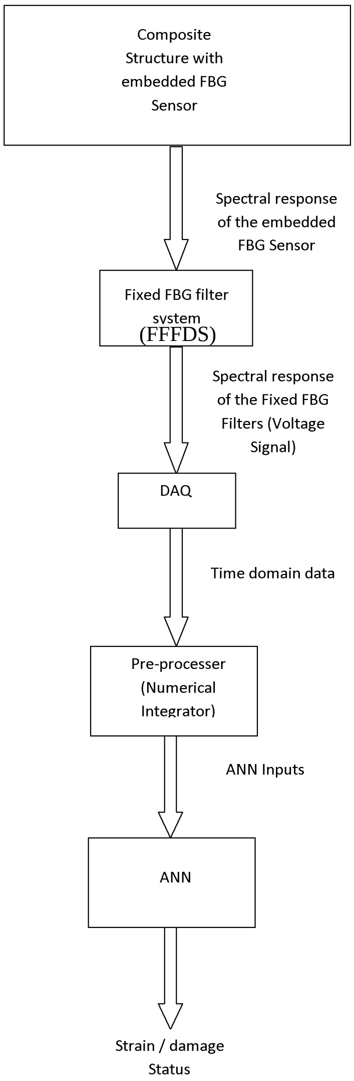

Figure 4-16: Flow chart of the process for the fixed FBG filter system

Figure 4-17 depicts a general arrangement of the proposed system. The system consists of a tuneable laser (TLS), three (3) fixed FBG filters (Filters 1-3), optical couplers (CP) and three (3) photo-detectors (PD). A high frequency data acquisition system (DAQ) was used to record (100 Hz) the photo-detector output voltages which are subsequently fed into the processor to determine the state of strain and damage.

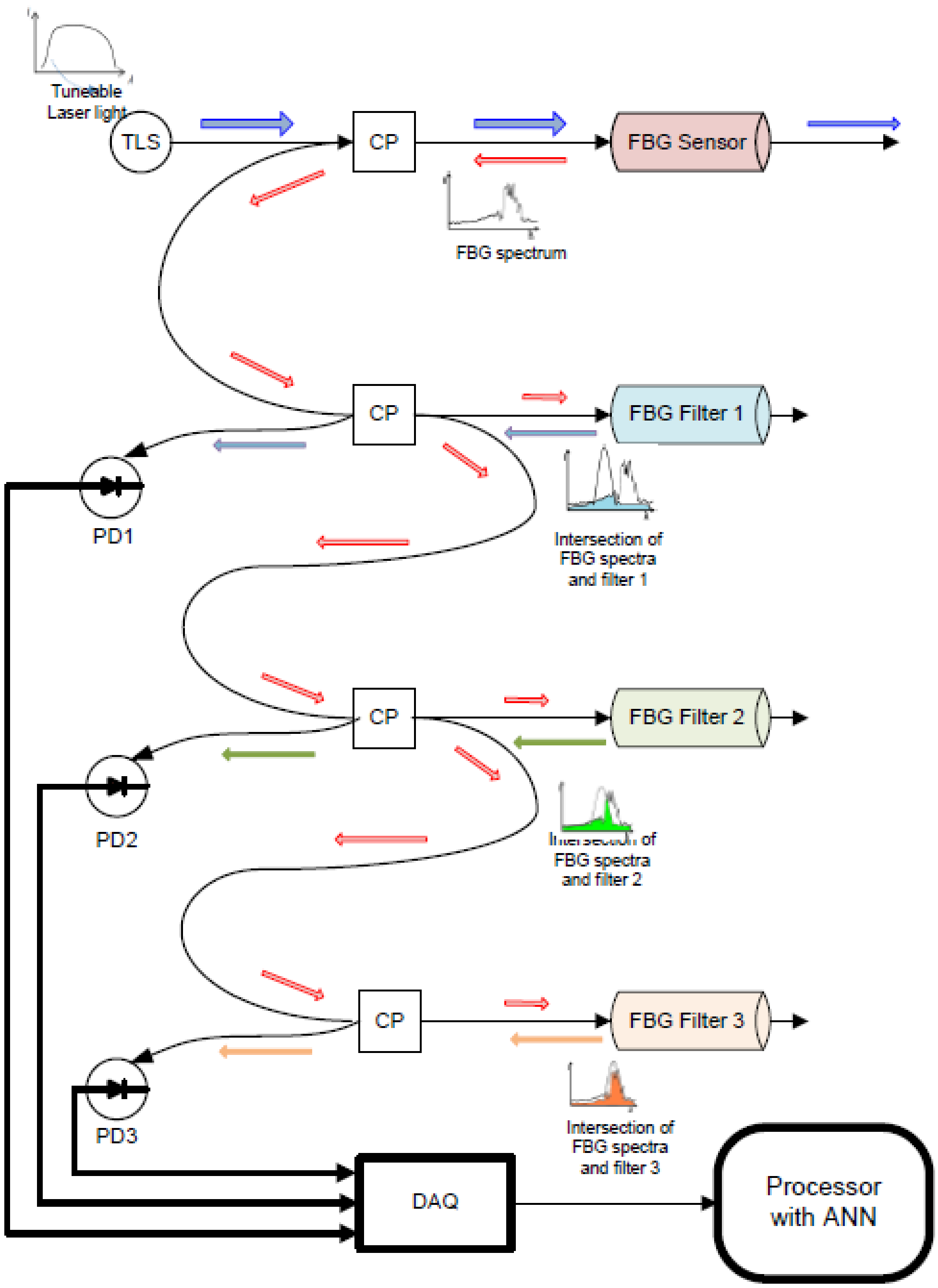

Figure 4-17: Fixed FBG Filter Decoding System (FFFDS)

Three (3) filters are used to increase the accuracy, operating range and robustness of the system, and the composite signal created by the photo-detectors represents a unique signature of the sensor spectrum. Furthermore, the output of the photo-detectors contains information relative to the sensor spectra in a form which can be used with an artificial neural network (ANN). The number of filters and FBG sensors is not limited to the example shown in this figure. Any one filter in the system is capable of covering an approximate range of 500 micro-strain/1 nm movement of the peak of the sensor spectrum. More filters can be used with the same system to cover a wider operating range of the embedded FBG sensors and to obtain more precise data.

4.6 Post-processing of FFFDS data using ANN

As discussed in earlier sections, under complex load conditions, the spectrum of the FBG distorts. Figure 4-18 shows the FBG sensor response of an FBG embedded in a composite structure during operation under several load cases. The complicated response makes it extremely difficult to model using mathematical transfer functions in order to estimate strain as well as damage. In such cases, an ANN provides promising functional approximations to the system.

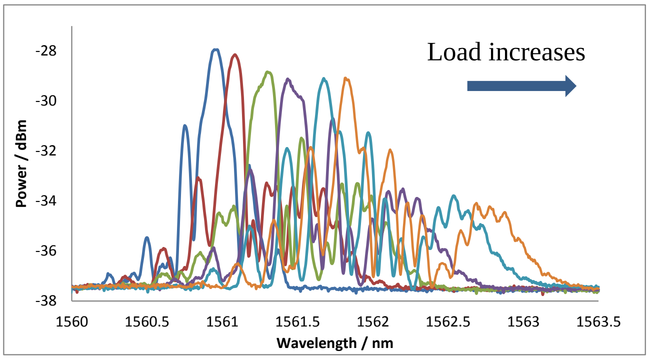

Figure 4-18: Distorted FBG response

One of the commonly used neural network architectures for function approximation is the Multi-Layer Perceptron (MLP). Back-Propagation (BP) algorithms are used in a wide range of applications to design a MLP successfully (N. Lopes & Ribeiro, 2001).

4.6.1 The ANN model

Figure 4-19 shows a general arrangement of the ANN used in this study. The ANN consists of three input neurons, which accommodate three FBG fixed filters, three hidden layers and an output layer.

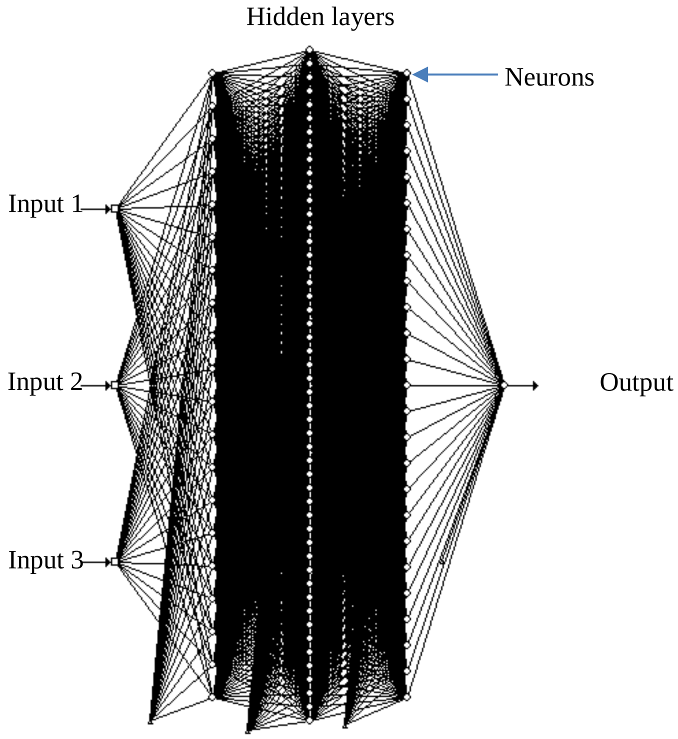

Figure 4-19: ANN developed to estimate strain

The neurons of the hidden layers are with Gaussian activation functions, and the K value used is 1, as shown in Figure 4-20(a). It takes a parameter that determines the centre (mean) value of the function used as a desired value. The neuron of the output layer is with sigmoid activation function with k=1, as shown in Figure 4-20(b). this function is especially advantageous for use in neural networks trained by back-propagation algorithms because it is easy to distinguish, and can minimize the computational capacity of training (Karlik & Olgac, 2010). Initial weights (at the start of the training process) of the neurons were randomly places between -1 and 1.

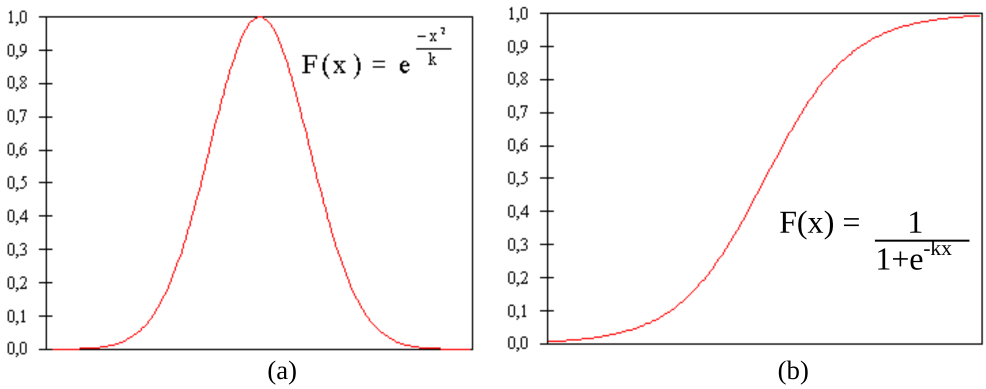

Figure 4-20: Activation functions of the neurons of ANN (a) Hidden layer neurons (b) Output neuron

Three different composite specimens, with embedded FBG sensors, were investigated using the developed system in order to evaluate the system performance for estimation of strain and/or damage.

4.7 Experimental study of the FFFDS with ANN

For the following case studies, an ANN with three (3) inputs was developed. The network consists of three hidden layers having 20, 50 and 25 neurons respectively. A back propagation algorithm was used as the training technique. Three pre-processed fixed filter readings were given to the ANN through three input neurons, and the strain at the sensor and damage was predicted through the output neuron/s.

The ANN is trained for the initial conditions of the specimens and the expected loading regime. The movement and distortions to the spectrum induced during this regime were set as the reference normal condition. The reference is used to identify unexpected changes to the FBG spectrum due to damage.

4.7.1 Case 1: Prediction of strain

In this case study, an FBG spectra of an FBG embedded in a composite specimen, which was highly distorted under loading was considered. With the distortion to the spectra, it was extremely difficult to detection the peak of the spectra.

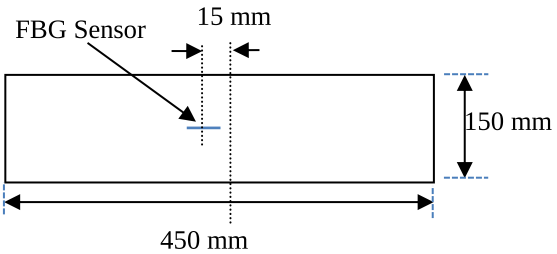

(a)

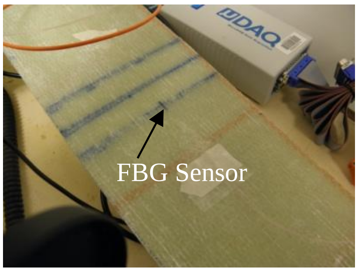

(b)

Figure 4-21: Sample with embedded FBG sensor

A rectangular 450 mm x 150 mm sample was fabricated with 10 layers of E-glass fibre in the orientation of [0/90/±45/90/0]s. Kenetix R246TX epoxy resin was used as the matrix material. A FBG sensor with a wavelength centred 1541 nm was embedded between non-parallel fibre layers, 3 and 4, at the location shown in Figure 4-21(a). A specimen was cured at 30 ^{0}C Figure 4-21(b) shows the specimen with embedded FBG sensor.

The filter circuit consisted of three filters to cover a wide range of wavelength (1537.5 nm - 1539 nm). A tuneable laser light with a swept frequency of 5nm per second (5 Hz) was connected to the embedded FBG sensor, through an optical coupler, C1. The reflected waveform of the FBG sensor was fed into three FBG fixed filters, F1, F2 and F3 through couplers C2, C3 and C4 respectively. Three PDs were used to read the reflections of the three filters (Figure 4-22). The PD's analogue voltage outputs were recorded using a DAQ at sampling frequency of 10 kHz. (Specifications of the tuneable laser light, optical couplers, photo diodes and the DAQ are given in Appendix C)

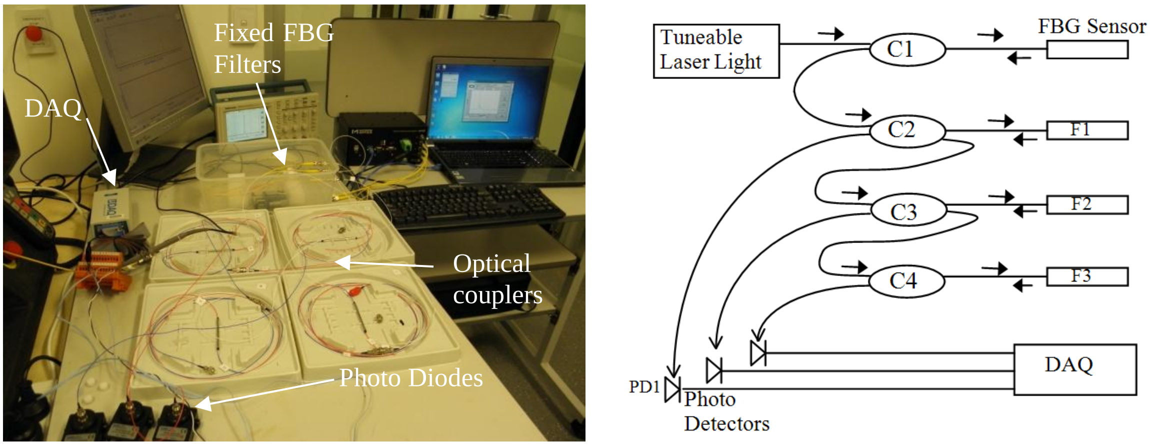

(a) (b)

Figure 4-22: (a) Optical circuit and the specimen (b) Layout of couplers and PD arrangement

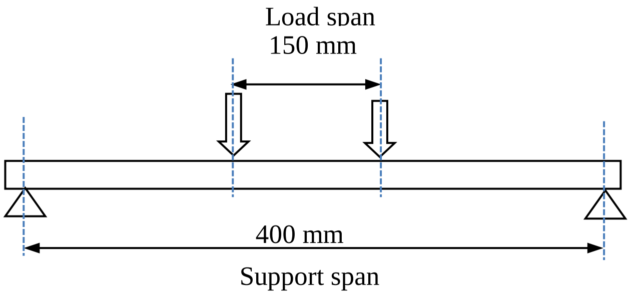

Figure 4-23: Experimental setup

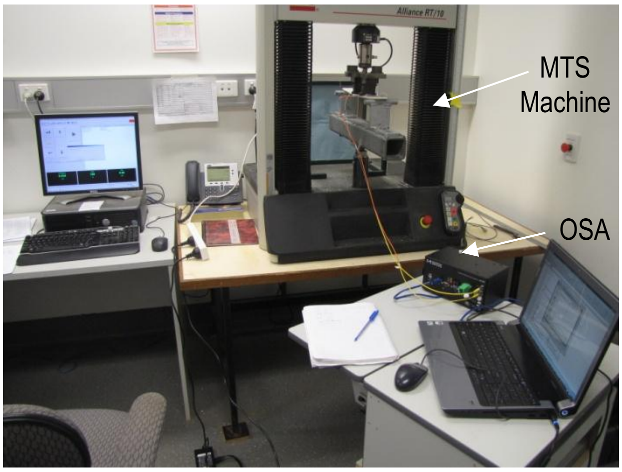

Figure 4-24: Loading the panel using MTS machine

The specimen was loaded in a four points bending test rig in steps of 25N up to 1000N (Figure 4-23) maximum load using a MTS 100kN uniaxial loading machine as shown in Figure 4-24. The readings from the DAQ were recorded at each of the loading steps.

A detailed finite element model (FEM) was developed for the specimen using the commercial software ABAQUS. The model consists of continuum shell elements as discussed in detail in Chapter 2. The model was loaded similar to the four point bending experiment. A part of the results, of the FEA was used to train the ANN and selected data points were kept for experimental validation of the system. Figure 4-25 shows the strain contours of layer 4 under flexural loading.

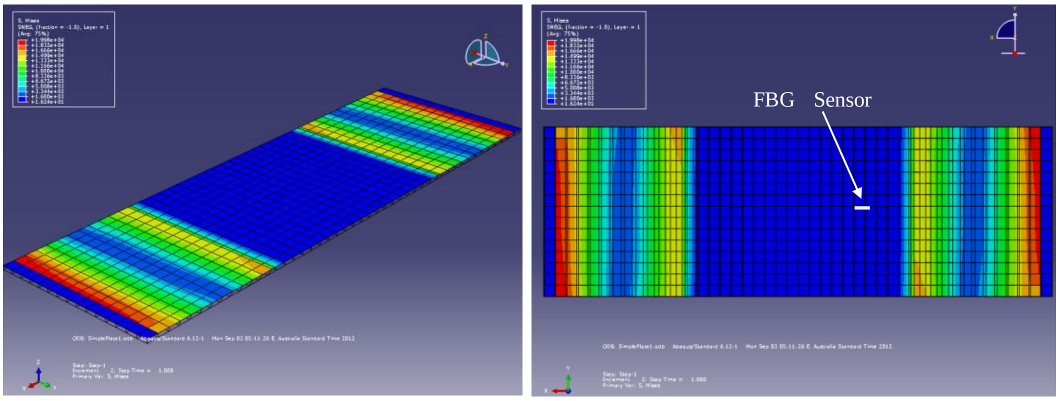

Figure 4-25: FEM of the specimen

The recorded PD readings were pre-processed using an algorithm written on MATLAB (Appendix D) and converted to time domain voltage data. Weighted, pre-processed data was subsequently fed into the ANN through the three input neurons.

The ANN was trained using the data set until the RMS error of the network output was reduced to 0.3%. The network took 35,000 epochs to reach the expected RMS error level of 0.3%. Final network weights are given in Appendix E.

4.7.1.1 Experimental Results

The FBG spectra distort significantly with the applied load. Figure 4-26 shows the distortions observed in the spectrum in three loading levels 50N, 500N and 1kN. With the increased load, the spectrum become complicated and locating the peak in order to estimate the strain it is an extremely complex task.

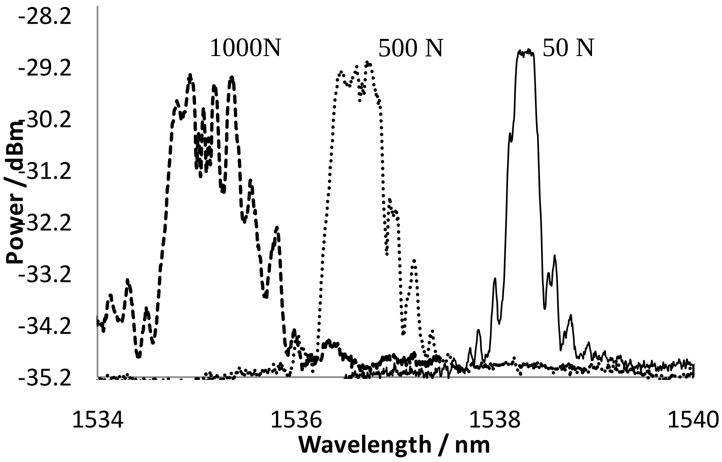

Figure 4-26: Distortion of the FBG spectrum with the loading

Figure 4-27 shows a plot of data recorded with the DAQ at an applied load of 725N. The response of all three PDs at this load level can be seen.

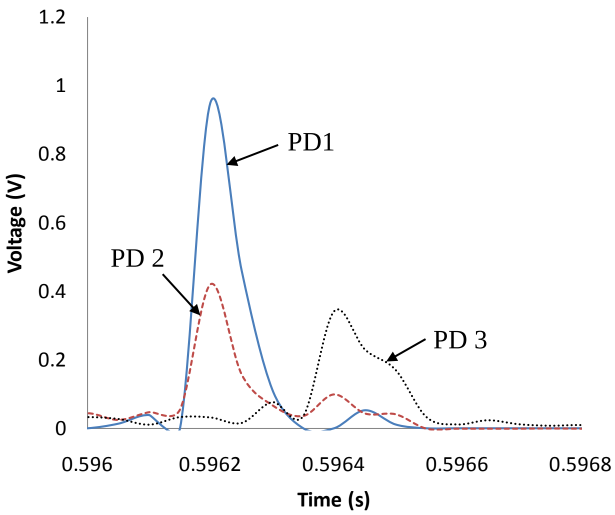

Figure 4-27: PD readings at 725 N load

Figure 4-28 shows the strain calculated using the highest peak value of the distorted spectrum. Non-linearity of the readings is caused by the distortions. It is clear that, with the observed distorted peaks, the calculated strain is not accurate. At higher loads, the distorted spectrum has multiple peaks, and highest peak fluctuates rapidly making peak tracking inaccurate.

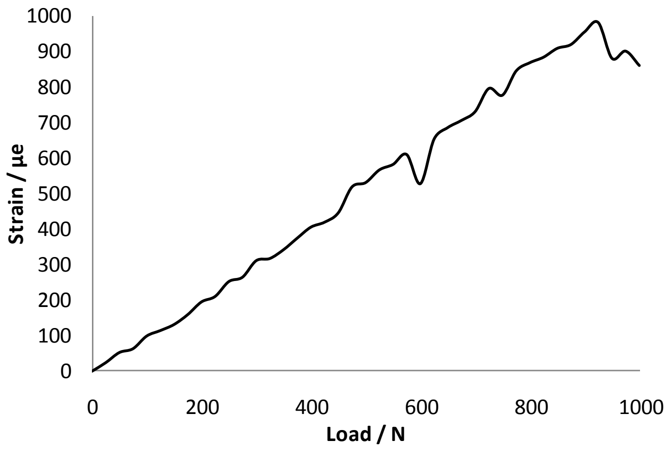

Figure 4-28: Variation of strain due to the distortions to the FBG spectrum

4.7.1.2 Analysis

The recorded PD readings were pre-processed using an algorithm (written on MATLAB) to read the time domain spectrum. Weighted and pre-processed data was subsequently fed into the ANN through the three input neurons (Figure 4-19). Figure 4-29 shows the PD reading observed while a 1000 N load was applied to the specimen.

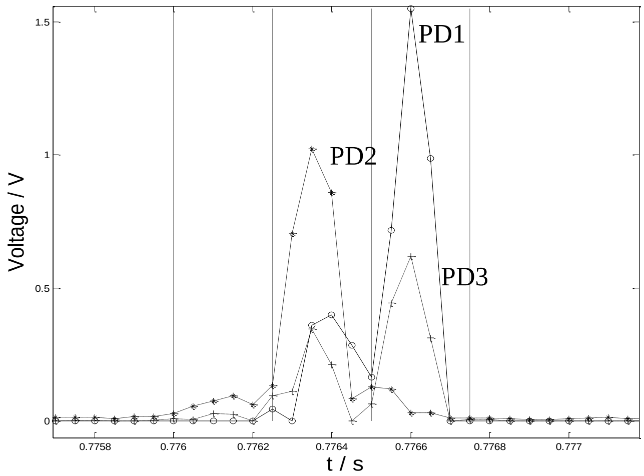

Figure 4-29: Extracted data from the FBG spectrum

The ANN was trained using the data set until the RMS error of the network output was reduced to 0.3%. The network took 35,000 epochs to reach the expected RMS error level. Figure 4-30 shows the training rate of the network.

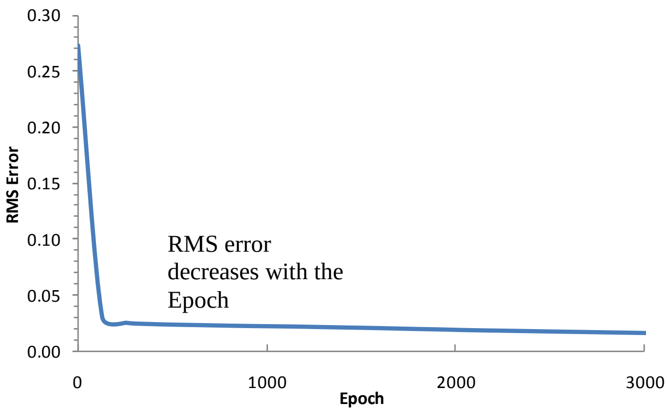

Figure 4-30: RMS error with the training process

4.7.1.3 Results and Discussion

The integrated PD data used to train the ANN are illustrated in Figure 4-31. The non-linearity of the data is caused by the spectra distortions shown in Figure 4-26. The flat region of the data set (0-600 N) in Figure 4-31 is due to the movement of the sensor spectra before reaching the filter spectrums. The sensor starts away from the filters, as shown in the Figure 4-32, and until the spectrum of the sensor reaches the location of the filter spectra, there is no considerable change in the PD readings.

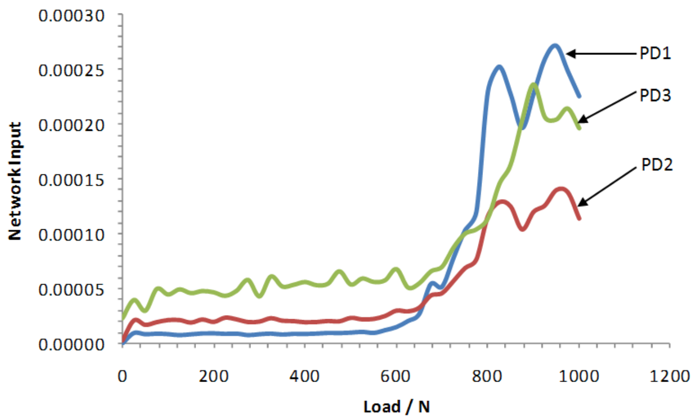

Figure 4-31: Variation of the integrated PD readings with applied load

The embedded FBG sensor peak's location with no loading is 1541 nm, 3 nm away from the first filter's spectrum (1538 nm). With loading, the sensor peak starts to move towards the bandwidth of the filters (1539 nm – 1537.5 nm). The accurate operating range of the filter system is shown in Figure 4-32. By selecting filters as appropriate, it is possible to set the system to work in any of the regions of the operating range of the sensor. By increasing the number of filters, it is possible to increase the operating bandwidth of the system. By optimising the filter bandwidth, it is possible to eliminate the non-intersected regions and improve the learning rates of the ANN.

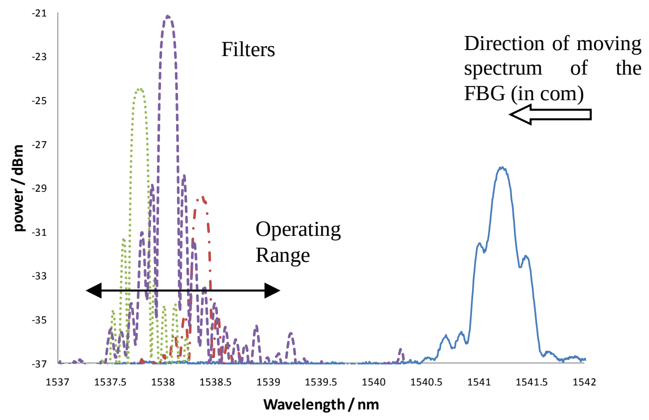

Figure 4-32: Operating range of the sensor

Figure 4-33 shows the network output and the desired output. The desired output is the FEA's estimated strain at the sensor location between layers 3-4. The ANN output closely matches with the desired output values. An initial mismatch was found due to values recorded out of the filter's operating range. Hence, the percentage error for the strain from the ANN at 250 N is higher as shown in the Table 4-1 (7.4628%).

As shown in Figure 4-26, the response spectra of the FBG sensor has been significantly distorted under higher loads, but the ANN has predicted the strain with high accuracy illustrating its ability to accommodate the distorted signal (Table 4-1).

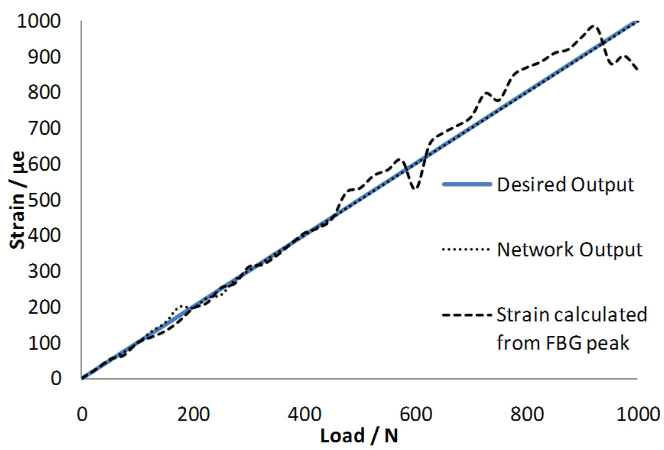

Figure 4-33: The network output and the desired output

As depicted in Figure 4-33, the overall prediction of the ANN has shown an excellent agreement with calculated strains. The maximum peak values show considerable variation with the desired strains, thus disqualifying its use it as a reliable measure.

Table 4-1 shows the error which was calculated relative to the desired value as:

$$Percentage\ Error = \frac{(\text{Desired Value} - \text{Strain from FBG peak or ANN})}{\text{Desired Value}}\ \%$$

Table 4-1: Percentage error of strain calculated from the FBG peak location and ANN

	Percentage Error	
Load /N	Strain calculated from FBG peak	ANN
50	-5.3421	0.3463
250	-1.0045	7.4628
500	-6.2716	0.1315
750	-3.6897	0.0029
1000	16.1156	0.0636

4.7.1.4 Conclusions

A spectrum of an embedded FBG sensor, which was highly distorted as a function of increased load, has been decoded with fixed FBG filters (FFFDS) and an ANN, and the strain in the loaded specimen was determined. The ANN produced an error level less than 0.3% compared with strain values calculated using an FEM. The agreement of ANN predictions and the calculated strains confirms that the developed ANN system accommodates the inherent distortions of the spectra induced by other factors (Section 3.5) besides damage. Further, the system is capable of understanding any abnormal event such as a surge of strain due to damage inside the specimen under four point bending loading. Additionally, the trained system acts as a reference for the particular specimen's strain response under four point loading.

Further work to train the ANN to identify damage (both qualitatively and quantitatively) when exposed to combined loadings, is the next logical step and will be discussed in the next section.

4.7.2 Case 2: Prediction of hole diameter

In this case a drill hole was used as the defect in a composite laminate plate. Defect growth was simulated as the increase in the hole diameter. With hole diameter growth, the stress pattern closer to the FBG sensor changes as in any case of defect growth. Even though the real defect is not closer to a drill hole, it was simulated as a defect for the controllability of the defect in this experiment.

4.7.2.1 Sample Fabrication

FBG sensors with a wavelength centred about 1550 nm were fabricated on 9μm core and 125μm clad diameter telecommunication grade glass fibre. The grating length was 10mm. To ensure maximum bonding between the FBG sensor and matrix of resin in the GFRP material, the acrylate layer of the fibre was removed. An extra protective layer of rubber was applied to the fibre to enhance the sensor robustness.

The sample was fabricated with 10 layers of E-Glass fibre in the orientation [0/90/±45/90/0]s. Kenetix R246TX epoxy resin was used as the matrix material. The FBG sensor was embedded between non-parallel fibre layers, 3 and 4, as shown in Figure 4-34.

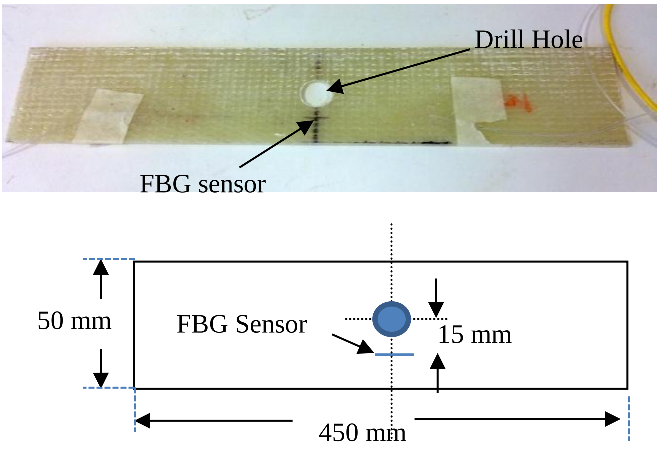

Figure 4-34: Sample with embedded FBG sensor

4.7.2.2 Experimental procedure

A tuneable laser light with a swept frequency of 5nm per second was injected into the FBG sensor through an optical coupler. The reflected waveform of the FBG sensor was fed into three FBG fixed filters. Three PDs were used to read the reflections of the three filters Figure 4-22(a)). The PD's analogue voltage outputs were recorded using a DAQ with sampling frequency of 10 kHz. The experimental setup is shown in Figure 4-22(b).

The specimen was loaded in three points in steps of 25N up to 100N maximum load using an MTS, as shown in Figure 4-35. To avoid loading directly above the defect or the FBG sensor, the load was applied to the specimen with 25 mm shift from the centre of the specimen as shown in the Figure 4-35.

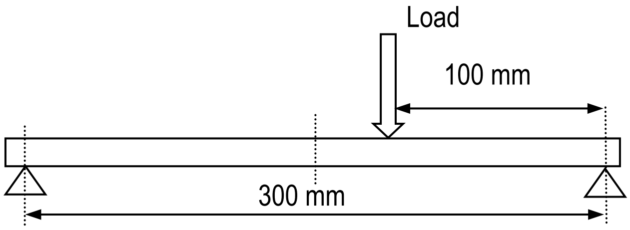

Figure 4-35: Experimental setup

Subsequently, the readings from the DAQ were recorded at each of the loading steps. Additionally, the FBG sensor spectra were recorded using an optical spectrum analyser for later verification purposes. The diameter of the hole was increased from 5 mm to 16 mm is several steps. The loading was repeated for the sample with defect sizes 0 mm, 5mm, 8mm, 10 mm, 12 mm and 16 mm.

4.7.2.3 Experimental Results

Figure 4-36 shows a plot of data recorded at an applied load of 20N in bending; Figure 4-36(a) for the initial sample which is with no hole and Figure 4-36(b) for the sample with 10 mm hole. The responses of all three PDs at this load level can be seen. The 10 mm hole has a significant effect on the readings.

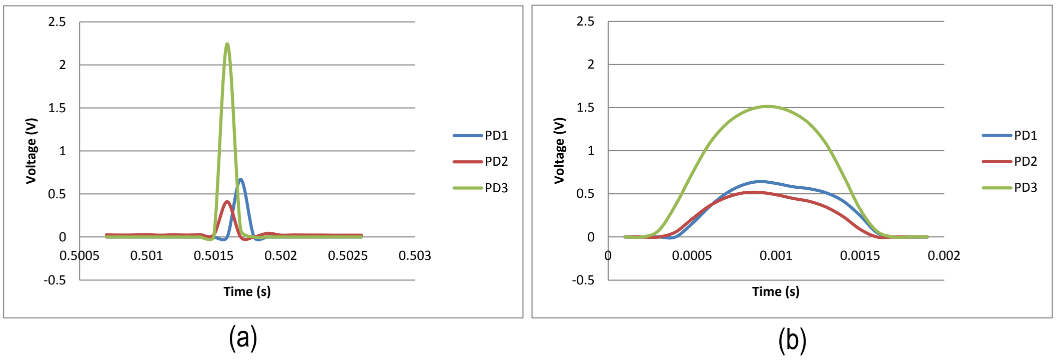

Figure 4-36: PD readings at 20N axial load for the damage size (a) No damage, (b) 10 mm hole

4.7.2.4 Analysis

The recorded PD readings were pre-processed using an algorithm (written on MATLAB) to read the time domain spectrum. Weighted, pre-processed data was subsequently fed into the ANN through the three input neurons of the ANN. Figure 4-37 shows the calculated inputs (I1, I2 and I3) to the ANN using PD data.

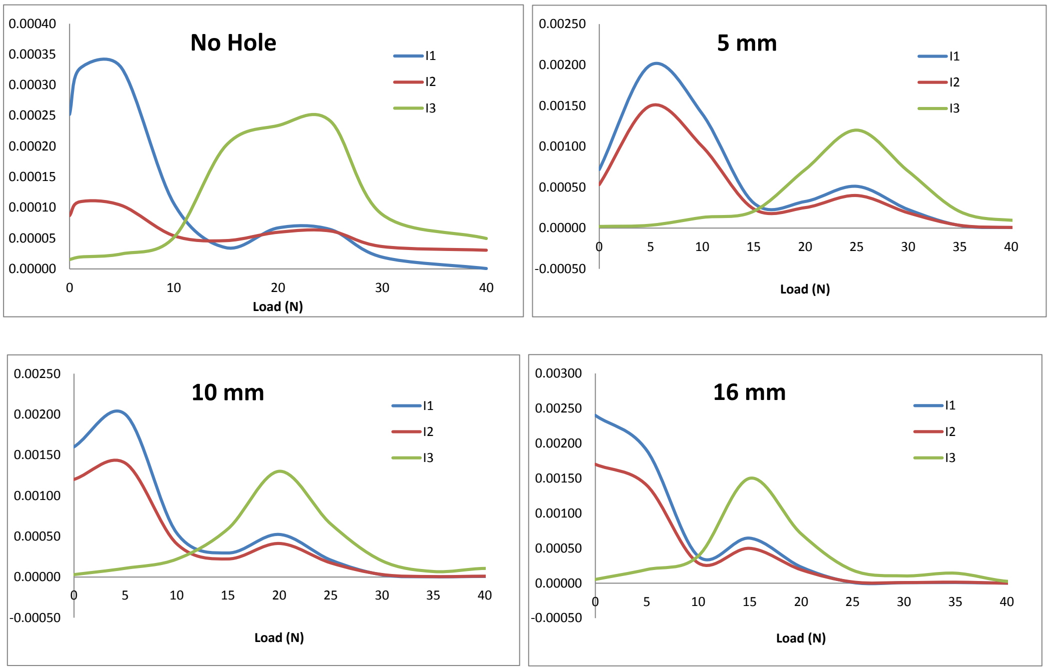

Figure 4-37: Extracted data from the FBG spectrum

The ANN was trained (using the data set) to estimate hole diameter until the RMS error of the network output was reduced to 0.3%. The network took 82,000 epochs to reach the expected RMS error level. Figure 4-38 shows the training rate of the network.

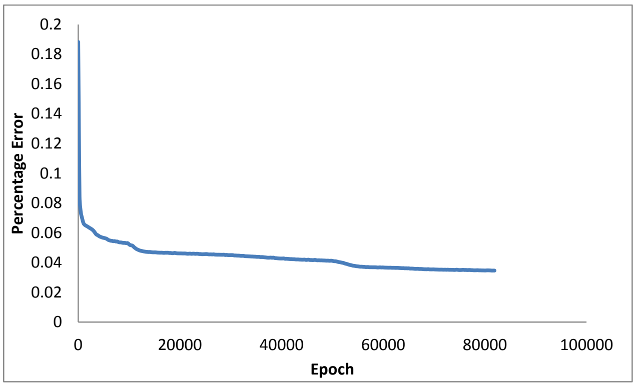

Figure 4-38: RMS error with the training process

4.7.2.5 Results and Discussion

The integrated PD data used to train the ANN are illustrated in Figure 4-36. Figure 4-39 shows the network output and the desired output. The desired output is the actual size of the drill hole. The ANN output closely matches with the desired output values. The response spectra of the FBG sensor has been significantly distorted under higher loads, but the ANN has predicted the hole diameter with high accuracy illustrating its ability to accommodate the distorted signal. As depicted in Figure 4-39, the overall prediction of the ANN has shown an excellent agreement with actual damage size.

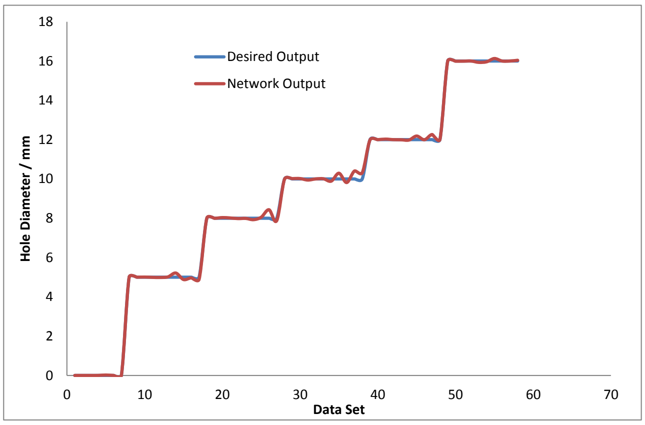

Figure 4-39: The network output and the desired output for hole diameter

4.7.2.6 Conclusions

A spectrum of an embedded FBG sensor, which is highly distorted as a function of increased load and damage size, has been decoded with an ANN and the diameter of the hole in the specimen was determined. The ANN produced an error level less than 0.3% compared with the actual diameter of the hole. The agreement of ANN predictions and the measured delamination confirms that the developed ANN system accommodates the inherent distortions of the spectra induced by other factors besides damage. Further, the system is capable of understanding any abnormal event such as a surge of strain due to damages inside the specimen under bending loading. Additionally, the trained system acts as a reference for the particular specimen's strain response under bi-axial loading.

4.7.3 Case 3: Prediction of Delamination Growth

Even though the growing hole was used as a controllable defect for simulation and verification of the FFFDS, a drill hole does not represent a real defect in an FRP composite structure. But for system verification it allows the FBG sensor to lie in a stress field as it is closer to a real defect. The next experiment was conducted to simulate a delamination, using a thing cut in between laminates. This is closer to a real defect. On the other hand, to represent multidirectional loading on composite component, in this case study, bi-directional loading was accommodated. To simulate real application, a sample with growing delamination under bi-axial loading was considered.

4.7.3.1 Sample Fabrication and Experimental procedure

The experimental setup is similar to the hole diameter experiment (Case 2) described in Section 4.7.2. The specimen was fabricated with a thin slot as a simulated delamination, as shown in the Figure 4-40. Test specimen was manufactured using a glass/epoxy composite with stack sequence of [0/0/90/90/-45/45/90/0]s. A rectangular slot was created during the fabrication of the specimen. Figure 4-41 shows the fabrication process of the specimen. A thin blade was used to create a rectangular cut which was used as the controllable defect for the experiment. The cut was located in between layers 6 and 7. The initial width of the cut was 10 mm. An FBG sensor was embedded above the cut in between layers 2 and 3, as shown in Figure 4-40.

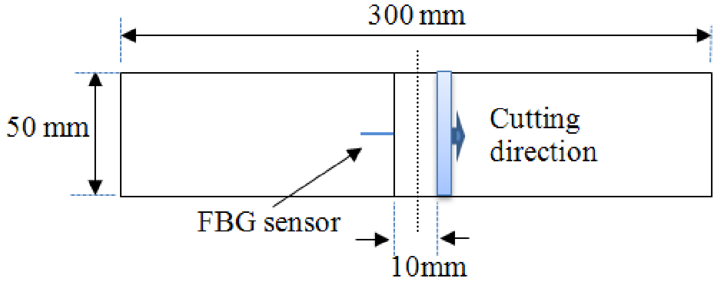

Figure 4-40: Location of the FBG sensor in the specimen between layers 3 and 4

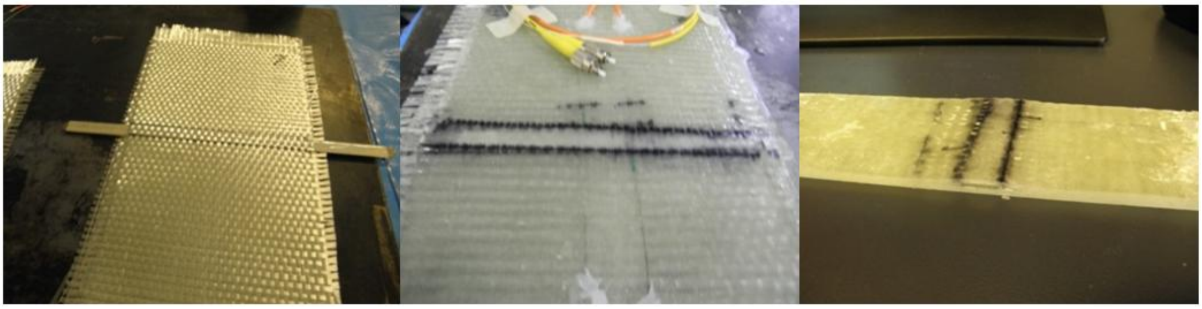

Figure 4-41: Fabrication of the specimen with damage

The specimen was loaded in biaxial loading as shown in Figure 4-42. An MTS machine was used to load the specimen in tension while a screw jack was used to apply a bending load. The spectral response of the sensor was recorded for loading in 100 N steps in tension up to 10 kN while the bending load was increased 10N steps up to 100N for each tensile loading step. The cut was increased in 1mm steps from 10 mm as shown in Figure 4-43, up to 20mm, and the experiment was repeated.

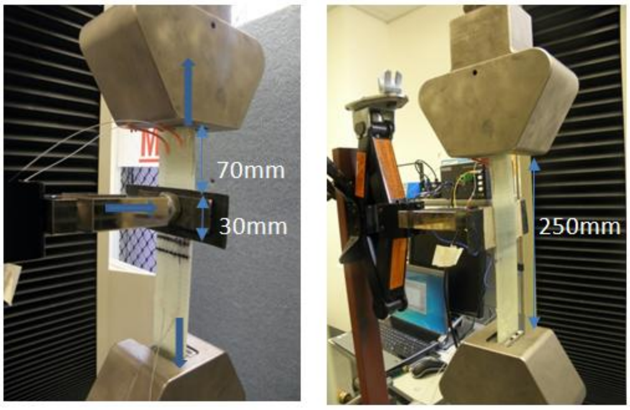

Figure 4-42: Experimental setup

Figure 4-43: Increasing the damage size by cutting

4.7.3.2 Experimental Results

The FBG spectra distort significantly with the applied load. Figure 4-44 shows the distortions observed in the spectrum in three load cases. With the increased load, the spectrum becomes complicated and locating the peak in order to estimate the strain is extremely difficult.

Figure 4-44(a) shows the distortions to the FBG sensor response under axial load only, and in Figure 4-44(b) the FBG sensor is loaded on bending only. The combined effect on the FBG sensor spectra, while the structure under tension and bending combined loading, is shown in the Figure 4-44(c). As expected, the increase of the delamination and the combined multi-axial loading has significantly distorted the response spectra of the embedded FBG sensor.

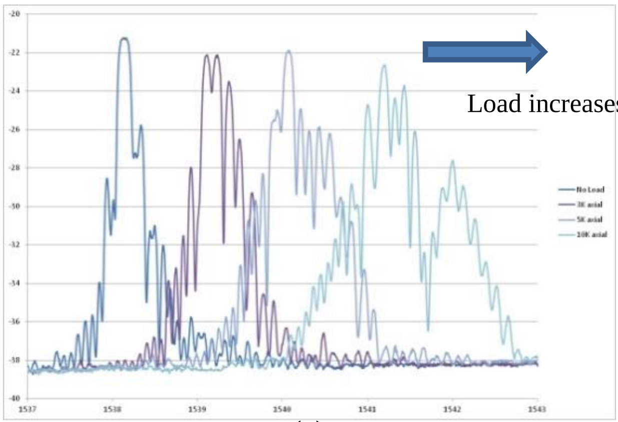

(a)

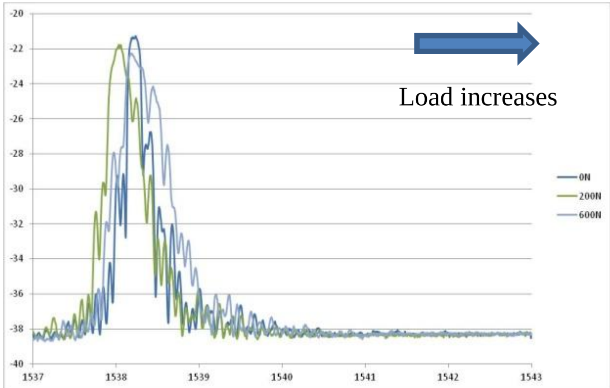

(b)

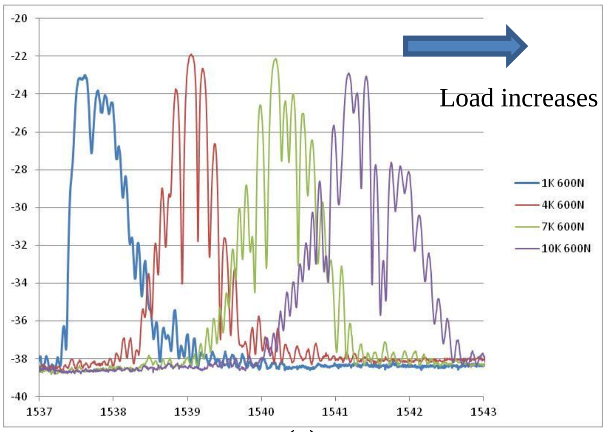

(c)

Figure 4-44: Distortion to the FBG spectrum with the multi-axial combined loading

Figure 4-45 shows a plot of data recorded at an applied load of 10kN axially and 1000N in bending. The response of all three PDs at this load level can be observed.

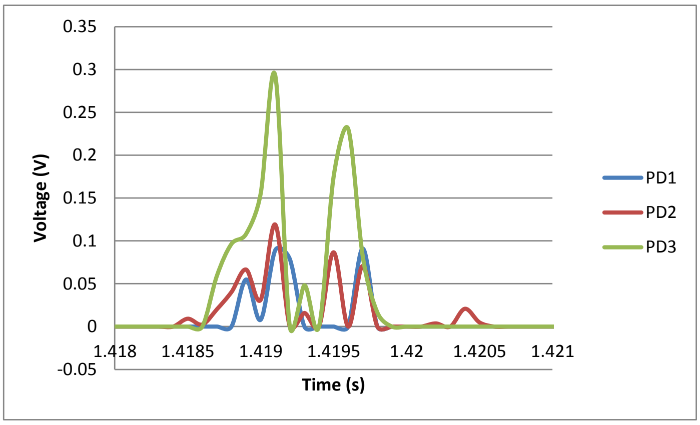

Figure 4-45: PD readings at 10 kN axial load and 1kN bending load

4.7.3.3 Analysis

The recorded PD readings were pre-processed using an algorithm (written on MATLAB) to read the time domain spectrum. Weighted, pre-processed data was subsequently fed into the ANN through the three input neurons of the ANN. Figure 4-46 shows the calculated inputs (I1, I2 and I3) to the ANN using PD data.

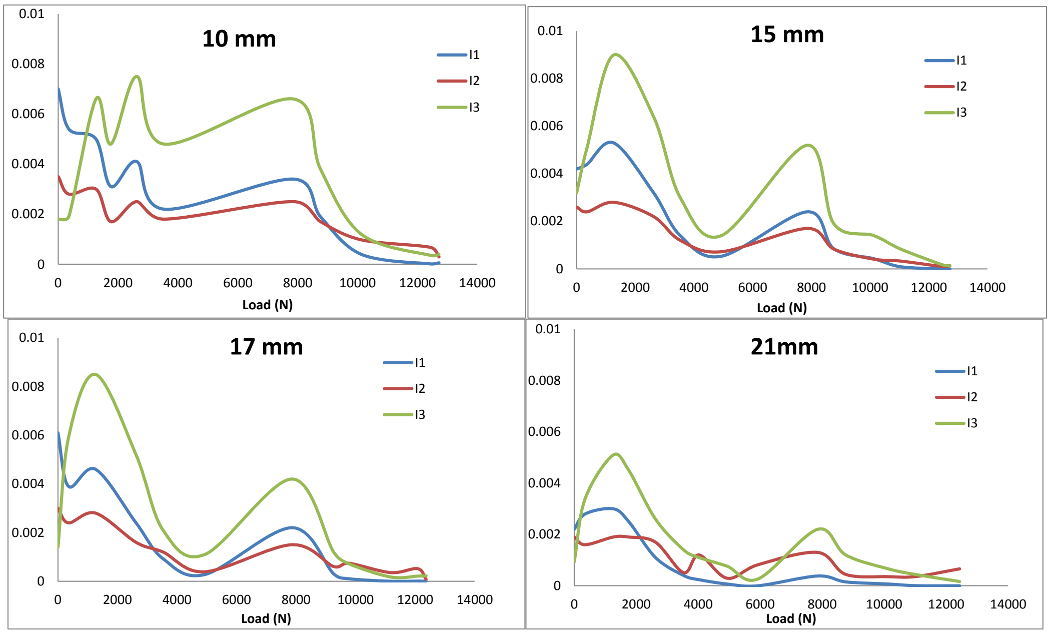

Figure 4-46: Extracted data from the FBG spectrum

The ANN was trained using the data set until the RMS error of the network output was reduced to 0.3%. The network took 35,000 epochs to reach the expected RMS error level. Figure 4-47 shows the training rate of the network.

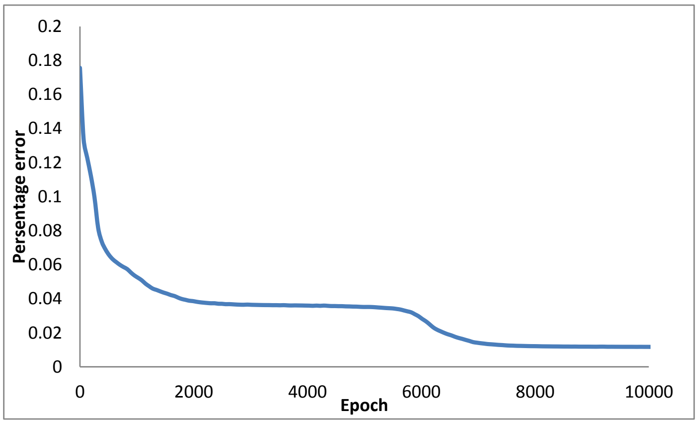

Figure 4-47: RMS error with the training process

4.7.3.4 Results and Discussion

The integrated PD data used to train the ANN are illustrated in Figure 4-46. The non-linearity of the data is caused by the spectra distortions shown in Figure 4-44.

Figure 4-48 shows the network output and the desired output. The desired output is the actual size of the delamination. The ANN output closely matches with the desired output values. As shown in Figure 4-44, the response spectra of the FBG sensor has been significantly distorted under higher loads, but the ANN has predicted the delamination with high accuracy illustrating its ability to accommodate the distorted signal. As depicted in Figure 4-48, the overall prediction of the ANN has shown an excellent agreement with actual delamination size.

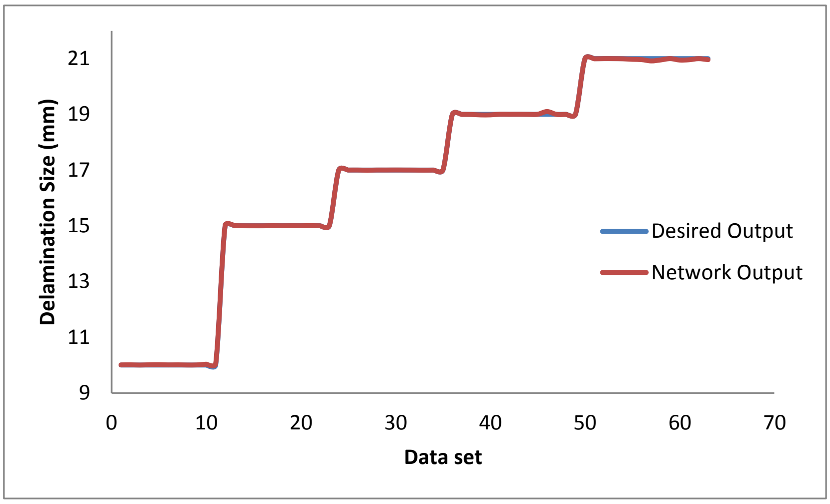

Figure 4-48: The network output and the desired output for delamination size

4.7.3.5 Conclusions

A spectrum of an embedded FBG sensor, which is highly distorted as a function of increased load and delamination size, has been decoded with an ANN and the delamination in the specimen was determined. The ANN produced an error level less than 0.1% compared with actual delamination size. The agreement of ANN predictions and the measured delamination confirms that the developed ANN system accommodates the inherent distortions of the spectra induced by other factors besides damage. Further, the system is capable of understanding any abnormal event such as a surge of strain due to damages inside the specimen under four point bending loading. Additionally, the trained system acts as a reference for the particular specimen's strain response under bi-axial loading.

4.7.4 Concluding remarks for the FFFDS

Two experiments were conducted with two simulated defects in vicinity of the embedded FBG sensor. The novel FFFDS was used to capture the distorted response spectra of the embedded FBG sensor while the FRP composite structure was under multi-axial loading. The recovered data was used to predict following parameters.

- Existence of defect
- Strain at FBG sensor location
- Defect size and growth

4.7.4.1 Existence of defect

In both experiments the system predicted the existence of defect with 100% accuracy. The ANN identified existence of damage after 9559 Epoch for hole diameter experiment and 11245 Epoch for delamination. Figure 4-49 shows the desired output, which is the existence of damage in this case, and the ANN predicted output.

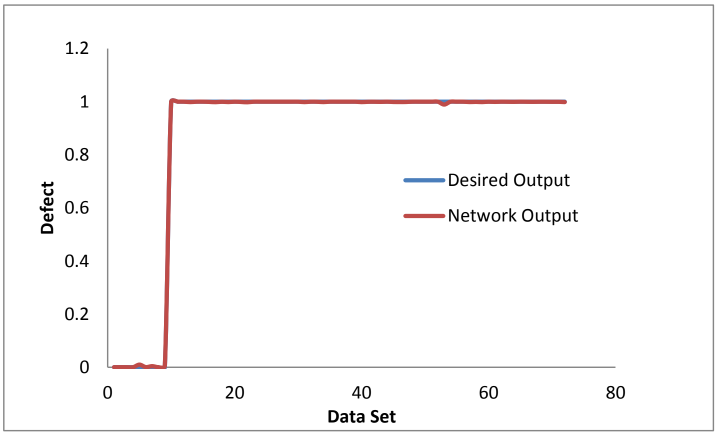

Figure 4-49: Identification of damage existence for hole experiment

In aerospace structures, identification of the existence of damage itself is a good achievement since that is the initiation point for a set of comprehensive testing for structural integrity. A reliable system that identifies the existence of defects will condense frequent NDT testing programs in the future.

4.7.4.2 Strain at FBG sensor location

With the distortions observed during operation of FBG sensors in aerospace composite structures, it is not possible to track the peak of the FBG sensor for strain readings. This will dramatically reduce the reliability of FBG sensor as a strain measuring sensor. In the both experiments the FFFDS predicted the strain as sensor location with 0.3% accuracy with the train values calculated from FEA results (Figure 4-33).

4.7.4.3 Defect size and growth

In the delamination experiment, the FFFDS was used to predict the size of the defect. During the training phase, the data captured while increasing the defect, was used to train the ANN and it was shown that, after the training, ANN could identify damage size accurately. The challenge here is training the ANN with more realistic data.

4.8 Working range of FFFDS

In the design stage of the FFFDS, it is important to identify the working range of the system. During the operating of embedded FBG sensors, the sensors will operate in a particular wavelength range. The FFFDS should be able to capture that wavelength range. Figure 4-50 shows a response spectrum of an FBG sensor at no load condition, and a fixed FBG filter. During the loading, the FBG sensor spectrum moves to the right side allowing the two spectra to intersect. Figure 4-51 shows the sensor at 100N load.

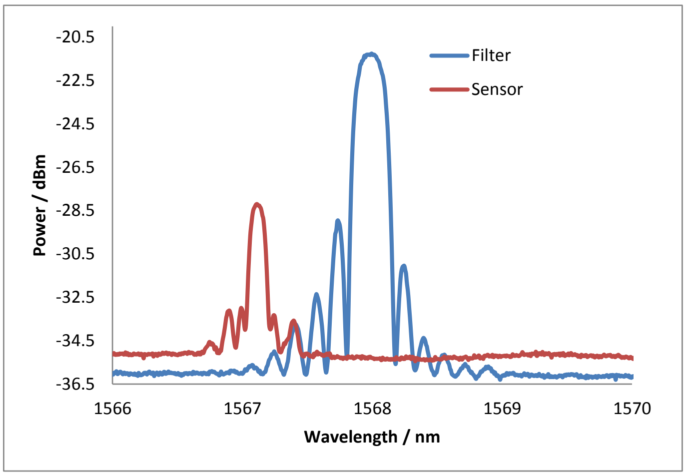

Figure 4-50: Response spectra of an FBG sensor (at no load) and a filter

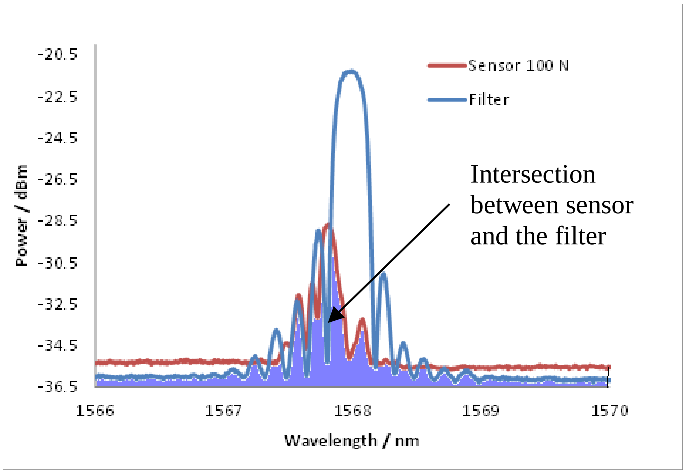

Figure 4-51: Intersection of FBG sensor at 100N and the filter

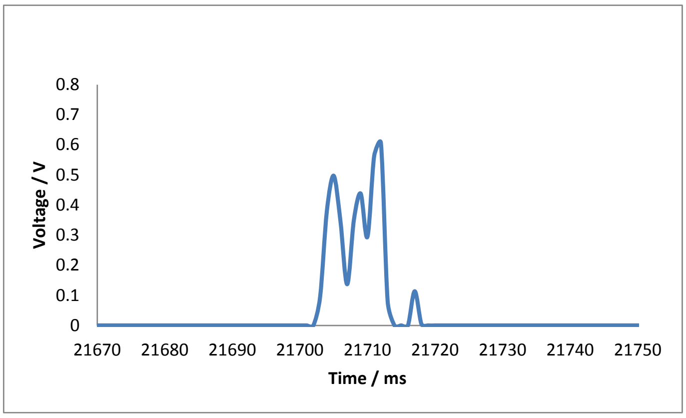

Figure 4-52: PD reading for intersection in Figure 4-8

Figure 4-52 illustrates the corresponding voltage recorded at the PD for the sensor filter intersection shown in the Figure 4-51.

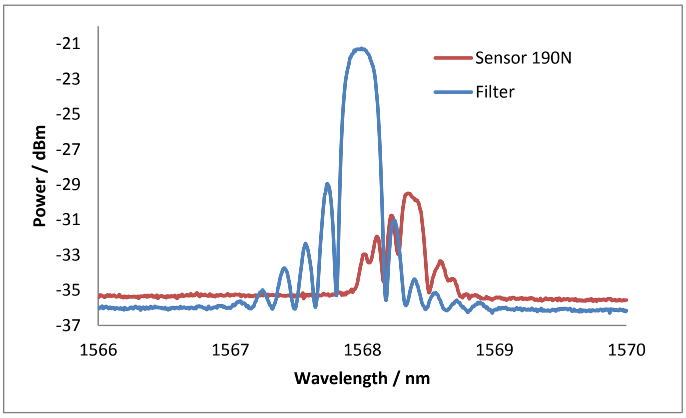

Figure 4-53: FBG response at 190 N loading

At load of 190 N, the sensor location is shown in the Figure 4-53. Further loading on the sensor will move the sensor spectra away from the filter and the intersection between the two spectra disappear. Hence, the PD voltage will not appear after a particular load (in this case 200 N). In the example above, the operating range of the system with one fixed FBG filter is about 1 nm. Using one filter will only provide a narrow operating range for the system and hence more filters need to be accommodated for a wide operating range. Figure 4-54 shows a system with three fixed FBG filters. Three fixed FBG filters will provide an operating range of about 3 nm.

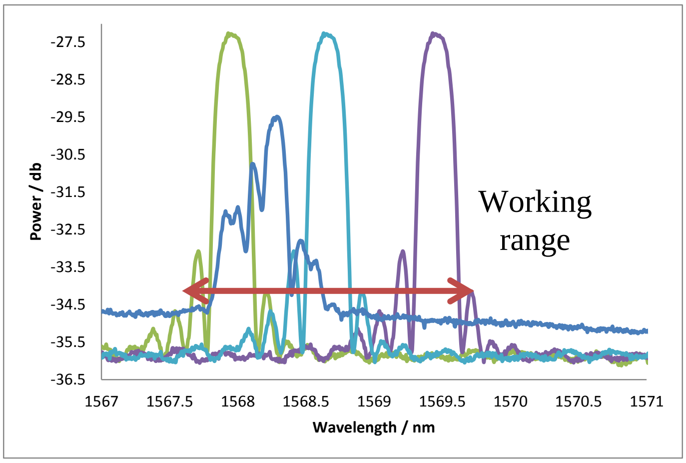

Figure 4-54: FBG response and spectrums of three filters

4.9 Using multiple FBG sensors with FFFDS

The fixed FBG filter decoding system has allowed the SHM system to identify presence of damage and the size of the damage. The presence of damage is comparatively easier to predict than the size of it. The main difficulty of prediction of size is the acquisition of data for the training stage of the ANN. On the other hand, identification of damage, not originally in the structure, is possible as all training data for an undamaged structure can be used for comparison. If the system is used to monitor an aerospace structure, data acquired using test flights and/or from first flights can be used as the undamaged data.

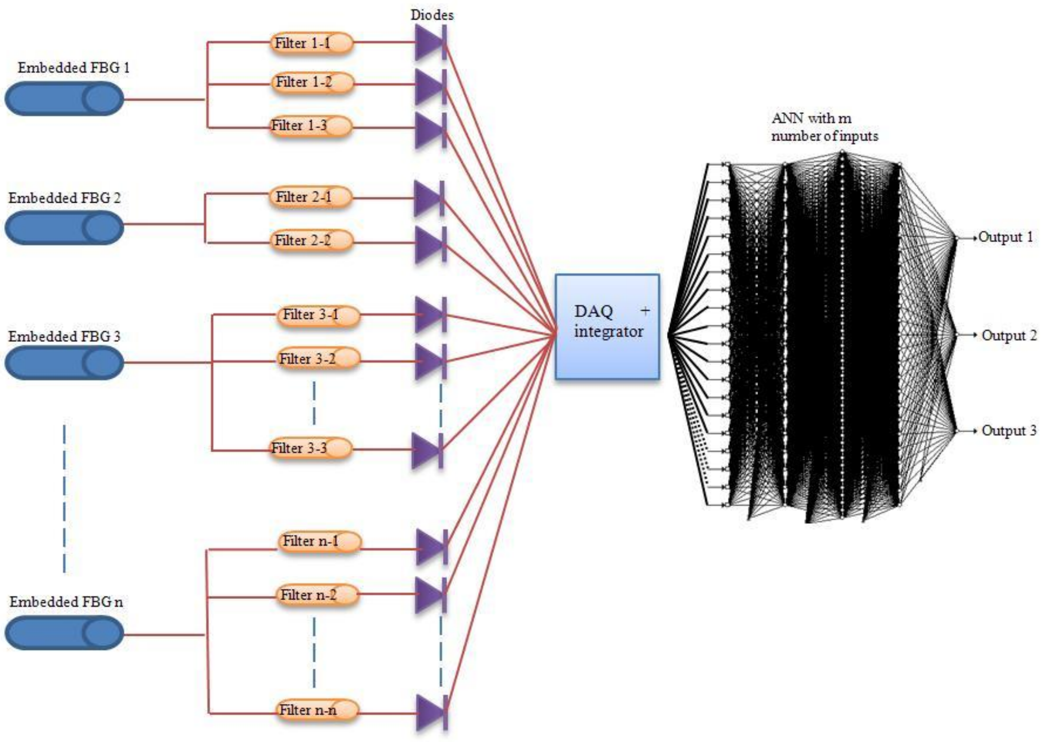

Figure 4-55: Use of multiple FBG sensors with FFFDS

One of the advantages of using FFFDS is the possibility of using multiple sensors for monitoring a structure using the same FFFDS. As the building block (shown in Figure 4-11), is a system with only one fixed FBG filter, and can be used to build the system with multiple fixed FBG sensors (Figure 4-17), it is possible to use the system shown in the Figure 4-17 as a building block to use multiple sensors for damage detection in a structure. Figure 4-55 shows a system of systems used to incorporate a multiple number of sensors to one SHM system. The total system consists of n number of embedded FBG sensors, and each sensor is connected to a multiple number of filters. As mentioned earlier, the effective number of filters needed for each sensor is dependent upon the operating rage of the sensor. Each filter is connected to a photo diode and then to a DAQ. Acquired data was post-processed using the numerical integrator and fed in to the ANN. ANN should have m number of input neurons, which is equal to number of filters (or photo diodes) used.

For an efficient detection of defect in a SHM system, it is essential to identify the number of sensors required, and the locations of each sensor. It is not efficient to use an excessive number of sensors as this will lead to delays in the post-processing of sensor data and also a high implementation cost. In the Chapter 5, a comprehensive study on optimisation of FBG sensor network is presented.

CHAPTER 5
Optimisation of the FBG sensor network

5.1 Introduction

With the increased use of FRP composites in load bearing structures especially in aerospace industry, it is crucial to have *in situ* SHM systems to ensure safe operation of the structure. When it comes to using FBG sensors for the task, it is not possible to monitor the structure using a single sensor. Consequently, many FBG sensors are needed for monitoring the integrity of a complex composite structure. Using randomly placed or uniform sensor networks is a loss of resources and hence an optimum layout of sensors for a particular structure is required for efficient detection of damage. On the other hand, there should not be a provision for error or insensitivity in the process of SHM.

The novel SHM system introduced in Chapter 4 can be readily applied to any established or new FBG sensor network. Consequently, establishing an efficient FBG sensor network is an equally important factor for efficiency of the SHM system. This chapter details a methodology for establishing an optimised FBG sensor network. For the optimisation of a FBG sensor network, strain data were utilised. For this process, FEA simulated data were used and then for verification, FFFDS estimated data were used. This data came from a real sample with embedded FBG sensors. The optimised number of sensors obtained from the FEA simulation was taken for the fabrication of sample. For efficient operation of FFFDS, it is important to have a lesser number of sensors. A large number of sensors in a network make the FFFDS complicated, as the decoding of each sensor uses a separate set of optical circulators and photo diodes.

As a case study, a helicopter blade base structure has been investigated. During the operation, helicopter blade base structures undergo complex loading conditions in the forms of axial, bending and torsion. FEA simulation is used to model the structure for possible load cases to identify stress concentrations (hot spots) which will be used to locate FBG sensors in vicinity of the hot spot. Finally, an optimised number of sensors is discussed. In case of sensor failure, reliability analysis is conducted to investigate the monitoring ability of the system without the failed (obsolete) sensor. The ability of the system to estimate an obsolete sensor has also been investigated.

In this study, the optimum number of sensors needed to monitor a delamination in a FRP helicopter blade base structure was investigated. A complete Finite Element Analysis (FEA) together with an experimental verification was used for the investigation. Initially, the critical sections of the component's critical locations were identified by using FEA simulation. Then a delamination was simulated in the same FEA mesh alone with several FBG sensors simulated in the same FEA mesh. The strain values at the simulated FBG sensors were used with an ANN (ANN1) to identify the delamination.

The procedure was repeated with varying numbers of FBG sensors until the prediction of the algorithm was reached within a 0.1% error level. The optimal number of FBGs was taken at 0.1% error level. It was found that the prediction levels of the algorithm had not significantly improved until the number of sensors reduced to the optimal number of sensors. Furthermore, the effect of obsolete sensors of an optimized sensor network, on prediction of the damage levels, was investigated.

The optimized network was physically fabricated and tested on a representative sample of a component with embedded FBG sensors. Similar delamination, as in

FEA simulation, was purposely created in the sample. With the presence of the delamination, the FBG readings were recorded for the similar load cases as in FEA, at the FBG locations using FFFDS. The decoded FBG readings obtained from FFFDS were fed into an ANN to estimate the strain at each sensor location (as discussed in Section 4.7.1). The estimated strain values were used to verify the optimised FBG sensor network obtained using the FEA simulation data. Further, the experiment was extended to investigate the effect of obsolete FBG sensors on the prediction error level.

5.2 Identification of the locations of FBG sensors in a composite structure to detect damage using FEA simulation

In order to locate FBG sensors in a FRP composite structure, a detailed FEA model has been used. Commercial FEA software, ABAQUS, provided the competency of comprehensive modelling of FRP laminate structures (Chapter 2). The capability of providing layer by layer stress variations can be used to identify potential locations for damage initialization. Hence, those locations can be covered by FBG sensors for damage detection.

5.2.1. The process of optimisation of FBG sensor network

The process of optimisation of the FBG sensor network is graphically illustrated in Figure 5-1. Initially, the critical load bearing structural component need to be identified. To identify the critical structural component, actual operating loading and/or the design loading can be used. To identify stress concentration as a whole and the stress variations in each layer, the component must be modelled in the FEA environment using all, or critical load cases.

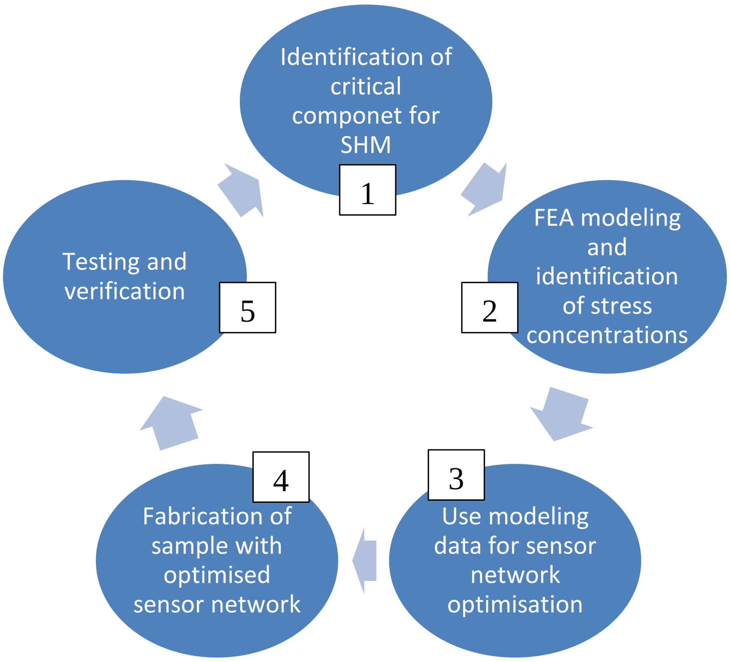

Figure 5-1: Process of optimisation of FBG sensor network

The strain values around the stress concentration have been used as strain readings of simulated FBG sensors in those particular locations. The FEA generated strain values (simulated FBG readings) have been used with an ANN in order to identify damage and/or damage initiation in the pre-identified stress concentration.

To decide on the number of sensor locations, the learning rate (epoch) of ANN was used as the measure. A higher epoch was observed irrespective of the number of FBG sensors. The optimum number of FBG sensors was identified at the lowest epoch, which is obtained when the ANN is operating with highest learning rate. The learning rate is a measure which gives the correlations in between ANN inputs. If the ANN inputs have strong correlation, learning of the ANN is efficient and hence the learning rate is higher. Consequently, the epoch reduces. If the correlation in between

ANN inputs is weak, the learning process is difficult and learning rate lower, and as a result, the epoch will be higher.

In this case study the ANN inputs are the strain reading from FBG sensors (simulated), and hence the learning rate or the epoch of ANN can be used as a measure of the correlation between each sensor in the sensor network. As a result, it is possible to identify the sensor network which gives the lowest epoch, indicating the identified sensor network where the sensors have strong correlation to each other. A trial and error method was used to find the lowest epoch using different numbers of sensors and network with the lowest epoch, was used as the optimised FBG sensor network.

With the optimised number of FBG sensors and their corresponding locations, a specimen was fabricated for verification of the performance of the network. Using the same load cases used in the FEA modelling environment, the specimen was tested. The experimental data was used with the ANN and the result obtained was used to verify the optimised FBG network.

The main advantage of this optimisation process is the possibility of deciding the number and the locations of FBG sensors in the modelling environment. The following study details the use of the proposed process to optimise the FBG sensor network in a helicopter blade base structure.

5.2.2. Case study: Optimisation of FBG sensor network in a helicopter blade base structure

The selected helicopter blade base structure was modelled with the commercial FEA software ABAQUS. The load cases were selected using the operation loads which a helicopter blade base would experience while in operation. Figure 5-2 shows the strain variation observed from simulation of a helicopter blade base under axial tension and torsion loading.

In the real testing environment, due to the limitations of the test equipment, it is difficult to load the specimen in axial, bending and torsion at the same time. Because of these limitations in the test rig, only axial and bending loading was used for the experiment. However, for the process of identifying stress concentrations in the modelling environment, axial, bending and torsional loading was used as shown in the Figure 5-2.

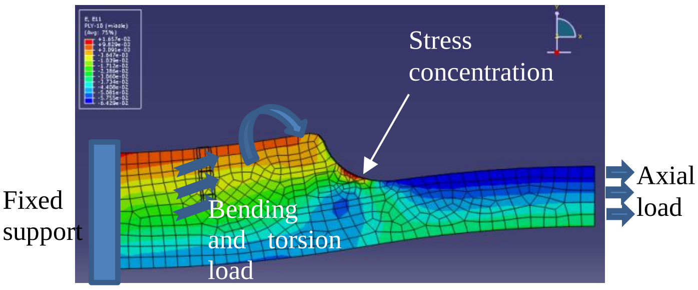

Figure 5-2: Strain variation in helicopter blade base combined loading

The process of selecting a critical structural component for monitoring is graphically illustrated in Figure 5-3. The selected structure has been analysed for all operational and critical load conditions using finite element analysis. The model is used to identify stress concentrations (hot spots) which can lead to damage. During the fabrication of the structure, FBG sensors can be embedded to detect that particular “hot spot” while the structure is in operation.

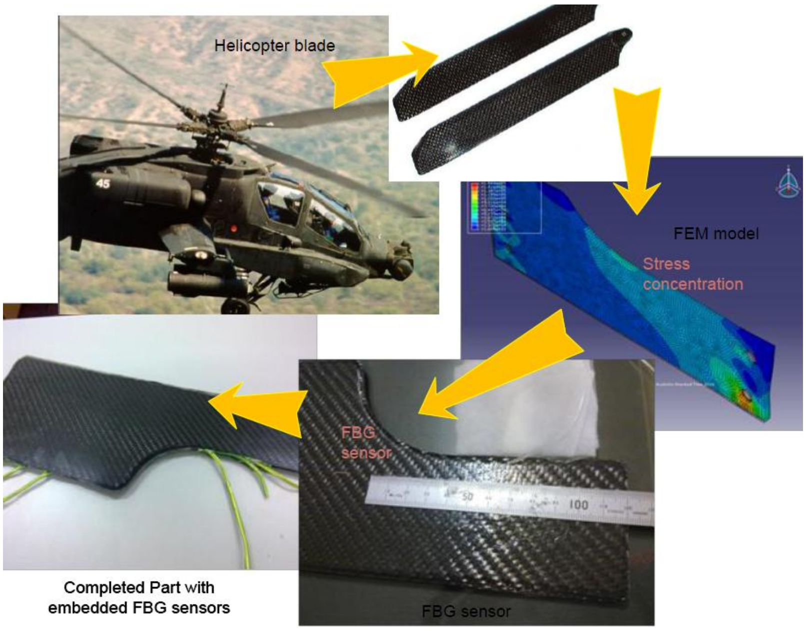

Figure 5-3: Process of locating FBG sensors

The following study details a case study on optimising the FBG sensor network to detect damage in the hot spot shown in Figure 5-2.

5.2.2.5. FEA model of the structure

The laminated structure with 16 layers with layup [0°/0°/90°/90°/-45°/+45°/90°/0°/]s, was modelled and the geometry of component is given in Figure 5-4. To accommodate the modelling of delamination, the structure was modelled in two parts as shown in Figure 5-5. The top part of the specimen consisted of 4 layers with lay-up [0°/0°/90°/90°] of the total thickness 2 mm. The bottom part consisted of 12 layers with lay-up [-45°/+45°/90°/0°/0°/90°/+45°/-45°/90°/90°/0°/0°] of the total thickness 6 mm. Part 1 and Part 2 were initially rigidly connected to each other to make one component using surface constrains available in ABAQUS.

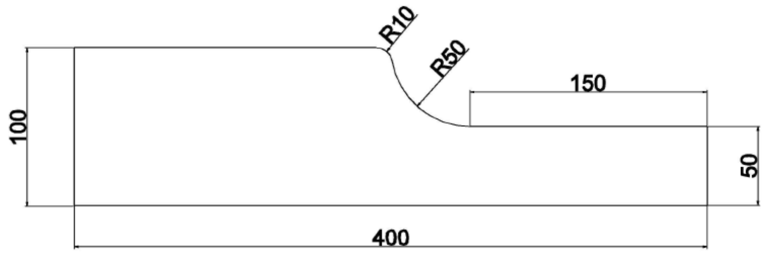

Figure 5-4: Specimen configuration (all dimensions are in millimetres)

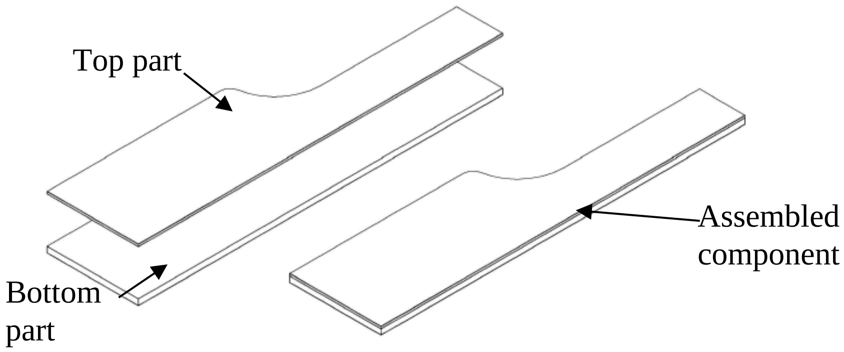

Figure 5-5: Two parts of the model

The bulk material properties were adopted as follows: E1=34.412 GPa, E2=6.531 GPa, E3=6.531 GPa, ν12=0.217, ν13=0.217, ν23=0.336, G12=2.433 GPa, G13=2.433 GPa, and G23=1.698 GPa in the direction of angle 0° (x axis). The model consisted of a mesh with 737 elements and 1674 nodes using SC8R elements which are 8-node quadrilateral in-plane general-purpose continuum shell elements. Use of SC8R elements reduces integration with hourglass control and finite membrane strains with the composite option for the cross-section description. The component was rigidly supported on one side as shown in Figure 5-6, and axial load of 10kN and bending load of 500N was applied in 20 steps. Table 5-1 shows the loading in each load case. The strain distribution of the component was observed for each layer of the laminate. The deformation of the structure at the end of loading steps is shown in the Figure 5-7. As the experimental setup limits the loading in torsion, only axial and bending loading was used for the comparison with the experimental results.

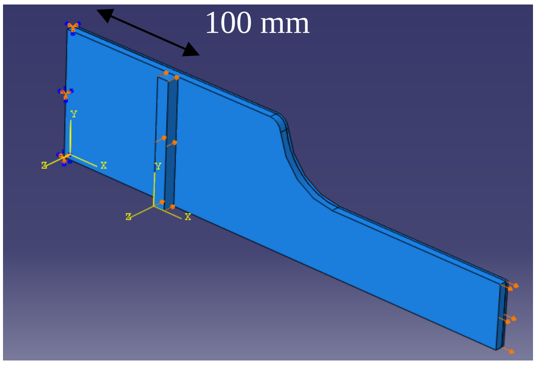

Figure 5-6: Applied load on the component

Table 5-1: Load cases used in the FEA modelling

Load case	Axial load (N)	Bending load (N)
1	500	25
3	1500	75
5	2500	125
8	4000	200
10	5000	250
12	6000	300
15	7500	375
17	8500	425
20	10000	500

Figure 5-7 shows the deformed shape of the 3D model at the end of the analyses (Step 20). The strain distribution of the component was observed for each layer of the laminate.

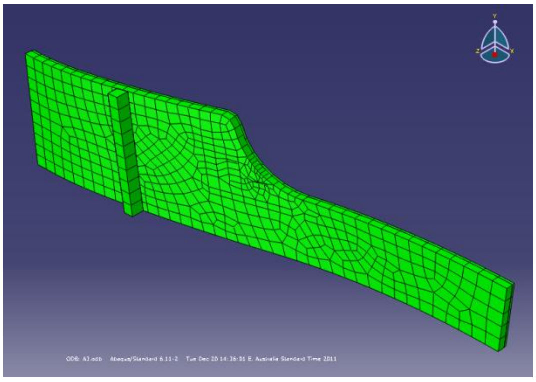

Figure 5-7: Deformed shape of the component

Figure 5-8 shows the stress concentrations in x direction (E11) in the adjacent layers, layers 4 and 5. The concentration point has shifted slightly from layer 4 to layer 5 (as shown in the Figure 5-8(a) and (b). Considering the mismatch in strain distribution, the stress concentration was identified as a potential point for damage initiation. After identifying the hot spot, in the next FEA model semicircular delamination was simulated in the “hot spot”.

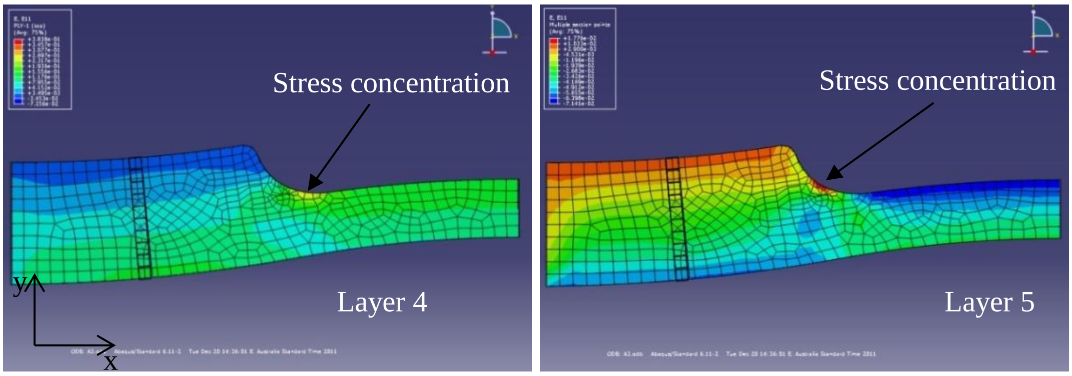

(a) (b)

Figure 5-8: Strain variation in x direction (E11) (a) layer 4 (b) layer 5

5.2.2.6. Modelling delamination in the helicopter blade base structure

For the modelling purposes the delamination used in this study was considered as “ideal delamination” with no friction between separated surfaces. In the simulation of delamination, the contact surface of the top part was partitioned as shown in Figure 5-9(a). Only the partitioned semicircular section Figure 5-9(b) was not connected to the bottom part and the surface interaction was set to “friction less”.

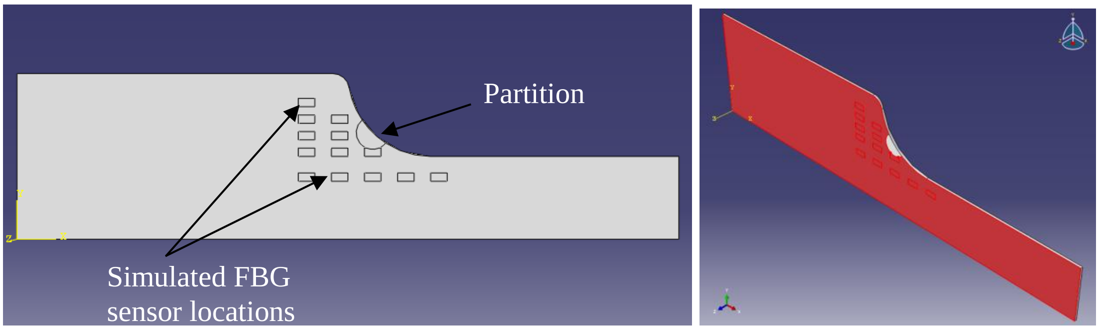

(a) (b)

Figure 5-9: Delamination in the component

Initially 13 locations (A to M) were selected as locations for FBG sensors, as shown in Figure 5-10. Initial placement was arbitrary and strain readings from the top surface of each layer (1 to 16) were extracted. The total number of locations for FBG sensors was 208 (13 x 16) in the beginning of the study. For an example, the notation “A1” provides the sensor in location “A”, layer 1. For the 20 loading steps, the strain reading in E11 direction were recorded.

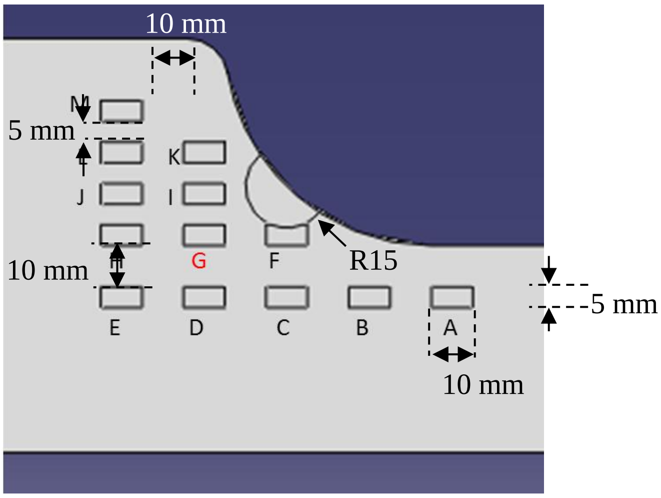

Figure 5-10: Locations of the FBG sensors

In the FEA model, rectangular elements, 10mm long and 5 mm wide, were used as FBG sensors. Average top surface strain in X direction (E11) is used as representation of strain calculated using the FBG sensors. Sensor G9 (which is the sensor in the location G and placed on top of layer 9) is used as the deteriorating sensor (obsolete sensor).

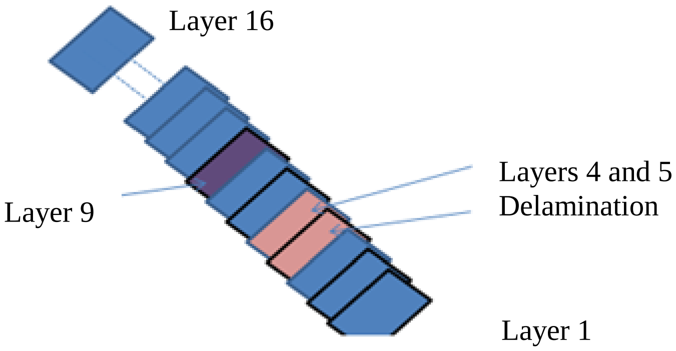

Figure 5-11: Layup of the structure

5.2.2.7. Analysis of FEA data

Extracted FEA data for E11 for all sensor locations for both models, first without delamination, and second with delamination, were used as representations of FBG readings in each load case. Strain readings in the location G for without delamination and with delamination models are given in Figure 5-12(a) and Figure 5-12(b) respectively.

As illustrated in Figure 5-12, there was a clear effect on the strain reading at location G resulting from delamination. Sensor G9 is selected as the sensor for identification of delamination in the model. The delamination is located in between layers 4 and 5. Sensor G9 was placed in layer 9 and hence was a fair distance away from the damage. Strain needs to be transferred through layers 6, 7 and 8 to layer 9. As illustrated in Figure 5-12, the strain level increased in layer 9 and in layer 11 the same strain levels decreased from model without and with delamination.

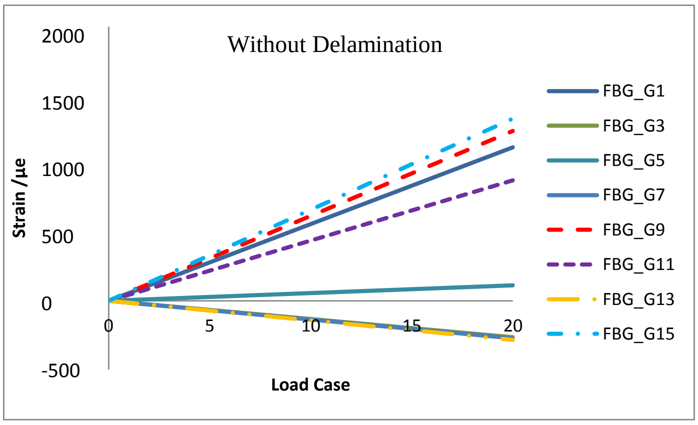

(a)

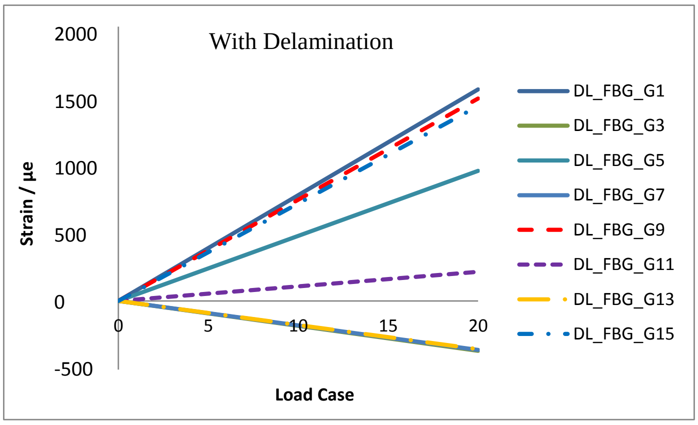

(b)

Figure 5-12: Variation of strain in location G under combined loading

5.2.2.8. Identification of delamination using FBG data generated by FEA

Generated FBG readings (E11 strain in each element location in each layer) were used to identify the existence of delamination using an ANN1. In both the models, with delamination and without delaminations, the data was extracted for each location (A to M) and each layer (1 to 16). But for the identification of delamination, it was found that even with a single sensor, the ANN could identify the delamination accurately. For the identification of the delamination in this study, an ANN which is with three hidden layers has been used. Hidden layers 1, 2 and 3 contain 20, 50 and 25 neurons, as shown in Figure 5-13 (ANN1). The parameters of the ANN are as in Section 4.7.1.

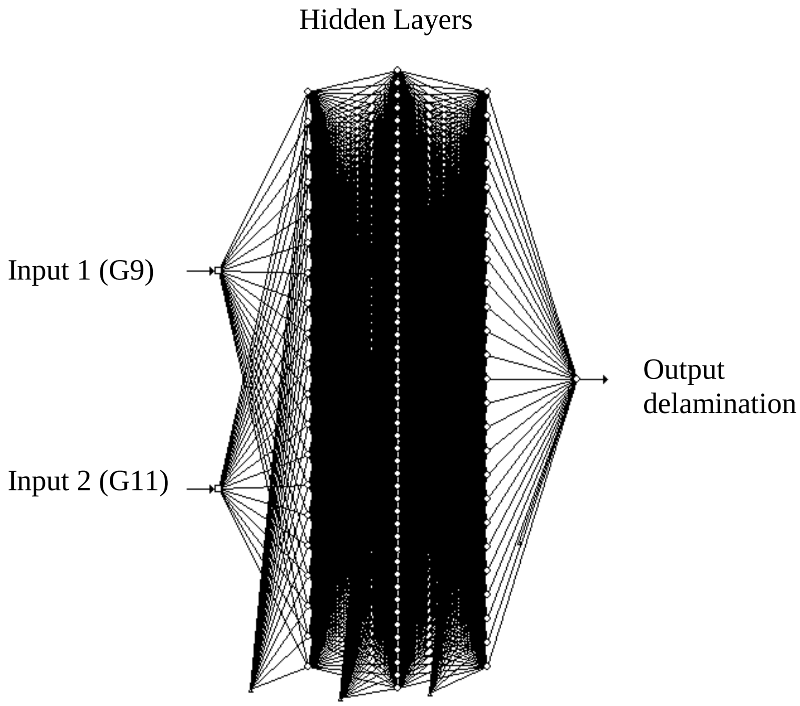

Figure 5-13: ANN used to identify delamination (ANN1)

Figure 5-14 gives the ANN output and the actual existence of delamination. With sensor readings G9 and G11 only the ANN predicted the existence of delamination in

1201 epoch. With sensor G9 only, it took 4878 epoch to identify delamination with 0.1% error. Figure 5-15 shows the learning rate of the ANN with two sensors and single sensor.

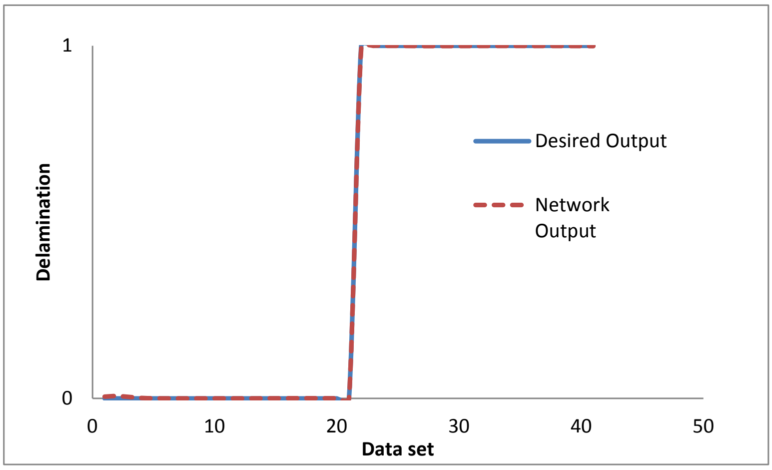

Figure 5-14: Identification of delamination using ANN1

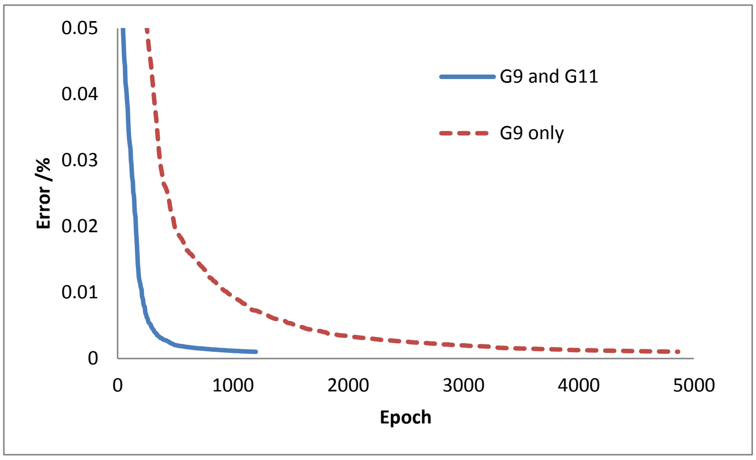

Figure 5-15: Learning rate of the ANN with two sensor data (G9 and G11) and single sensor data (G9)

From the study, it was shown that the identification of delamination is possible with even a single sensor in the modelling environment. It is also important to investigate the effect of losing an embedded sensor to the efficient functionality of the damage detection mechanism.

5.2.3. Prediction of failed (obsolete) FBG sensor

In an FRP composite component, identification of damage using embedded FBG sensors depends on the sensitivity of the FBG sensors to the strain field generated by the existence of a defect. After estimating the possible locations for the initiation of damage with FEA modelling techniques, it is crucial to locate FBG sensors within the modelled strain field in order to identify damage. An optimised number of sensors are needed for the robust operation of the damage detection system. It is not acceptable to have a system depend on a single or small number of FBG sensors. If a sensor accidently failed, (FBG sensors are brittle) the effect of that failure on the system should be investigated. The failure of the sensor may or may not be caused by damage in the FRP structure. If the failure of sensor is caused by structural defect, that defect should be significant and should have been identified in advance by the SHM system. For the following study it was assumed that sensor failure was not caused by damage growth in the FRP structure. One possible cause of the sensor failure is breakage from the egress end of the sensor.

5.2.3.5. Estimation of obsolete FBG sensor reading with multiple FBG sensors

In this study the sensor G9 was the sensor used to identify the existence of a defect in the FRP structure. The location of the sensor G9 is shown in Figure 5-16.

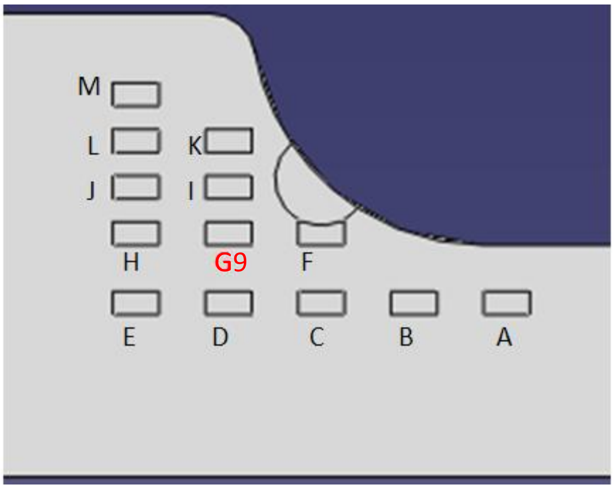

Figure 5-16: Location of the Sensor G9

For the prediction of sensor G9, using surrounding sensors, a different ANN (ANN2) was used. Initially for prediction, a large number of sensors were used. To accommodate the number of sensor inputs to the ANN2, a similar number of input neurons were used. A number of hidden layers was fixed to three layers and other parameters of the ANN were as discussed in Section 4.7.1. Starting with 64 sensors (inputs), it was found that, until the sensor number was reduced to 14, the network took significantly high training epoch (15000+) due to excess data. Even through it is easier to correlate ANN2 inputs with extra amount of data, the excess data overloads the network resulting in a higher training epoch.

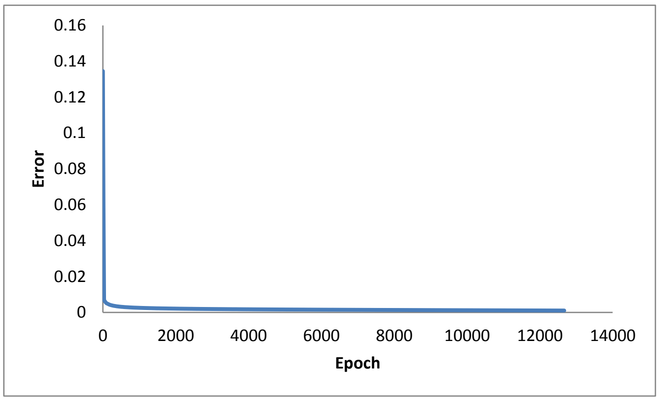

Figure 5-17: Prediction of sensor G9: learning rate with 14 sensors

For the final prediction of sensor G9, 14 sensors in locations I, H, E, D and G were used (I9,I11,I13,H9,H11,H13,E9,E11,E13,D9,D11,D13,G11 and G 13). With the 14 sensors, after 12696 epoch, the ANN predicted sensor G9 with 0.1% accuracy. By reducing the number of sensors the prediction of sensor G9 was carried out. It was observed that the optimum number of sensors to predict G9 was six sensors in locations D13, E13, G13, H13, G11 and I13.

Table 5-2 shows the corresponding epoch for each number of sensors and Figure 5-18 shows the variation of epoch for each number of sensors.

Table 5-2: Prediction of sensor G9 with different numbers of sensors

Number of sensors	Epoch
14	12696
12	12051
10	11932
8	10841
6	9236
4	14227
2	18394

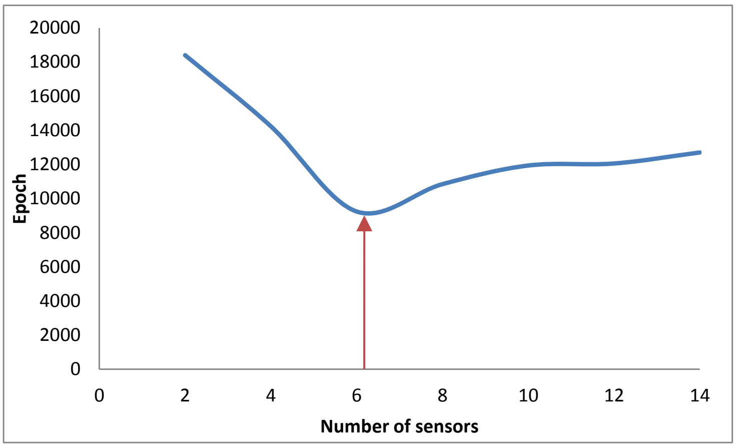

Figure 5-18: Variation of epoch with number of sensors

It was found that, in this case study, the optimum number of sensors to detect delamination in the selected FRP helicopter blade structure is seven. With the use of additional sensors, the system was found to be overloaded which delayed the damage detection process. With the identified optimum number of sensors, the system performed faster and the required accuracy, 0.1%, was obtained. It was observed that it is possible to detect the delamination with just one FBG sensor in the strain field created by the damage. But, to improve the robustness of the system, a total number of seven sensors were used. The proposed technique can address the effect of lost critical sensors for the damage detection process, and hence robustness of the system is improved.

The proposed technique can be used to determine the optimum number of sensors for a particular structure for efficient detection of damage using FBG sensors in the modelling stage.

5.3 Experimental validation of the optimised system – estimation of obsolete sensor

Using the FEA analysed data and the ANN, the optimum number of sensors has been determined. Furthermore, the locations of the sensors also been identified. With the results from the aforementioned study, an FRP specimen was fabricated with embedded FBG sensors in identified locations (G9, D13, E13, G13, H13, G11 and I13).

5.3.1. Fabrication of the specimen

The structural component was fabricated with E glass fibre mats using epoxy resin. The laminate was fabricated with fibre orientation [0/0/90/90/-45/45/90/0]s, similar to the FEA model. The geometry of the specimen is illustrated in Figure 5-4. The woven fabric fibre layup is shown in the

Figure 5-19(a). The locations of the FBG sensors have been decided using the FEA analysis with the use of ANN1. The sensor G9 was used as the sensor to identify the delamination. During the fabrication of the sample, seven FBG sensors, in locations G9, D13, E13, G13, H13, G11 and I13, were embedded.

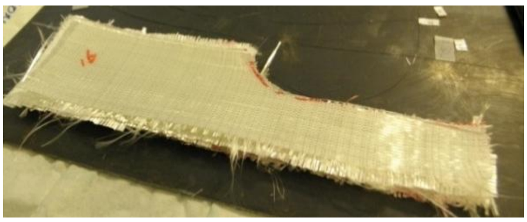

(a)

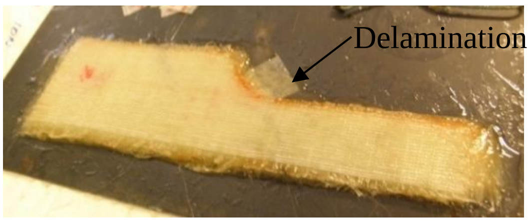

(b)

Figure 5-19: The fabrication of the specimen with embedded FBG sensors

Furthermore, simulated delamination was created in the specimen as shown in the Figure 5-19 (b). The completed specimen is shown in the Figure 5-20.

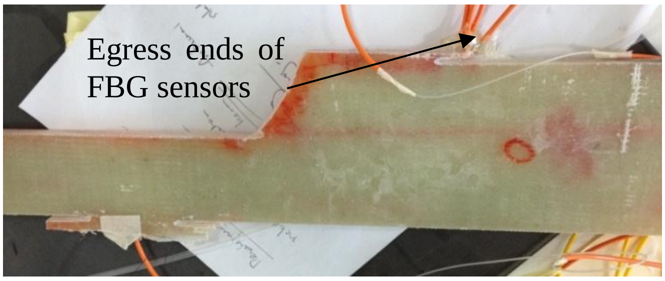

Figure 5-20: Specimen with FBG sensors

5.3.2. Experimentation

The component was rigidly supported on one side as shown in Figure 5-21(a), and axial load of 10kN and bending load of 500N were applied in 20 steps. The loading arrangement is shown in the Figure 5-21(b).

The FBG reading in each load case was decoded, using FFFDS, and recoded for post processing. The load cases are given in the Table 5-3.

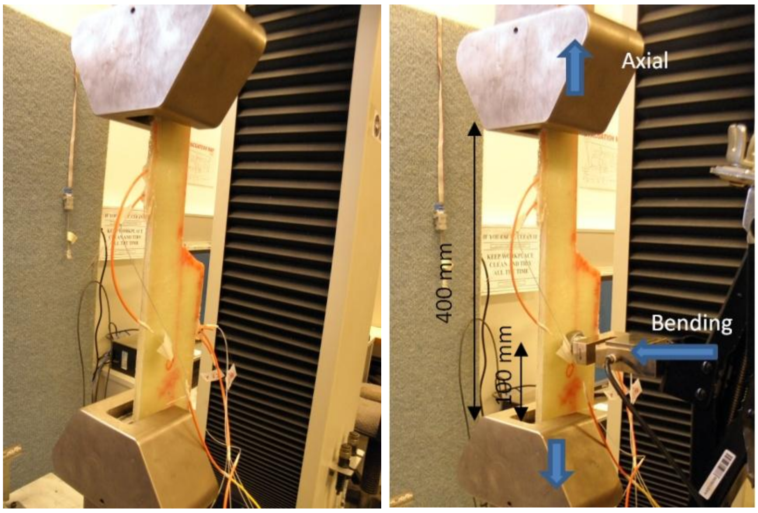

(a) (b)

Figure 5-21: Experimental setup

Table 5-3: Load cases for the loading of the component

Load case	Axial load	Bending load
1	500N	25N
5	2500N	125N
10	5000N	250N
15	7500N	375N
20	10000N	500N

5.3.3. Results and discussion

The strain reading at each load case was estimated using the FFFDS readings and ANN as discussed in Section 4.7.1. The predicted strain readings are shown in Figure 5-22.

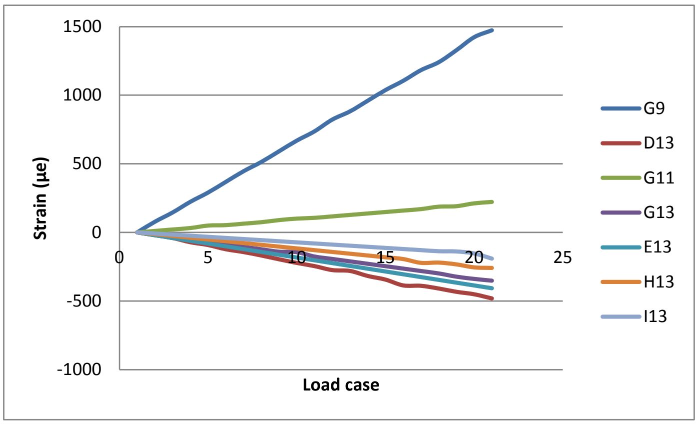

Figure 5-22: Strain estimated form the FFFDS and ANN for each load cases

Figure 5-23 shows the comparison of FEA generated strain and FFFDS estimated strain for sensor G9. The predictions for other sensors have also shown similar accuracy.

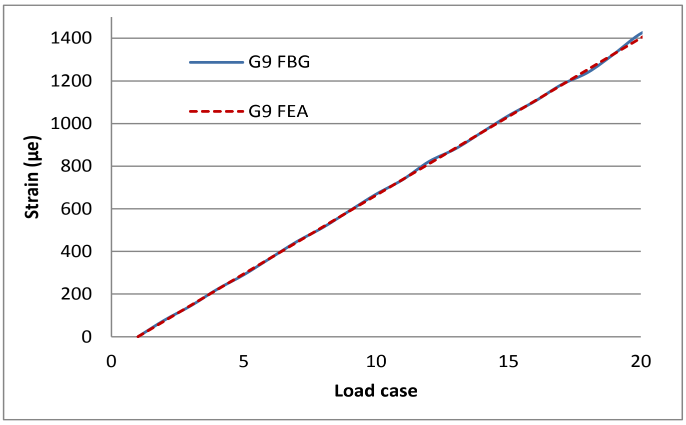

Figure 5-23: Comparison of FEA results with FBG readings for sensor G9

Subsequently, the sensor G9 was disconnected and the other sensor readings were used to predict G9 reading. Similarly, as in previous case discussed in Section 5.3.1.1, the FBG estimated with FFFDS for sensors D13, E13, G13, H13, G11 and I13, were used with an ANN to predict the sensor G9 as shown in the Figure 5-24. The ANN (ANN2) used was with six input neurons and one output neuron. Three hidden layers, 1, 2, and 3, were used with 20, 50 and 25 neurons respectively.

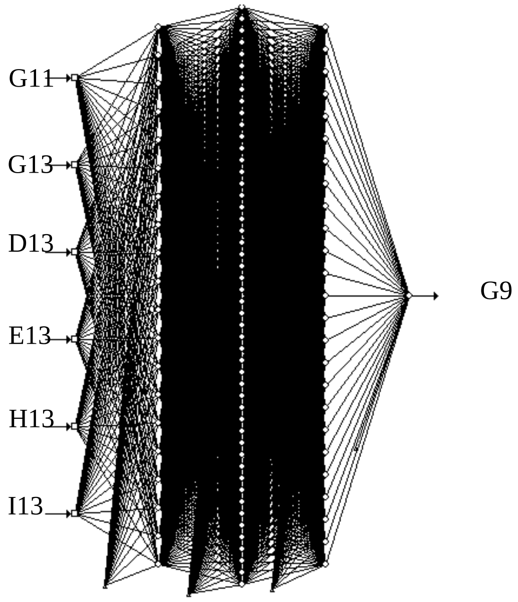

Figure 5-24: ANN used to predict sensor G9 (ANN2)

The ANN predicted the sensor G9 with 0.1% accuracy after 13719 epoch as shown in the Figure 5-25.

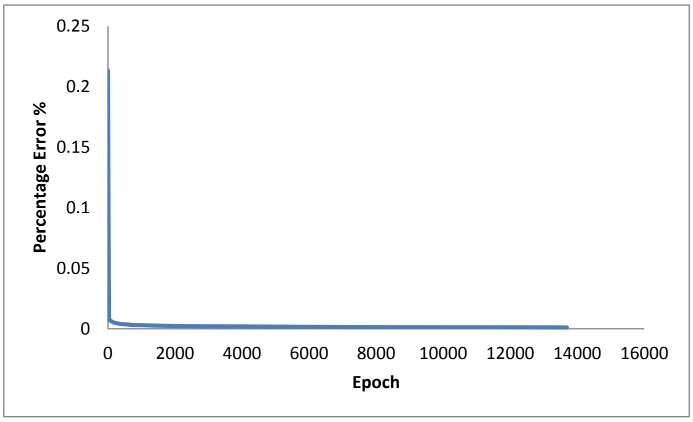

Figure 5-25: Training rate of the ANN

The optimum number of sensors required to identify potential damage in a composite structure was discussed. A complete FEA model was used to identify the sensor locations, to efficiently detect a defect. With the results, the number and locations of the FBG sensors obtained from the modelling environment, an FRP sample was fabricated with embedded FBG sensors. The FRP sample was loaded and the FBG results were used with the ANN for prediction of obsolete sensor.

Compared to the training epoch 9236 obtained from the FEA data, the experimental data took 13719 epoch to predict the obsolete sensor with 0.1% accuracy.

5.4 Conclusions for optimisation of FBG sensor network

A process for setting up an FBG sensor network in an FRP structure was proposed using FEA modelling and ANNs. As a case study, the FBG sensor network in a root of a helicopter blade was investigated. The optimised FBG sensor network was fabricated into a FRP composite helicopter blade structure. The performance of the FBG network was found to be excellent.

Furthermore, the case of a lost critical FBG sensor from an optimised network while in operation, was investigated. It was found that the operational data acquired from the FBG network while the obsolete sensor was in operation, can be used with an ANN to estimate the obsolete sensor. Hence, it was found that the use of an ANN for managing FBG sensor networks and post-processing FBG sensor network data, increases the efficiency and robustness of the SHM system.

CHAPTER 6
Conclusions

This thesis intended to investigate and find corrective measures for current unresolved issues associated with the development of FBG-based SHM systems. A well planned research methodology has been proposed to identify the niche areas of SHM system development and was executed successfully to its completion.

This chapter summarizes the outcomes of this work and discusses possible further work. The breakthrough technologies and procedures achieved under the project can be grouped into three categories:

1. Efficient use of FBG sensors for SHM in advanced composite structures
2. Effective use of FBG spectral data for SHM of advanced composite structures
3. Use of ANN with FBG data for damage detection for SHM.

6.1 Principal achievements

This study planned to solve the unresolved problems associated with applications of FBG-based SHM systems. Six objectives were investigated during the study. All the set objectives of the research were achieved with a great confidence level.

- Identification of general damage matrix which can be monitored using FBG-based SHM system:

Critical damage in composites has been identified. Delamination was selected as the critical damage in this study, as it is difficult to detect from conventional techniques and can have serious consequences if not detected in advance. Delamination was modelled in FEA and simulated in a real composite structure experimentally. Both results were found to be in good agreement.

- Identification of spectral distortion of an FBG sensor in general environment in vicinity of damage:

The embedment process of an FBG sensor in a composite structure was investigated. It was found that pre-tensioning the FBG sensor minimised the spectral distortion. For the protection of FBG sensors while in the manufacturing of composite structures, several protective measures were suggested. By using FEA modelling and testing many samples with embedded FBG sensors, it was verified that the presence of damage can be detected by FBG sensors using the distortion of FBG spectra.

- Identification of limitations of FBG in detection of damage:

Distortion of FBG sensor spectra was thoroughly investigated. It was found that data from existence of damage as well as other effects are imparted into the distortion of FBG response spectra. Using the reduction method to isolate distortion solely due to the damage was found to be impossible as the other effects are non-unique and non-repeatable. It was found that once the optical signal (FBG response) is received, it is impossible to regenerate the strain field using FBG data. The FBG spectral data do not carry location details along with strain data. Consequently, FBG spectral data was found to be one directional. This phenomenon was identified as a major limitation of using FBG sensors for damage detection in composite structures.

- Development of method to quantify spectral distortion with respect to the quality of damage:

A novel method to quantify distortion, “Ds” of FBG response was introduced. The peak power and the HWHM were used to calculate distortion. Furthermore, a novel index was introduced “Distortion Index, DI” for the quantification of spectral distortion with reference to original FBG spectra. It was found that the Distortion Index increases with the increasing damage in composite structures. Consequently, the Distortion Index can be used to identify damage as well as for the quantification of damage.

- Optimisation of FBG network:

Novel methodology is introduced to optimize the FBG sensor network in a composite structure. FEA modelling is used to model the structure in order to generate the strain field of the structure while in operational loading. An ANN was used to find the correlations between FBG locations for optimisation of FBG sensor networks. For a critical location of FBG sensor, several other FBG sensors with correlations were located, so that those FBG sensors could be used to estimate the critical sensor in a failed sensor scenario. The optimised FBG sensor was tested with representative specimen and found to be in excellent agreement with modelling results.

- Development of a damage detection matrix and decision making algorithms and the development of FBG-based SHM systems:

The key achievement of this study is the FFFDS. FFFDS is used to decode distorted FBG response using fixed FBG filters. The decoded data was used to identify damage in composite structures using an ANN. Even through ANN is well known for processing non-linear data; there was no method to feed FBG spectral data into an ANN. The newly developed FFFDS do the above without losing important data in the spectra. In other words the FFFDS made it possible for FBGs to talk to ANN. The capability of ANN was used to train the ANN with FBG data in order to create a reference for the non-damaged structure. The created reference was used to identify initiation of damage.

The research work on FBG-based SHM systems were focused on absolute and/or general systems, but the novelty of the proposed approach is that it uses the non-damage status as a reference for damage detection. The training functionality of ANN was used for referencing. As a result of the reference, it was found that detections of initiation of damage have been confidently achieved. The experimental verification of the system was also found to be excellent.

As a consequence the outcome of this research is the first of its kind and the outcomes are innovative technologies in the FBG-based SHM field. FFFDS is in the process of patenting at the US patent office.

6.2 Summary

Delamination, which is the failure of interface between two layers, is identified as a critical defect in composite structures. Detection of delamination using surface mounted sensors and non-destructive test methods is extremely difficult.

Consequently, embedded sensors have been identified as a solution to overcome weaknesses of surface sensors. The layered construction of the composites, allow the embedding of sensors. For the embedded sensors, the Fibre Bragg Grating (FBG) sensor was identified as the most suitable candidate. It has been shown that the diminutive FBG sensor can be embedded in any location of the composite without compromising the strength of the structure. It is identified that the sensor should be embedded in the stress field of a damage to detect that damage. Embedding the sensor external to a stress concentration makes the sensor insensitive to that stress concentration.

Despite the favourable characteristics of FBG sensors, it was found that the response of an FBG becomes complicated when it is embedded in a complicated structure, while the structure is under complex loading. Several other effects, micro-bending and transverse loading on the FBG sensor have been identified as the causes for this discrepancy. Those effects have been individually identified using a set of experiments. It was found that, with all aforementioned effects and the existence of damage, creates a distorted the FBG spectrum. As a result, the response spectra of an FBG embedded in a complicated structure while the structure is under complex loading, becomes complicated and non-linear. Consequently, is has been identified that for post-processing FBG responses need sophisticated algorithms.

Artificial Neural Networks (ANN) have been identified as a post-processor for processing complicated non-linear signals for identification problems. A novel decoding system was used for decoding FBG spectra using fixed FBG filters to feed into ANN. The wavelength of the fixed FBG filters makes the decoded data wavelength dependent. Several filters were used to cover a broad wavelength range.

It was found that a proper learning session will train an ANN to identify damage even with complicated response spectra. The trained network identified the damage both quantitatively and qualitatively.

Several experimental studies have been used to investigate the decoding system and performance of ANN for damage detection in composite structures. After the learning process, the system identified a growing delamination with 0.01% error using an embedded FBG sensor.

Finally, a case study was conducted to develop an optimum FBG sensor network for efficient damage detection in a composite structure. Proposed methodology used finite element analysis (FEA) data for the optimisation process and hence can be used to locate FBG sensors while the structure is been fabricated. The methodology was experimentally verified using a representative sample.

It can be concluded that all the set objectives of the project was successfully achieved. Therefore, research work presented in this thesis addressed the recognised unsolved problems in FBG-based SHM systems. As a consequence, knowledge gained from this research is the first of its kind. The outcomes are ground-breaking technologies in the SHM field.

6.3 Future work

The ANN used for the study is a general one and was selected for its simplicity and availability. As the development of a decoding technique enabled use of any ANN for damage detection using FBGs, the optimum ANN for damage detection requires investigated. The training technique, back-propagation, may not be the optimum technique for training the ANN. Other training techniques must also be investigated.

For the training of ANN, alternative techniques should be investigated as a means of generating data.

The performance of the FBG-based SHM system needs to be experimented in real application environments. As learning of ANN is a major reason for the successful operation of the system, collecting real data for the learning needs to be investigated. The suggested data collection from initial operations of the structure for training needs to be experimentally verified.

Optimising the ANN, specifically for the damage detection needs to be investigated with the real structure in real working environment. For the application of developed systems in real structures, the development of miniature systems needs to be investigated. As the novel system is only using comparatively miniature equipment, it is possible to develop miniature unit.

References

Adams, R. D., Cawley, P., Pye, C. J., & Stone, B. J. (1978). A vibration technique for non-destructively assessing the integrity of structures. *Journal of Mechanical Engineering Science*, *20*, 93-100.

Akers, L. A. (1989). *VLSI Implementation of Neural Systems in the computer and the brain: Prespective on Humen and Artificial Intelligence*. New York: North Holland.

Alfano, G., & Crisfield, M. A. (2001). Finite element interface models for the delamination analysis of laminated composites: mechanical and computational issues. *International Journal for Numerical Methods in Engineering, 50*(7), 1701-1736. doi: 10.1002/nme.93

Anderson, D. Z., Mizrahi, V., Erdogan, T., & White, A. E. (1993). *Production of in fiber gratings using a diffractive optical element*. *Electronic Letters,* ***29***, 566-568.

Barbero, E. J., & Reddy, J. N. (1991). Modeling of delamination in composite laminates using a layer-wise plate theory. *International Journal of Solids and Structures, 28*(3), 373-388. doi: 10.1016/0020-7683(91)90200-y

Barenblatt, G. I., H.L. Dryden, T. v. K. r. n. G. K. F. H. v. d. D., & Howarth, L. (1962). The Mathematical Theory of Equilibrium Cracks in Brittle Fracture *Advances in Applied Mechanics* (Vol. Volume 7, pp. 55-129): Elsevier.

Bernardin, J. P., & Lawandy, N. M. (1990). Dynamics of the formation of Bragg gratings in germanosilicate optical fibers. *Optics Communications, 79*(3-4), 194-199.

Bishop, C. (1995). *Neural Networks for Pattern Recognition*. Oxford: Oxford University Press.

Chang, F., & Chang, K. (1987). A progressive damage model for laminated composites containing stress concentrations. *Journal of Composite Materials, 21*, 834-855.

Chang, F. K. (2003). *Structural Health Monitoring*. Lancaster: DESTechnol Publications.

Che-Hsien, L. I., Nishiguti, K., & Miyatake, M. (2008). *PPP-BOTDA method to achieve 2cm spatial resolution in Brillouin distributed measuring technique*. Paper presented at the OFT2008.

Crawley, E. F., & Lazarus, K. B. (1989). *Induced strain actuation of composite plates*. Paper presented at the 30th AIAA Structural dynamics and materials conference, Alabama.

d'Almeida, J. R. M., & Monteiro, S. N. (1998). The resin/hardener ratio as a processing parameter for modifying the mechanical behaviour of epoxy-matrix/glass microsphere composites. *Composites Science and Technology, 58*(10), 1593-1598.

D.L.Alkon, & Rasmussen, H. (1988). A Spatial-Temporal Model of Cell Activation. *ScienceMeg, l.239*(4843), 998-1005.

Daniel, I. M., & Ishai, O. (2005). *Engineering Mechanics of Composite Materials* (Vol. 13): Oxford University Press.

Eccles, J. C. (1977). *The Understanding of the Brain*. New York: McGraw-Hill.

Epaarachchi, J. A., & Clegg, R. (2006). An experimental investigation of the properties of cross-ply laminate used for manufacturing of small aircraft components. *Composite Structures, 75*(1-4), 93-99.

Eric, U. (1995). *Fibre Optic Smart Structures*. New York: Jhon & Wiley publications.

Fitzer, E., & Heine, M. (1988). Fibre Reinforcements for Composite Materials. *Composite Materials Series, 2*, 73-148.

Freeman, J. A., & Skapura, D. M. (2007). *Neural Networks, Algorithms, Applications, and Programming Techniques*: Pearson Education.

Garg, A. K., Roy Mahapatra, D., Suresh, S., Gopalakrishnan, S., & Omkar, S. N. (2004). Estimation of composite damage model parameters using spectral finite element and neural network. *Composites Science and Technology, 64*(16), 2477-2493.

Hand, D. P., & Russell, P. S. J. (1990). Photoinduced refractive-index changes in germanosilicate fibers. *Opt. Lett., 15*(2), 102-104.

Haykin, S. (1998). *NeuralNetworks A Comprehensive Foundation* (2 ed.): Prentice Hall.

Hill, K. O., Fujii, Y., Johnson, D. C., & Kawasaki, B. S. (1978). Photosensitivity in optical fiber waveguides: Application to reflection filter fabrication. *Applied Physics Letters, 32*(10), 647-649. doi: 10.1063/1.89881

Hill, K. O., Malo, B., Bilodeau, F., Johnson, D. C., & Albert, J. (1993). *Bragg gratings fabricated in monomode photosensitive optical fiber by UV exposure through a phase mask*. *Applied Physics Letters,* ***62***, 1035-1037.

Hill, K. O., & Meltz, G. (1997). Fiber Bragg grating technology fundamentals and overview. *Lightwave Technology, Journal of, 15*(8), 1263-1276. doi: 10.1109/50.618320

Hill, P. C., & Eggleton, B. J. (1994). Strain gradient chirp of fibre Bragg gratings. *Electronics Letters, 30*(14), 1172-1174. doi: 10.1049/el:19940772

Hinton, M. J., Soden, P. D., & Kaddour, A. S. (2004). Failure Criteria in Fibre-Reinforced-Polymer Composites,. Composite Science and Technology, 64.

Hodgkinson, J. M. (2000). Mechanical Testing of Advanced Fibre Composites. Boca Raton: Woodhead Publications.

Hosni Elhewy, A., Mesbahi, E., & Pu, Y. (2006). Reliability analysis of structures using neural network method. *Probabilistic Engineering Mechanics, 21*(1), 44-53.

Jha, M., & Charalambides, P. G. (1998). Crack-tip micro mechanical fields in layered elastic composites: crack parallel to the interfaces. *International Journal of Solids and Structures, 35*(1â€“2), 149-179.

Kahandawa, G., Epaarachchi, J., Wang, H., & Lau, K. Use of FBG sensors for SHM in aerospace structures. *Photonic Sensors, 2*(3), 203-214. doi: 10.1007/s13320-012-0065-4

Kahandawa, G. C., Epaarachchi, J. A., Wang, H., & Canning, J. (2010). *Effects of the self distortions of embedded FBG sensors on spectral response due to torsional and combined loads.* Paper presented at the APWSHM3, Tokyo, Japan.

Kahandawa, G. C., Epaarachchi, J. A., Wang, H., Followell, D., Birt, P., Canning, J., & Stevenson, M. (2010). *An investigation of spectral response of embedded* Fibre Bragg Grating (FBG) sensors in a hollow composite cylindrical beam under pure torsion and combined loading. Paper presented at the ACAM 6, Perth, Australia.

Kamiya, S., & Sekine, H. (1996). Prediction of the fracture strength of notched continuous fiber-reinforced laminates by interlaminar crack extension analysis. *Composites Science and Technology, 56*(1), 11-21.

Karlik, B., & Olgac, A. V. (2010). Performance Analysis of Various Activation Functions in Generalized MLP Architectures of Neural Networks. *International Journal of Artificial Intelligence And Expert Systems (IJAE), 1*(4), 111-122.

Kartalopoulos, S. V. (1995). *Undertanding Neural Networks and Fuzzy Logic: Basic Concepts and Applications*
IEEE Press.

Kashyap, R. (1999). *Fiber Bragg Gratings* (Vol. 1). San Diego: Acadamic Press.

Kersey, A. D., Davis, M. A., Patrick, H. J., LeBlanc, M., Koo, K. P., Askins, C. G., . . . Friebele, E. J. (1997). Fiber grating sensors. *Lightwave Technology,* Journal of, 15(8), 1442-1463. doi: 10.1109/50.618377

Kortscho, M. T., & Beaumont, P. W. R. (1990). Damage mechanics of composite materials: I- measurements of damage and strength. Composites Science and Technology, 39(4), 289-301.

Lam, D. K. W., & Garside, B. K. (1981). Characterization of single-mode optical fiber filters. Appl. Opt., 20(3), 440-445.

Le Blanc, M., Huang, S. Y., Ohn, M. M., & Measures, R. M. (1994). Tunable chirping of a fibre Bragg grating using a tapered cantilever beam. *Electronics Letters, 30*(25), 2163-2165. doi: 10.1049/el:19941476

Lee, C. S., Hwang, W., Park, H. C., & Han, K. S. (1999). Failure of carbon/epoxy composite tubes under combined axial and torsional loading 1. Experimental results and prediction of biaxial strength by the use of neural networks. *Composites Science and Technology, 59*(12), 1779-1788.

Lewis, E., Sheridan, C., O'Farrell, M., King, D., Flanagan, C., Lyons, W. B., & Fitzpatrick, C. (2007). Principal component analysis and artificial neural network based approach to analysing optical fibre sensors signals. *Sensors and Actuators A: Physical, 136*(1), 28-38.

Liu, P. F., Hou, S. J., Chu, J. K., Hu, X. Y., Zhou, C. L., Liu, Y. L., . . . Yan, L. Finite element analysis of postbuckling and delamination of composite laminates using virtual crack closure technique. *Composite Structures, 93*(6), 1549-1560.

Lopes, N., & Ribeiro, B. (2001, 2001). *Hybrid learning in a multi-neural network architecture.* Paper presented at the Neural Networks, 2001. Proceedings. IJCNN '01. International Joint Conference on.

Lopes, P. A. M., Gomes, H. M., & Awruch, A. M. Reliability analysis of laminated composite structures using finite elements and neural networks. *Composite Structures, 92*(7), 1603-1613.

Lopes, P. A. M., Gomes, H. M., & Awruch, A. M. (2010). Reliability analysis of laminated composite structures using finite elements and neural networks. *Composite Structures*, *92*, 1603-1613.

Mallick, P. K. (1997). *Composite Engineering Handbook* (Vol. 1). New York: Marcel Dekker Inc.

Marshall, D. B., Cox, B. N., & Evans, A. G. (1985). The mechanics of matrix cracking in brittle-matrix fiber composites. *Acta Metallurgica*, *33*(11), 2013-2021.

Martelli, C., Canning, J., Gibson, B., & Huntington, S. (2007). Bend loss in structured optical fibres. *Optical Society of America*, *15*.

Mastro, S. (2005). Optomechanical behavior of Bragg Grating sensors under transverse load. *SEM Proceedings*.

Mastro, S. A. (2005). *Optomechanical Behavior of Embedded Fiber Bragg Grating Strain Sensors.* PhD, Drexel University.

McCartney, L. N. (1998). Prediction transverce crack formation in cross-ply laminates. *Composites Science and Technology, 58*(7), 1069-1081.

McCartney, L. N. (2002). Prediction of ply crack formation and failure in laminates. *Composites Science and Technology, 62*(12â€“13), 1619-1631.

Meltz, G., Morey, W. W., & Glenn, W. H. (1989). Formation of Bragg gratings in optical fibers by a transverse holographic method. *Opt. Lett., 14*(15), 823-825.

Nicholls, J. C., Martin, A. R., & Wallance, B. G. (1992). *From Neuron to Brain* (3 ed.). Sunderland: Sinauer Associates, inc.

Nunes, L. C. S., Olivieri, B. S., Kato, C. C., Valente, L. C. G., & Braga, A. M. B. (2007). FBG sensor multiplexing system based on the TDM and fixed filters approach. *Sensors and Actuators A: Physical, 138*(2), 341-349.

Nunes, L. C. S., Valente, L. C. G., & Braga, A. M. B. (2004). Analysis of a demodulation system for Fiber Bragg Grating sensors using two fixed filters. *Optics and Lasers in Engineering, 42*(5), 529-542.

Okabe, Y., Yashiro, S., Kosaka, T., & Takeda, N. (2000). Detection of transverse cracks in CFRP composites using embedded fiber Bragg grating sensors. *Smart Materials and Structures, 9*(6), 832.

Paterno, A. S., Silva, J. C. C., Milczewski, M. S., Arruda, L. V. R., & Kalinowski, H. J. (2006). Radial-basis function network for the approximation of FBG sensor spectra with distorted peaks. *Measurement Science and Technology, 17*(5), 1039.

Procopio, A. T., Zavaiangos, A., & Cunnigham, J. C. (2003). *Analysis of the Diametrical Compression Test and the Applicability to Plastically Deforming Materials. Journal of Materials Science, 38*, 3629-3639.

Proctor, B., & Yale, B. (1980). New Fibres and their Composites. *Royal Society of London Phil Trans Roy Soc Lond*(A294), 427-436.

Puck, A., & Scharmann, H. (1998). FAILURE ANALYSIS OF FRP LAMINATES BY MEANS OF PHYSICALLY BASED PHENOMENOLOGICAL MODELS. *Composites Science and Technology, 58*(7), 1045-1067.

Reddy, J. N. (1993). An evaluation of equivalent-single-layer and layerwise theories of composite laminates. *Composite Structures, 25*(1–4), 21-35. doi: 10.1016/0263-8223(93)90147-i

Rego, G., Romero, R., Frazao, O., Marques, P. V. S., & Salgado, H. M. (2002, 2002). *Apodisation of uniform fibre Bragg gratings using electric arc* discharges. Paper presented at the Fibre and Optical Passive Components, 2002. Proceedings of 2002 IEEE/LEOS Workshop on.

Reveley, M. S., Kurtoglu, T., Leone, K. M., Briggs, J. L., & Withrow, C. A. (2010). Assessment of the State of the Art of Integrated Vehicle Health Management Technologies as Applicable to Damage Conditions,. NASA/TM- 2010-216911.

Sceats, M. G., Atkins, G. R., & Poole, S. B. (1993). PHOTOLYTIC INDEX CHANGES IN OPTICAL FIBERS. [Review]. Annual Review of Materials Science, 23, 381-410. doi: 10.1146/annurev.ms.23.080193.002121

Sorensen, L., Botsis, J., Gmur, T., & Cugnoni, J. (2007). Delamination detection and characterisation of bridging tractions using long FBG optical sensors. *Composites Part A: Applied Science and Manufacturing, 38*(10), 2087-2096.

Sun, C. T. (Ed.). (2000). *Strength Analysis of Unidirectional Composites and Laminates*. Oxford: Elsevier Science Ltd.

Takeda, S., Okabe, Y., & Takeda, N. (2002). *Detection of delamination in composite laminates using small-diameter FBG sensors*, San Diego, CA, United states.

Takeda, S., Okabe, Y., & Takeda, N. (2003). *Application of Chirped FBG Sensors for Detection of Local Delamination in Composite Laminates*, San Diego, CA, United states.

Takeda, S., Okabe, Y., & Takeda, N. (2008). Monitoring of delamination growth in CFRP laminates using chirped FBG sensors. *Journal of Intelligent Material Systems and Structures, 19*(4), 437-444.

Veiga, C. L. N., Encinas, L. S., & Zimmermann, A. C. (2008). *Neural networks improving robustness on fiber Bragg gratings interrogation systems under optical power variations*.

Waldron, K., Ghoshal, A., Schulz, M. J., Sundeaesan, M. J., Furguson, F., & F.Pai, P. (2002). Damage detection using Finite element and laser operational. *Finite Elements in Analysis and Design, 38*(3), 193-226.

Wang, H., Ogin, S. L., Thorne, A. M., Reed, G. T., & Ussorio, M. (2007). The sensitivity of a polarimetric sensor embedded in unidirectional and cross-ply composite laminates. *Smart Materials and Structures, 16*(3), 642.

Wang, Y., Bartelt, H., Ecke, W., Willsch, R., Kobelke, J., Kautz, M., . . . Rothhardt, M. (2008, 7-9 Nov. 2008). *Fiber Bragg gratings in small-core Ge-Doped photonic crystal fibers.* Paper presented at the Optical Fiber Sensors Conference, 2008. APOS '08. 1st Asia-Pacific.

Watt, W. (1970). *Strong Fibrous Solids.* Paper presented at the Discussion Meeting on Strong Fibrous Solids.

Wildy, S., Cazzolato, B., & Kotousov, A. (2010). Detection of delamination damage in a composite laminate beam utilising the principle of strain compatibility. *Engineering Materials, 417-418*, 269-272.

Wimmer, G., & Pettermann, H. E. (2008). A semi-analytical model for the simulation of delamination in laminated composites. *Composites Science and Technology, 68*(12), 2332-2339.

Wimmer, G., Schuecker, C., & Pettermann, H. E. (2009). Numerical simulation of delamination in laminated composite components â€“ A combination of a strength criterion and fracture mechanics. *Composites Part B: Engineering, 40*(2), 158-165.

Yiping, W., Bartelt, H., Ecke, W., Willsch, R., Kobelke, J., Kautz, M., . . . Rothhardt, M. (2008, 7-9 Nov. 2008). *Fiber Bragg gratings in small-core Ge-Doped photonic crystal fibers.* Paper presented at the Optical Fiber Sensors Conference, 2008. APOS '08. 1st Asia-Pacific.

Zhang, J., Zhao, H., & Rong, X.-w. (2008). *Application of BP neural network in FBG* sensing system performance improvement. Paper presented at the Electronic Packaging Technology & High Density Packaging, 2008. ICEPT-HDP 2008. International Conference on.

Zhou, G., & Sim, L. M. (2002). Damage detection and assessment in fibre-reinforced composite structures with embedded fibre optic sensors-review. Smart Materials and Structures, 11(6), 925-939.

Zimmermann, A. C., Veiga, C., & Encinas, L. S. (2008). Unambiguous Signal Processing and Measuring Range Extension for Fiber Bragg Gratings Sensors Using Artificial Neural Networks— A Temperature Case. Sensors Journal, IEEE, 8(7), 1229-1235. doi: 10.1109/jsen.2008.926523

Appendices

Appendix A Patent Documents

Filing Recept of the patent application

UNITED STATES PATENT AND TRADEMARK OFFICE

UNITED STATES DEPARTMENT OF COMMERCE
United States Patent and Trademark Office
Address: COMMISSIONER FOR PATENTS
P.O. Box 1450
Alexandria, Virginia 22313-1450
www.uspto.gov

APPLICATION NUMBER	FILING or 371(c) DATE	GRP ART UNIT	FIL FEE REC'D	ATTY.DOCKET.NO	TOT CLAIMS	IND CLAIMS
[redacted]	04/06/2012	2422	1250	11-1266-US-NP (24691-499)	20	3

CONFIRMATION NO. 6332

FILING RECEIPT

OC000000053832019

60476
JOHN S. BEULICK (24691)
ARMSTRONG TEASDALE LLP
7700 Forsyth Boulevard
Suite 1800
St. Louis, MO 63105

Date Mailed: 04/24/2012

Receipt is acknowledged of this non-provisional patent application. The application will be taken up for examination in due course. Applicant will be notified as to the results of the examination. Any correspondence concerning the application must include the following identification information: the U.S. APPLICATION NUMBER, FILING DATE, NAME OF APPLICANT, and TITLE OF INVENTION. Fees transmitted by check or draft are subject to collection. Please verify the accuracy of the data presented on this receipt. **If an error is noted on this Filing Receipt, please submit a written request for a Filing Receipt Correction. Please provide a copy of this Filing Receipt with the changes noted thereon. If you received a "Notice to File Missing Parts" for this application, please submit any corrections to this Filing Receipt with your reply to the Notice. When the USPTO processes the reply to the Notice, the USPTO will generate another Filing Receipt incorporating the requested corrections**

Applicant(s)

David A. Followell, Wildwood, MO;
Gayan Chanaka Kahandawa Appuhamillage, Kearneys Spring, AUSTRALIA;
Hao Wang, Middle Park, AUSTRALIA;
Jayantha Epaarachchi, Middle Park, AUSTRALIA;

Power of Attorney: None

Domestic Priority data as claimed by applicant

Foreign Applications (You may be eligible to benefit from the **Patent Prosecution Highway** program at the USPTO. Please see http://www.uspto.gov for more information.)

If Required, Foreign Filing License Granted: 04/19/2012

The country code and number of your priority application, to be used for filing abroad under the Paris Convention, is [redacted]

Projected Publication Date: Request for Non-Publication Acknowledged

Non-Publication Request: Yes

Early Publication Request: No

Title

SIGNAL MONITORING SYSTEM AND METHODS OF OPERATING SAME

Preliminary Class

348

PROTECTING YOUR INVENTION OUTSIDE THE UNITED STATES

Since the rights granted by a U.S. patent extend only throughout the territory of the United States and have no effect in a foreign country, an inventor who wishes patent protection in another country must apply for a patent in a specific country or in regional patent offices. Applicants may wish to consider the filing of an international application under the Patent Cooperation Treaty (PCT). An international (PCT) application generally has the same effect as a regular national patent application in each PCT-member country. The PCT process **simplifies** the filing of patent applications on the same invention in member countries, but **does not result** in a grant of "an international patent" and does not eliminate the need of applicants to file additional documents and fees in countries where patent protection is desired.

Almost every country has its own patent law, and a person desiring a patent in a particular country must make an application for patent in that country in accordance with its particular laws. Since the laws of many countries differ in various respects from the patent law of the United States, applicants are advised to seek guidance from specific foreign countries to ensure that patent rights are not lost prematurely.

Applicants also are advised that in the case of inventions made in the United States, the Director of the USPTO must issue a license before applicants can apply for a patent in a foreign country. The filing of a U.S. patent application serves as a request for a foreign filing license. The application's filing receipt contains further information and guidance as to the status of applicant's license for foreign filing.

Applicants may wish to consult the USPTO booklet, "General Information Concerning Patents" (specifically, the section entitled "Treaties and Foreign Patents") for more information on timeframes and deadlines for filing foreign patent applications. The guide is available either by contacting the USPTO Contact Center at 800-786-9199, or it can be viewed on the USPTO website at http://www.uspto.gov/web/offices/pac/doc/general/index.html.

For information on preventing theft of your intellectual property (patents, trademarks and copyrights), you may wish to consult the U.S. Government website, http://www.stopfakes.gov. Part of a Department of Commerce initiative, this website includes self-help "toolkits" giving innovators guidance on how to protect intellectual property in specific countries such as China, Korea and Mexico. For questions regarding patent enforcement issues, applicants may call the U.S. Government hotline at 1-866-999-HALT (1-866-999-4158).

LICENSE FOR FOREIGN FILING UNDER

Title 35, United States Code, Section 184

Title 37, Code of Federal Regulations, 5.11 & 5.15

GRANTED

The applicant has been granted a license under 35 U.S.C. 184, if the phrase "IF REQUIRED, FOREIGN FILING LICENSE GRANTED" followed by a date appears on this form. Such licenses are issued in all applications where the conditions for issuance of a license have been met, regardless of whether or not a license may be required as

page 2 of 3

set forth in 37 CFR 5.15. The scope and limitations of this license are set forth in 37 CFR 5.15(a) unless an earlier license has been issued under 37 CFR 5.15(b). The license is subject to revocation upon written notification. The date indicated is the effective date of the license, unless an earlier license of similar scope has been granted under 37 CFR 5.13 or 5.14.

This license is to be retained by the licensee and may be used at any time on or after the effective date thereof unless it is revoked. This license is automatically transferred to any related applications(s) filed under 37 CFR 1.53(d). This license is not retroactive.

The grant of a license does not in any way lessen the responsibility of a licensee for the security of the subject matter as imposed by any Government contract or the provisions of existing laws relating to espionage and the national security or the export of technical data. Licensees should apprise themselves of current regulations especially with respect to certain countries, of other agencies, particularly the Office of Defense Trade Controls, Department of State (with respect to Arms, Munitions and Implements of War (22 CFR 121-128)); the Bureau of Industry and Security, Department of Commerce (15 CFR parts 730-774); the Office of Foreign AssetsControl, Department of Treasury (31 CFR Parts 500+) and the Department of Energy.

NOT GRANTED

No license under 35 U.S.C. 184 has been granted at this time, if the phrase "IF REQUIRED, FOREIGN FILING LICENSE GRANTED" DOES NOT appear on this form. Applicant may still petition for a license under 37 CFR 5.12, if a license is desired before the expiration of 6 months from the filing date of the application. If 6 months has lapsed from the filing date of this application and the licensee has not received any indication of a secrecy order under 35 U.S.C. 181, the licensee may foreign file the application pursuant to 37 CFR 5.15(b).

Appendix B Torsion test equipment

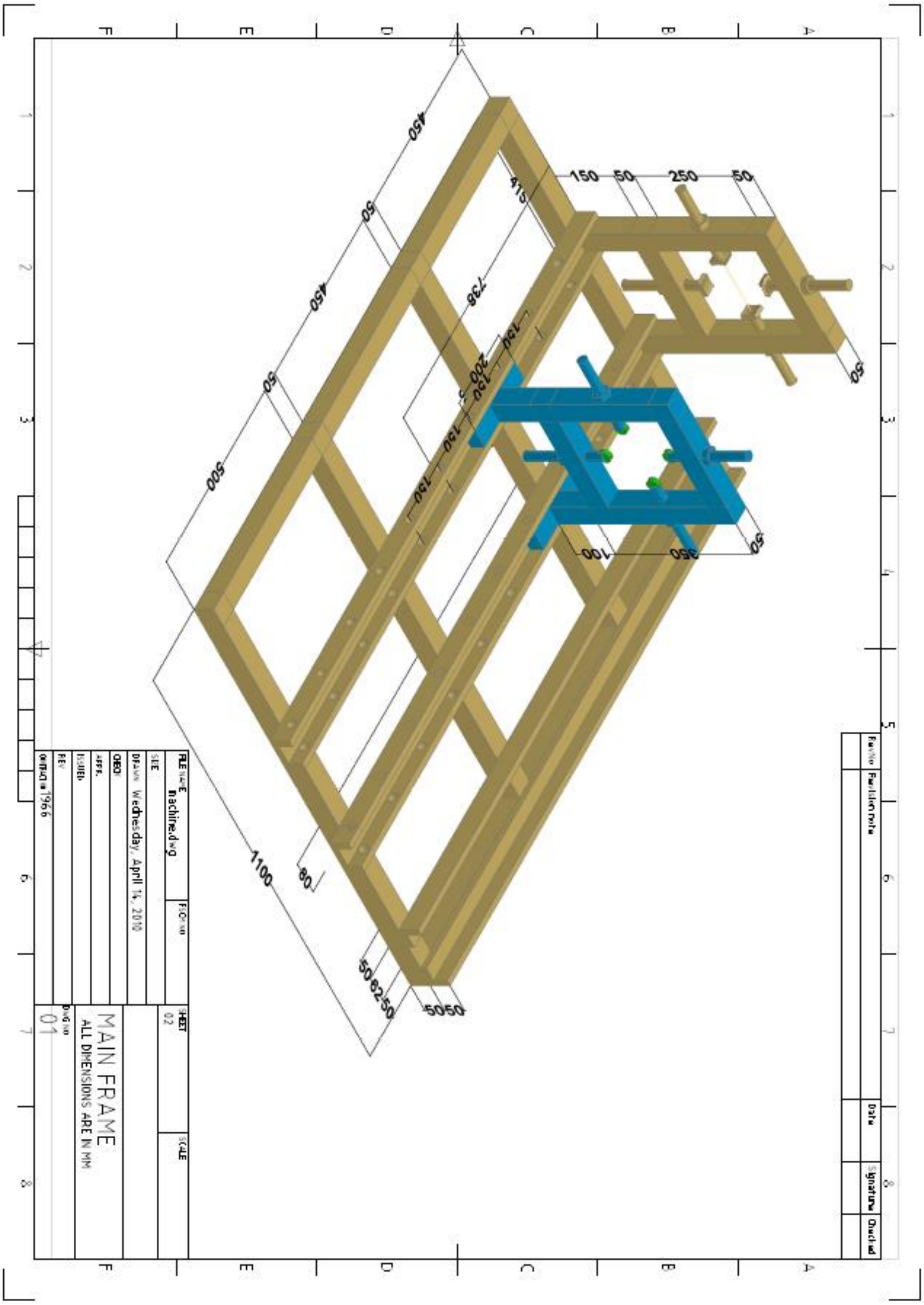

Appendix C Specifications of Equipment used for FFFDS

Photo Diode

PDA20CS
InGaAs Switchable Gain Detector

Chapter 6: Specifications

6.1. Response Curve

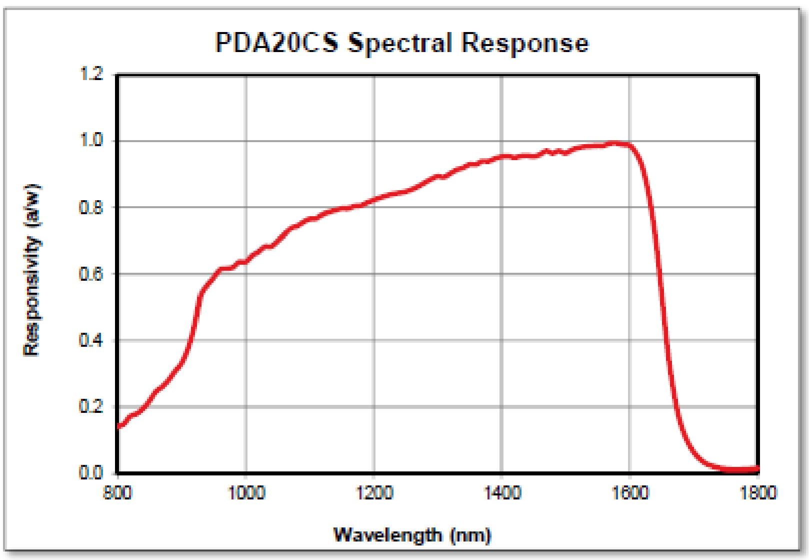

Chapter 2 Description

The PDA20CS is an amplified, switchable-gain, silicon detector designed for detection of light signals over 800 – 1800nm wavelength range. An eight-position rotary switch allows the user to vary the gain in 10 dB steps. A buffered output drives 50 Ω load impedances up to 5 V. The PDA20CS housing includes a removable threaded coupler (SM1T1) and retainer ring (SM1RR) that is compatible with any number of Thorlabs 1" threaded accessories. This allows convenient mounting of external optics, light filters, apertures, as well as providing an easy mounting mechanism using the Thorlabs cage assembly accessories.

Chapter 3 Setup

The detector can be set up in many different ways using our extensive line of adapters. However, the detector should always be mounted and secured for best operation.

1. Unpack the optical head, install a Thorlabs TR-series ½" diameter post into one of the #8-32 (M4 on -EC version) tapped holes, located on the bottom and side of the head, and mount into a PH-series post holder.
2. Connect the power supply 3-pin plug into the power receptacle on the PDA20CS.
3. Plug the power supply into a 50-60Hz, 100-120VAC outlet (220-240VAC for -EC version).
4. Attach a 50Ω coax cable (i.e. RG-58U) to the output of the PDA. When running cable lengths longer than 12" we recommend terminating the opposite end of the coax with a 50Ω resistor (Thorlabs p/n T4119) for maximum performance. Connect the remaining end to a measurement device such as an oscilloscope or high speed DAQ card. Caution: Many high speed oscilloscopes have input impedances of 50Ω. In this case, do not install a 50Ω terminator. The combined loads will equal 25Ω which could allow ~135mA of output current. This will damage the output driver of the PDA20CS.
5. Power the PDA20CS on using the power switch located on the top side of the unit.

Electrical Specifications		
Detector		InGaAs
Active Area		Ø2.0 mm (3.14 mm^2)
Wavelength Range	λ	800 to 1800 nm
Peak Wavelength	λ_p	1550 nm (Typ)
Peak Response	$\Re(\lambda_p)$	0.95 A/W (Typ)
Amplifier GBP		600 MHz
Output Impedance		50 Ω
Max Ouput Current	I_{OUT}	20 mA
Load Impedance		50 Ω to Hi-Z
Gain Adjustment Range		0 dB to 70 dB
Gain Steps		8 x 10dB Steps
Output Voltage	V_{OUT}	0 to 1 V (50 Ω) 0 to 2 V (Hi-Z)

General	
On/Off Switch	Slide
Gain Switch	8 Position Rotary
Output	BNC (DC Coupled)
Package Size	2.76" x 2.06" x 0.88" (70.1 mm x 52.3 mm x 22.4 mm)
PD Surface Depth	0.16" (4.1 mm)
Weight, Detector Only	0.2 lbs
Accessories	SM1T1 Coupler SM1RR Retainer Ring
Operating Temp	0 to 70 °C
Storage Temp	-20 to 125 °C
AC Power Supply	AC – DC Converter
Input Power[4]	31 W 100 – 200 VAC (50 to 60Hz) 220 – 240 VAC (50 to 60 Hz)

[4] *Although the power supply is rated for 31 W the PDA20CS actual usage is <5 W over the full operating range.*

Optical Coupler

Thorlab 10202A-50-FC

2 x 2 Single Mode Fiber Couplers and Taps (Page 1 of 2)

NEW versions

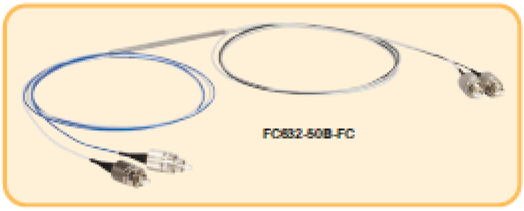

Thorlabs offers single mode 2 x 2 fiber couplers with center wavelengths from 488 nm to 1550 nm. Split ratios of 50:50, 90:10, and 99:1 are available, with the 99:1 versions typically referred to as fiber optic taps. All fiber leads are 0.8 m long (1 m for 10202A) and have a Ø900 µm Hytrel jacket. All specifications below are valid for couplers without connectors.

Feature

- Three Split Ratios Offered
  - 50:50
  - 90:10
  - 99:1
- Center Wavelengths from 488 to 1550 nm
- Termination Options: FC/PC, FC/APC, or Unconnectorized
- FC Connectors Feature 2.0 mm Narrow Keys
- Polarization Insensitive
- High Directivity
- Bidirectional
- 0.8 m Fiber Leads (1 m for 10202A)
- Dual-Wavelength Model for 1310 & 1550 nm
- Custom Connectors Available

Specifications Provided for Unconnectorized Couplers

SERIES	FC488	FC532	FC632	FC780
Center Wavelength	488 nm	532 nm	632 nm	780 nm
Bandwidth	±15 nm	±15 nm	±15 nm	±15 nm
Coupling Ratio	50:50 90:10 99:1	50:50 90:10 99:1	50:50 90:10 99:1	50:50 90:10 99:1
Insertion Loss (Coupling Ratio + Excess Loss)	4.0/4.0 dB (50:50) 1.2/11 dB (90:10) 21/0.7 dB (99:1)	4.0/4.0 dB (50:50) 1.2/11 dB (90:10) 21/0.7 dB (99:1)	3.7/3.7 dB (50:50) 11/1.0 dB (90:10) 21/0.6 dB (99:1)	3.6/3.6 dB (50:50) 11/0.8 dB (90:10) 21/0.4 dB (99:1)
Excess Loss (Typical)	1.0 dB	1.0 dB	≤0.3 dB	0.3 dB
PDL	0.2/0.2 dB (50:50) 0.1/0.2 dB (90:10) 0.05/0.22 dB (99:1)	0.2/0.2 dB (50:50) 0.1/0.2 dB (90:10) 0.05/0.22 dB (99:1)	0.2/0.2 dB (50:50) 0.1/0.2 dB (90:10) 0.05/0.22 dB (99:1)	0.2/0.2 dB (50:50) 0.1/0.2 dB (90:10) 0.05/0.22 dB (99:1)
Directivity	≥50 dB	≥50 dB	>55 dB	≥50 dB
Operating Temperature	-40 to 85 °C	-40 to 85 °C	-40 to 85 °C	-40 to 85 °C
Fiber Type*	460-HP or Equivalent	460-HP or Equivalent	SM600	HI780C

* Equivalent fiber types may be substituted.

SERIES	FC830	FC980	FC1064	10202A
Center Wavelength	830 nm	980 nm	1064 nm	1310 and 1550 nm
Bandwidth	±15 nm	±15 nm	±15 nm	±40 nm
Coupling Ratio	50:50 90:10 99:1	50:50 90:10 99:1	50:50 90:10 99:1	50:50 90:10 99:1
Insertion Loss (Coupling Ratio + Excess Loss)	3.1 - 3.5/3.1 - 3.5 dB (50:50) 9.5 - 10.5/0.4 - 0.7 dB (90:10) 20 - 22/0.15-0.35 dB (99:1)	3.1 - 3.5/3.1 - 3.5 dB (50:50) 9.5 - 10.5/0.4 - 0.7 dB (90:10) 20 - 22/0.15-0.35 dB (99:1)	3.1 - 3.5/3.1 - 3.5 dB (50:50) 9.5 - 10.5/0.4 - 0.7 dB (90:10) 20 - 22/0.15-0.35 dB (99:1)	3.8/3.8 dB (50:50) 12.7/0.8 dB (90:10) 21.6/0.4 dB (99:1)
Excess Loss (Typical)	0.15 dB	0.12 dB	0.12 dB	0.2 dB
PDL	<0.2 dB	<0.15 dB	<0.2 dB	<0.15 dB
Directivity	>55 dB	>55 dB	>55 dB	>60 dB
Operating Temperature	-40 to 85 °C	-40 to 85 °C	-40 to 85 °C	-40 to 85 °C
Fiber Type*	SM800	HI1060FLEX	HI1060FLEX	SMF-28e+

* Equivalent fiber types may be substituted.

Note: Thorlabs uses both narrow (2.0 mm) and wide (2.14 mm) key FC connectors in its product line. Narrow key connectors are used on connectorized fiber, while wide key connectors are used on fiber bulkheads (with few exceptions). This ensures that our connectorized fibers are compatible with all of our mating components.

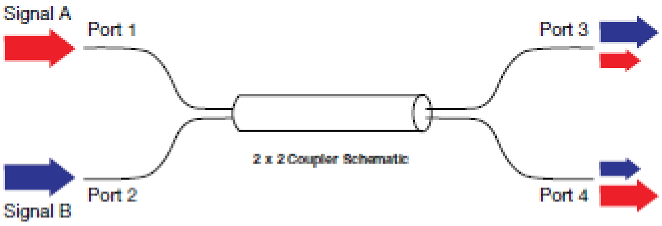

2 x 2 Coupler Schematic

2 x 2 Single Mode Fiber Couplers and Taps (Page 2 of 2)

NEW versions

ITEM #	CENTER WAVELENGTH	COUPLING RATIO	CONNECTORS	$	£	€	RMB
FC488-50B-FC	488 nm	50:50	FC/PC	$ 360.00	£ 259.20	€ 313,20	¥2,869.20
FC488-50B-APC	488 nm	50:50	FC/APC	$ 400.00	£ 288.00	€ 348,00	¥3,188.00
FC488-90B-FC	488 nm	90:10	FC/PC	$ 360.00	£ 259.20	€ 313,20	¥2,869.20
FC488-90B-APC	488 nm	90:10	FC/APC	$ 400.00	£ 288.00	€ 348,00	¥3,188.00
FC488-99B-FC	488 nm	99:1	FC/PC	$ 360.00	£ 259.20	€ 313,20	¥2,869.20
FC488-99B-APC	488 nm	99:1	FC/APC	$ 400.00	£ 288.00	€ 348,00	¥3,188.00
FC532-50B-FC	532 nm	50:50	FC/PC	$ 330.00	£ 237.60	€ 287,10	¥2,630.10
FC532-50B-APC	532 nm	50:50	FC/APC	$ 370.00	£ 266.40	€ 321,90	¥2,948.90
FC532-90B-FC	532 nm	90:10	FC/PC	$ 330.00	£ 237.60	€ 287,10	¥2,630.10
FC532-90B-APC	532 nm	90:10	FC/APC	$ 370.00	£ 266.40	€ 321,90	¥2,948.90
FC532-99B-FC	532 nm	99:1	FC/PC	$ 330.00	£ 237.60	€ 287,10	¥2,630.10
FC532-99B-APC	532 nm	99:1	FC/APC	$ 370.00	£ 266.40	€ 321,90	¥2,948.90
FC632-50B	632 nm	50:50	None	$ 150.00	£ 108.00	€ 130,50	¥1,195.50
FC632-50B-FC	632 nm	50:50	FC/PC	$ 190.00	£ 136.80	€ 165,30	¥1,514.30
FC632-50B-APC	632 nm	50:50	FC/APC	$ 230.00	£ 165.60	€ 200,10	¥1,833.10
FC632-90B	632 nm	90:10	None	$ 150.00	£ 108.00	€ 130,50	¥1,195.50
FC632-90B-FC	632 nm	90:10	FC/PC	$ 190.00	£ 136.80	€ 165,30	¥1,514.30
FC632-90B-APC	632 nm	90:10	FC/APC	$ 230.00	£ 165.60	€ 200,10	¥1,833.10
FC632-99B	632 nm	99:1	None	$ 150.00	£ 108.00	€ 130,50	¥1,195.50
FC632-99B-FC	632 nm	99:1	FC/PC	$ 190.00	£ 136.80	€ 165,30	¥1,514.30
FC632-99B-APC	632 nm	99:1	FC/APC	$ 230.00	£ 165.60	€ 200,10	¥1,833.10
FC780-50B-FC	780 nm	50:50	FC/PC	$ 190.00	£ 136.80	€ 165,30	¥1,514.30
FC780-50B-APC	780 nm	50:50	FC/APC	$ 230.00	£ 165.60	€ 200,10	¥1,833.10
FC780-90B-FC	780 nm	90:10	FC/PC	$ 190.00	£ 136.80	€ 165,30	¥1,514.30
FC780-90B-APC	780 nm	90:10	FC/APC	$ 230.00	£ 165.60	€ 200,10	¥1,833.10
FC780-99B-FC	780 nm	99:1	FC/PC	$ 190.00	£ 136.80	€ 165,30	¥1,514.30
FC780-99B-APC	780 nm	99:1	FC/APC	$ 230.00	£ 165.60	€ 200,10	¥1,833.10
FC830-50B	830 nm	50:50	None	$ 150.00	£ 108.00	€ 130,50	¥1,195.50
FC830-50B-FC	830 nm	50:50	FC/PC	$ 190.00	£ 136.80	€ 165,30	¥1,514.30
FC830-50B-APC	830 nm	50:50	FC/APC	$ 230.00	£ 165.60	€ 200,10	¥1,833.10
FC830-90B	830 nm	90:10	None	$ 150.00	£ 108.00	€ 130,50	¥1,195.50
FC830-90B-FC	830 nm	90:10	FC/PC	$ 190.00	£ 136.80	€ 165,30	¥1,514.30
FC830-90B-APC	830 nm	90:10	FC/APC	$ 230.00	£ 165.60	€ 200,10	¥1,833.10
FC830-99B	830 nm	99:1	None	$ 150.00	£ 108.00	€ 130,50	¥1,195.50
FC830-99B-FC	830 nm	99:1	FC/PC	$ 190.00	£ 136.80	€ 165,30	¥1,514.30
FC830-99B-APC	830 nm	99:1	FC/APC	$ 230.00	£ 165.60	€ 200,10	¥1,833.10
FC980-50B	980 nm	50:50	None	$ 150.00	£ 108.00	€ 130,50	¥1,195.50
FC980-50B-FC	980 nm	50:50	FC/PC	$ 190.00	£ 136.80	€ 165,30	¥1,514.30
FC980-50B-APC	980 nm	50:50	FC/APC	$ 230.00	£ 165.60	€ 200,10	¥1,833.10
FC980-90B	980 nm	90:10	None	$ 150.00	£ 108.00	€ 130,50	¥1,195.50
FC980-90B-FC	980 nm	90:10	FC/PC	$ 190.00	£ 136.80	€ 165,30	¥1,514.30
FC980-90B-APC	980 nm	90:10	FC/APC	$ 230.00	£ 165.60	€ 200,10	¥1,833.10
FC980-99B	980 nm	99:1	None	$ 150.00	£ 108.00	€ 130,50	¥1,195.50
FC980-99B-FC	980 nm	99:1	FC/PC	$ 190.00	£ 136.80	€ 165,30	¥1,514.30
FC980-99B-APC	980 nm	99:1	FC/APC	$ 230.00	£ 165.60	€ 200,10	¥1,833.10
FC1064-50B	1064 nm	50:50	None	$ 150.00	£ 108.00	€ 130,50	¥1,195.50
FC1064-50B-FC	1064 nm	50:50	FC/PC	$ 190.00	£ 136.80	€ 165,30	¥1,514.30
FC1064-50B-APC	1064 nm	50:50	FC/APC	$ 230.00	£ 165.60	€ 200,10	¥1,833.10
FC1064-90B	1064 nm	90:10	None	$ 150.00	£ 108.00	€ 130,50	¥1,195.50
FC1064-90B-FC	1064 nm	90:10	FC/PC	$ 190.00	£ 136.80	€ 165,30	¥1,514.30
FC1064-90B-APC	1064 nm	90:10	FC/APC	$ 230.00	£ 165.60	€ 200,10	¥1,833.10
FC1064-99B	1064 nm	99:1	None	$ 150.00	£ 108.00	€ 130,50	¥1,195.50
FC1064-99B-FC	1064 nm	99:1	FC/PC	$ 190.00	£ 136.80	€ 165,30	¥1,514.30
FC1064-99B-APC	1064 nm	99:1	FC/APC	$ 230.00	£ 165.60	€ 200,10	¥1,833.10
10202A-50	1310 nm & 1550 nm	50:50	None	$ 96.80	£ 69.70	€ 84,22	¥ 771.50
10202A-50-FC	1310 nm & 1550 nm	50:50	FC/PC	$ 136.80	£ 98.50	€ 119,02	¥1,090.30
10202A-50-APC	1310 nm & 1550 nm	50:50	FC/APC	$ 176.80	£ 127.30	€ 153,82	¥1,409.10
10202A-90	1310 nm & 1550 nm	90:10	None	$ 80.50	£ 57.96	€ 70,04	¥ 641.59
10202A-90-FC	1310 nm & 1550 nm	90:10	FC/PC	$ 120.50	£ 86.76	€ 104,84	¥ 960.39
10202A-90-APC	1310 nm & 1550 nm	90:10	FC/APC	$ 160.50	£ 115.56	€ 139,64	¥1,279.19
10202A-99	1310 nm & 1550 nm	99:1	None	$ 100.90	£ 72.65	€ 87,78	¥ 804.17
10202A-99-FC	1310 nm & 1550 nm	99:1	FC/PC	$ 140.90	£ 101.45	€ 122,58	¥1,122.97
10202A-99-APC	1310 nm & 1550 nm	99:1	FC/APC	$ 180.90	£ 130.25	€ 157,38	¥1,441.77

CHAPTERS
Fiber Patch Cables
Bare Fiber
Fiber Optomechanics
Fiber Components
Test and Measurement
SECTIONS
Collimators
Couplers
WDMs
RGB Combiner
Circulators
Fiber Isolators
Faraday Mirrors
Fiber Attenuators
Polarization Controllers
Optical Switches
Mating Sleeves
Terminating Connectors
Termination

Data Acquisition System

MicroDAQ USB-26/30

USB-26/30

USB 250/400KHz 14 Bit A/D Unit with 4x D/A & 24DIO

Ideal for Desktop/Laptop use

DESCRIPTION

The MicroDAQ USB-26/30 is a multi function data acquisition device for the USB bus. The unit has a 14-bit resolution and is the perfect measurement device for portable, laboratory or classroom use.

The MicroDAQ USB-26/30 has two interface options and sample speeds. The A variant is a USB 1.1 device with a sampling rate of 250kHz. The B variant is one of our first data acquisition products featuring the high speed USB 2.0 interface. The 480Mbps bandwidth which USB 2.0 offers allows this unit to have an analog sampling rate of 400kHz across the analog input channels*. This speed is unprecedented in external USB data acquisition products.

Featuring 16 or 32** analog inputs, the unit can be used to measure voltage signals from sensors, transducers, accelerometers and much more. It also features four analog outputs (USB-30 model) which can be used as reference voltages and many other applications. The digital I/O is available in 3 sets of 8 channels which can be programmed as inputs or outputs.

FEATURES

- USB Interface
- 16 / 32 Single Ended or 8/16 Differential Analog Input Channels
- 250kHz / 400kHz (model dependent) Total Sampling speed across 16 channels**
- 4 x 14-bit Analog Outputs (USB-30 Model)
- Onboard 16K FIFO
- 4x Analog Outputs (14-bit)
- 24x DIO lines (3x 8-bit ports)
- I/O Connector: 2x DB25 Male (1 for A/D & 1 for DIO)
- LED indication for power & USB connection
- Ideal for Portable/Laptop Use
- Housing: Plastic ABS with rubber feet
- Operating Temp: 0 to 70°C
- O/S Support for Windows 98/ME/XP/2000 & Linux
- Includes EDRE SDK, EDRE-Labview, EDRE-Testpoint and WaveView for Windows
- Power: Supplied with a 1A 9VDC external PSU
- Power Consumption: 500mA typ @ 9VDC
- Dimensions: 45(H) x 80(W) x 148(L) mm

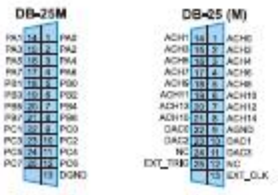

Specifications

Analog Inputs (A/D)	
Input Characteristics	
Input Channels:	16 / 32** Single Ended (Model Dependent)
Input Ranges:	± 2.5V ±5V ± 10V 0-5V 0-10V
Gain Scale:	1 / 10 / 100
Resolution:	14-bit
Input Coupling:	DC
Max Sampling Rate:	250kHz / 400kHz* (Model Dependent)
Clock Source:	Internal 10MHz
	External – Convert (EXT_CLK)
Gate Source:	External – Convert (EXT_GATE)
Input Impedance:	1M Ohm
System Noise:	±1 LSB
Analog Outputs (D/A)	
Output Characteristics	
Output Channels:	None / 4 / 8 (Model Dependent)
Output Range:	± 10V
Resolution:	14-bit
Full Scale Error:	± 2 LSB
Settling Time:	1mS to 0.1% of full scale
Output Drive	+/-10V @ 5mA
Power-On State:	0V
Digital I/O (DIO)	
No. of TTL Lines:	24
Logic Levels:	
Input Low Voltage:	-0.5V to 0.8V
Input High Voltage:	2.0V to 5.0V
Output High Voltage Min:	2.4V
Output Low Voltage Max:	0.45V
Maximum Output Current:	2mA

Ordering Information

Supplied with EDR Enhanced Software, 1.8 Mtr. USB Cable & Universal Switch Mode 9V PSU

USB-26A16	USB 16(SE) or 8(DIFF) Channel 250KHz 14-bit A/D, 24 DIO
USB-26B16	USB2.0 16(SE) or 8(DIFF) Channel 400KHz 14-bit A/D, 24 DIO
USB-26A32	USB 32(SE) or 16(DIFF) Channel 250KHz 14-bit A/D, 24 DIO
USB-26B32	USB2.0 16(SE) or 8(DIFF) Channel 400KHz 14-bit A/D, 24 DIO
USB-30A16	USB 16(SE) or 8(DIFF) Channel 250KHz 14-bit A/D, 4 x 14-bit DACS, 24 DIO
USB-30B16	USB2.0 16(SE) or 8(DIFF) Channel 400KHz 14-bit A/D, 4 x 14-bit DACS, 24 DIO
USB-30A32	USB 32(SE) or 16(DIFF) Channel 250KHz 14-bit A/D, 8 x 14-bit DACS, 24 DIO
USB-30B32	USB2.0 32(SE) or 16(DIFF) Channel 400KHz 14-bit A/D, 8 x 14-bit DACS, 24 DIO

Please Note:

* Please note that a PC with a USB 2.0 compliant interface is required to achieve these speeds.

** On models with 32 inputs, the channels can only be sampled in banks of 16. If you are

Appendix D MATLAB code for numerical integration of FBG spectral data

MATLAB Programme

```
clc;
dt = 0.05;
%t = Time;
%y = PD1;
%yy = PD2;
%yyy = PD3;

a1 = xlsread('850N.xls');

t = a1(:,1);
y = a1(:,2);
yy = a1(:,3);
yyy = a1(:,4);
 % Find % --------------------------
 yyd = 0.007;
 idi1 = find(yyy>= yyd);
  idi2a = idi1(1);
idi2b = idi1(length(idi1));
ta = t(idi2a)
 tb = t(idi2b)
```

```
  %ta = 0.765;

%tb = 0.768;


% Integration ------------------------

idi_t1 = find(t>=ta & t<=tb);

t1 = t (idi_t1);

y1 = y(idi_t1);

yy1 = yy(idi_t1);

yyy1 = yyy(idi_t1);


I1 = trapz(t1,y1)

I2 = trapz(t1,yy1)

I3 = trapz(t1,yyy1)

 I = {I1,I2,I3}

 xlswrite('Intval.xls',I, 'sheet1', 'A2');

 % Plot % ------------------------------

figure(1)

plot(t,y,'o')

plot(t,yy,'+')

plot(t,yyy,'*')

 hold on

plot (t, y); hold all; plot (t, yy); plot (t, yyy);

plot(t.*0+ta,y)

plot(t.*0+tb,y)

xlabel('t')
```

ylabel('y')

grid on

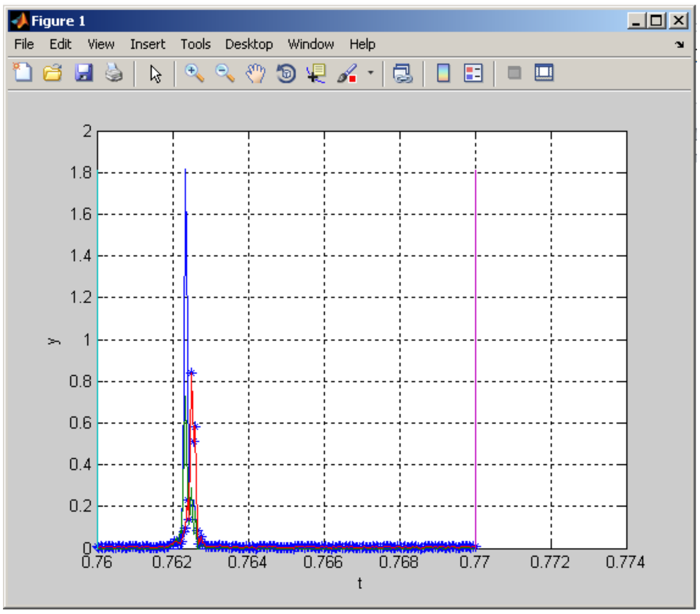

Figure C-0-1: Plot of data at load 850N

Integrated Outputs

ta =

0.7600

tb =

0.7700

I1 = 2.2656e-004

I2 = 1.2761e-004

I3 = 1.9434e-004

Input matrix vales for ANN

I =

[2.2656e-004] [1.2761e-004] [1.9434e-004]

>>

Table C-1: The output data for all load steps (0N to 1000N)

Load	I1	I2	I3
0	0	2.72E-06	2.30E-05
25	9.52E-06	2.11E-05	3.97E-05
50	8.39E-06	1.70E-05	2.98E-05
75	8.94E-06	1.95E-05	4.97E-05
100	8.48E-06	2.14E-05	4.46E-05
125	7.57E-06	2.14E-05	4.93E-05
150	8.36E-06	1.91E-05	4.59E-05
175	9.16E-06	2.19E-05	4.78E-05
200	9.25E-06	1.97E-05	4.66E-05
225	8.73E-06	2.36E-05	4.34E-05
250	8.97E-06	2.20E-05	4.81E-05
275	7.63E-06	1.96E-05	5.79E-05
300	8.42E-06	2.00E-05	4.29E-05
325	9.00E-06	2.31E-05	6.11E-05
350	8.12E-06	2.08E-05	5.19E-05
375	8.79E-06	2.04E-05	5.35E-05
400	8.64E-06	1.94E-05	5.60E-05
425	9.03E-06	1.96E-05	5.31E-05
450	9.61E-06	2.05E-05	5.45E-05
475	9.49E-06	2.02E-05	6.58E-05
500	9.89E-06	2.34E-05	5.37E-05
525	1.06E-05	2.20E-05	5.92E-05

Load	I1	I2	I3
550	9.64E-06	2.24E-05	5.61E-05
575	1.21E-05	2.51E-05	5.76E-05
600	1.50E-05	3.00E-05	6.78E-05
625	2.04E-05	2.93E-05	5.10E-05
650	2.69E-05	3.27E-05	5.49E-05
675	5.40E-05	4.37E-05	6.56E-05
700	5.18E-05	4.60E-05	7.00E-05
725	7.81E-05	5.71E-05	8.75E-05
750	1.03E-04	6.88E-05	1.00E-04
775	1.20E-04	7.68E-05	1.04E-04
800	2.29E-04	1.16E-04	1.14E-04
825	2.52E-04	1.29E-04	1.45E-04
850	2.27E-04	1.27E-04	1.94E-04
875	1.96E-04	1.04E-04	2.03E-04
900	2.27E-04	1.20E-04	2.36E-04
925	2.59E-04	1.26E-04	2.06E-04
950	2.71E-04	1.40E-04	2.04E-04
975	2.48E-04	1.38E-04	2.14E-04
1000	2.25E-04	1.14E-04	1.96E-04

Appendix E ANN for strain estimation

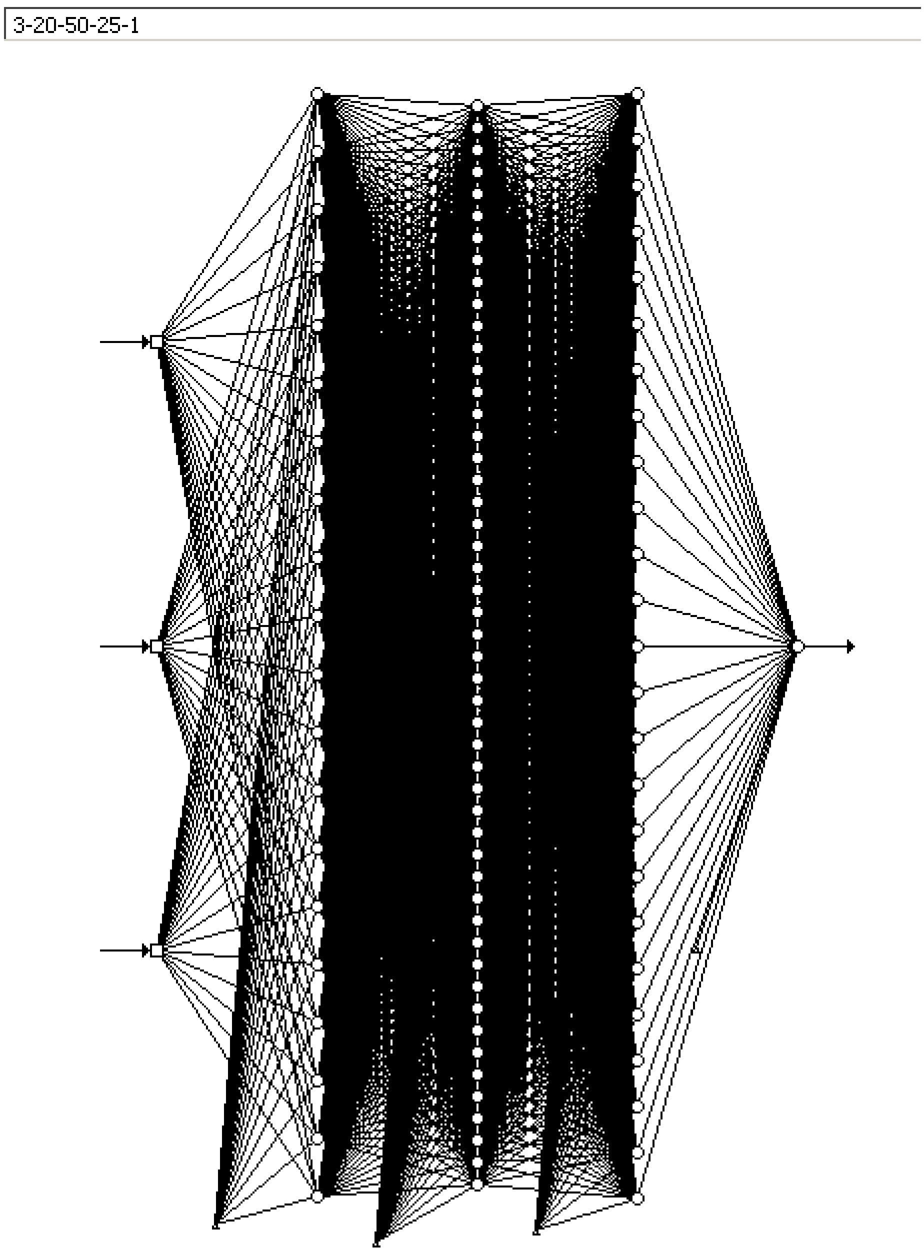

Figure D-0-2: The ANN used for strain estimation

C Code for the ANN

```
/**
 Created by Gayan Kahandawa
*/
#include <math.h>
/**
 inputs  - array of 3 element(s), containing the network input(s).
 outputs - array of 1 element(s), that will contain the network output(s).
 Note : The array inputs will also be changed. Its values will be rescaled between -1
and 1.
*/
void Gayan(double * inputs, double * outputs) {
        double mainWeights[] = {2.872879740189390, -2.583549979881009, -
0.752151018781287, -1.135131192390938, 0.681420177946371,
1.948531337507985, -0.411732541894937, 1.910039666244582, -
2.298438136085826………0.238498234388381, 2.578971596556626, -
2.278428291720948, 1.652815002197443, 2.172203084927900,
0.086502529849448, -0.219379239230267, 0.446856695586866,
1.047303263489046, -1.363940625633989, 2.281928793835090, -
1.744765031520035, 0.190683540058157, 0.094383493902343, -
1.972993259677275, -1.191859815593576};
        double * sw = spaceWeights;
        double mk[95];
        double *m = mk;
        double hiddenLayer1outputs[20];
```

```
double hiddenLayer2outputs[50];
double hiddenLayer3outputs[25];
int c;

inputs[0] = -1.0 + (inputs[0] - 0.000000000000000) / 0.000135500000000;
inputs[1] = -1.0 + (inputs[1] - 0.000002720000000) / 0.000068640000000;
inputs[2] = -1.0 + (inputs[2] - 0.000023000000000) / 0.000106500000000;
mk[0] = *sw++;
for(c = 0; c < 3; c++) mk[0] += *sw++ * inputs[c];
mk[0] = 1.0 / (1.0 + exp(-mk[0]));
mk[1] = *sw++;
for(c = 0; c < 3; c++) mk[1] += *sw++ * inputs[c];
mk[1] = 1.0 / (1.0 + exp(-mk[1]));
mk[2] = *sw++;
for(c = 0; c < 3; c++) mk[2] += *sw++ * inputs[c];
mk[2] = 1.0 / (1.0 + exp(-mk[2]));
mk[3] = *sw++;
for(c = 0; c < 3; c++) mk[3] += *sw++ * inputs[c];
mk[3] = 1.0 / (1.0 + exp(-mk[3]));
mk[4] = *sw++;
for(c = 0; c < 3; c++) mk[4] += *sw++ * inputs[c];
mk[4] = 1.0 / (1.0 + exp(-mk[4]));
mk[5] = *sw++;
………………………………………………..
mk[92] = *sw++;
```

```
for(c = 0; c < 3; c++) mk[92] += *sw++ * inputs[c];
hiddenLayer1outputs[3] = exp(-(hiddenLayer1outputs[3] * hiddenLayer1outputs[3]));
hiddenLayer1outputs[3] *= *m++;
hiddenLayer1outputs[4] = *mw++;
for(c = 0; c < 3; c++) hiddenLayer1outputs[4] += *mw++ * inputs[c];
hiddenLayer1outputs[4] = exp(-(hiddenLayer1outputs[4] * hiddenLayer1outputs[4]));
hiddenLayer1outputs[4] *= *m++;
hiddenLayer1outputs[5] = *mw++;
…………………………..
for(c = 0; c < 25; c++) outputs[0] += *mw++ * hiddenLayer3outputs[c];
outputs[0] = 1.0 / (1.0 + exp(-outputs[0]));
outputs[0] = 0.000000000000000 + (outputs[0] - 0.000000) * 1000.000000000000000;
}
```

Final network weights: Main network

Table D-2: Weights of the main network

	From the input layer			
To the 1st hidden layer	bias	1th neuron	2th neuron	3th neuron
1st neuron	2.87288	-2.58355	-0.75215	-1.13513
2nd neuron	0.68142	1.94853	-0.41173	1.91004
3th neuron	-2.29844	-1.4724	-1.65286	-0.53848
4th neuron	-2.15219	-0.86625	-1.86924	0.05886
5th neuron	-2.16003	1.22267	-0.24768	0.806822
6th neuron	0.779424	1.79353	-1.10349	2.70755
7th neuron	-0.04136	-0.06319	-2.24885	-1.08254
8th neuron	1.60604	-0.88724	-2.55918	3.38869
9th neuron	-1.64867	-0.23778	2.76324	-1.00212
10th neuron	1.48818	-0.08192	-0.06689	-3.05389
11th neuron	-0.02124	1.76989	2.93786	-0.31239
12th neuron	-1.18936	-0.16613	0.617685	-1.18058
13th neuron	0.555094	-0.39536	-0.15492	2.82352
14th neuron	0.511283	-2.79541	-2.77048	-1.84054
15th neuron	-2.2698	1.05565	-2.06892	1.94697
16th neuron	0.510544	0.377473	-2.60716	2.94021
17th neuron	-1.65615	-0.51197	-2.39026	0.601149
18th neuron	-1.77626	-0.46264	0.183825	-0.42747
19th neuron	1.29329	2.87221	0.346652	-0.37826
20th neuron	1.52543	0.009152	-2.08735	2.98758